

https://dspace.org/

A study of WC-X systems for potential binders for WC

Kumi, David Ofori

2012-01-31
http://hdl.handle.net/10539/11218

Downloaded from a DSpace repository. https://dspace.org/

A STUDY OF WC-X SYSTEMS FOR POTENTIAL BINDERS FOR WC

David Ofori Kumi

A dissertation submitted to the Faculty of Engineering and the Built Environment, University of the Witwatersrand, in fulfilment of the requirements for the degree of Master of Science in Engineering (Metallurgy and Materials Engineering)

JOHANNESBURG, 2011

DECLARATION

I David Ofori Kumi, declare that this dissertation is my own unaided work. It is being submitted for the degree of Master of Science in Engineering to the University of the Witwatersrand, Johannesburg. It has not been submitted before for any degree or examination to any other university

…… ……

Signature Date

ABSTRACT

This work was done to select a possible replacement for cobalt as a binder through a phase diagram approach using selected WC-X systems. The study was in two parts; experimental and calculations using Thermo-Calc. Potential binders were identified by searching for solid solution formation, a similar melting point to cobalt, and a small solubility for WC as main requirements, from phase diagrams. The experimental samples were designed to be 50 at.% WC and 50 at.% binder for easy manufacturing and analysis, even though this is not an optimum amount for application. Twelve different alloy compositions were prepared and were analysed in both as-cast and heat treated conditions. The samples were annealed at 1000ºC for 168 hours under vacuum. Microstructure characterization was carried out on two scanning electron microscopes with EDX, and X-ray diffraction was done. Two sets of calculations were made, with one comprising the same composition studied experimentally (50 at.% WC and 50 at.% binder), and a more realistic composition comprising 90 at.% WC and 10 at.% binder. The latter was done to give a better understanding to the experimental microstructures.

Most of the WC decomposed into W_2C; this was attributed to the high temperature of the arc-melter and should not occur on normal hard metal preparation. Most of the compositions calculated had solid solution binders and WC. Thermo-Calc could not predict the decomposition of the carbide phase at high temperature. Some phases identified were similar in both the experiments and calculations. Sample $W_{25}:C_{25}:Ni_{43}:V_7$ had the binder phase initially solidifying as (Ni) but transformed into ~Ni_2V on cooling; it was identified as the most likely alloy to replace cobalt but will still need further work such as preparing a more realistic composition, manufacturing by sintering, and comparing properties such as hardness with WC-Co. Thus, the binder composition was selected from the Ni-V binary system.

DEDICATION

I dedicate this dissertation to the ALMIGHTY GOD for His divine guidance and protection, my family especially, my mum and my uncles; Dr. Seth and Dr. Alex Kumi.

ACKNOWLEDGEMENT

I give thanks to the Most High God for His favour, divine protection, wisdom and understanding. I humbly express my deepest appreciation to the following persons for their immense contributions towards the completion of my study.

- **Prof L.A. Cornish** for providing guidance and assistance throughout my entire study period. Many thanks to her for given me the opportunity to do this project and teaching me so much, even though I had no background in metallurgy
  Prof, I am highly indebted to you.

- DST/NRF Centre of Excellence in Strong Materials and the National Research Foundation for your financial assistance in funding my studies in South Africa.

- Stephan Coetzee at the Electron Microscopy Unit, University of Botswana, and Clive Oliphant at NMISA, Pretoria.

- Edson Mahuma for manufacturing my samples.

- Colleagues in my research group, especially Brendon M. Shongwe.

- Finally, my warm appreciation to my family and friends (South Africa and Ghana) who contributed in diverse ways, especially Juliet Jackson-Okine. God bless you all for your support.

TABLE OF CONTENTS

CHAPTER 1 1

1.0. Background 1

CHAPTER 2 5

LITERATURE REVIEW 5

2.0 Introduction 5

2.1 Cobalt 5

2.2 Co-C 6

2.3 Co-W 7

2.4 W-C 8

2.5 Properties of WC-Co 12

2.6 Concept of binder 14

2.7 Alternative Binders to Cobalt 15

2.7.1 Ni Systems 15

2.7.2 Fe as a binder 17

2.7.3 Fe-Ni as binder 18

2.7.4 Fe-Co-Ni as a binder 21

2.7.5 Fe-Ni-Cr as a binder 22

2.7.6 Fe-Mn as a binder 23

2.7.7 FeAl as a binder 25

CHAPTER 3 27

RATIONALE FOR THE NEW BINDERS 27

3.1 Introduction 27

3.1.1 Solid solution 27

3.1.2 Small solubility with tungsten 27

3.1.3 Melting point range 28

3.1.4. Novelty 29

3.2. Potential New Binder Systems 29
3.2.1. Co-Mn System 29
3.2.2 Cu-Ni System 30
3.2.3 Ni-V System 31
3.2.4 Ni-Zn System 32
3.2.5 Cu-Zn System 33
3.2.6 Mn-V System 34
CHAPTER 4 36
MATERIALS AND EXPERIMENTAL PROCEDURES 36
4.1 Preparation of alloy 36
4.2 Microstructure examination 36
4.3 Scanning electron microscopy 36
4.4 X-ray diffraction 36
4. 5. Heat treatment 37
CHAPTER 5 38
EXPERIMENTAL RESULTS 38
5.1 Microstructure characterization-cast samples 38
5.1.1 W_{25}:C_{25}:$Ni_{47.5}$:$V_{2.5}$ (at.%) 38
5.1.2 Nominal $W_{25}C_{25}Ni_{43}$:V_7 (at.%) 41
5.1.3 Nominal W_{25}:C_{25}:$Ni_{42.5}$:$Zn_{7.5}$ (at.%) 45
5.1.4 Nominal W_{25}:C_{25}:Ni_{45}:Zn_5 (at.%) 49
5.1.5 Nominal W_{25}:C_{25}:Co_{30}:Mn_{20} (at.%) 52
5.1.6 Nominal W_{25}:C_{25}:$Co_{12.5}$:$Mn_{37.5}$ (at.%) 54
5.1.7 Nominal W_{25}:C_{25}:$Cu_{42.5}$:$Ni_{7.5}$ (at.%) 58
5.1.8 Nominal W_{25}:C_{25}:Cu_{40}:Ni_{10} (at.%) 60
5.1.9 Nominal W_{25}:C_{25}:Mn_{25}:V_{25} (at.%) 64
5.1.10 Nominal W_{25}:C_{25}:$Cu_{47.5}$:$Mn_{2.5}$ (at.%) 67
5.1.11 Nominal W_{25}:C_{25}:Cu_{45}:Zn_5 (at.%) 70

5.1.12 Nominal $W_{25}:C_{25}:Cu_{40}:Zn_{10}$ (at.%) 72
5.2 Phase analysis of alloys – annealed at 1000 ºC for 168 hours 75
5.2.1 Nominal $W_{25}:C_{25}:Ni_{45}:V_{2.5}$ (at.%) 75
5.2.2 Nominal $W_{25}:C_{25}:Ni_{43}:V_{7}$ (at.%) 78
5.2.3 Nominal $W_{25}:C_{25}:Ni_{42.5}:Zn_{7.5}$ (at.%) 81
5.2.4 Nominal $W_{25}:C_{25}:Ni_{45}:Zn_{5}$ 85
5.2.5 Nominal $W_{25}:C_{25}:Co_{30}:Mn_{20}$ (at.%) 87
5.2.6 Nominal $W_{25}:C_{25}:Co_{12.5}:Mn_{37.5}$ (at.%) 89
5.2.7 Nominal $W_{25}:C_{25}:Cu_{42.5}:Ni_{7.5}$ (at.%) 92
5.2.8 Nominal $W_{25}: C_{25}: Cu_{40}: Ni_{10}$ (at.%) 95
5.2.9 Nominal $W_{25}:C_{25}:Mn_{25}:V_{25}$ (at.%) 99
5.2.10 Nominal $W_{25}:C_{25}:Cu_{40}:Zn_{10}$ (at.%) 101
5.2.11 Nominal $W_{25}:C_{25}:Cu_{45}:Zn_{5}$ (at.%) 103
5.2.12 Nominal $W_{25}:C_{25}:Cu_{47.5}:Mn_{2.5}$ (at.%) 106
CHAPTER 6 110
CALCULATED RESULTS 110
6.1. Calculation of equilibrium phases 110
6.1 90% Carbide-10% binder calculations 110
6.1.1 $W_{45}:C_{45}:Ni_{9.5}:V_{0.5}$ (at.%) 111
6.1.2 $W_{45}:C_{45}:Ni_{8.6}:V_{1.4}$ (at.%) 116
6.1.3 $W_{45}:C_{45}:Ni_{8.5}:Zn_{1.5}$ (at.%) 119
6.1.4 $W_{45}:C_{45}:Ni_{9.0}:Zn_{1.0}$ (at.%) 121
6.1.5 $W_{45}:C_{45}:Co_{6}:Mn_{4}$ (at.%) 123
6.1.6 $W_{45}:C_{45}:Co_{2.5}:Mn_{7.5}$ (at.%) 126
6.1.7 $W_{45}:C_{45}:Cu_{8.5}:Ni_{1.5}$ (at.%) 128
6.1.8 $W_{45}:C_{45}:Cu_{8}:Ni_{2}$ (at.%) 130
6.1.9 $W_{45}:C_{45}:Cu_{9}:Zn_{1}$ (at.%) 132
6.1.10 $W_{45}:C_{45}:Cu_{9.5}:Zn_{0.5}$ (at.%) 134

6.1.11 W_{45}:C_{45}:Mn5:V_5 (at.%) 136

6.1.12 W_{45}:C_{45}:$Mn_{0.5}$:$Cu_{9.5}$ (at.%) 139

6.2 50% Binder replacement 141

6.2.1 W_{25}:C_{25}:Ni_{45}:V_5 (at.%) 141

6.2.2 W_{25}:C_{25}:Ni_{43}:V_7 (at.%) 147

6.2.3 W_{25}:C_{25}:$Ni_{42.5}$:$Zn_{7.5}$ (at.%) 150

6.2.4 W_{25}:C_{25}:Ni_{45}:Zn_5 (at.%) 153

6.2.5 W_{25}:C_{25}:Co_{30}:Mn_{20} (at.%) 155

6.2.6 W_{25}:C_{25}:$Co_{12.5}$:$Mn_{37.5}$ (at.%) 157

6.2.7 W_{25}: C_{25}:$Cu_{42.5}$:$Ni_{7.5}$ (at.%) 160

6.2.8 W_{25}:C_{25}:Cu_{40}:Ni_{10} (at.%) 162

6.2.9 W_{25}:C_{25}:Cu_{40}:Zn_{10} (at.%) 165

6.2.10 W_{25}:C_{25}:Cu:$_{45}$:Zn_5 (at.%). 167

6.2.11 W_{25}:C_{25}:Mn_{25}:V_{25} (at.%) 169

6.2.12 W_{25}:C_{25}:$Mn_{2.5}$:$Cu_{47.5}$ (at.%) 172

CHAPTER 7 176

7.1 Energy Dispersive Spectroscopy 176

7.2 As-cast samples 181

7.3 Heat treated samples 184

7.4 Summary the calculation of equilibria phases (Thermo-Calc) 194

7.4.1 90% Carbide 10% binder calculations 194

7.4.2 90% Carbide-10% binder calculations 196

CHAPTER 8 200

8.1 Conclusions 200

8.2 Recommendations for future work 202

REFERENCES 204

APPENDICES 213

A. XRD pattern for plasticine matched with $CaCO_3$ 236

B. XRD reference peaks for identified phases, from the International Centre for Diffraction Data, Powder Diffraction Search Manual……237

C. E-mail describing the different standards used in analyzing the as-cast samples (UB)……244

D. Presentations during the course of this study……254

E. Codes for the samples……255

LIST OF FIGURES

Figure 1.1. SEM micrograph of WC-12 wt% Co showing light WC and dark Co phases [2003Sud]....1

Figure 1.2. Schematic flow chart for WC-Co production [1998Bro]......3

Figure 2.1. Co-C phase diagram …….. ……..7

Figure 2.2. Co – W phase diagram 8

Figure 2.3. WC equilibrium diagram.....12

Figure 2.4. Isothermal section of the WC-Co system at 1425°C. 13

Figure 2.5. Ternary W-Ni-C system, a) liquidus projection, and b) isothermal section at 1300°C. 16

Figure 2.6. W-Fe-C isothermal section at 1000°C].....18

Figure 2.7. Vickers' hardness and TRS plots of WC-10 wt% (Co-Ni-Fe) hard metals, sintered at 1350°C and 1400°C for 1 h in dry hydrogen......19

Figure 2.8. Properties of WC-10 wt% (Co-Ni-Fe) hard metals, sintered at 1350°C and 1400°C for 1 h in dry hydrogen......20

Figure 2.9. Liquidus projection for Co-Fe-Ni. 21

Figure 2.10. Liquidus projection for Ni-Fe-Cr.....23

Figure 2.11. Fe –Mn phase diagram. 24

Figure 2.12. Fe –Al W phase diagram 25

Figure 3.1 Mechanisms for solid solution formation (a) substitutional (b) and interstitial……
……...……...28

Figure 3.2. Assessed phase diagram for Co-Mn......30

Figure 3.3. Cu-Ni assessed phase diagram. 30

Figure 3.4. Assessed Ni-V binary phase diagram......31

Figure 3.5. Ni-Zn assessed phase diagram......33

Figure 3.6. Assessed Cu-Zn phase diagram. 34

Figure 3.7. Assessed Mn-V phase diagram……35

Figure 5.1. SEM-BSE image of nominal W_{25}:C_{25}:$Ni_{47.5}$:$V_{2.5}$ (at.%) in the as-cast condition showing: light ~W_2C dendrites surrounded by medium dark ~Ni_3V dendrites and ~W_2C (light) + ~Ni_3V (dark) eutectic......38

Figure 5.2. SEM-BSE image of nominal $W_{25}:C_{25}:Ni_{47.5}:V_{2.5}$ (at.%) in as-cast condition showing: light ~W_2C dendrites surrounded by medium dark ~Ni_3V dendrites and ~W_2C (light) + ~Ni_3V (dark) eutectic. 39

Figure 5.3. XRD pattern of nominal $W_{25}:C_{25}:Ni_{47.5}:V_{2.5}$ in as-cast condition, showing ~W_2C and ~Ni_3V peaks. 41

Figure 5.4. SEM -BSE image of nominal as-cast $W_{25}:C_{25}:Ni_{43}:V_7$ (at.%) showing ~W_2C dendrites and cored medium dark ~Ni_2V. 42

Figure 5.5. SEM-BSE image of nominal as-cast $W_{25}:C_{25}:Ni_{43}:V_7$ (at.%) showing ~W_2C dendrites, cored ~Ni_2V medium dark dendrites and oxides (black). 42

Figure 5.6. XRD pattern of nominal $W_{25}:C_{25}:Ni_{43}:V_7$ (at.%) in as-cast condition, showing ~W_2C and ~Ni_2V peaks. 45

Figure 5.7. SEM-BSE images of nominal $W_{25}:C_{25}:Ni_{42.5}:Zn_{7.5}$ (at.%) in as-cast condition: showing a) overview of the sample with different regions, b) dense area with ~W_2C (light) globules, medium-dark matrix (Ni) and with small areas of ~W_2C (light) + (Ni) (medium-dark) eutectic, and c) less dense area with ~W_2C (light) globules, medium-dark matrix (Ni) and with much more ~W_2C (light) + (Ni) (medium-dark) eutectic. 46

Figure 5.8. XRD pattern of nominal $W_{25}:C_{25}:Ni_{42.}5:Zn_{7.5}$ (at.%) in as-cast condition, showing ~W_2C and (Ni) peaks. 48

Figure 5.9. SEM-BSE image of nominal $W_{25}:C_{25}:Ni_{45}:Zn_5$ (at.%) in the as-cast condition: light ~W_2C; (Ni) medium grey; eutectic ~W_2C + (Ni). 49

Figure 5.10. XRD pattern of nominal $W_{25}:C_{25}:Ni_{45}:Zn_5$ (at.%) in as-cast condition, showing ~W_2C and (Ni) peaks. 51

Figure 5.11. SEM-BSE images of nominal $W_{25}:C_{25}:Co_{30}:Mn_{20}$ in as-cast condition: showing a) the major medium flakes, b) light dendrites enclosed by flakes in dark cored matrix and c) dark phases in matrix at higher magnification. 52

Figure 5.12. XRD pattern nominal $W_{25}:C_{25}:Co_{30}:Mn_{20}$ (at.%) in as-cast condition showing ~WC (Co) and ~Co_7W_6. 54

Figure 5.13. SEM-BSE image of nominal $W_{25}:C_{25}:Co_{12.5}:Mn_{37.5}$ (at.%) in as-cast condition, showing the two different regions of the sample with cracks in the dark phase of the less dense carbide portion. 55

Figure 5.14. SEM-BSE image of nominal $W_{25}:C_{25}:Co_{12.5}:Mn_{37.5}$ (at.%) in as-cast condition showing: the denser region with light carbide particles and dark matrix. 55

Figure 5.15. SEM-BSE image of nominal $W_{25}:C_{25}:Co_{12.5}:Mn_{37.5}$ in as-cast condition showing the less dense area with cracks, ~WC light phase and dark (Mn). 56

Figure 5.16. XRD pattern nominal $W_{25}:C_{25}:Co_{12.5}:Mn_{37.5}$ (at.%) in as-cast condition showing ~WC and (Mn). 57

Figure 5.17. BSE-SEM image of nominal $W_{25}:C_{25}:Cu_{42.5}:Ni_{7.5}$ (at.%) in as-cast condition showing different regions: single phase W [1], dark (Cu,Ni) single phase [2], dark and lower carbide proportion [3] and the high proportion carbide region [4]. 58

Figure 5.18. BSE-SEM image of nominal $W_{25}:C_{25}:Cu_{42.5}:Ni_{7.5}$ (at.%) in as-cast condition: light and medium dark phases. 59

Figure 5.19. XRD pattern for nominal $W_{25}:C_{25}:Cu_{42.5}:Ni_{7.5}$ (at.%) in as-cast condition showing W, ~W_2C and (Cu). 60

Figure 5.20. BSE-SEM image of nominal $W_{25}:C_{25}:Cu_{40}:Ni_{10}$ (at.%) in as-cast condition showing different regions: two large mainly carbide two-phase regions [A,B] and the dark (Cu,Ni) single phase region [C]. 61

Figure 5.21. BSE-SEM image of nominal $W_{25}:C_{25}:Cu_{40}:Ni_{10}$ (at.%) in as-cast condition showing the light ~W_2C carbide and dark (Cu,Ni). 61

Figure 5.22. BSE-SEM image of nominal $W_{25}:C_{25}Cu_{40}:Ni_{10}$ (at.%) in as-cast condition showing the dark (Cu,Ni) single phase region with porosity and a portion of the light carbide. 62

Figure 5.23. XRD pattern nominal $W_{25}:C_{25}:Cu_{42.5}:Ni_{7.5}$ (at.%) in as-cast condition showing ~W_2C, Cu and some unidentified peaks. 64

Figure 5.24. SEM-BSE images of nominal $W_{25}:C_{25}:Mn_{25}:V_{25}$ in as-cast condition showing: a) overall view of the sample, light ~V_2C and dark (V) phase, b) higher magnification view. 65

Figure 5.25. XRD pattern nominal $W_{25}:C_{25}:Mn_{25}:V_{25}$ (at.%) in as-cast condition showing ~V_2C and (V). 66

Figure 5.26. SEM-BSE image of nominal as-cast $W_{25}:C_{25}:Cu_{47.5}:Mn_{2.5}$ (at.%) showing the three different areas in the sample, (Cu,Mn) [3], the improperly melted light carbide grain region [2], and the innermost two-phase region [1]. 67

Figure 5.27. SEM-BSE image of nominal as-cast $W_{25}:C_{25}:Cu_{47.5}:Mn_{2.5}$ (at.%) showing middle two-phase region ([1] in Figure 5.25) comprising cored carbides. 68

Figure 5.28. SEM-BSE image of nominal as-cast $W_{25}:C_{25}:Cu_{47.5}:Mn_{2.5}$ (at.%) showing the outermost dark single phase region ([3] in Figure 5.27) with a crack (top), few carbide patches and porosity. . 68

Figure 5.29. XRD pattern of nominal $W_{25}:C_{25}:Cu_{47.5}:Mn_{2.5}$ (at.%) in as-cast condition showing W_2C and (Cu). 70

Figure 5.30. SEM-BSE image of nominal as-cast $W_{25}:C_{25}:Cu_{45}:Zn_5$ (at.%) showing the single carbide phase and irregular porosity. 71

Figure 5.31. XRD pattern nominal $W_{25}:C_{25}:Cu_{45}:Zn_5$ (at.%) in as-cast condition showing both ~WC, ~W_2C and some a small unidentified peaks. 72

Figure 5.32. SEM-BSE image of nominal as-cast $W_{25}:C_{25}:Ni_{40}:Zn_{10}$ (at.%) showing an overall view, and the two phase-region in the middle surrounded by the dark (Cu,Zn) phase. 73

Figure 5.33. SEM-BSE images of nominal annealed $W_{25}:C_{25}:Ni_{40}:Zn_{10}$ (at.%) showing: a) light carbide phase in a dark matrix, b) a dark single phase with some round porosity. 73

Figure 5.34. XRD pattern nominal $W_{25}:C_{25}:Cu_{40}:Zn_{10}$ (at.%) in as-cast condition, showing ~W_2C and (Cu) peaks. 74

Figure 5.35. SEM-BSE image of nominal $W_{25}:C_{25}:Ni_{47.5}:V_{2.5}$ (at.%) after annealing at 1000ºC for 168 hours: light ~W_2C dendrites surrounded by medium dark ~Ni_2V and ~W_2C (light) + ~Ni_2V (dark) eutectic. 75

Figure 5.36. SEM-BSE image of nominal $W_{25}:C_{25}:Ni_{47.5}:V_{2.5}$ (at.%) after annealing at 1000ºC for 168 hours, showing large amounts of eutectic. 76

Figure 5.37. XRD pattern of nominal $W_{25}:C_{25}:Ni_{47.5}:V_{2.5}$ (at.%) in annealed condition, showing ~W_2C and ~Ni_2V peaks. 77

Figure 5.38. SEM-BSE image of nominal $W_{25}:C_{25}:Ni_{43}:V_7$ (at.%) in annealed condition showing ~W_2C dendrites, medium needles, light precipitates and dark (Ni). 79

Figure 5.39. SEM-BSE image of nominal $W_{25}:C_{25}:Ni_{43}:V_7$ (at.%) in annealed condition showing ~W_2C dendrites with medium contrast dendrite edges (see arrow) and precipitation of a light phase (~W_2C). 79

Figure 5.40. XRD pattern of nominal $W_{25}:C_{25}:Ni_{47.5}:V_{2.5}$ (at.%) in the annealed condition, showing ~W_2C, ~Ni_3V and (Ni) peaks. 81

Figure 5.41. SEM-BSE images of nominal $W_{25}:C_{25}:Ni_{42.5}:Zn_{7.5}$ (at.%) in annealed condition: showing different regions with different proportions of phases, with light ~W_2C globules and dark matrix (Ni) and a ~W_2C (light) + (Ni) dark eutectic, a) the overall view of the sample, b) the high carbide proportion area c) lower carbide proportion area. 82

Figure 5.42. XRD pattern of nominal $W_{25}:C_{25}:Ni_{42.5}:Zn_{7.5}$ (at.%) in annealed condition, showing ~W_2C and (Ni) peaks. 84

Figure 5.43. SEM-BSE image of nominal $W_{25}:C_{25}:Ni_{45}:Zn_5$ (at.%) in the annealed condition: light ~W_2C; (Ni) medium grey needles (see arrow); eutectic ~W_2C + (Ni). 85

Figure 5.44 XRD pattern of nominal $W_{25}:C_{25}:Ni_{42.5}:Zn_{7.5}$ (at.%) in annealed condition, showing ~W_2C and (Ni) peak. 87

Figure 5.45. SEM-BSE images of nominal $W_{25}:C_{25}:Co_{30}:Mn_{20}$ (at.%) in annealed condition: showing light needles and flakes in dark matrix. 87

Figure 5.46. XRD pattern of nominal $W_{25}:C_{25}:Co_{30}:Mn_{20}$ in annealed condition showing ~W_2C and (Co) with some unmatched peaks. 89

Figure 5.47. SEM-BSE image of nominal $W_{25}:C_{25}:Co_{30}:Mn_{20}$ (at.%) in annealed condition, showing overall view of the sample with finer and coarser areas: ~W_2C (light) and dark (Mn). 90

Figure 5.48. SEM-BSE image of nominal $W_{25}:C_{25}:Co_{30}:Mn_{20}$ (at.%) in annealed condition, showing with cracks in the dark phase: ~W_2C (light) and dark (Mn). 90

Figure 5.49. XRD pattern nominal $W_{25}:C_{25}:Co_{12.5}:Mn_{37.5}$ (at.%) in the annealed condition, showing ~W_2C and (Mn). 92

Figure 5.50. BSE-SEM images of nominal $W_{25}:C_{25}:Cu_{42.5}:Ni_{7.5}$ (at.%) in annealed condition showing: a) overview of the sample with single ~W_2C [1] and (Cu,Ni) [2], two-phase region with higher carbide [3] and the lower carbide two-phase regions [4] and [5], b) higher magnification of the denser carbide area [3], c) higher magnification of the less dense area with (~W_2C and (Cu,Ni)) [4], and d) two-phase region [5]. 93

Figure 5.51. XRD pattern nominal $W_{25}:C_{25}:Cu_{42.5}:Ni_{7.5}$ (at.%) in annealed condition showing (Cu) and ~W_2C peaks. 95

Figure 5.52. BSE-SEM image of nominal $W_{25}:C_{25}:Cu_{40}:Ni_{10}$ (at.%) in the annealed condition showing the different regions. 96

Figure 5.53. BSE-SEM image of nominal $W_{25}:C_{25}:Cu_{40}:Ni_{10}$ (at.%) in the annealed condition, showing light ~W_2C phase with dark (Cu,Ni) matrix in the high carbide proportion region. 96

Figure 5.54. BSE-SEM image of nominal $W_{25}:C_{25}:Cu_{40}:Ni_{10}$ (at.%) in annealed condition: a) light ~W_2C and dark (Cu,Ni), b) single dark phase (Cu,Ni) with few carbides and porosity. 97

Figure 5.55. XRD pattern nominal $W_{25}:C_{25}:Cu_{40}:Ni_{10}$ (at.%) in annealed condition, showing ~W_2C and (Cu) peaks. 98

Figure 5.56. SEM-BSE images of nominal $W_{25}:C_{25}:Mn_{25}:V_{25}$ (at.%) in annealed condition, a) overall view, b) varying proportions of carbide (top and bottom), c) less dense area with light dendrites, medium phase and porosity (dark contrast), and d) more dense area with light and dark interdendritic phase. 99

Figure 5.57. XRD pattern of nominal $W_{25}:C_{25}:Mn_{25}:V_{25}$ (at.%) in annealed condition showing ~V_2C and (V). 101

Figure 5.58. SEM-BSE images of nominal annealed $W_{25}:C_{25}:Cu_{40}:Zn_{10}$ (at.%) showing: a) a single phase which formed the bulk of the alloy, b) porosity and the small amount of carbide phase, c) light carbide phase at the edge of the sample with a "bubble", and d) a portion at the edge with light phase and dark matrix. 102

Figure 5.59. XRD pattern nominal $W_{25}:C_{25}:Cu_{40}:Zn_{10}$ (at.%) in annealed condition, showing ~W_2C and (Cu) peaks. 103

Figure 5.60. SEM-BSE image of nominal annealed $W_{25}:C_{25}:Cu_{45}:Zn_5$ (at.%) showing the single carbide phase with porosity. 104

Figure 5.61. XRD pattern nominal $W_{25}:C_{25}:Cu_{45}:Zn_5$ (at.%) in annealed condition showing ~W_2C and some small unidentified peaks. 105

Figure 5.62. SEM-BSE image of nominal annealed $W_{25}:C_{25}:Cu_{47.5}:Mn_{2.5}$ (at.%) showing the three different areas in the sample: (Cu,Mn) [3], unmelted light carbide grain regions [2], and innermost two-phase region [1] 106

Figure 5.63. SEM-BSE image of nominal annealed $W_{25}:C_{25}:C_{47.5}:Mn_{2.5}$ (at.%) showing the innermost two-phase-region (labelled 1 in Figure 4.27). 107

Figure 5.64. SEM-BSE image of nominal annealed $W_{25}:C_{25}:C_{47.5}:Mn_{2.5}$ (at.%) showing particles in middle two-phase-region (labelled 2 in Figure 5.61). 107

Figure 5.65. XRD pattern nominal $W_{25}:C_{25}:Cu_{47.5}:Mn_{2.5}$ (at.%) in annealed condition showing ~W_2C and (Cu) and unmatched peaks. 108

Figure 6.1. Phase proportion diagram of $W_{45}:C_{45}:Ni_{9.5}:V_{0.5}$ (at.%). 111

Figure 6.2. Composition of MC_SHP for $W_{45}:C_{45}:Ni_{9.5}:V_{0.5}$ (at.%). 113

Figure 6.3. Composition of FCC_A1#1 at 2200-2500ºC for $W_{45}:C_{45}:Ni_{9.5}:V_{0.5}$ (at.%). 113

Figure 6.4. Composition of FCC_A1#1 at 800-1400ºC for $W_{45}:C_{45}:Ni_{9.5}:V_{0.5}$ (at.%). 114

Figure 6.5. Composition of the FCC_A1#2 for $W_{45}:C_{45}:Ni_{9.5}:V_{0.5}$ (at.%). 115

Figure 6.6. Composition of graphite for $W_{45}:C_{45}:Ni_{9.5}:V_{0.5}$ (at.%.) 115

Figure 6.7. Phase proportions of $W_{45}:C_{45}:Ni_{8.6}:V_{1.4}$ (at.%). 116

Figure 6.8. Composition of FCC_1A#1 for $W_{45}:C_{45}:Ni_{8.6}:V_{1.4}$ (at.%). 117

Figure 6.9. Composition diagram of the FCC_1A#1 for $W_{45}:C_{45}:Ni_{8.6}:V_{1.4}$ (at.%) showing carbon and vanadium. 118

Figure 6.10. Composition of FCC_1A#2 for $W_{45}:C_{45}:Ni_{8.6}:V_{1.4}$ (at.%). 119

Figure 6.11. Phase proportions of $W_{45}:C_{45}:Ni_{8.5}:Zn_{1.5}$ (at.%). 120

Figure 6.12. Composition of FCC_A1 for $W_{45}:C_{45}:Ni_{8.5}:Zn_{1.5}$ (at.%). 121

Figure 6.13. Phase proportions of $W_{45}:C_{45}:Ni_{9.0}:Zn_{1.0}$ (at.%). 122

Figure 6.14. Composition diagram of the FCC_A1 for $W_{45}:C_{45}:Ni_{9.0}:Zn_{1.0}$ (at.%). 123

Figure 6.15. Phase proportions of $W_{45}:C_{45}:Co_6:Mn_4$ (at.%). 124

Figure 6.16. Composition diagram of the HCP_A3 for $W_{45}:C_{45}:Co_6:Mn_4$ (at.%). 125

Figure 6.17. Composition of the $M_{12}C$ $W_{45}:C_{45}:Co_6:Mn_4$ (at.%). 125

Figure 6.18. Phase proportions of $W_{45}:C_{45}:Co_{2.5}:Mn_{7.5}$ (at.%). 126

Figure 6.19. Composition of HCP_A3 in $W_{45}:C_{45}:Co_{2.5}:Mn_{7.5}$ (at.%). 127

Figure 6.20. Composition of $M_{12}C$ $W_{45}:C_{45}:Co_{2.5}:Mn_{7.5}$ (at.%). 128

Figure 6.21. Phase proportion diagram of $W_{45}:C_{45}:Cu_{8.5}:Ni_{1.5}$ (at.%). 129

Figure 6.22. Composition of FCC_A1 in $W_{45}:C_{45}:Cu_{8.5}:Ni_{1.5}$ (at.%). 130

Figure 6.23. Phase proportion diagram of $W_{45}:C_{45}:Cu_8:Ni_2$ (at.%). 131

Figure 6.24. Composition diagram of the FCC_A1 for $W_{45}:C_{45}:Ni_{9.0}:Zn_{1.0}$ (at.%). 132

Figure 6.25. Phase proportion diagram of $W_{45}:C_{45}:Cu_9:Ni_1$ (at.%.). 133

Figure 6.26. Composition diagram of the FCC_A1 for $W_{45}:C_{45}:Cu_9:Ni_1$ (at.%). 134

Figure 6.27. Phase proportions of $W_{45}:C_{45}:Cu_{9.5}:Zn_{0.5}$ (at.%). 135

Figure 6.28. Composition diagram of the FCC_A1 for $W_{45}:C_{45}:Cu_{9}:Ni_{1}$ (at.%). 136

Figure 6.29. Phase proportion diagram of $W_{45}:C_{45}:Mn_{5}:V_{5}$ (at.%). 137

Figure 6.30. Composition of BCC_A2 for $W_{45}:C_{45}:Mn_{5}:V_{5}$ (at.%). 138

Figure 6.31. Composition of V_3C_2 for $W_{45}:C_{45}:Mn_{5}:V_{5}$ (at.%). 138

Figure 6.32. Phase proportion of $W_{45}:C_{45}:Mn_{0.5}:Cu_{9.5}$ (at.%). 139

Figure 6.33. Composition diagram of the FCC_A1 for $W_{45}:C_{45}:Mn0._{5}:Cu_{9.5}$ (at.%). 140

Figure 6.34. Phase proportions of $W_{25}:C_{25}:Ni_{45}:V_{5}$ (at.%). 142

Figure 6.35. Composition of the FCC_A1#1 at 800-1400ºC for $W_{25}:C_{25}:Ni_{45}:V_{5}$ (at.%). 143

Figure 6.36. Composition of FCC_A1#1 at 2200-2450ºC for $W_{25}:C_{25}:Ni_{45}:V_{5}$ (at.%). 144

Figure 6.37. Composition of FCC_A1#2 for $W_{25}:C_{25}:Ni_{45}:V_{5}$ (at.%). 145

Figure 6.38. Composition of graphite for $W_{25}:C_{25}:Ni_{45}:V_{5}$ (at.%). 146

Figure 6.39. Composition of MC_SHP for $W_{25}:C_{25}:Ni_{45}:V_{5}$ (at.%). 146

Figure 6.40. Phase proportions of $W_{25}:C_{25}:Ni_{43}:V_{7}$ (at.%). 148

Figure 6.41. Composition of the FCC_A1#1 for $W_{25}:C_{25}:Ni_{43}:V_{7}$ (at.%). 149

Figure 6.42. Composition of FCC_A1#2 at for $W_{25}:C_{25}:Ni_{43}:V_{7}$ (at.%). 149

Figure 6.43. Phase proportions of $W_{25}:C_{25}: Ni_{42.5}: Zn_{7.5}$ (at.%). 151

Figure 6.44. Composition of FCC_A1 for $W_{25}:C_{25}: Ni_{42.5}: Zn_{7.5}$ (at.%). 152

Figure 6.45. Phase proportions of $W_{25}:C_{25}:Ni_{45}:Zn_{5}$ (at.%). 153

Figure 6.46. Composition of FCC_A1 for $W_{25}:C_{25}:Ni_{45}:Zn_{5}$ (at.%). 154

Figure 6.47. Phase diagram of $W_{25}:C_{25}:Co_{30}:Mn_{20}$ (at.%). 155

Figure 6.48. Composition of HCP_A3 for $W_{25}:C_{25}:Co_{30}:Mn_{20}$ (at.%.). 156

Figure 6.49. Composition of the $M_{12}C$ in $W_{25}:C_{25}:Co_{30}:Mn_{20}$ (at.%). 157

Figure 6.50. Phase proportions of $W_{25}:C_{25}:Co_{12.5}:Mn_{37.5}$ (at.%). 158

Figure 6.51. Composition of BCC_A2 for $W_{25}:C_{25}:Co_{12.5}:Mn_{37.5}$ (at.%). 159

Figure 6.52. Composition diagram of HCP_A3 of $W_{25}:C_{25}:Co_{12.5}:Mn_{37.5}$ (at.%). 160

Figure 6.53. Phase proportions diagram of $W_{25}: C_{25}:Cu_{42.5}:Ni_{7.5}$ (at.%). 161

Figure 6.54. Composition of FCC_A1 for $W_{25}: C_{25}:Cu_{42.5}:Ni_{7.5}$ (at.%). 162

Figure 6.55. Phase proportions diagram of $W_{25}:C_{25}:Cu_{40}:Ni_{10}$ (at.%). 163

Figure 6.56. Composition of FCC_A1 for $W_{25}:C_{25}:Cu_{40}:Ni_{10}$ (at.%). 164

Figure 6.57. Phase proportions diagram of $W_{25}:C_{25}:Cu_{40}:Ni_{10}$ (at.%). 165

Figure 6.58. Composition of FCC_A1 for $W_{25}:C_{25}:Cu_{40}:Zn_{10}$ (at.%). 166

Figure 6.59. Phase proportions diagram of $W_{25}:C_{25}:Cu:_{45}:Zn_5$ (at.%). 167

Figure 6.60. Composition of FCC_A1 for $W_{25}:C_{25}:Cu:_{45}:Zn_5$ (at.%). 168

Figure 6.61. Phase proportions diagram of $W_{25}:C_{25}:Mn_{25}:V_{25}$ (at.%) 169

Figure 6.62. Composition of BCC_A2 for $W_{25}:C_{25}:Mn_{25}:V_{25}$ (at.%). 170

Figure 6.63. Composition of V_3C_2 for $W_{25}:C_{25}:Mn_{25}:V_{25}$ (at.%). 171

Figure 6.64. Phase proportions diagram of $W_{25}:C_{25}:Mn_{2.5}:Cu_{47.5}$ (at.%). 172

Figure 6.65. Composition of FCC_A1 for $W_{25}:C_{25}:Mn_{2.5}:Cu_{47.5}$ (at.%). 173

LIST OF TABLES

Table 2.1. Lattice parameters and coordination numbers in W_2C structures [1967Tel]. 8

Table 2.2. Properties of representative grades of cemented carbide [1989ASM]. 14

Table 5.1. EDS phase analyses for nominal $W_{25:}C_{25}:Ni_{47.5}:V_{2.5}$ (at.%) in the as-cast condition using standards derived from elements which samples were prepared (done at University of Botswana, UB).……40

Table 5.2. EDS phase analyses for nominal $W_{25}:C_{25}:Ni_{47.5}:V_{2.5}$ (at.%) in the as-cast condition analysed without standards (done at University of Botswana, UB). 40

Table 5.3. EDS phase analyses for nominal $W_{25:}C_{25}:Ni_{47.5}:V_{2.5}$ (at.%) in the as-cast condition using pre-loaded standards (done at NMISA). 40

Table 5.4. EDX phase analyses for nominal $W_{25}:C_{25}:Ni_{43}:V_7$ (at.%) in as-cast condition using standards derived from the elements from which samples were prepared (done at University of Botswana, UB). N.B. O was ignored in the oxide analysis. 43

Table 5.5. EDX phase analyses for nominal $W_{25}:C_{25}:Ni_{43}:V_7$ (at.%) in as-cast condition without standards (done at University of Botswana, UB). N.B. O was ignored in the oxide analysis. 43

Table 5.6. EDX phase analyses for nominal $W_{25}:C_{25}:Ni_{43}:V_7$ (at.%) in as-cast condition using pre-loaded standards (done at NMISA). 44

Table 5.7. EDX phase analyses for nominal $W_{25}:C_{25}:Ni_{43}:V_7$ (at.%) in as-cast condition using a carbon standard derived from vanadium carbide (done at NMISA). 44

Table 5.8. EDX phase analyses for nominal $W_{25}:C_{25}:Ni_{42.5}:Zn_{7.5}$ (at.%) in as-cast condition using standards made from the elements from which samples were prepared (done at University of Botswana, UB). 47

Table 5.9. EDX phase analyses for nominal $W_{25}:C_{25}:Ni_{42.5}:Zn_{7.5}$ (at.%) in as-cast condition using pre-loaded standards (done at NMISA). 47

Table 5.10. EDX phase analyses for nominal $W_{25}:C_{25}:Ni_{42.5}:Zn_{7.5}$ (at.%) in as-cast condition using a carbon standard derived from vanadium carbide (done at NMISA). 48

Table 5.11. Unmatched XRD peak from nominal $W_{25}:C_{25}:Ni_{42.5}:Zn_{7.5}$ (at.%) in as-cast condition. 49

Table 5.12. EDX phase analyses for nominal $W_{25}:C_{25}:Ni_{45}:Zn_5$ (at.%) in the as-cast condition using standards made from the elements which samples were prepared (done at University of Botswana, UB). 50

Table 5.13. EDX phase analyses for nominal $W_{25}:C_{25}:Ni_{45}:Zn_5$ (at.%) in the as-cast condition without standards (done at NMISA). 50

Table 5.14. EDX phase analyses for nominal $W_{25}:C_{25}:Ni_{45}:Zn_5$ (at.%) in the as-cast condition using pre-loaded standards (done at NMISA).+ 51

Table 5.15. EDX phase analyses for nominal $W_{25}:C_{25}:Co_{30}:Mn_{20}$ (at.%) in as-cast condition using pre-loaded standards (done at NMISA). 53

Table 5.16. EDX phase analyses for nominal $W_{25}:C_{25}:Co_{30}:Mn_{20}$ (at.%) in as-cast condition without standards (done at University of Botswana, UB). 53

Table 5.17. Unidentified XRD peaks in nominal $W_{25}:C_{25}:Co_{30}:Mn_{20}$ (at.%)(A9) in as-cast condition. 54

Table 5.18. EDX phase analyses for nominal $W_{25}:C_{25}:Co_{12.5}:Mn_{37.5}$ (at.%) in as-cast condition using pre-loaded standards (done at NMISA). 56

Table 5.19. EDX phase analyses for nominal $W_{25}:C_{25}:Co_{12.5}:Mn_{37.5}$ (at.%) in as-cast condition without standards (done at University of Botswana, UB). 56

Table 5.20. Unidentified XRD peaks in nominal $W_{25}:C_{25}:Co_{12.5}:Mn_{37.5}$ (at.%) in as-cast condition. ... 57

Table 5.21. EDX phase analyses for nominal $W_{25}:C_{25}:Cu_{42.5}:Ni_{7.5}$ (at.%) in as-cast condition using standards made from the elements from which samples were prepared (done at University of Botswana, UB). 59

Table 5.22. Unidentified XRD peak in nominal $W_{25}:C_{25}:Cu_{42.5}:Ni_{7.5}$ (at.%) in as-cast condition. 60

Table 5.23. EDX phase analyses for nominal $W_{25}:C_{25}:Cu_{40}:Ni_{10}$ (at.%) in as-cast condition using standards made from the elements from which samples were prepared (done at University of Botswana, UB). 63

Table 5.24. Unidentified XRD peaks in nominal $W_{25}:C_{25}:Cu_{42.5}:Ni_{7.5}$ (at.%) in as-cast condition. 63

Table 5.25. EDX phase analyses for nominal $W_{25}:C_{25}:Mn_{25}:V_{25}$ (at.%) in as-cast condition, without standards (done at University of Botswana, UB). 66

Table 5.26. EDX phase analyses for nominal $W_{25}:C_{25}:Cu_{47.5}:Mn_{2.5}$ (at.%) in as-cast condition without standards (done at University of Botswana, UB). 69

Table 5.27. Unidentified XRD peak in nominal $W_{25}:C_{25}:Cu_{47.5}:Mn_{2.5}$ (at.%) in as-cast condition. 70

Table 5.28. EDX phase analyses for a portion of nominal $W_{25}:C_{25}:Cu_{45}:Zn_5$ (at.%) in as-cast condition without standards (done at University of Botswana, UB). 71

Table 5.29. Unidentified XRD peak in nominal $W_{25}:C_{25}:Cu_{45}:Zn_5$ (at.%) in as-cast condition. 72

Table 5.30. EDX phase analyses for a portion of nominal $W_{25}:C_{25}:Cu_{40}:Zn_{10}$ (at.%) in as-cast condition without standards(done at University of Botswana, UB). 74

Table 5.31. Unidentified XRD peaks in nominal $W_{25}:C_{25}:Cu_{40}:Zn_{10}$ (at.%) in as-cast condition. 74

Table 5.32. Phase analyses for nominal $W_{25.}C_{25}:Ni_{47.5}:V_{2.5}$ (at.%) after annealing at 1000°C for 168 hours using pre-loaded standards (done at NMISA). 77

Table 5.33. Unidentified XRD peaks in nominal $W_{25}:C_{25}:Ni_{45}:V_5$ (at.%) in annealed condition. 78

Table 5.34. EDX phase analyses for nominal $W_{25}:C_{25}:Ni_{43}:V_7$ (at.%) in the annealed condition using pre-loaded standards (done at NMISA). 80

Table 5.35. EDX phase analyses for nominal $W_{25}:C_{25}:Ni_{42.5}:Zn_{7.5}$ (at.%) in the annealed condition using pre-loaded standards (done at NMISA). 83

Table 5.36. Unidentified XRD peaks in nominal $W_{25}:C_{25}:Ni_{42.5}:Zn_{7.5}$ (at.%), in annealed condition. .. 84

Table 5.37. EDX phase analyses for nominal $W_{25}:C_{25}:Ni_{45}:Zn_5$ (at.%) in the annealed condition using pre-loaded standards (done at NMISA). 86

Table 5.38. EDX phase analyses for nominal $W_{25}:C_{25}:Co_{30}:Mn_{20}$ (at.%) in the annealed condition using pre-loaded standards (done at NMISA). 88

Table 5.39. Unidentified XRD peaks in nominal $W_{25}:C_{25}:Co_{30}:Mn_{20}$ (at.%) in annealed condition. ... 88

Table 5.40. EDX phase analysis of nominal $W_{25}:C_{25}:Mn_{25}:V_{25}$ in annealed condition using pre-loaded standards (done at NMISA). 91

Table 5.41. Unidentified XRD peaks in nominal $W_{25}:C_{25}:Co_{12.5}:Mn_{37.5}$ (at.%) in annealed condition. 91

Table 5.42. EDX phase analyses of the sample $W_{25}: C_{25}:Cu_{42.5}:Ni_{7.5}$ (at.%) in annealed condition using pre-loaded standards (done at NMISA). 94

Table 5.43. Unidentified XRD peaks in nominal $W_{25}:C_{25}:Cu_{42.5}:Ni_{7.5}$ (at.%) in annealed condition.... 94

Table 5.44. EDX phase analyses of nominal $W_{25}:C_{25}:Cu_{40}:Ni_{10}$ (at.%) in annealed condition using pre-loaded standards (done at NMISA). 98

Table 5.45. EDX phase analysis of nominal $W_{25}:C_{25}:Mn_{25}:V_{25}$ (at.%) in annealed condition using pre-loaded standards (done at NMISA). 100

Table 5.46. Unidentified XRD peaks in nominal $W_{25}:C_{25}:Co_{30}:Mn_{20}$ (at.%) in annealed condition. .. 101

Table 5.47. EDX phase analyses of the annnealed $W_{25}:C_{25}:Cu_{40}:Zn_{10}$ sample (at.%) using pre-loaded standards (done at NMISA). 103

Table 5.48. EDX phase analyses of the sample $W_{25}:C_{25}:Cu_{45}:Zn_5$ (at.%) in the annealed condition using pre-loaded standards (done at NMISA). 105

Table 5.49. Unidentified XRD peaks in nominal $W_{25}:C_{25}:Cu_{45}:Zn_5$ (at.%) in annealed condition. 105

Table 5.50. EDX phase analyses of the sample $W_{25}:C_{25}:Cu_{47.5}:Mn_{2.5}$ (at.%) in the annealed in condition using pre-loaded standards (done at NMISA). 108

Table 5.51. Unidentified XRD peaks in nominal $W_{25}:C_{25}:Cu_{47.5}:Mn_{2.5}$ (at.%) in annealed condition. 109

Table 6. 1. Summary of phase proportions of $W_{45}:C_{45}:Ni_{9.5}:V_{0.5}$ (at.%)……..... 112

Table 6. 2. Summary of phase proportions of $W_{45}:C_{45}:Ni_{8.6}:V_{1.4}$ (at.%). 117

Table 6. 3. Summary of phase proportions of $W_{45}:C_{45}:Ni_{8.5}:Zn_{1.5}$ (at.%). 120

Table 6. 4. Summary of phases proportions of $W_{45}:C_{45}:Ni_{9.0}:Zn_{1.0}$ (at.%). 122

Table 6. 5. Summary of phase proportions of $W_{45}:C_{45}:Co_6:Mn_4$ (at.%). 124

Table 6. 6. Summary of phase proportions of $W_{45}:C_{45}:Co_{2.5}:Mn_{7.5}$ (at.%). 127

Table 6. 7. Summary of phase proportion of $W_{45}:C_{45}:Cu_{8.5}:Ni_{1.5}$ (at.%). 129

Table 6. 8. Summary of phase proportion of $W_{45}:C_{45}:Cu_{8}:Ni_{2}$ (at.%). 131

Table 6. 9. Summary of phase proportion of $W_{45}:C_{45}:Cu_{9}:Ni_{1}$ (at.%). 133

Table 6. 10. Summary of phase proportion of $W_{45}:C_{45}:Cu_{9.5}:Zn_{0.5}$ (at.%). 135

Table 6. 11. Summary of phase proportion of $W_{45}:C_{45}:Mn_{5}:V_{5}$ (at.%). 137

Table 6. 12. Summary of phase proportion of $W_{45}:C_{45}:Mn0._{5}:Cu_{9.5}$ (at.%). 140

Table 6. 13. Calculated solidification temperature ranges for all the binder phases, and carbide compositions. 141

Table 6. 14. Summary of phase proportions of $W_{25}:C_{25}:Ni_{45}:V_{5}$ (at.%). 142

Table 6.15. Phases, compositions and proportions at 1000ºC for $W_{25}:C_{25}:Ni_{45}:V_{5}$ (at.%). 147

Table 6.16. Summary of phase proportion of $W_{25}:C_{25}:Ni_{43}:V_{7}$ (at.%). 148

Table 6.17. Phases, compositions and proportions at 1000ºC for $W_{25}:C_{25}:Ni_{43}:V_{7}$ (at.%). 150

Table 6.18. Summary of phase proportion of $W_{25}:C_{25}: Ni_{42.5}: Zn_{7.5}$ (at.%). 151

Table 6.19. Phases, compositions and proportions at 1000ºC for $W_{25}:C_{25}:Ni_{42.5}: Zn_{7.5}$ (at.%). 153

Table 6.20. Summary of phase proportions of $W_{25}:C_{25}:Ni_{45}:Zn_{5}$ (at.%). 154

Table 6.21. Phases, compositions and proportions at 1000ºC for $W_{25}:C_{25}:Ni_{45}:Zn_{5}$ (at.%). 155

Table 6.22. Summary of phase proportions of $W_{25}:C_{25}:Co_{30}:Mn_{20}$ (at.%). 156

Table 6.23. Phases, compositions and proportions at 1000ºC for $W_{25}:C_{25}:Co_{30}:Mn_{20}$ (at.%). 157

Table 6.24. Summary of phase proportion of $W_{25}:C_{25}:Co_{12.5}:Mn_{37.5}$ (at.%). 158

Table 6.25. Phases, compositions and proportions at 1000ºC for $W_{25}:C_{25}:Co_{12.5}:Mn_{37.5}$ (at.%). 160

Table 6.26. Summary of phase proportions of $W_{25}:C_{25}:Cu_{42.5}:Ni_{7.5}$ (at.%). 161

Table 6.27. Phases, compositions and proportions at 1000ºC for $W_{25}:C_{25}:Cu_{42.5}:Ni_{7.5}$ (at.%). 162

Table 6.28. Summary of phase proportions of $W_{25}:C_{25}:Cu_{40}:Ni_{10}$ (at.%). 163

Table 6.29. Phases, compositions and proportions at 1000ºC for $W_{25}:C_{25}:Cu_{40}:Ni_{10}$ (at.%). 164

Table 6.30. Summary of phase proportions of $W_{25}:C_{25}:Cu_{40}:Ni_{10}$ (at.%). 165

Table 6.31. Phases, compositions and proportions at 1000ºC for $W_{25}:C_{25}:Cu_{40}:Zn_{10}$ (at.%). 166

Table 6.32. Summary of phase proportions of $W_{25}:C_{25}:Cu:_{45}:Zn_{5}$ (at.%). 168

Table 6.33. Phases, compositions and proportions at 1000ºC for $W_{25}:C_{25}:Cu:_{45}:Zn_{5}$ (at.%). 169

Table 6.34. Summary of phase proportions of nominal $W_{25}:C_{25}:Mn_{25}:V_{25}$ (at.%). 170

Table 6.35. Phases, compositions and proportions at 1000ºC for $W_{25}:C_{25}:Mn_{25}:V_{25}$ (at.%). 172

Table 6.36. Summary of phase proportions of $W_{25}:C_{25}:Mn_{2.5}:Cu_{47.5}$ (at.%). 173

Table 6.37. Phases, compositions and proportions at 1000ºC for $W_{25}:C_{25}:Mn_{2.5}:Cu_{47.5}$ (at.%). 175

Table 6.38. Calculated solidification temperature ranges for all the binder phases, and carbide compositions. 175

Table 7.1. EDX analyses of carbide phases showing results from UB, using standards made from elements which samples were prepared, UB analyses without standards, NMISA analyses using pre-loaded standards and NMISA analyses with carbon standard made from VC. 179

Table 7.2. EDX analyses of matrices showing results from UB, using standards made from elements which samples were prepared, UB analyses without standards, NMISA analyses using pre-loaded standards and NMISA analyses with carbon standard made from VC. 180

Table 7.3. Summary of carbide phases identified for as-cast and annealed samples. 191

Table 7.4. Summary of carbide phases identified for as-cast and annealed samples 193

Table 7.5. Phases identified experimentally and by calculation. 199

CHAPTER 1

1.0. Background

For many years, the cemented carbides industry has been interested in substituting cobalt as the binder metal. The reasons include price fluctuation of cobalt, and especially the health implications of the powdered cobalt used for manufacturing [1992Tra], since the powder can be carcinogenic (cancer causing).

One of the most important groups of cutting tool materials at present is tungsten carbide-based cemented carbides, owing to their high hardness and abrasion resistance. At least 70% of the cutting tools in use are cemented carbides, a significant portion of those are WC–Co based [1991Bha]. The main constituents of cemented carbides are tungsten carbide (WC) and cobalt (Co), as shown in Figure 1.1.

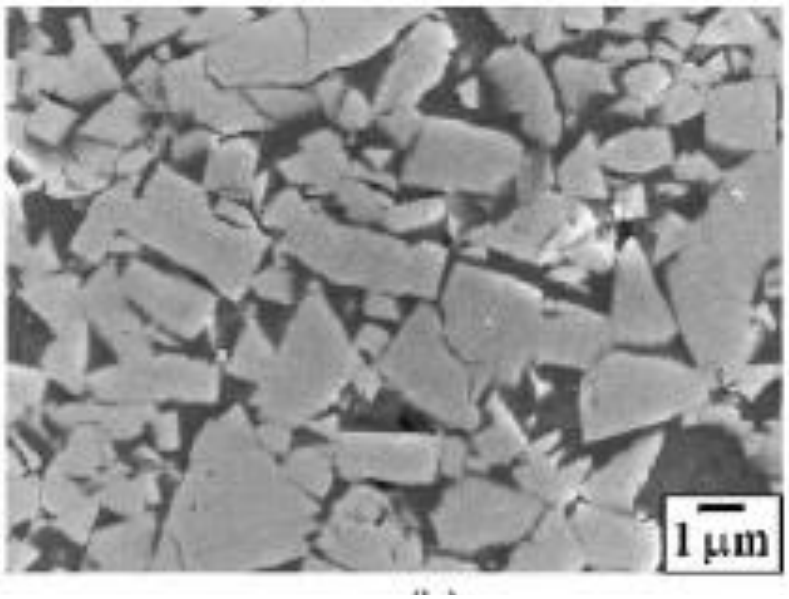


Figure 1.1. SEM micrograph of WC-12 wt% Co showing light WC and dark Co phases [2003Sud].

The WC phase imparts the alloys with the necessary strength and wear resistance, whereas Co contributes to the toughness and ductility of the alloys. Other carbides are added to the WC–Co for various purposes. For example, vanadium carbide can be added to the binder to restrict local tungsten carbide crystal grain growth, which improves the strength of the material [1998Bro]. The cemented carbides WC–Co are typically used as drilling or cutting

tools and wear-resistant tools because of their excellent hardness and wear resistance. Their major usage is as cutting tools, for example, turning, facing and milling operations; glass cutting; swaging dies, drawing dies, and other metal-deformation applications, such as cold heading and Sendzimir mill rolls, and tools for mining operations such as oil well, coal mining and tunnel boring [1979Yih].

Besides Germany being recognized for major breakthroughs [1958Lan], a great deal of work in the development of WC-Co also took place in USA, Austria, Sweden, Japan and other countries [1998Upa]. Presently, the largest producer of carbides is the Swedish company Sandvic Corporation [1998Upa]. Much work has also been done in South Africa. Throughout the development of tungsten carbide, there have been consistent attempts in saving the scarce tungsten by introducing other transition metal hard carbides [1995Bro].

WC-Co alloy is mainly produced by powder metallurgy and sintering, as shown in Figure 1.2 [1998Bro]. The powders are mixed and pressed, then sintered in the liquid cobalt phase at approximately 1300-1500ºC [1996Ooq, 1998Bro, 2001And]. Due to their differences in thermal expansion coefficients, in general, the WC grains are under compression, while binder is under tension [1990Lar].

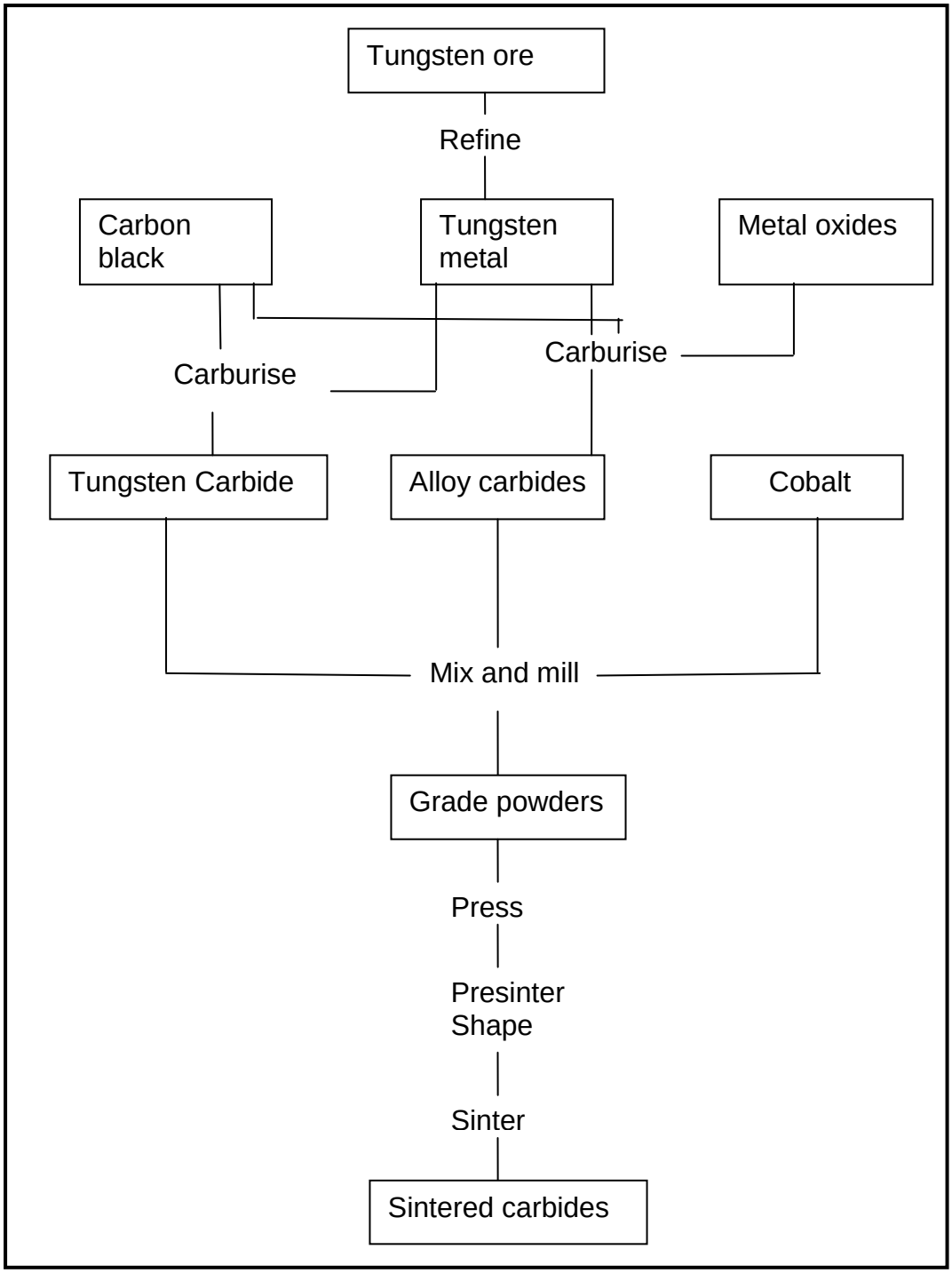


Figure 1.2. Schematic flow chart for WC-Co production [1998Bro].

A lot of work has been done on the WC-Co cemented carbides, including attempts to replace cobalt as a binder through various approaches (e.g. conventional sintering and nano-synthesis) [1992Tra].

The current research was to a large extent limited to phase diagram studies on the different combination of binders that have not been used, in order to select or identify the best possible candidates. In this project, the emphasis was on identifying the properties necessary for the selection of the best binder candidate to replace Co with the aid of phase diagrams. The main criteria used in selecting the binder alloys for this study were:

- sintering temperature (melting point range for sintering cobalt),
- solid solutions composition for binder alloys, and
- reasonable solubility for of the binders for WC to allow reprecipitation.

This dissertation is structured in the following manner: Chapter 1 is the introduction where the motivation for the research is explained. Chapter 2 is the literature survey that reviews WC-Co system, briefly discusses the concept of binders and discusses alternative binders already described in the literature. Chapter 3 describes the rationale for the choice of new binders and Chapter 4 gives the experimental techniques. The experimental results are presented in Chapter 5, and calculated results in Chapter 6 since both parts were large. Chapter 7 is the discussion and Chapter 8 provides the conclusions and recommendations.

CHAPTER 2

LITERATURE REVIEW

2.0 Introduction

This section reviews the WC-Co system, briefly discusses the concept of binders and the alternative binders to Co that exist in literature.

2.1 Cobalt

Two allotropic modifications of cobalt are known: the close-packed hexagonal form, ε, stable at temperature below 400°C and the face-centred cubic form, which is stable at high temperatures. Hexagonal conversion to the cubic form at temperatures in the region of the magnetic transformation (1100°C–1150°C) is uncertain. This is largely attributed to interstitial impurities.

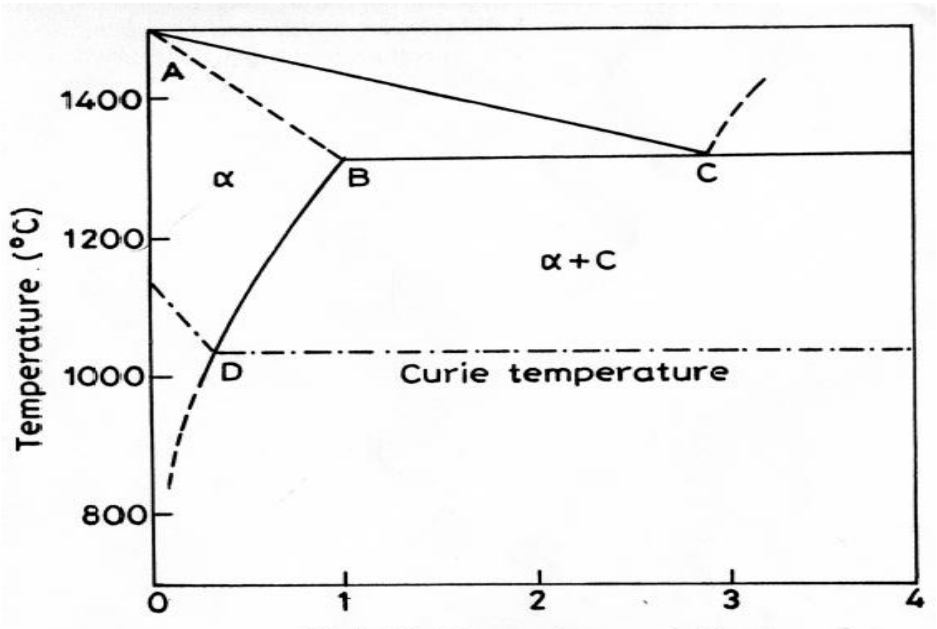
The temperature of the allotropic transformation (εCo→αCo) relies on purity and on the rate of temperature change, but for the highest purity material (about 99.998%) and slow temperature changes, the transformation temperature is 421.5°C [1982Bet], while other sources claim 417°C [1952Hes]. Free energy changes accompanying the transformations are low, about 500 J/mol for ε→α and about 360 J/mol for α→ ε. This explains the sluggishness in the changes and its sensitivity to experimental conditions. The stability of the two allotropes is affected by grain size, with finer grain size opting for the cubic form. Cobalt powder and or evaporated thin films or flaws may maintain a mainly cubic structure at ambient temperature. A proportion of the metastable cubic phase will always be present when solid cobalt is subjected to some deformation, subsequently annealed, and slowly cooled to normal temperature. This allows the structure to not be hexagonal. Hexagonal cobalt amounts increases up to 100% during milling of the cobalt powder, in a typical mixture of the hexagonal and cubic phases [1961Hin, 1965Fis].

Cobalt used as a binder for WC has a cubic lattice which cannot be transformed by annealing. This is ascribed to mechanical constraints; due to the stabilization of cubic modification by dissolving tungsten and carbon [1979Fre]. The mechanical strain was confirmed by studies carried out by Gardon *et al.* [1989Gar], who studied the binder phase of WC–Co cemented carbide using chemical spectrometry. Three different grades of WC-Co cemented carbides

with 8%, 15% and 20% Co were investigated by Yi and Singhui [1988Ho]. They observed that during heating, the transformation temperature of the hcp cobalt binder phase to fcc was around 442°C, 777°C and 821°C for grades of 8%, 15% and 20% Co in WC-Co respectively [1988Ho]. They concluded that the transformation temperature of cobalt mainly depends on the tungsten content, contained within the cobalt; higher tungsten content in the cobalt phase gives higher transformation temperature.

2.2 Co-C

Dissolved carbon in cobalt masks or depresses the solidification temperature. Liquid cobalt dissolves about 3 wt% carbon at the melting point, and α–cobalt retains about 1% carbon in solution at the eutectic, which forms α–cobalt + graphite at 1309°C [1982Bet]. The solid solubility falls with decreasing temperature. The temperature range of stability for the formation of metastable Co_2C and Co_3C, both exhibiting orthorhombic crystal structures, by carburization of solid cobalt was not established [1982Bet]. They both decompose gradually to (εCo) with stacking faults and graphite; this starts at 450°C and 470°C and terminates at 469°C and 491°C, respectively. The (αCo) ↔ (εCo) martensitic transformation (M_s) occurs at a relatively low temperature. The M_s temperature is lowered by addition of carbon, whereas the reduction or absence of carbon increases A_s [1985Has].



Point	A	B	C	D
°C	1495	1309	1309	1035
% C	0	~1	~2.9	~0.33

Figure 2.1. Co-C phase diagram [1982Bet].

Figure 2.1 shows the Co-C equilibrium diagram [1982Bet]. Hansen and Anderko [1958Han] compiled quantitative data on the system. The thermodynamics of the Curie temperature (T_c) variation with carbon content were also studied by Wagner [1972Wag]. Data on thermodynamic analyses were reported by Schmid [1980Sch] and Gabriel [1984Gab]. Ohtani *et al.* [1984Oha] and Hasebe [1985Has] reported experimental data on solubility of carbon in the fcc phase and subjected the whole Co-C phase diagram to analysis. Their findings differed slightly from earlier results [1958Han]. They suggested a smaller effect on the carbon content on the Curie temperature [1984Oha, 1985Has]. Guillermet [1987Gul] made some thermodynamic estimations on the Co-C system and his conclusions were similar to those of Ohtani *et al.* [1984Oha] and Hasebe [1985Has] regarding the composition dependence of T_c. Other analyses of Co-C system are by Ishida and Nishizawa [1991Ish], Rud *et al.* [1987Rud] and Kajihara *et al.* [1986Kaj].

2.3 Co-W

The Co-W phase diagram in Figure 2.2 shows the liquidus passing through a local maximum at 1505°C and 10 at.% W. A eutectic exists at 1471°C and at 21 at.% W between (αCo) and Co_7W_6. There is a peritectic reaction at 1689°C involving the liquid phase of composition 32 at.% W and (W) of composition 99.1 at.% W forming Co_7W_6 (48.5 at.% W) [1967Neu]. The Co_7W_6 phase has a rhombohedral crystal structure. The solid solution fcc (αCo), has a maximum solubility of 17.5 at.% W. The Co_3W phase is formed as a result of a peritectoid reaction at 1093°C at 25.3 at.% W and has a hexagonal crystal structure. Finally, a solid solution (W) has a maximum solid solubility at 0.9 at.% Co at 1689°C.

The assessed phase diagram (Figure 2.2) is similar to that of Hansen and Anderko [1958Han] and Kua's calculated phase diagram [1978Kua].

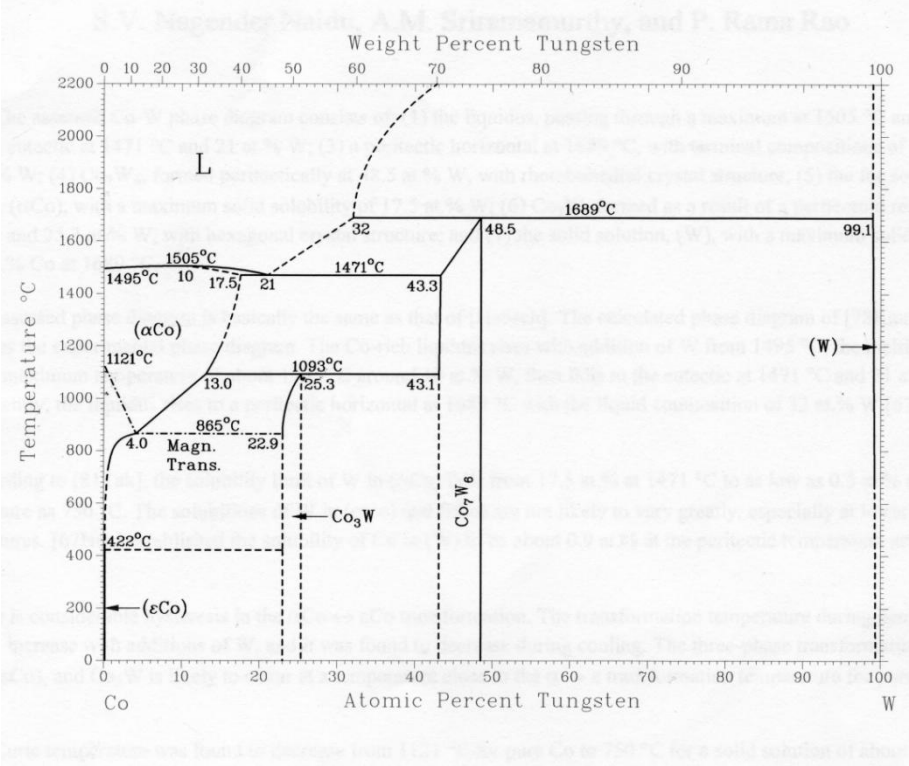


Figure 2.2. Co – W phase diagram [1990Mas].

2.4 W-C

There are three main carbides in the W-C system, W_2C, WC and α–$WC_{1-X.}$ Lander and Gemer [1958Lan] studied the modification of α–W_2C and established a hexagonal type CdI_2 structure and lattice parameters of a = 29.992nm, c = 47.21nm, a/c = 15.758nm, and three atoms in the unit cell, by electron diffraction [1960But].

Arbuzor and Kayerko used neutron diffraction to show that WC has a structure group P612-D_{3h} [1971Arb]. The lattice parameters of W_2C are shown in Table 2.1.

Structure	**Lattice Parameter (nm)**	**Coordination number**
	a = 2.992	6
W_2C (hexagonal)	$\sqrt{3}$a = 5.182	6
	c = 4.721	
W_2C (rhombic)	a = 4.721	4
	b = 6.030	4
	c = 5.180	2

Table 2.1. Lattice parameters and coordination numbers in W_2C structures [1967Tel].

The position of carbon atoms in W_2C was reported by Yvon *et al.* [1968Yvo]. They established that the structures of the carbides quenched from high temperatures (2100°C–2400°C) were ordered, but not completely. Tungsten monocarbide, WC, has a hexagonal structure with an AAA…. metal atom layer packing. This packing is not observed in pure metals, this is due to the presence of planes of carbon atoms.

A key observation noticed when WC ↔ W_2C + graphite reacts is a primary redistribution of the hexagonal planes. Transformation of the simple hexagonal structure to a close packed structure occurs when there is segregation of carbon atoms during the conversion of WC to W_2C [1967Gol], as in Equation 2.1:

$$WC \leftrightarrow W_2C + \text{graphite} \qquad \text{Eq. (2.1)}$$
$$ACACAC \leftrightarrow A^{1/2}CB^{1/2}CA^{1/2}CB^{1/2}C + \text{graphite}$$

Westgren and Phargmen [1926Wes] studied the structure of WC and reported that the tungsten atoms were located at the nodes of a simple hexagonal lattice, while the carbon atoms take positions ½, ⅔, ½.

In addition to the hexagonal form of WC, which is stable at a temperature range of 2500°C to 2750°C [1965Sar, 1967Kra] is a face-centred cubic form, β–WC, stable above 2525°C [1958Lan,1967Kra,1967Rud]. Cubic WC shows a similar structure to NaCl with a wide homogeneity range, and is described as $\beta–WC_{1-x}$ with $0 \leq x \leq 0.41$ (near the solidus point). There is a considerable reduction in the range, of homogeneity for $\beta–WC_{1-x}$ at lower temperatures; this decreases to two compositions at the eutectics [1965Sar]. A rapid quenching method used to preserve β–WC to room temperature by electric spark discharge was reported by Willens and Behier [1965Wil].

The maximum solubility of carbon in tungsten with temperature dependence can be represented by a straight line as shown in Equation 2.2 [1966Geb]:

$$\text{In } C_{max} = 4.67 - 15.0 * 10^3 / T \qquad \text{Eq. (2.2)}$$

where:

C_{max} = Maximum carbon concentration

T.....= Temperature at the maximum concentration of carbon

The maximum solubility of carbon in tungsten is 0.7 at.% at the eutectic temperature 2710°C [1966Geb]. Hultgren *et al.* [1973Hul], Nagakur and Oketani [1968Nag] and Holleck [1981Hol] studied thermodynamic properties and reviewed structural data. Goldschmidt and Brand [1963Gol], Gebhardt *et al.* [1966Geb] and Kuhlmann [1973Kuh] reported solubility of carbon in the bcc phase, at 1400°C – 2640°C. Values of the Gibbs energy of formation of WC were calculated by Glaiser and Chipman [1962Gla] and Coltters and Belton [1983Clo]. The accepted phase diagram of the W-C system is largely based on the work done by Rudy *et al*. [1966Rud]. They reported a saturated carbon composition in W-C melts at high temperature [1966Rud].

Becker [1928Bec] reported lattice parameters of W_2C as a = 29.8nm and c = 47.1nm. Another phase was discovered, and was considered as a polymorphous modification of β–WC [1928Bec], which converts to α-W_2C when subjected to mechanical working, indicating the instability of β–WC.

Three modifications of W_2C are [1967Rud]:

1. η–W_2C: a disordered hexagonal modification stable between 2450°C and the melting point.
2. β–W_2C: an orthorhombic modification on sublattice ordering of ξ-Fe_2N type, stable between 2100°C and 2400°C.
3. α–W_2C: hexagonal ordered or pseudo-hexagonal C_6 type structure, stable at 2100°C – 1250°C (eutectoid temperature).

Sara [1965Sar] described a second modification of β–WC, besides the simple hexagonal lattice known for the carbide α–WC [1926Wes, 1954Pfe, 1962Par]. The β–WC was observed to crystallize in a cubic lattice and was stable above 2525°C after quenching the alloys in tin, and also after electrospark erosion, [1967Rud]. Annealing of the specimen at 900°C for 1 hour helped the disappearance of the fcc WC and its transformation to hexagonal carbide [1968Fil].

Figure 2.3 shows a revised WC equilibrium diagram [1990Mas] (with different symbols from above). There are three forms of tungsten carbide that have been established: the hexagonal W_2C has three modifications which crystallises in the form PbO_2, Fe_2N, and CdI_2 types, represented as ′ and β″ respectively, WC_{1-x} cubic sub-carbide denoted by γ which crystallises in the NaCl structure and δ which denotes hexagonal WC. A wide homogeneity

range is exhibited by W_2C between 25.5 at.% and 34 at.% C at 2715°C. This phase melts congruently at 2785°C. The system is characterized by the reactions $\gamma \leftrightarrow \beta + \delta$, $\beta \leftrightarrow \beta' + \delta$ and $\beta' \leftrightarrow$ (W) + δ at temperatures 2535°C, 2361°C and 1250 °C respectively. The γ-phase can be obtained at room temperature by extremely rapid cooling, for example in a plasma sprayed layers [1994Tel]. The phases of W_2C stoichiometry are obtained as intermediate products during WC production [1994Tel].

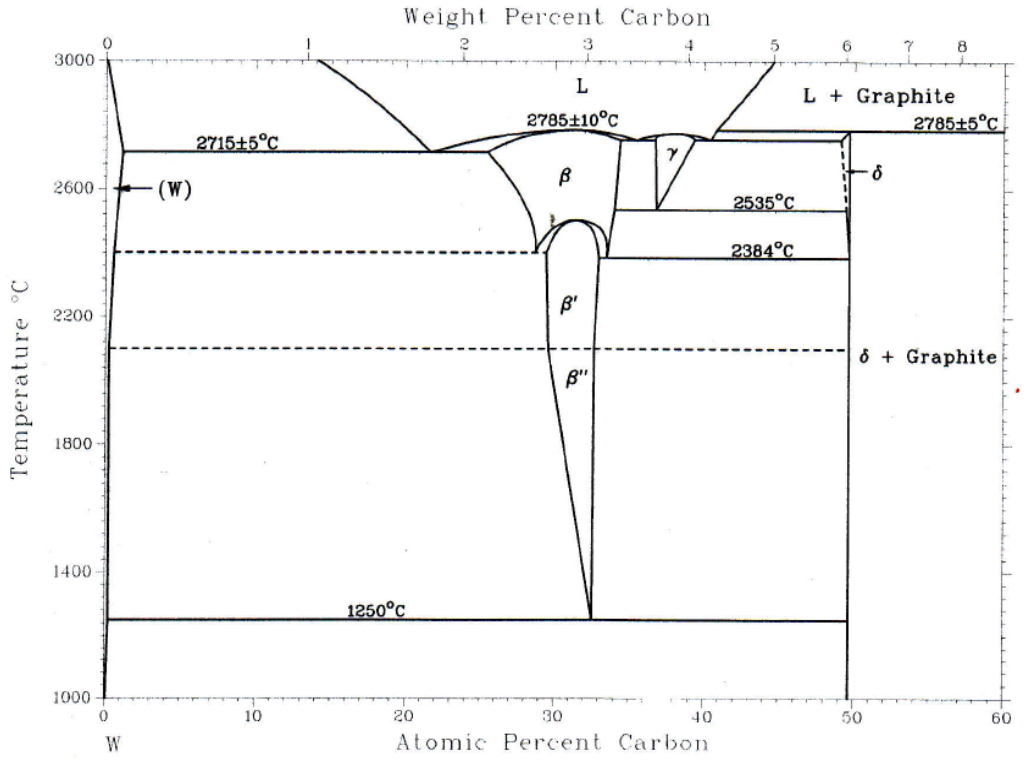


Figure 2.3. WC equilibrium diagram [1990Mas].

2.5 Properties of WC-Co

The final composition and structure of sintered WC-Co significantly determines its properties [1981Sar]. Any undesirable phase, normally graphite and a ternary phase called eta (η-phase), is avoided by the control of carbon, especially around the stoichiometry level in WC. These phases contribute considerably to degrading of mechanical properties and cutting performances of the cemented carbide. Therefore, carbon content is maintained within a narrow limit to obtain the desired composite with optimum properties [1992Tra].

Two types of η-phase phases are well known in this system - $M_{12}C$ (Co_6W_6C) of substantially constant composition, and M_6C which varies in composition within a range of Co_2W_4C to $Co_{3.2}W_{2.8}C$. During the sintering process, M_6C type nucleates and grows; this is possible because M_6C is in equilibrium with the liquid phase. It embrittles the structure by replacing the binder phase with a brittle phase and also reduces the effective contribution of the WC to the strength of the composite. Conversely, during solid state cooling, $M_{12}C$ type is formed with small grains distributed all over the matrix; it is effectively less embrittling [1992Tra].

Figure 2.4 shows an isothermal section of WC-Co phase at 1425°C [1994McH], giving information in the sintering range of commercial WC-Co cermets, i.e. the overall cermet composition has to lie in the Co-WC two-phase field. Depending on the application, different amounts of cobalt are used. Table 2.2 provides some cemented carbide grades with their properties [1989ASM].

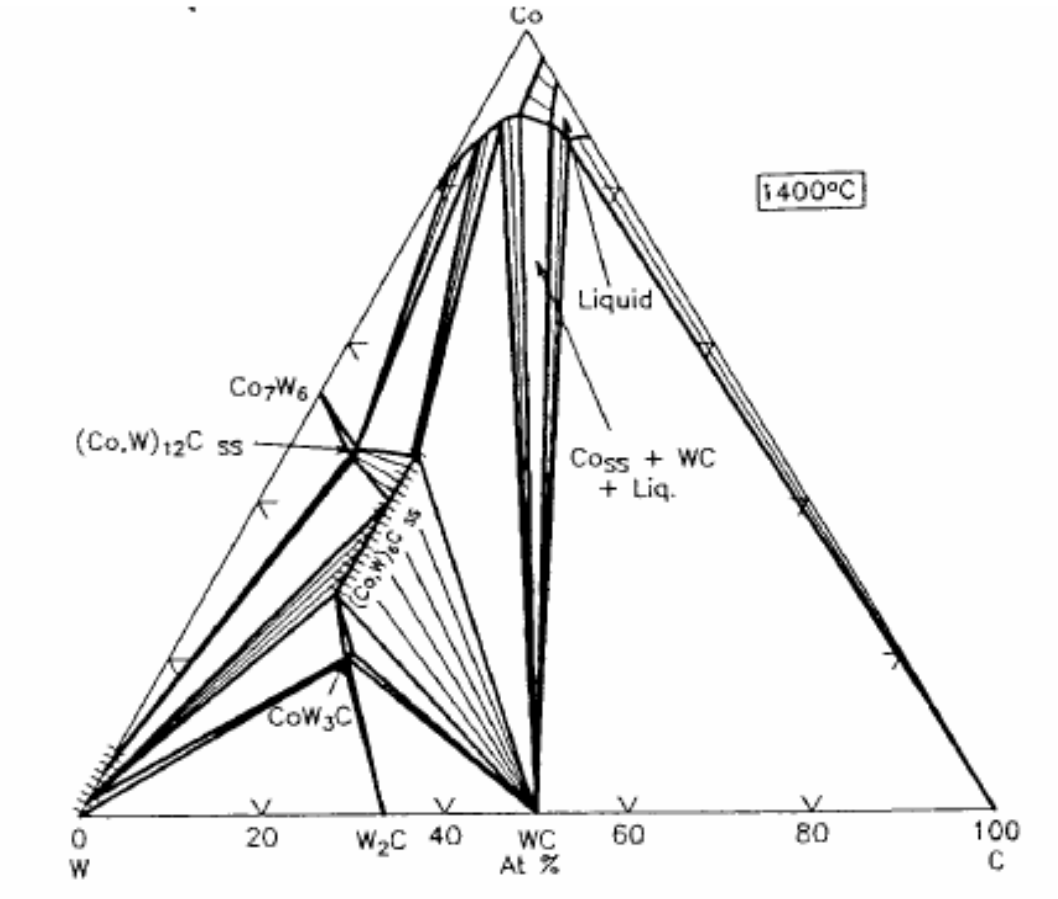


Figure 2.4. Isothermal section of the WC-Co system at 1425°C [1994McH].

Cemented carbide	Room temp, hardness (HV)	Modulus of elasticity (GPa)	Transverse rapture strength (MPa)	Coefficient of thermal expansion (10^{-6}/K)	Thermal conductivity (W/m·K)	Density (g/cm^3)
WC-20 wt% Co	1050	490	2850	6.4	100	13.55
WC 10wt% Co	1625	580	2280	5.6	110	14.50
WC-3 wt% Co	1900	673	1600	5.0	110	15.25
WC- 10 wt% Co-22wt% (Ti, Ta, Nb)C	1500	510	2000	6.1	40	11.40

Table 2.2. Properties of representative grades of cemented carbide [1989ASM].

2.6 Concept of binder

The binder melt compatibility with the refractory carbide at the sintering temperature is an essential precondition to liquid phase sintering. Group VI metal carbide (tungsten carbide), has outstanding wettability with iron group transition metals, compared with group IV or V transition metal carbides. Chemical bindings form the basis of the explanation to the outstanding wettability [1984Upa]. The above reasoning also explains the solubility of carbide phase in the binder melt, which is critical parameter for efficient liquid phase sintering.

The liquid phase sinterability criteria were discussed by German [1985Ger] from the viewpoint of phase equilibria, and the conditions proposed were:

(1) The additive should have high solubility for the base component, rather than vice versa,

(2) The temperature difference between the base component melting point and the eutectic should be as high as possible,
(3) The liquidus and solidus should decrease drastically in order to give rise to additive segregation at the interparticle interfaces, so as to enhance sintering.

WC/cobalt (Co), the most commonly used hardmetal, is usually referred to as straight grades. Co is the most preferred binder metal and it has a good wettability and favourable solubility with WC, producing good mechanical properties [1985Ger].

There are toxicity concerns, especially at higher levels, which have called for its replacement. Additionally, Co has recently been in scarce supply, resulting in price increase, and the unstable price [2001Han].

2.7 Alternative Binders to Cobalt

In the attempt to replace or reduce cobalt, various works have partially or completely substituted cobalt by nickel, iron and other alloys [1988Upa, 1992Tra]. This has normally resulted in composites with high ductility, but with a significant reduction in hardness.

2.7.1 Ni Systems

Cobalt has been a traditional and the most predominant binder metal for tungsten carbide (WC). Nickel can be a plausible candidate to replace Co [1992Tra], but for somewhat confused reasons, nickel has remained commercially not viable, probably due to its inferior mechanical properties. Cobalt has superior communition characteristics, which makes it a preferred binder to nickel [1988Upa].

Solubility of WC in nickel and cobalt differs. At high temperatures, cobalt dissolves more WC than nickel [1964Edw] but it is vice versa at low temperatures [1936Tak]. However, many researchers disagree, claiming that solubility in cobalt at high temperatures is almost the same for nickel, especially in the existence of excess carbon, within the specific range for hard metal composition [1964Cha]. Nickel is believed to be more susceptible to the formation of brittle double carbides of the type $Ni_xW_yC_z$ than cobalt, particularly when the Ni-W-C system is deficient in carbon [1954Whi, 1975Bar].

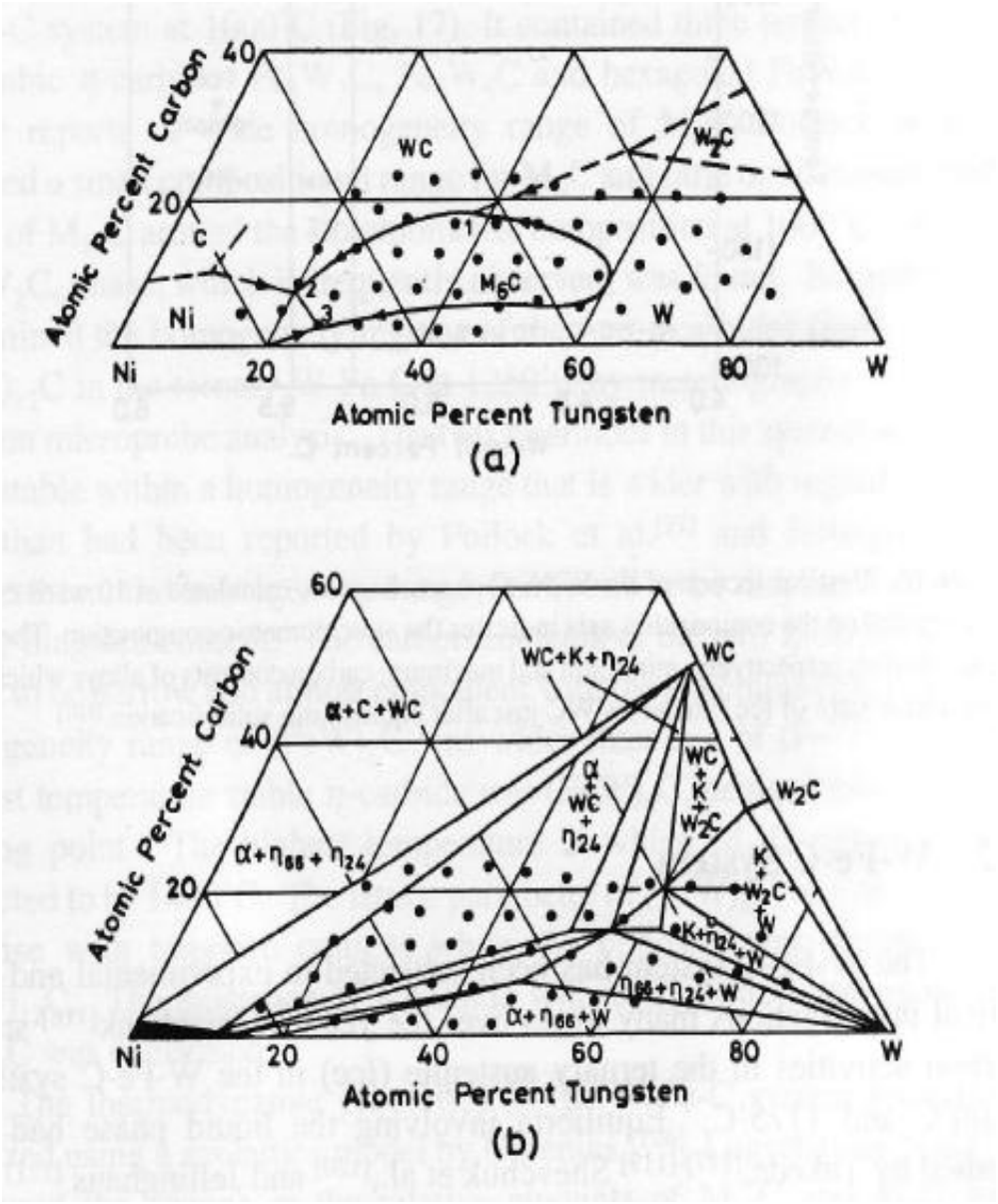


Figure 2.5. Ternary W-Ni-C system, a) liquidus projection, and b) isothermal section at 1300°C [1975Fie].

The first work on the W-Ni-C system is credited to Fiedle and Stadelmaier [1975Fie], who reported the liquidus projection and an isothermal section at 1300°C shown in Figure 2.5. Three main ternary phases were seen by quenching the alloy from 1300°C: two cubic η-carbides, Ni_2W_4C and Ni_6W_6C, and a hexagonal X-carbide NiW_3C [1975Fie].

Gabriel *et al.* [1986Gab] presented a partial isothermal section at 1500°C. They observed that solubility of WC in the liquid varied more with the tungsten content than the carbon content. At 1445±5°C, a peritectic reaction: liquid + M_6C↔ WC + fcc was observed. The temperature of the four-phase reaction between liquid, fcc, WC and graphite was also found to be 1340°C and termed peritectic [1986Gab]. They further revealed that the solubility of WC is lower in

nickel than in cobalt, and the lowest temperature at which liquid forms in the W-Ni-C system is higher than in the W-Co-C system [1986Gab]. A thermodynamic study on W-Ni-C systems reported by Gustafon *et al.* [1987Gus] gave a calculated isothermal section of the system at 1300°C and a liquidus projection. They gave parameters describing the Gibbs energy of each individual phase. However, the thermodynamic description led to higher tungsten content of the liquid in equilibrium with graphite and WC and also a greater slope in the liquid / WC isothermal line than in experimental data [1987Gus]. A thermodynamically calculated vertical section at 10 wt % Ni was presented by Guillermet [1989Gui].

2.7.2 Fe as a binder

Over the years, the W-Fe-C system has had experimental and theoretical investigations. Uhrenius and Harvig [1977Uhr] used a capsule technique to control carbon activity and comprehensibly studied the equilibria involving carbides and ferrite or austenite at 1000°C. They reported carbon activities ranging from 0.012 to 0.97 in W-Mo-Fe-C, W-Fe-C and Mo-Fe-C systems. In the ternary W-Fe-C system, they observed equilibria between ferrite and M_6C; austenite and M_6C; austenite and WC and finally, austenite and cementite.

Subsequently, the carbide / austenite equilibria was studied at 900°C, 1000°C and 1100°C in the quaternary W-Fe-Cr-C system by Uhrennius and Frondell [1977Uhr]. The $M_{23}C_6$ carbide is destabilized, in comparison with the M_6C carbide, and $M_{23}C_6$ carbide when the W/Cr ratios is increased. The $M_{23}C_6$ phase is metastable in the ternary W-Fe-C system in this temperature range. This observation confirmed the work by Kuo [1953Kuo] at 700°C.

Greenbank [1971Gre] researched carbon activities in ternary austenite (fcc) in the W-Fe-C system at 1100°C and 1175°C. Takeda studied equilibria involving the liquid phase [1931Tak, 1931Tak2] and also was studied by Shevchuk *et al.* [1978She] and Jellinghaus. [1968Jel]. The four carbide phases that have been reported in the W-Fe-C system are M_4C, M_6C, $M_{12}C$ and $M_{23}C$.

An isothermal section at 1000°C of W-Fe-C (Figure 2.6) was presented by Pallock and Stadelmaier [1970Pal] which included three ternary phases: two cubic η-carbides Fe_3W_3C and Fe_6W_6C, and a hexagonal FeW_3C. Pallock *et al*. [1970Pal] reported a small composition range for M_6C and little or no homogeneity range for $M_{12}C$ around the stoichiometric composition, compared with earlier reports of a wide homogeneity range reported for M_6C

[1998Upa]. Also, no $Fe_{21}W_2C_6$ phase was found, as usually seen [1970Pal]. Through metallography, XRD and electron microprobe analyses, Bergstram [1977Ber] revealed the homogeneity regions of the two η-carbides $(FeW)_6C_6$ and $(FeW)_{12}C$ at 1250°C. The η-carbides were stable in a similar homogeneity range to Pallock *et al.* [1970Pal] and Jellinghaus [1968Jel]. The homogeneity range was reported to be displaced towards higher tungsten content [1977Ber].

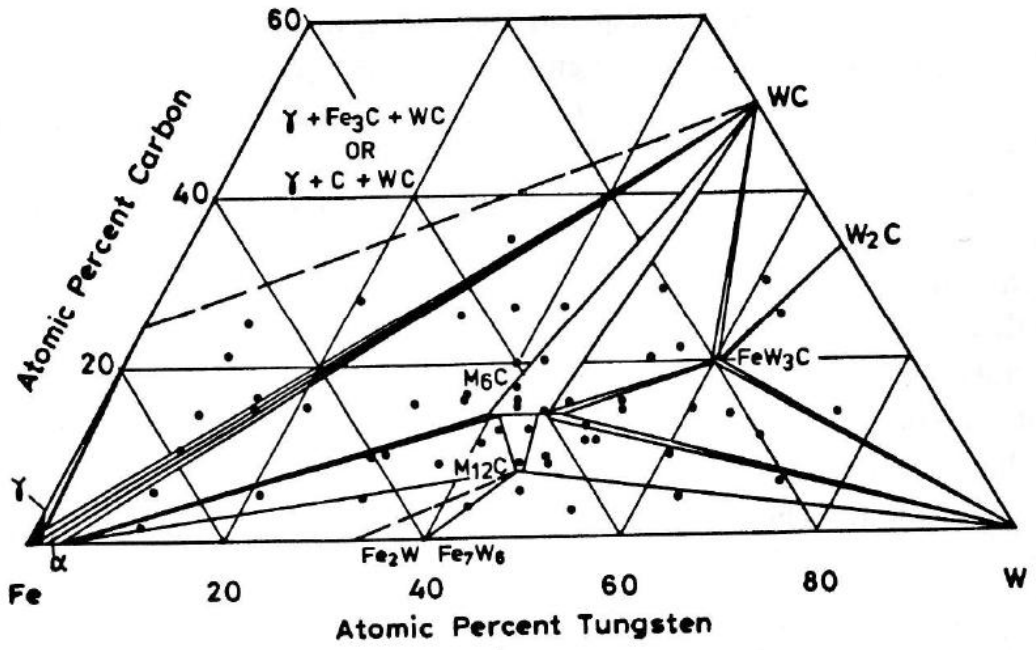


Figure 2.6. W-Fe-C isothermal section at 1000°C [1970Pal].

2.7.3 Fe-Ni as binder

Aqte [1959Aqt] and Moskowitz *et al.* [1977Mos] indicated that excess carbon Fe-Ni–bonded hard metals with optimum properties could be produced. Moskowitz *et al.* [1977Mos] reported the optimum nickel content in Fe-Ni-bonded hardmetals alloy to be around 10 wt%. Austenite was stabilized by higher nickel content. The useful range of Fe-Ni-C binders could be enlarged through the use of cobalt as an additional alloying element. Co acts as solid solution binder and most often raises M_s. This means Co increases the martensite in the binder phase [1967Tan]. In the binder during cooling, the temperature at which the transformation of austenite to martensite begins (M_s) is depressed by both nicked and carbon. This is said to be equivalent to stabilization of austenite.

In spite of the superior transverse rupture strengths (TRS) and abrasive wear resistance of Fe-Ni-bonded WC materials compared to cobalt-bonded WC, it is yet to be applied commercially. Although the abrasion resistance is good, the hardness (4120-4460 MPa) is even higher. However, the former property is more significant for potential industrial application [1970Mos].

Upadhyaya and Bhaumik [1988Upa] researched the sputtering of submicron (0.78μm) WC-10 wt% Co hardmetal by partially, or completely, substituting the cobalt binder with nickel or iron. They concluded that complete cobalt substitution in WC-10 wt% Co hardmetal by Ni-Fe binder imparts better properties compared with substitution by either iron or nickel alone. They also found that the grain size of the carbide phase increased with increased nickel content in the binder. The oxidation resistance of WC-10 wt% Co hardmetal decreased on substitution of the cobalt binder by nickel. The densification and mechanical properties of submicron WC-10 wt% Co hard metals deteriorated on increased substitution level of cobalt by nickel, as shown in Figures 2.7 and 2.8.

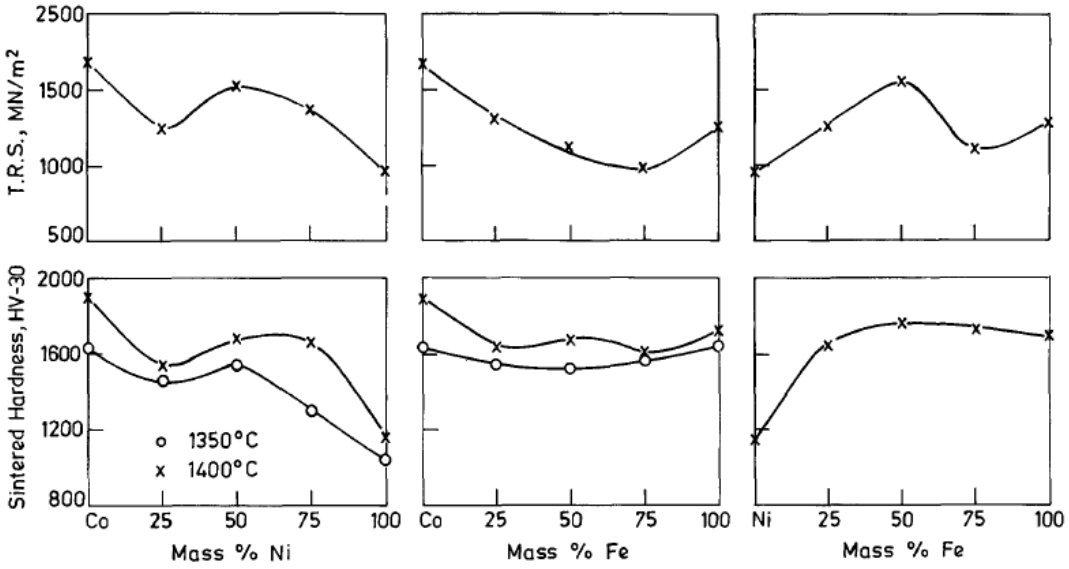


Figure 2.7. Vickers' hardness and TRS plots of WC-10 wt% (Co-Ni-Fe) hard metals, sintered at 1350°C and 1400°C for 1 h in dry hydrogen [1988Upa].

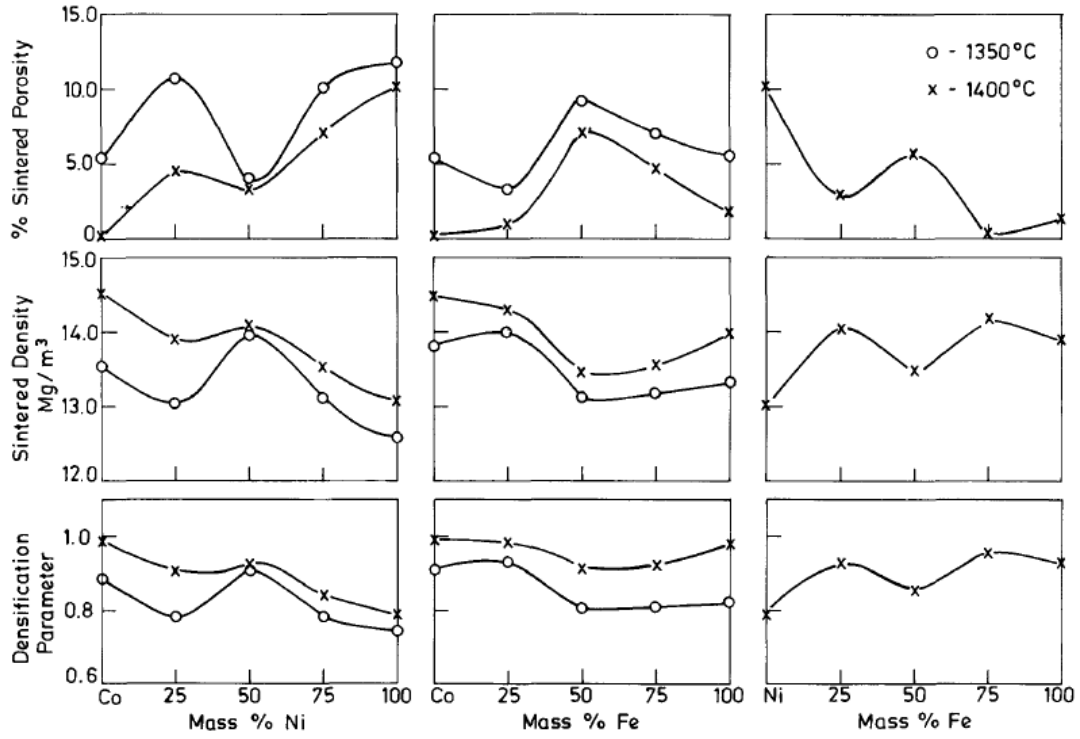


Figure 2.8. Properties of WC-10 wt% (Co-Ni-Fe) hard metals, sintered at 1350°C and 1400°C for 1 h in dry hydrogen [1988Upa].

Kakeshita and Wayman [1991Kak] prepared WC cermets with a metastable austenitic-Fe-23Ni-1.5C binder. X-ray measurements showed that the cermet consisted of two phases: WC and a polycrystalline austenitic phase (fcc). The WC particles were about 3μm across and were hexagonal and/or rectangular, as determined by SEM and TEM. X-ray measurements also showed that the binder in as-sintered-and-hot-isostatically-pressed cermets expanded, despite the constraint of the WC phase. The constraint is derived from the thermal stress produced by the difference in thermal expansion coefficients of the binder and WC phases. Thermally and deformation-induced martensites were both formed. The M_s for the thermally induced martensite was about 253K according to differential scanning calorimetric (DSC) measurements, which is ~80K higher than for martensite forming in a bulk Fe-Ni-C alloy of the binder composition. The difference may also be a consequence of thermal stress [1991Kak].

The WC-(Fe-Ni-C) fracture toughness was ~23 MPa $m^{½}$, which was much higher than for a conventional WC-Co cermet, although there was no significant difference in hardness on comparing the two. It was thought that the fracture toughness may be further improved by

suitable heat treatment and/or by changing the volume ratio of the binder phase. The increase in fracture toughness arises from transformation toughening from the martensite.

TEM revealed many dislocations in the binder phase, probably arising from relaxation of the thermal stress, as found by Kakeshita and Wayman [1991Kak]. The morphology of the thermally induced martensite was thin plates with internal transformation twins, which was different from the deformation-induced martensite with dislocations. In the deformed cermets, stacking faults were observed in WC; these play an important role in stress relaxation and increasing the toughness. Analytical transmission electron microscopy showed no precipitates in or near the ceramic-metal interfaces [1991Kak].

2.7.4 Fe-Co-Ni as a binder

Figure 2.9 shows a liquidus surface projection of Co-Fe-Ni [1995Vil], with two different solid solution surfaces: (Fe(HT1)) and (Co(HT),Fe(HT2).Ni). The major phase was the Ni- and Co-rich (Co(HT),Fe(HT2).Ni).

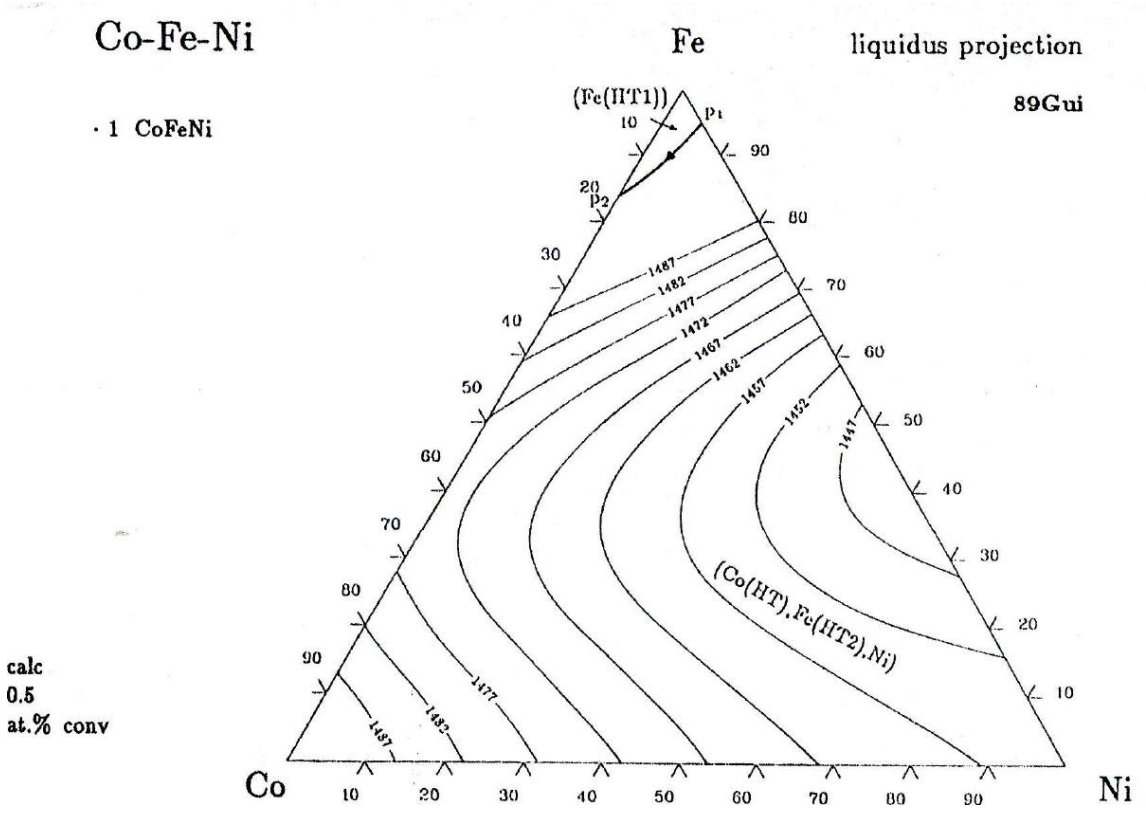


Figure 2.9. Liquidus projection for Co-Fe-Ni [1995Vil].

Prakash [1977Pra] researched the properties of WC hardmetals with 20 wt% Fe-Co-Ni as a binder. These hardmetals were found to have more superior hardness and abrasion resistance, with slightly inferior TRS to conventional WC-Co hardmetals. The strength of the martensite phase was increased by increasing the carbon content and at the same time stabilized the softer austenite phase [1977Pra, 1978Pra].

2.7.5 Fe-Ni-Cr as a binder

Chromium has been employed in limited amounts to regulate grain growth and improve oxidation and corrosion resistance [1988Pen]. Both Fe and Cr have a strong affinity for carbon, resulting in carbide formation, encouraging brittle behaviour and impairing mechanical properties. To date, a systematic study of thermal reactivity between metallic elements employed in partial or total substitution of cobalt and tungsten carbide has yet to be achieved to control brittle phases.

Fernandes *et al.* [2009Fer] studied the thermal reactivity between WC and Cr/Fe/Ni with different carbon affinities. They used conventional powder preparation techniques and a coated powder process by sputter-coating WC particles. In their samples, they replaced 10 wt% Co with different compositions of Fe-Ni-Cr.

Fernandes *et al.* [2009Fer] concluded that no carbide phases were detected for the conventionally prepared cermet with 10 wt% Fe after the thermal treatment at 1400°C. The WC, bcc ferrite Fe (α) and fcc austenite Fe (γ), phases were there. The substitution of 0.5 wt% Fe by Ni stabilized the austenite, Fe (γ). The formation of the Cr_2C carbide was induced by introducing 3.3 wt% Cr to the binder composition. The formation of the $(Fe,Cr)_3(Ni,W)_3C$ eta-phase, instead of Cr_xC carbides was as a results of reducing the Cr content in a sputter-coated powder, which may contain all the metallic elements. An excess of 3.6 wt% Cr relative to the stoichiometric carbon was added in to remove the eta-phase. This completely inhibited the carbide formation and led to the formation of the more desired austenite, Fe (γ) phase. This cermet had good chemical, structural and microstructural characteristics, giving high hardness from WC phase, high toughness from the austenitic and high oxidation and corrosion resistance from the Cr content and the austenitic structure. The uniform binder distribution, due to the sputter-coated process, and the controlled final grain size, due to Cr addition were also beneficial.

Figure 2.10 shows a solidus projection for Ni-Fe-Cr [1995Vil], with two different solids, (Cr,Fe(HT1)) and (Fe(HT2),Ni), and a two-phase field between them. Obviously, a two-phase binder may be problematic.

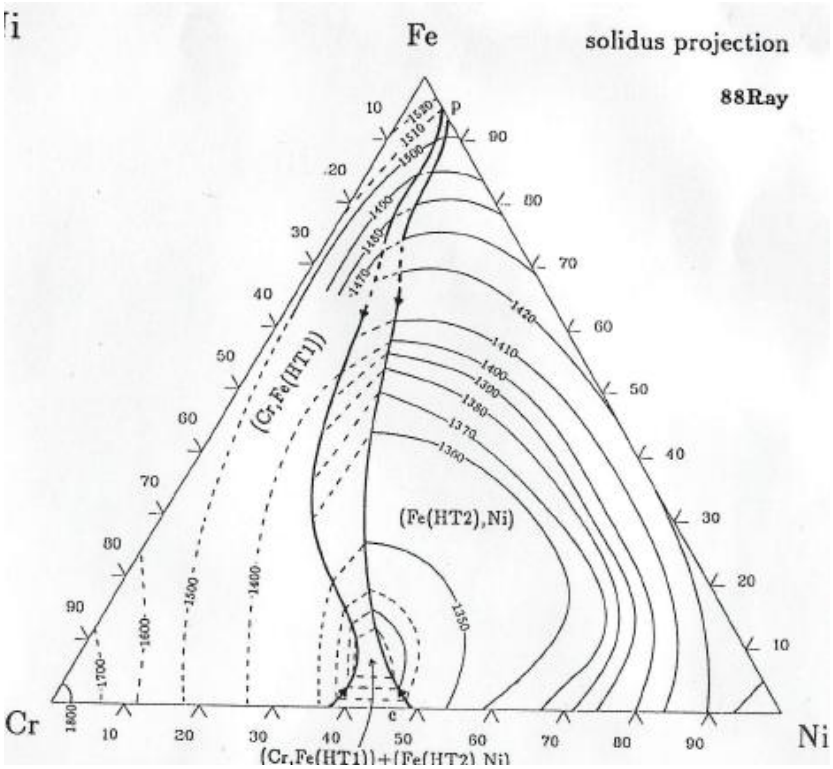


Figure 2.10. Solidus projection for Ni-Fe-Cr [1995Vil].

2.7.6 Fe-Mn as a binder

Figure 2.11 is an assessed binary diagram of Fe-Mn [1993Kat]. The Mn-rich end of the Fe-Mn binary phase diagram has three different solid solutions, which were: (αMn), (βMn) and (δMn). The (δMn) exists at high temperatures (1138°C to 1246°C) and within a composition range of about 88 at.% Mn to 100 at.% Mn. The (βMn) which transforms to (αMn) at 727°C had a maximum temperature of about 1130°C. Both (βMn) and (αMn) have almost the same composition range, above 69 at.% Mn.

The Fe-rich end was composed of (δFe) and (αFe). The (δFe) formed between 1400°C and 1538°C, within a composition range of 100 at.% Fe to about 11 at.% 86 at.% Fe.

There was a complete miscibility in all proportions (γFe,γMn) which narrowed from 100 at.% Fe at 912°C to about 30 at.% Fe at 400°C. The complete miscibility range was very small at the Mn rich end (1138°C to 1100°C).

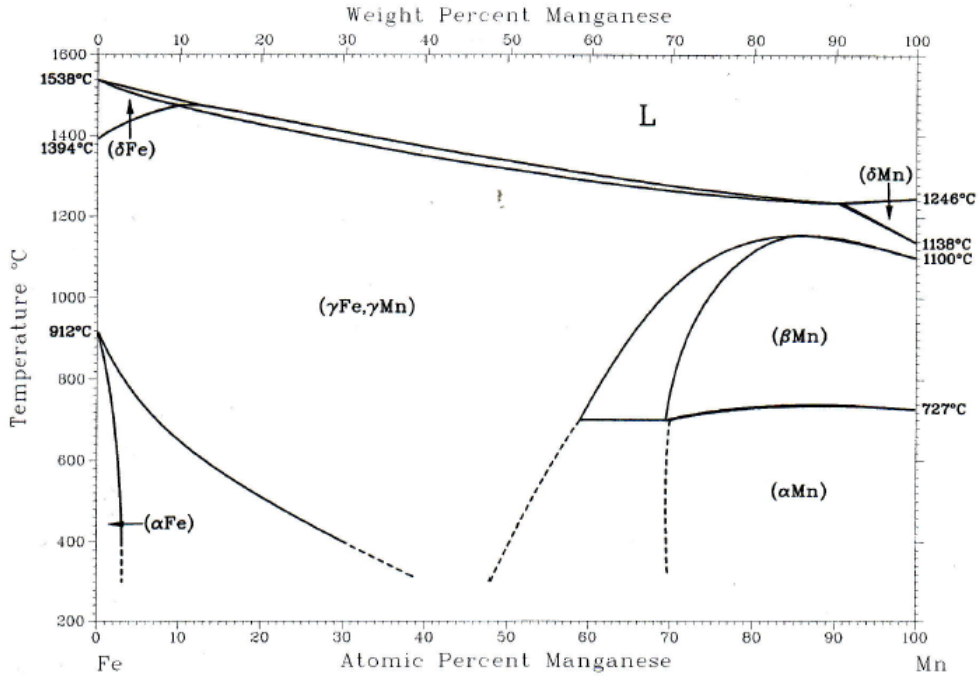


Figure 2.11. Fe –Mn phase diagram [1990Mas].

The Fe-13.5 wt% Mn alloy demonstrates comparable characteristics to cobalt, such as melting temperature, crystal structure and a γ(fcc) → ε(hcp) phase transformation on cooling [2001Han]. Manganese steel (Fe-13-14 wt% Mn -1-2 wt% C) is known for high wear resistance, which would be advantageous when employed as a binder in WC-based hardmetals. Additionally, the Fe-Mn, is a less expensive alloy and a good alternative to Co binders because it is non-toxic. Mn stabilizes the austenite just like Ni, but when alloyed with Fe, it is almost twice as effective as Ni. The Fe-13.5 wt% Mn alloy possesses full or partial austenitic structure at ambient temperature, whereas a Fe-Ni alloy takes about 30 wt% Ni [1986Sch, 1978 Shi] for a similar structure. Also, Mn is cheaper than Ni and has no reported health hazard.

Hanyaloglu *et al*. [2001Han] studied the WC/Fe-Mn system and to produced bonded WC hardmetals with a fully stoichiometric microstructure (i.e. no free carbon or η-phase) and with toughness and hardness values close to those of similar Co-bonded hardmetals. Fe-13.5

wt % Mn bonded WC hardmetals with a fully austenitic binder phase were produced with a good enough sintering temperature range of 1350°C-1430°C. High-performance WC/Fe–Mn hardmetals were produced, which showed potential as alternatives to WC/Co alloys. Moderate Vickers hardness values of 14–15 $GN.m^{-2}$ were obtained, and Palmqvist-type cracks of nearly identical lengths formed. They also observed that as the binder proportion increased, the hardness and fracture toughness values decreased.

After sintering under strongly carburising atmospheres, the microstructure was composed of angular WC grains in austenitic Fe–Mn, and was free of the η-phase. Failure to maintain sufficient carbon resulted in a pronounced tendency to form η-phase carbides.

2.7.7 FeAl as a binder

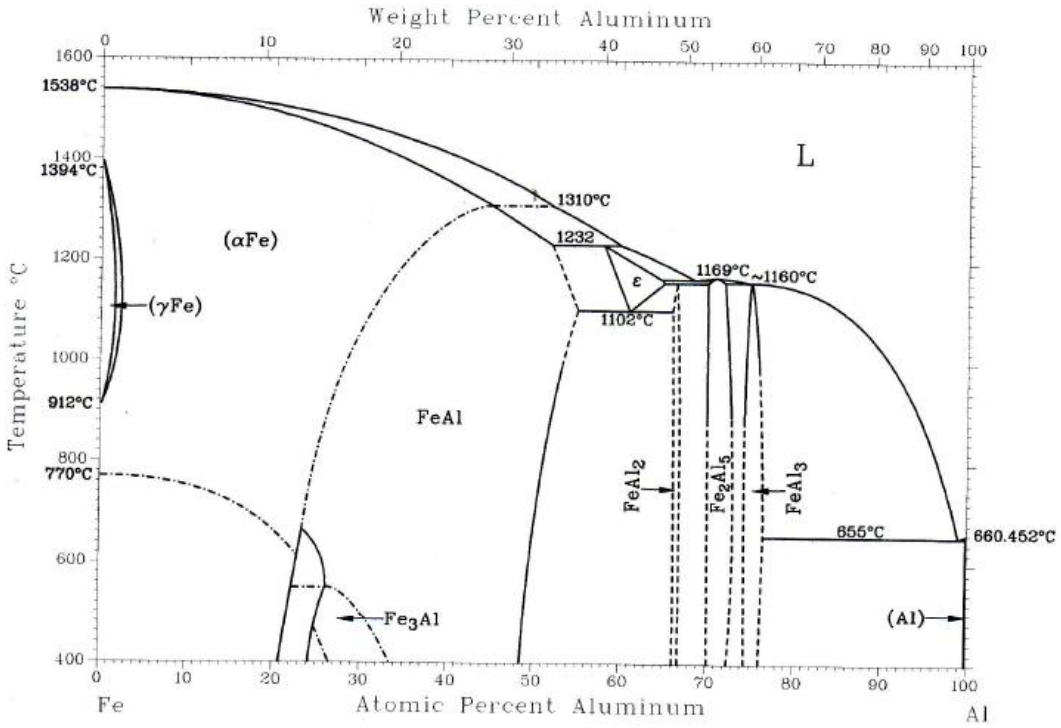


Figure 2.12. Fe –Al W phase diagram [1993Kat].

Figure 2.12 is an assessed binary phase diagram for the Al-Fe system. This is largely based on the work of Dix [1925Dix], Gwyer and Philips [1927Gwy], Lee [1960Lee], Rocquet, Jegaden and Petit [1967Roc], Allen and Cahn [1975All], Kosester and Goedecke [1980Kos], Schuermann and Kaiser [1980Sch], Griger [1986Gri] and Wachtel and Bahle [1987Wac]. The Fe-Al system was yet to be completely and precisely determined [1993Kat]. More work

needs to be done on the reaction temperatures and phase boundaries, even though the existence of the equilibrium intermediate seems to be reliably established.

Over the last decade, iron aluminide (B2-FeAl) based on the ordered B2 structures have been investigated for a possible application in high-temperature structural materials [1997Mun, 1996Sto]. The iron aluminide can be potential binder phase for hard ceramic particles such as WC, Ti, TiB_2 and ZrB_2. Iron aluminide is generally known for high oxidation and sulfidation resistance, high strength, low density, high work hardening, and also comprises inexpensive raw materials [1997Sch]. Excellent wear resistance of B2-FeAl was obtained by the high oxidation and corrosion resistance with a high strength and work hardening combination [1989Ant, 1989Fle]. Low tensile ductility and fracture toughness are the major shortcomings of B2-FeAl intermetallic compounds, although these are not as essential for wear applications as they are for structural applications [1996Sto, 1989Ant]. In wear applications, hardness, strength and work hardening ability are the more critical properties [1989Ant].

B2-iron aluminide with 40 at.%.Al was shown to possess a significant level of ductility when it is a matrix in a composition with hard ceramic phases like WC [1997Sch]. Thus, this could be a potential binder.

Mosbah *et al.* [2005Mos] compared of the abrasive wear behaviour of WC-40% $Fe_{60}Al_{40}$ composites and WC-Co hardmetals to understand the role of the binder material in composite abrasive wear resistance. They found that the FeAl with 40 at.% Al was a superior matrix material than Co metal, based on the abrasive wear conditions they used (pin-on-drum wear testing). Secondly, the WC-40% $Fe_{60}Al_{40}$ composites and WC-10%Co with similar grain sizes exhibited comparable strength and abrasive wear rates, when tested under identical conditions.

CHAPTER 3

RATIONALE FOR THE NEW BINDERS

3.1 Introduction

A number of binders (elements and alloys) have been used in an attempt to replace cobalt as binder to WC as discussed in Chapter 2. There were some key requirements for selection of the new binder alloys used in this project and they are described in this section. They are:

- formation of solid solution,
- small solubility with tungsten and carbon,
- melting point range near cobalt,
- novelty.

3.1.1 Solid solution

Solid solutions occur when foreign atoms are incorporated into a crystal structure of other solid elements as in Figure 3.1. A crystal can only dissolve a different element's atom by two mechanisms. An interstitial solid solution is formed when the solute atom is small enough to fit into spaces between larger atoms comprising the solvent crystals. Hydrogen, nitrogen, carbon and boron are some of the only solute atoms small enough to typically fit into interstices of metal crystals. Most of the elements dissolve in different solid metal crystals by replacing atoms of the solvent at lattice sites to form substitutional solid solutions [1935Mar]. Solid solution compositions from binary phase diagrams were chosen for all binder alloys used in this study, since single elements have been tried, e.g. Ni [1975Fie], Fe [1971Gre].

3.1.2 Small solubility with tungsten

Solid solubility can be unlimited or limited. Solute and solvent are mutually soluble in all proportions when unlimited solid solubility occurs, an example is Cu-Ni or W-V. In these instances, the Hume-Rothery rules [1969Hum] are met, resulting in a complete solid solution. The rules are:

- The relative size ratio for the two elements should be below approximately 15%.
- the crystal structure must be the same,

- electronegativity difference must be within ± 0.4 e.u., and
- their valencies must be the same.

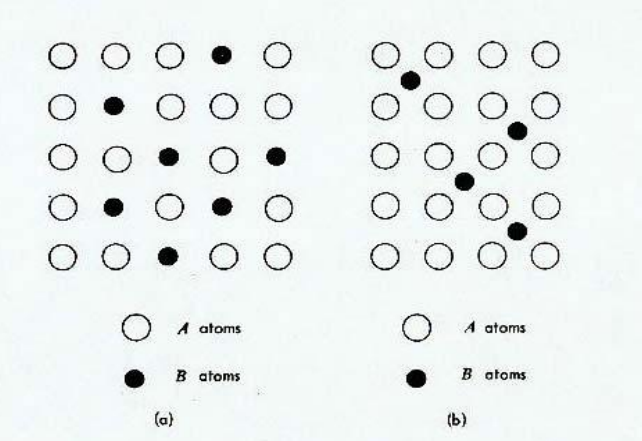


Figure 3.1 Mechanisms for solid solution formation (a) substitutional (b) and interstitial [1973Bar].

Limited or partial solid solubility occurs when there is a limit to how much of the solute can dissolve in the solvent before saturation is achieved, e.g., Pb-Sn or W-Co systems. These systems normally do not obey the Hume-Rothery rules and the result is multiple phases.

In the choice of new binders for this study, considerable solubility between WC and the binder alloys was a factor. A very high solubility between the soft binder phase and the hard carbide phase may result in inferior mechanical properties of the target alloy in terms of hardness [1998Upa]. Copper has very low solubility for WC [1975Hup], and was alloyed with elements like nickel, zinc and manganese which have been reported to improve solubility of copper for WC [2003Gua, 2003Cos]. Thus, intermediate solid solubility is required, as well as good wettability.

3.1.3 Melting point range

Another key requirement considered for selection of new binder alloys was melting point range. All selected binders have their melting point in the range within the range of the sintering temperature for cobalt. This was considered with the aim of achieving similar properties and maintaining current manufacturing procedures for WC-Co. Manufacturers would be unwilling to change their current process too much, and higher temperatures would

not be popular. This is because more power would be necessary, and would increase cost, and the current sintering equipment might have temperatures limits.

3.1.4. Novelty

Novel binders were selected; the replication of binders already in use was avoided. Literature was checked at the outset of the study, and revealed that no work has been published on the binders selected here to replace or reduce the amount of cobalt.

The binder phase should be ductile enough and possibly should not form a eutectic in the binder phase, since it can negatively affect the ductility of the binder, as a eutectic acts like a composite. Additionally, eutectics usually have a more limited melting range than solid solutions, which could compromise the binder.

3.2. Potential New Binder Systems

3.2.1. Co-Mn System

The Co-Mn phase diagram (Figure 3.2) [1990Mas] is primarily based on the work of Hellawell and Hume-Rothery [1957Hel], Tsioplaka *et al*. [1971Tsi] and Hasebe *et al.* [1982Has]. The phases include liquid, terminal solid solutions and the δ phase, which forms at about 50 at.% Mn and below 545ºC. The solid solutions are: hcp (εCo), Mn-rich bcc (δMn), A13 (βMn) and complex cubic (αMn) below 710ºC.

The peritectic reaction L + (αCo) ↔ (βMn) was reported by Hellawell and Hume-Rothery [1957Hel] to occur at 1161ºC, which is in agreement with 1160ºC determined by Tsioplaka *et al*. [1971Tsi]. There is a minimum in the liquidus and solidus at about 63 at.% Mn and 1160ºC [1957Hel]. According to Tsioplaka *et al.*, the peritectic L + (δMn) ↔ (βMn) occurs at 1190ºC [1971Tsi], but Hellawell and Hume-Rothery gave ~1185ºC [1957Hel], although the current phase diagram [1990Mas] gives 1185ºC.

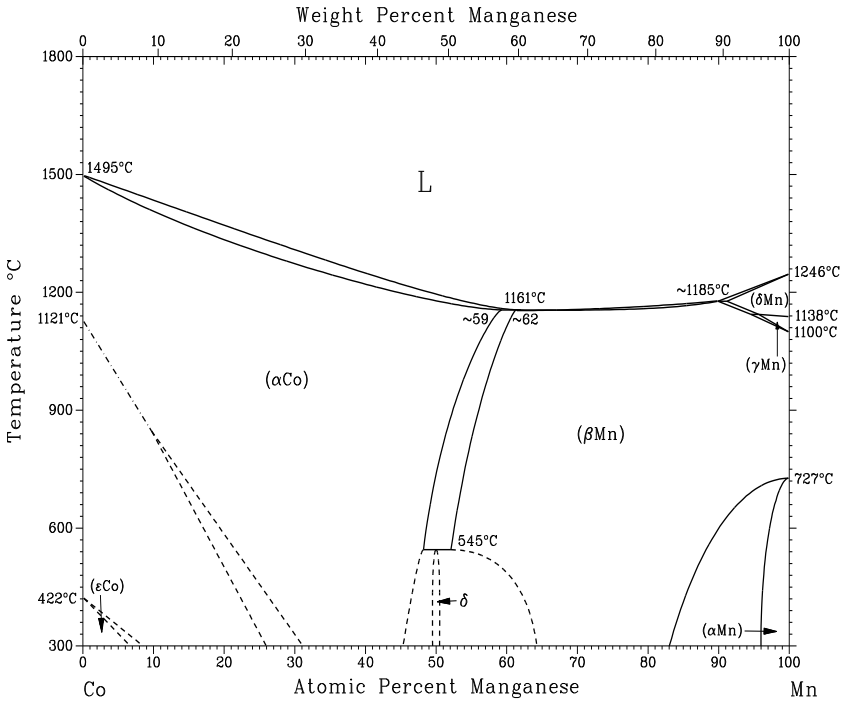


Figure 3.2. Assessed phase diagram for Co-Mn [1990Mas].

3.2.2 Cu-Ni System

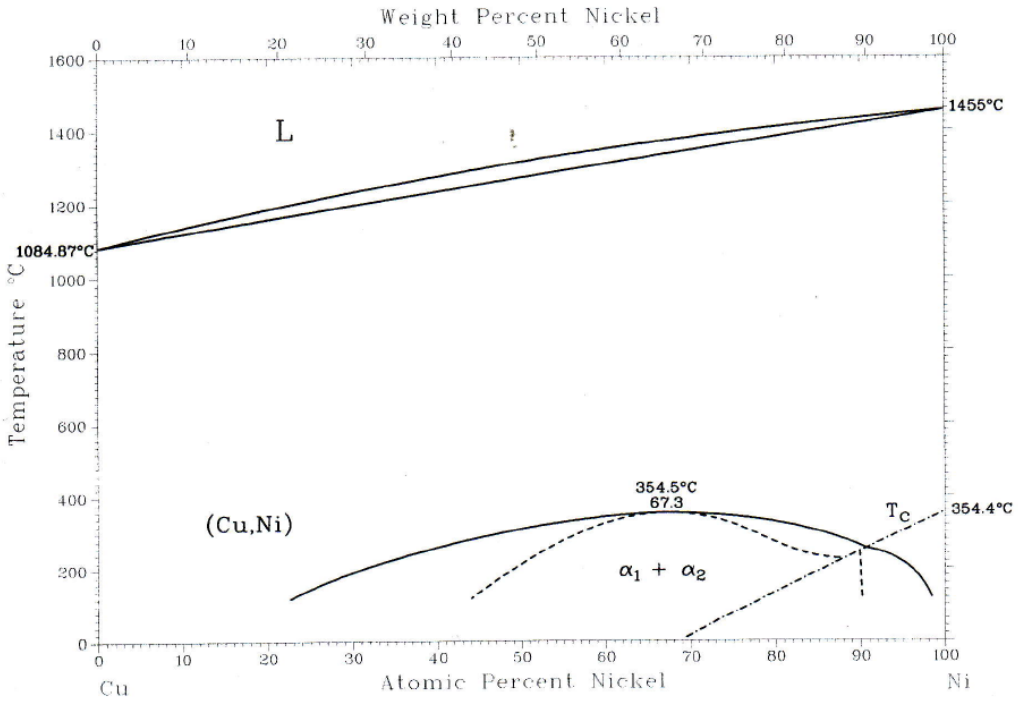


Figure 3.3. Cu-Ni assessed phase diagram [1990Mas].

The liquid phase and the fcc (Cu,Ni) phase make up most of the Cu-Ni equilibrium phase diagram (Figure 3.3). The liquid phase has high stability and complete miscibility in all proportions down until the melting point of Cu at 1084.87ºC. A separation of the solid (Cu,Ni) phase is encountered at 354.5ºC and 67.3 at.% Ni to form α_1 and α_2 [1991Cha]. The α_2 phase changes from the paramagnetic state to a ferromagnetic state below T_C [1991Cha].

The accepted liquidus and solidus are based on the work by Bastow and Kirkwood [1971Bas], Feest and Doherty [1971Fee], and Schurmann and Schulz [1971Sch] for melting of Cu at 1084.87ºC and Ni at 1455ºC.

Meijering predicted a miscibility gap that closes at 177ºC based on thermodynamic analysis [1957Mei] and below 334.5ºC the phase equilibria were thermodynamically calculated by Chakrabarti [1991Cha].

3.2.3 Ni-V System

The major part of the Ni-rich end of the Ni-V assessed diagram (Figure 3.4) is credited to Pearson and Hume-Rothery [1952Pea], whereas the V-rich end is largely credited to Stevens and Carlson [1970Ste].

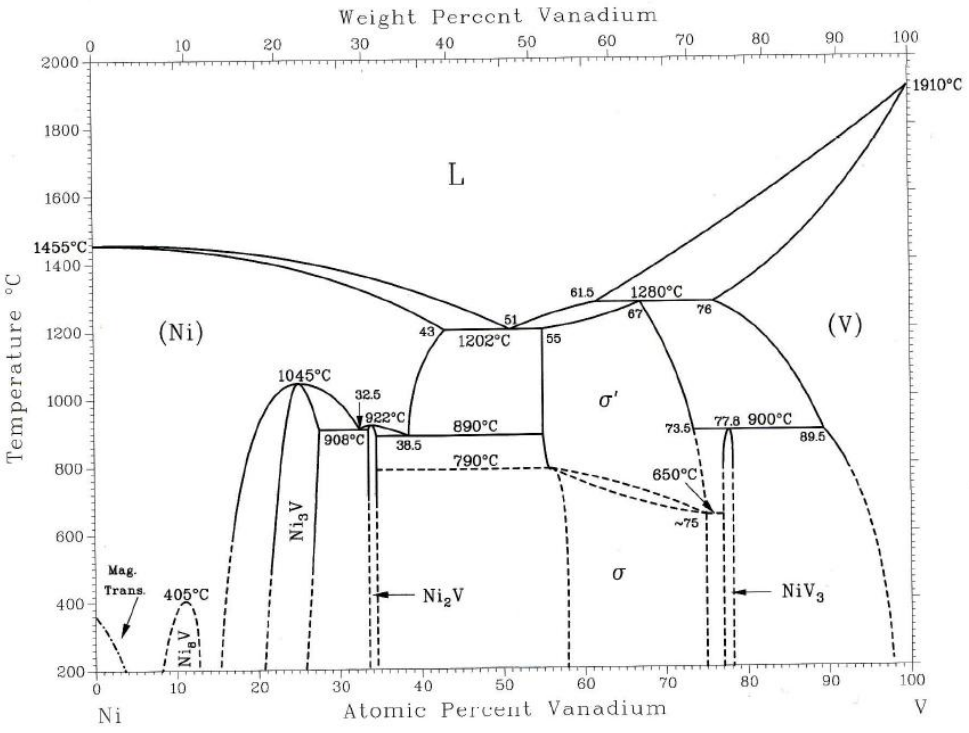


Figure 3.4. Assessed Ni-V binary phase diagram [1990Mas].

Addition of V decreases the Curie temperature of (Ni) [1937Mar] (Figure 3.4). The Ni_8V phase was identified as having ordered fct stoichiometry; this was done using electrical resistivity and electron diffraction techniques by Moreen *et al.* [1971Mor]. This phase forms by an order-disorder reaction from the solid solution of the Ni-rich end.

The Ni-rich boundary of the σ phase of was placed at 55 at.% V and the Ni-poor boundary above 65 at.% V at high temperatures by Pearson [1952Pea]. The σ phase was found to be ferromagnetic at lower temperatures by Nevitt and Beck [1955Nev], and at 64.2 at.% V was found to have a Curie temperatures of 52K.

Enough evidence of the existence of a phase with an ideal stoichiometry of NiV_3 was found [1989Smi], but with a V-rich stoichiometry. The NiV_3 phase crystallises with the Cr_3Si-type structure [1989Smi]. The formation of this phase may be influenced by factors such as kinetics or impurities; this is because not all investigators find this phase. This disagrees with thermodynamic calculations [1989Smi].

The (Ni) solid solution range was observed to extend to ~43 at.% V, with no detectable difference within the range of the cooling rates of the rates of the experiments (10^5 to 10^9 $^oC/s$).

3.2.4 Ni-Zn System

The assessed Ni-Zn diagram (Figure 3.5) conforms to Hansen's previous evaluations [1936Han]. The (Ni) boundary is based on the work of Schramm [1938Sch] and Budurov and Nenchev [1974Bud]. The single phase region γ was suggested by Morton [1979Mor] by combining the previous γ and γ_1 [1991Nas] phase regions. Inversion anti-phase domain (IAPD) structure is seen in the Ni-rich portion of the γ phase region. A very small amount of Ni goes into solution in (Zn).

The magnetic transformation is from 354.2ºC in pure Ni and about 19.1 at.% Zn at room temperature. The cubic β phase of CsCl-type transforms to the AuCu-type fct β_1; this was revealed by metallographic and X-ray examination [1972Lia]. The alloys quenched in water or liquid nitrogen revealed a martensitic-type transformation. Murakami *et al.* [1984Mur] studied this transformation by optical and electron microscopy in a $Ni_{50}Zn_{50}$ alloy and found martensite on quenching, and massive transformation on slow cooling.

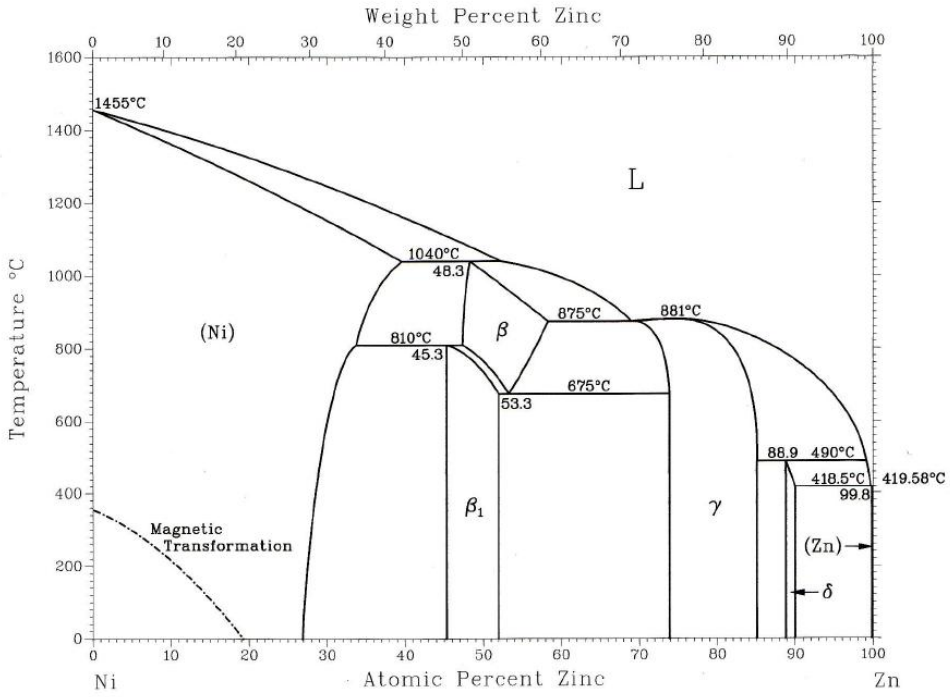


Figure 3.5. Ni-Zn assessed phase diagram [1990Mas].

3.2.5 Cu-Zn System

The current assessed Cu-Zn phase diagram (Figure 3.6) [1990Mas] is a modification from Hansen's work [1936Han] tailored with reviews of Haughton and Bingham [1921Hau], Imai [1922Ima], Genders and Bailey [1925Gen], Bauer and Hansen [1927Bau], Ruer and Kremers [1929Rue], Schramm [1935Sch1, 1935Sch2] and Massalski and King [1962Mas]. There is a slight difference between phase boundaries of the assessed and those of Hansen [1936Han] and that of Raynor [1944Ray]. Due to the marginal differences of the phase boundaries [1936Han, 1944Ray], other work [1994Mio] focused on clarifying the short-range order in the α phase, the order-disorder transformation in β, polymorphism in γ, and the defect structure of the δ phase. This has resulted in considerable data on the martensitic transformation in the β phase.

The liquidus curve of the assessed diagram is credited largely to Buaer and Hansen [1927Bau], Ruer and Kremers [1929Rue], and Schramm [1935Sch], which are accurate within ±3ºC with Raynor's results [1944Ray]. Bauer and Hansen determined the liquidus from 54 at.% Zn to 100 at.% Zn [1927Bau].

A monoclinic and triclinic product was reported when cooling the β' phase to liquid nitrogen temperatures [1962Kun], and an orthorhombic cell for an alloy with 38.3 at.% Zn quenched from 840ºC [1963Jol] and various metastable tetragonal phases were found [1959Hor].

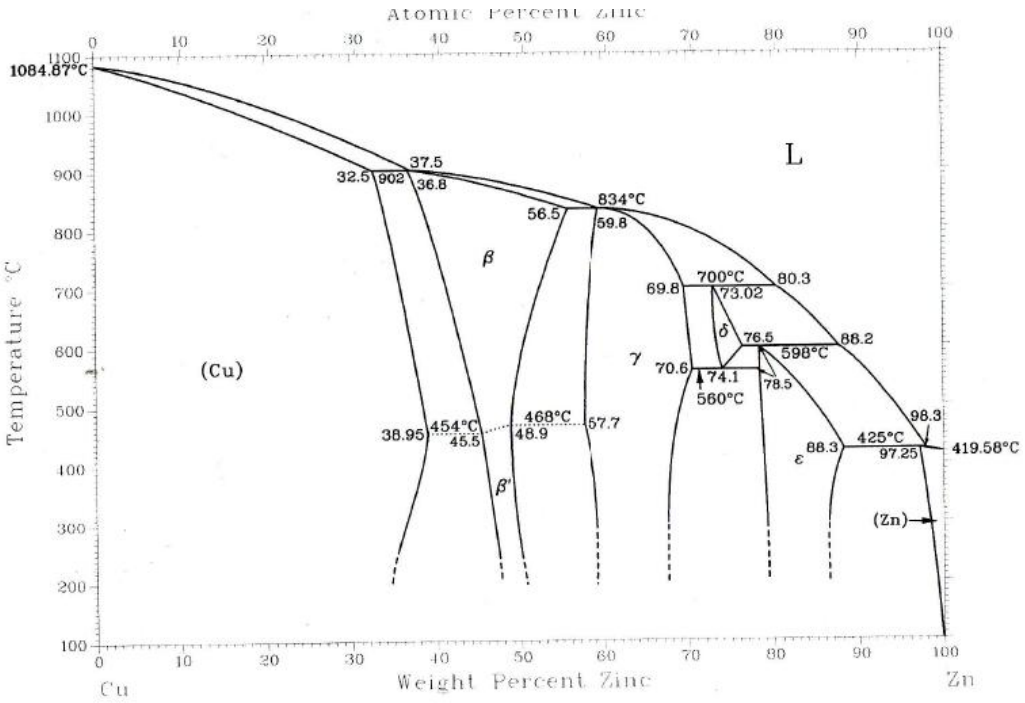


Figure 3.6. Assessed Cu-Zn phase diagram [1990Mas].

3.2.6 Mn-V System

Figure 3.7 [1990Mas] shows an assessed phase diagram for Mn-V, where Waterstrat's work was the basis [1962Wat], with small modifications from Hellawell and Hume-Rothery [1957Hel]. Lugscheider and Ettmayer [1971Lug] established the existence of a complete series of solid solutions between bcc V and δMn. The existence of an σ phase is also well known [1991Smi]. The structure of the σ is of tetragonal-type; this is normally observed in transition metal systems. There is some uncertainty regarding phase equilibra above 85 at.% Mn, although Lugscheider and Ettmayer [1971Lug] suggested a possible existence of two additional intermediate phases.

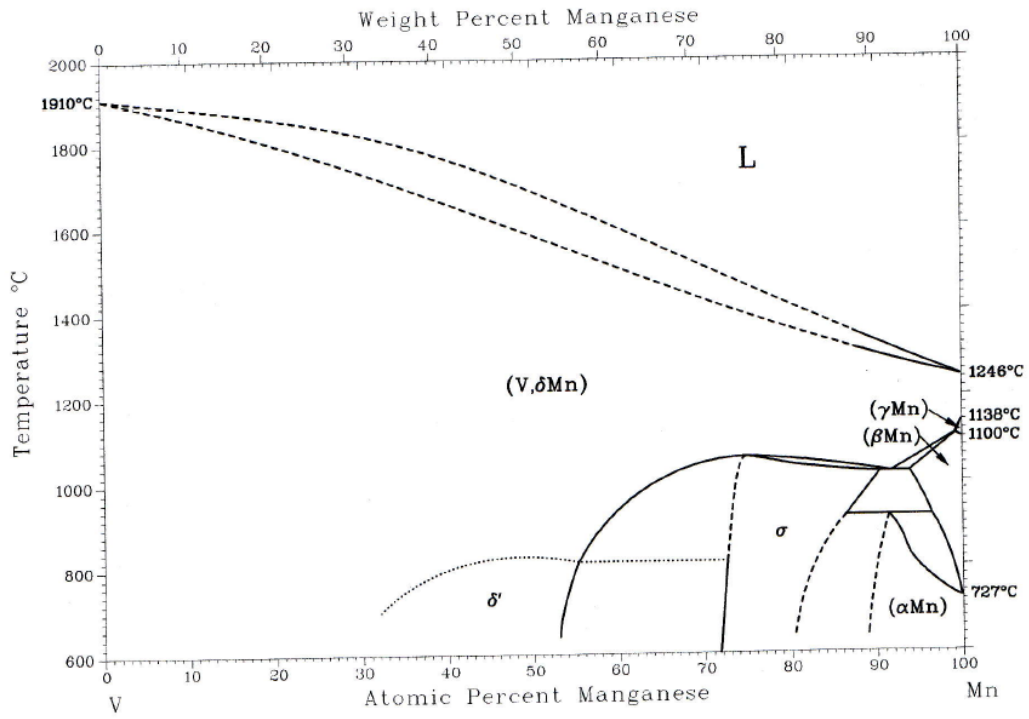


Figure 3.7. Assessed Mn-V phase diagram [1990Mas].

Through X-ray scattering using CrKα radiation, Waterstrat was able to differentiate between the V and Mn species in the bcc δ which have close atom scattering factors for X-rays. They observed CsCl-type superlattice lines in a $V_{52.2}Mn_{47.8}$ alloy that had been quenched from 1150ºC, crushed, and annealed for extended time. The order-disorder temperatures as a function of composition were determined by Suzuki and Hagiwara [1975Suz] using specific heat measurements and differential thermal analyses.

The presence of a congruent transformation of the high temperature (V,δMn) solid solution to the low temperature tetragonal σ phase near 75 at.% Mn at 1050°C was indicated by Waterstrat [1962Wat]. However, the extent of the σ phase field is not certain [1982Smi].

CHAPTER 4

MATERIALS AND EXPERIMENTAL PROCEDURES

4.1 Preparation of alloy

Selected alloy sample components were weighed individually, to give a final button of ~3g, and were arc-melted under an argon environment, on a water cooled-hearth. The melting process was repeated at least three times, aiming at complete mixing. The as-cast button samples were then sectioned into two halves using diamond blade wheel.

4.2 Microstructure examination

The as-cast half of the samples were hot mounted and polished on 320, 400, 600, 800, 1000 and 1200 grit paper followed by 9, 6, 3 and finally 1 micron polishing on diamond media. The samples were then polished using 50% Struers OP-S suspension in water (as a lubricant), on a Struers AP-Chem cloth. The samples were examined in a light microscope to make sure they were well polished.

4.3 Scanning electron microscopy

The samples were examined on a XL30 ESEM Philips SEM (University of Botswana) and a LEO 1525 SEM (NMISA, Pretoria), both with EDX. A 20 kV accelerating voltage was used in both SEMs. Imaging was done in backscattered and secondary electron modes. Phase composition analyses were undertaken using energy dispersive X-ray spectroscopy (EDX) using pure element standards, and in some instances, no standards. A minimum of five analyses were collected per phase in most cases, unless otherwise indicated. Averages and standard deviations were calculated for all phase analyses. Typical overall readings were taken in from areas of 0.4 x 0.4mm in size and specific phase analyses were mostly collected from spots where phases were more than 3μm across.

4.4 X-ray diffraction

The samples were taken out of the resin mount and analysed using a Philips PW 1710 and a D2 PHASER XRD. A continuous scan was done for each sample from 10° to 130° 2θ, with step size of 0.02° and a dwell time of 0.5s, using Cu Kα radiation. The runs took 45 minutes

on the Philips, and 12 minutes on the D2 PHASER. XRD was used to confirm phases and identify phases in some samples.

Bragg's diffraction is the key concept that XRD is based on. A monochromatic source of X-rays is used to irradiate a crystalline material; reflections occur from various lattice planes in the crystal and are characteristic for a specific crystal structure. The X-ray beams are governed by the relationship

$n\lambda=2d \sin \theta$

where

λ = wavelength of the incident radiation

d = interplanar spacing

θ = incident angle of radiation with the plane

n = a small integer.

XRD phase identification of the samples was done by matching the experimental peaks to standard patterns, which have been provided by the International Crystallography Diffraction Database (ICDD).

4. 5. Heat treatment

The other half of the sectioned sample was sealed in a silica glass tube under vacuum. This was done to avoid the samples being oxidized. A horizontal tube furnace was used to heat treat the samples at 1000°C for 168 hrs (7 days). The samples were water quenched and prepared metallographically for SEM and XRD analyses.

CHAPTER 5

EXPERIMENTAL RESULTS

During the arc-melting of the samples, thick smoke was observed when the samples were heated. The upper chamber of the arc melt was covered with soot-like powder after the melting process. This could be carbon being lost from the samples, causing carbon deficiency which resulted in ~W_2C compositions.

5.1 Microstructure characterization-cast samples

5.1.1 W_{25}:C_{25}:$Ni_{47.5}$:$V_{2.5}$ (at.%)

The W_{25}:C_{25}:$Ni_{47.5}$:$V_{2.5}$ sample had two distinct phases and a eutectic. The facetted light contrast ~W_2C dendrites were in different orientations. The bulk of the alloy comprised medium dark contrast dendrites ~Ni_3V which were cored (Figure 5.1). There was a eutectic comprising the light and dark phases. There were contrasts differences between the medium dark ~Ni_3V dendrites (Figure 5.2) and the darker ~Ni_3V component of the eutectic. The darker eutectic phase contained carbon and with less W than the medium dark phase, although this was probably due to pick-up of the carbide component of the eutectic.

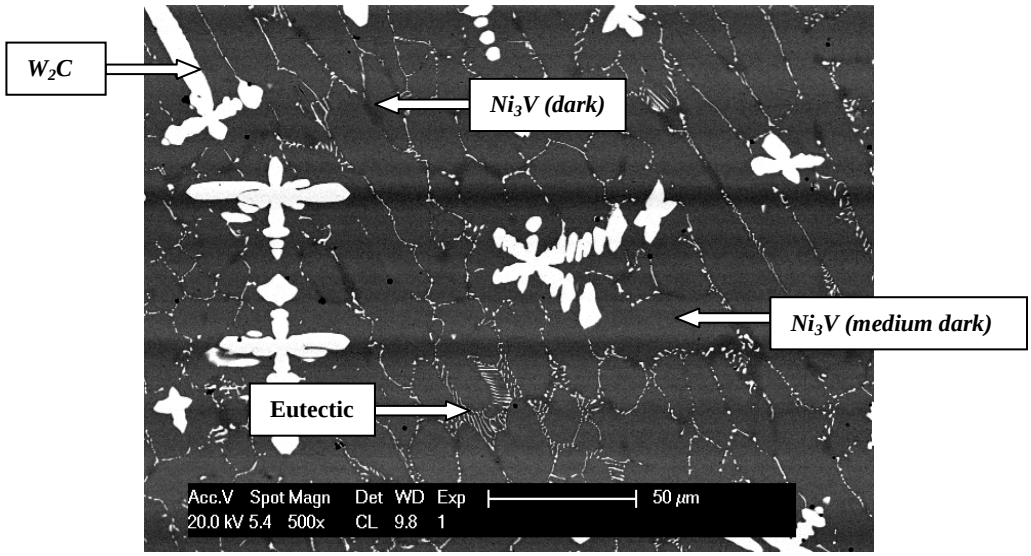


Figure 5.1. SEM-BSE image of nominal W_{25}:C_{25}:$Ni_{47.5}$:$V_{2.5}$ (at.%) in the as-cast condition showing: light ~W_2C dendrites surrounded by medium dark ~Ni_3V dendrites and ~W_2C (light) + ~Ni_3V (dark) eutectic.

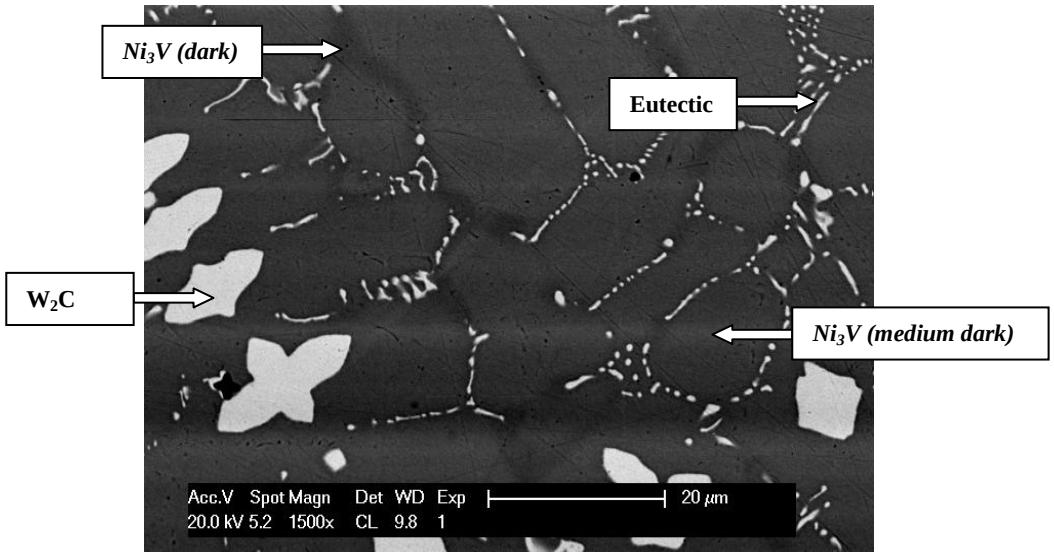


Figure 5.2. SEM-BSE image of nominal W_{25}:C_{25}:$Ni_{47.5}$:$V_{2.5}$ (at.%) in as-cast condition showing: light ~W_2C dendrites surrounded by medium dark ~Ni_3V dendrites and ~W_2C (light) + ~Ni_3V (dark) eutectic.

Table 5.1 gives phase analyses of nominal $W_{25:}C_{25}$:$Ni_{47.5:}V_{2.5}$ (at.%) using standards made from elements from which the samples were prepared. The light phase showed large errors for W and C. The dark phase was less than 3µm across, but a few readings were taken to observe the trend of differences from the other phases. The medium phase had very low vanadium content, even though it was identified as ~Ni_3V.

Table 5.2 has analyses taken without standards; they had large errors. Both EDX results from UB were dissimilar. The analyses without standards had higher carbon contents in all phases than the analyses with standards. Table 5.3 shows analyses done at NMISA in Pretoria. The phase analyses had very high carbon contents and large errors which made them doubtful. These analyses were ignored.

Phase description	W	C	Ni	V	Phase deduced
Overall	18.8 ± 0.2	13.8 ± 0.5	63.6 ± 0.6	3.8 ± 0.1	-
Light	72.4 ± 4.2	23.8 ± 5.3	2.9 ± 0.7	0.9 ± 0.7	~W_2C
Medium	17. 2 ± 0.6	0.0 ± 0.0	78.7 ± 0.5	4.1 ± 0.1	~Ni_3V
Dark	12.6 ± 0.3	13.3 ± 0.4	69.0 ± 0.9	5.1 ± 0.5	~Ni_3V
Eutectic	18.8 ± 0.2	9.9 ± 0.8	67.7 ± 0.7	3.6 ± 0.1	~W_2C +~Ni_3V

Table 5.1. EDX phase analyses for nominal W_{25}:C_{25}:$Ni_{47.5}$:$V_{2.5}$ (at.%) in the as-cast condition using standards derived from elements which samples were prepared (done at University of Botswana, UB).

Phase description	W	C	Ni	V	Phase deduced
Overall	16.5 ± 0.3	33.7 ± 0.8	46.9 ± 0.6	2.9 ± 0.1	-
Light	57.2 ± 9.1	39.8 ± 9.9	2.1 ± 0.6	0.9 ± 0.2	~W_2C ?
Medium	14.5 ± 2.3	21.6 ± 11.7	60.8 ± 8.9	3.1 ± 0.5	~Ni_3V ?
Dark	10.8 ± 0.3	33.8 ± 1.6	51.6 ± 1.4	3.8 ± 0.5	~Ni_3V ?
Eutectic	17.2 ± 2.5	28.2 ± 9.9	51.8 ± 7.3	2.8 ± 0.4	W_2C +~Ni_3V ?

Table 5.2. EDX phase analyses for nominal W_{25}:C_{25}:$Ni_{47.5}$:$V_{2.5}$ (at.%) in the as-cast condition analysed without standards (done at University of Botswana, UB).

Phase description	W	C	Ni	V	Phase deduced
Overall	24.2 ± 2.4	52.5 ± 0.9	21.5 ± 2.1	1.8 ± 0.1	-
Light	23.5 ± 3.1	75.0 ± 2.7	1.2 ± 1.1	0.3 ± 0.1	~C_2W ?
Medium	5.5 ± 0.8	62.8 ± 5.5	30.2 ± 4.3	1.5 ± 0.3	~C_2Ni ?
Dark	7.0 ± 0.6	56.1 ±3.4	34.8 ± 2.4	2.1 ± 0.3	~C_2Ni ?
Eutectic	10.6 ± 0.9	42.2 ± 3.8	44.4 ± 3.2	2.8 ± 0.1	~C_2W+~C_2Ni?

Table 5.3. EDX phase analyses for nominal W_{25}:C_{25}:$Ni_{47.5}$:$V_{2.5}$ (at.%) in the as-cast condition using pre-loaded standards (done at NMISA).

Since there was so much difference between the EDX analyses, XRD was used to verify the phases. XRD patterns confirmed the two phases from Table 5.1; this is shown in Figure 5.3. The XRD had a good pattern with sharp peaks and low background.

The solidification sequence was as follows:

$L \rightarrow \sim W_2C$

$L \rightarrow (Ni)$

$L \rightarrow \sim W_2C + (Ni)$.

It was thought that the (Ni) formed before the eutectic because of fast cooling. Subsequently, (Ni) transformed to ~Ni_3V in the solid state. XRD showed that (Ni) had transformed to ~Ni_3V after solidification.

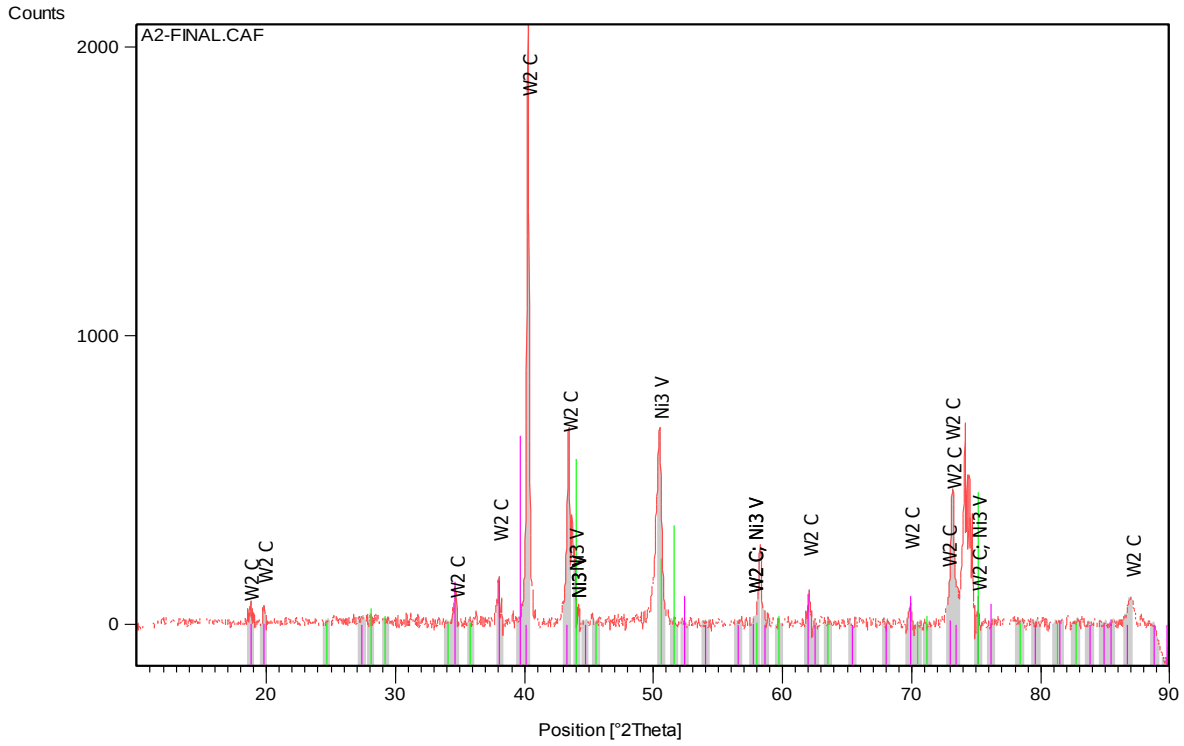


Figure 5.3. XRD pattern of nominal W_{25}:C_{25}:$Ni_{47.5}$:$V_{2.5}$ in as-cast condition, showing ~W_2C and ~Ni_3V peaks.

5.1.2 Nominal $W_{25}C_{25}Ni_{43}$:V_7 (at.%)

The as-cast W_{25}:C_{25}: Ni_{43}:V_7 (at.%) sample showed two distinct phases: light dendrites and cored ~Ni_2V medium dark dendrites which formed the bulk of the alloy (Figure 5.4). There was a dark phase which was between the cored (Ni) medium dark dendrites (Figure 5.5), which was much more visible at higher magnification.

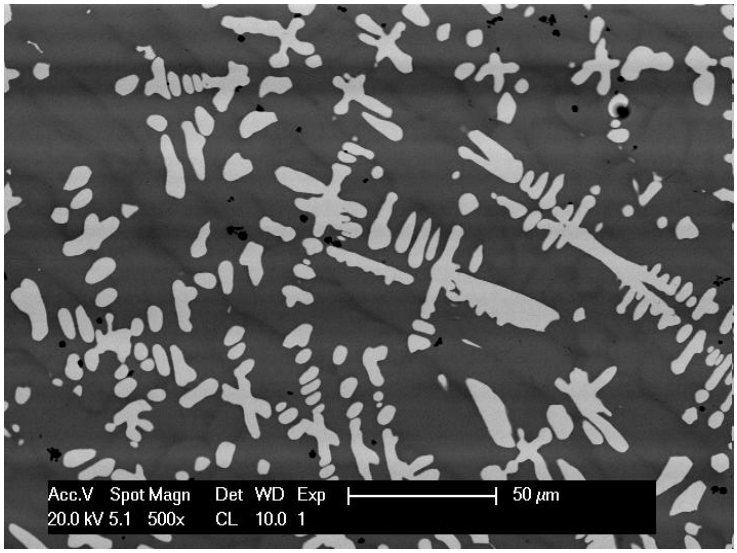


Figure 5.4. SEM -BSE image of nominal as-cast W_{25}:C_{25}:Ni_{43}:V_7 (at.%) showing ~W_2C dendrites and cored medium dark ~Ni_2V.

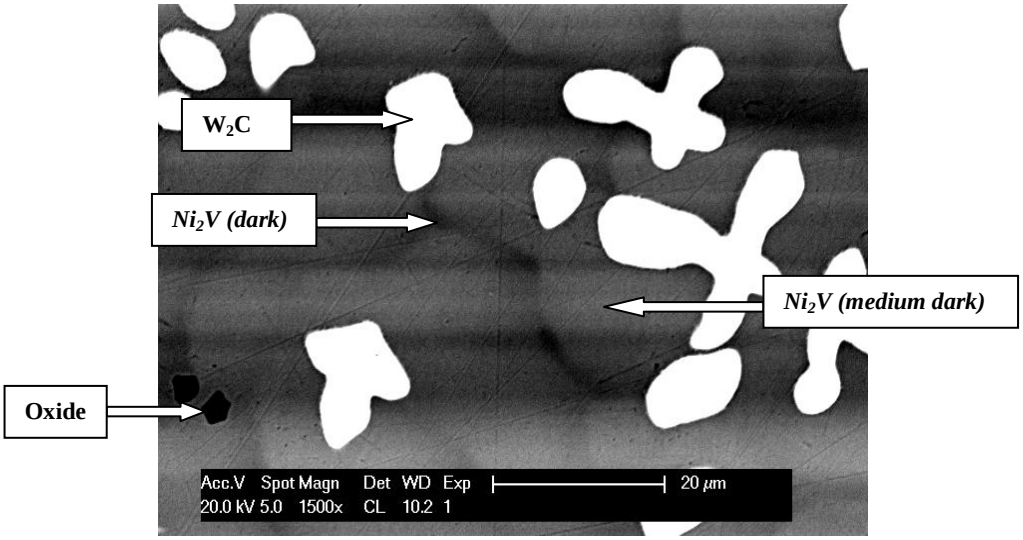


Figure 5.5. SEM-BSE image of nominal as-cast W_{25}:C_{25}:Ni_{43}:V_7 (at.%) showing ~W_2C dendrites, cored ~Ni_2V medium dark dendrites and oxides (black).

EDX data could not be collected on the light dendritic phase (Table 5.4) which could be due a software problem on the EDX, but it was suspected to be ~W_2C based on the similar XRD pattern to W_{25}:C_{25}:$Ni_{47.5}$:$V_{2.5}$ (at.%). Both samples had same elements, but with different proportions.

EDX analyses (Table 5.4) also showed that the interdendritic dark phase (Figure 5.5) between the medium ~Ni_2V phases was also the same phase, but with slight differences in composition, as seen in the previous as-cast sample W_{25}:C_{25}:$Ni_{47.5}$:$V_{2.5}$ (at.%) (Figure 5.2).

There was carbon, which was probably picked up from the surrounding phases, due to fact that they were less than 3µm across. There were a few dark oxide particles, with the oxygen peak being clearly seen in the spectrum. These were analysed, although the EDX analyses were set to ignore oxygen in order to obtain the other element values. The oxide contained 1.5 at.% aluminium.

Phase description	**W**	**C**	**Ni**	**V**	**Phase deduced**
Overall	19.1 ± 0.4	8.4 ± 0.7	62.0 ± 0.9	10.5 ± 0.1	-
Medium	10.1 ± 0.2	7.1 ± 0.3	73.1 ± 0.4	9.7 ± 0.1	~Ni_2V
Medium dark	8.1 ± 0.7	6.8 ± 0.6	71.9 ± 0.6	13.2 ± 0.9	~Ni_2V
Light	-	-	-	-	Could not analyse
Dark Oxide					
W	**C**	**Ni**	**V**	**Al**	
0.6 ± 0.3	0.0	5.8 ± 2.2	92.7 ± 2.4	1.5 ± 0.1	Oxide

Table 5.4. EDX phase analyses for nominal $W_{25}:C_{25}:Ni_{43}:V_7$ (at.%) in as-cast condition using standards derived from the elements from which samples were prepared (done at University of Botswana, UB). N.B. O was ignored in the oxide analysis.

Table 5.5 has analyses taken without standards. The results for carbon and nickel were different from analyses done with standards. The light phase could not be analysed using standards, but it was analysed without the standards. Using EDS, the light phase was analysed as ~WC (Table 5.5), but the major peaks in the XRD were ~W_2C.

Phase description	**W**	**C**	**Ni**	**V**	**Phase deduced**
Overall	16.5 ± 3.2	26.1 ± 14.7	49.3 ± 9.8	8.1 ± 1.7	-
Medium	8.2 ±0.2	29.5 ± 0.8	55.2 ± 0.7	7.1 ± 0.1	~Ni_2V ?
Dark	6.8 ± 0.4	28.9 ± 1.6	54.7 ± 1.2	9.6 ± 0.8	~Ni_2V ?
Light	49.7 ± 2.7	45.8 ± 2.7	2.5 ± 0.4	2.0 ± 0.1	~WC/~W_2C ?
Dark Oxide					
W	**C**	**Ni**	**V**	**Al**	
2.6 ± 1.8	0.0 ± 0.0	7.3 ± 2.7	89.1 ± 4.0	1.0 ± 0.5	Oxide

Table 5.5. EDX phase analyses for nominal $W_{25}:C_{25}:Ni_{43}:V_7$ (at.%) in as-cast condition without standards (done at University of Botswana, UB). N.B. O was ignored in the oxide analysis.

Tables 5.6 and 5.7 were phase analyses taken at NMISA. Table 5.7 has data analysed using a carbon standard derived from vanadium carbide and Table 5.6 was done using preloaded standards. The carbon content was high in Table 5.6, but even higher in the analyses done using the carbon standard from VC. The oxide had oxygen, but the very low content aluminium was ignored.

Phase description	**W**	**C**	**Ni**	**V**	**Phase deduced**
Overall	22.5 ± 1.3	47.1 ± 1.1	28.3 ± 1.6	2.1 ± 0.7	-
Medium	6.4 ± 0.6	60.2 ± 1.7	31.2 ± 0.8	2.2 ± 0.5	~C_2Ni?
Medium dark	5.9 ± 0.7	60.1 ± 1.5	31.9 ± 0.8	2.1 ± 0.5	~C_2Ni ?
Light	31.2 ± 2.5	66.7 ± 3.0	1.3 ± 0.5	0.8 ± 0.3	~C_2W ?
Dark Oxide					
W	**C**	**Ni**	**V**	**O**	
6.1 ± 0.7	41.9 ± 1.2	6.2 ± 0.9	39.7 ± 2.4	6.1 ± 0.1	Oxide

Table 5.6. EDX phase analyses for nominal $W_{25}:C_{25}:Ni_{43}:V_7$ (at.%) in as-cast condition using pre-loaded standards (done at NMISA).

Phase description	**W**	**C**	**Ni**	**V**	**Phase deduced**
Overall	1.7 ± 0.1	91.1 ± 0.5	5.2 ± 2.4	2.0 ± 2.5	-
Medium	0.9 ± 0.0	90.5 ± 0.9	7.5 ± 0.7	1.1 ± 0.1	~$C_{12}Ni$?
Medium dark	0.7 ± 0.1	89.9 ± 0.1	8.4 ± 0.1	1.0 ±0.04	~$C_{12}Ni$?
Light	3.8 ± 0.4	95.8 ± 0.7	0.3 ± 0.1	0.1 ± 0.01	?
Dark Oxide					
W	**C**	**Ni**	**V**	**O**	
0.1 ± 0.7	90.6 ± 1.2	0.2 ± 0.9	7.7 ± 2.4	1.4 ± 0.1	Oxide

Table 5.7. EDX phase analyses for nominal $W_{25}:C_{25}:Ni_{43}:V_7$ (at.%) in as-cast condition using a carbon standard derived from vanadium carbide (done at NMISA).

The solidification sequence was as follows:
L → ~W_2C
L → (Ni).

The phases were confirmed by XRD (Figure 5.6). The background was low and the pattern was good with sharp peaks. Since ~Ni_2V was found rather than (Ni), it shows that the (Ni) transformed after solidification.

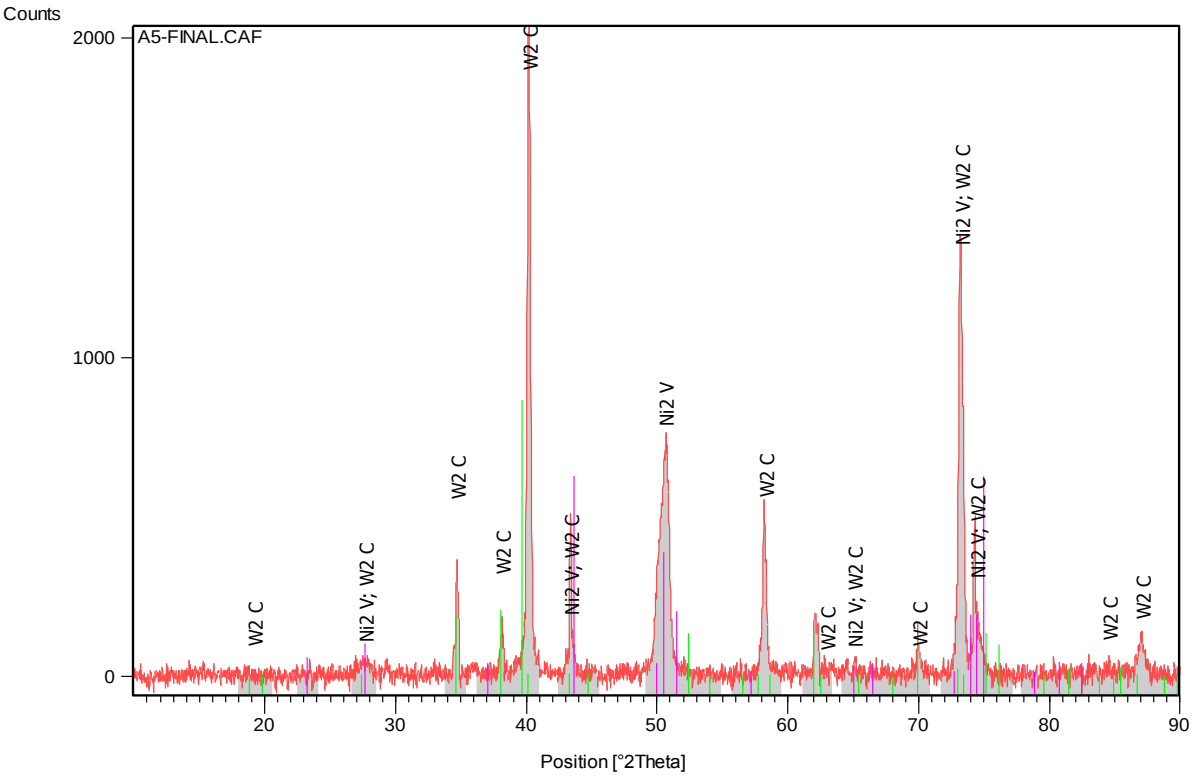


Figure 5.6. XRD pattern of nominal W_{25}:C_{25}:Ni_{43}:V_7 (at.%) in as-cast condition, showing ~W_2C and ~Ni_2V peaks.

5.1.3 Nominal W_{25}:C_{25}:$Ni_{42.5}$:$Zn_{7.5}$ (at.%)

As-cast W_{25}:C_{25}:$Ni_{42.5}$:$Zn_{7.5}$ (at.%) had different regions with varying proportions of the carbide (Figure 5.7a). Both regions had two phases, and the bulk of the smaller region comprised ~W_2C formed in globules, with a medium dark matrix and a small amount of eutectic (Figure 5.7a).

The medium dark phase surrounding the light ~W_2C globules phases formed the bulk of the larger region and had much more eutectic than the smaller region (Figures 5.7b and c).

There was no discernable zinc from the EDX analysis which could be due to evaporation of the low melting point zinc during the high temperature arc-melting. The matrix is believed to be (Ni) and showed a large solubility for carbon.

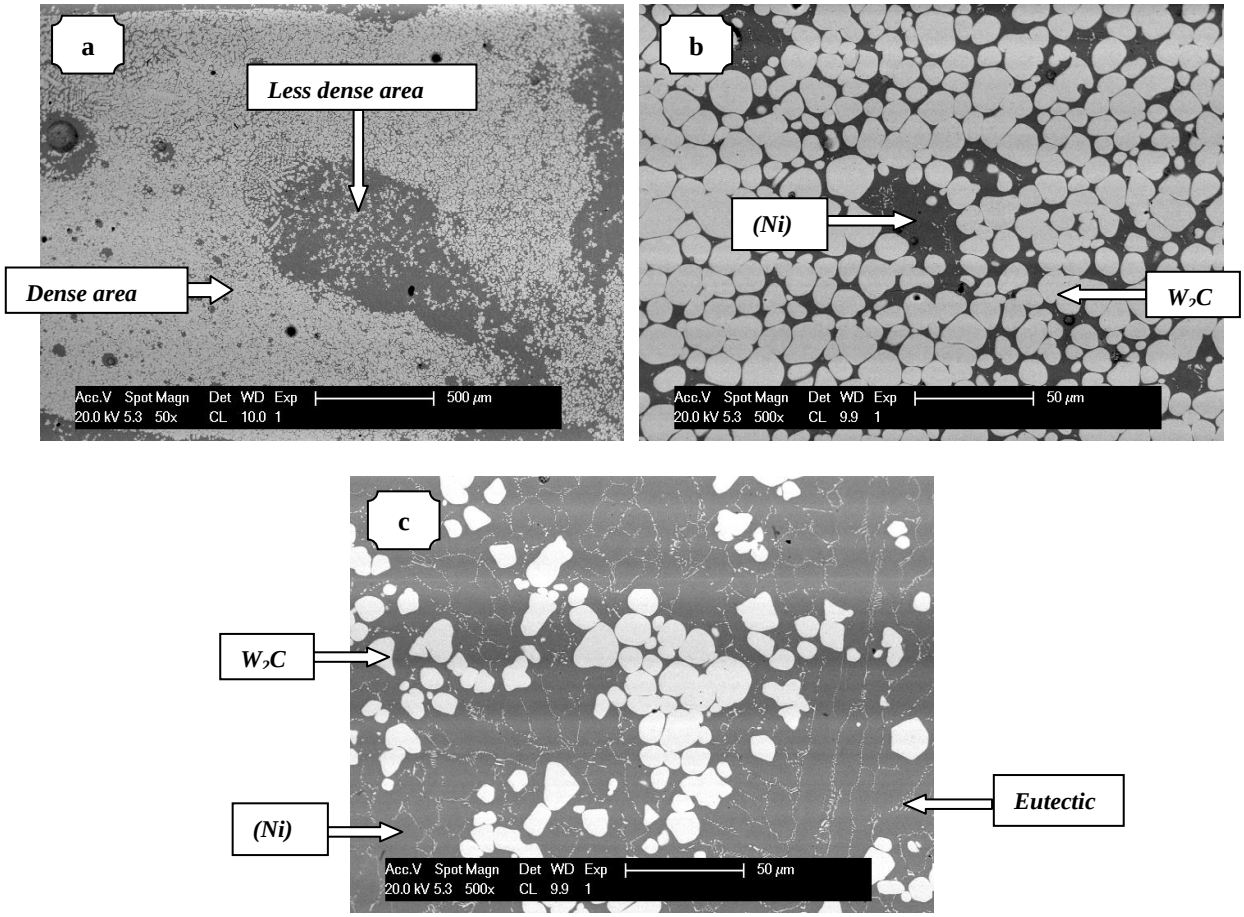


Figure 5.7. SEM-BSE images of nominal W_{25}:C_{25}:$Ni_{42.5}$:$Zn_{7.5}$ (at.%) in as-cast condition: showing a) overview of the sample with different regions, b) dense area with ~W_2C (light) globules, medium-dark matrix (Ni) and with small areas of ~W_2C (light) + (Ni) (medium-dark) eutectic, and c) less dense area with ~W_2C (light) globules, medium-dark matrix (Ni) and with much more ~W_2C (light) + (Ni) (medium-dark) eutectic.

Table 5.8 shows phase analyses for the nominal as-cast sample W_{25}:C_{25}:$Ni_{42.5}$:$Zn_{7.5}$ (at.%), and large errors were observed in the overall analyses. Carbon had larger errors, especially in the light phases in both separate regions, while W had large errors in only the light phases.

Tables 5.9 and 5.10 were analyses done at NMISA. Analyses in Table 5.10 were done using a carbon standard from VC; it had overestimated carbon content in all the phases, while analyses in Table 5.9 were done from preloaded standards. The carbon contents were relatively high. The analyses were different from the results in Tables 5.9 and 5.10, collected in UB. However, the results from UB were confirmed by XRD.

Phase description	W	C	Ni	Zn	Phase deduced
Higher proportion area					
Overall	60.1 ± 5.1	21.6 ± 3.3	18.3 ± 7.7	-	-
Medium	16.3 ± 0.3	11.3 ± 1.2	72.4 ± 1.1	-	(Ni)
Light	73.3 ± 1.3	24.1 ± 1.8	2.6 ± 1.0	-	~W_2C
Lower proportion area					
Overall	21.0 ± 0.4	14.7 ± 1.9	64.3 ± 1.6	-	
Light	69.4 ± 2.7	28.2 ± 2.9	2.4 ± 0.5	-	~W_2C
Medium	15.6 ± 0.5	11.5 ± 1.9	72.9 ± 1.6	-	(Ni)
Eutectic overall	22.3 ± 2.4	12.9 ± 1.7	64.8 ± 2.6	-	~W_2C + (Ni)

Table 5.8. EDX phase analyses for nominal W_{25}:C_{25}:$Ni_{42.5}$:$Zn_{7.5}$ (at.%) in as-cast condition using standards made from the elements from which samples were prepared (done at University of Botswana, UB).

Phase description	W	C	Ni	Zn	Phase deduced
Higher proportion area					
Overall	26.9 ± 1.1	53.5 ± 1.2	19.6 ± 3.1	-	-
Medium	9.3 ± 0.5	57.1 ± 3.5	33.6 ± 4.1	-	C_2Ni ?
Light	31.3 ± 2.0	67.3 ± 2.4	1.4 ± 0.8	-	C_2W ?
Lower proportion area					
Overall	18.5 ± 0.3	60.4 ± 2.4	21.1 ± 2.0	-	-
Light	21.1 ± 2.9	77.6 ± 1.9	1.3 ± 1.1	-	C_2W ?
Medium	7.7 ± 0.4	58.4 ± 2.8	33.9 ±2.6	-	C_2Ni ?
Eutectic	11.2 ± 1.7	48.4 ± 5.3	40.4 ±3.9	-	C_2W + C_2Ni ?

Table 5.9. EDX phase analyses for nominal W_{25}:C_{25}:$Ni_{42.5}$:$Zn_{7.5}$ (at.%) in as-cast condition using pre-loaded standards (done at NMISA).

Phase description	W	C	Ni	Zn	Phase deduced
Higher proportion area					
Overall	3.3 ± 0.1	95.5 ± 0.2	1.2 ± 0.1	-	-
Medium	0.5 ± 0.3	95.4 ± 1.6	4.1 ± 1.4	-	?
Light	2.9 ± 0.3	97.0 ± 0.4	0.1 ± 0.01	-	?
Lower proportion area					
Overall	1.6 ± 0.3	92.4 ± 0.5	6.0 ± 0.3	-	-
Light	1.9 ± 0.8	97.8 ± 0.7	0.3 ± 0.2	-	?
Medium	0.9± 0.1	93.9 ± 1.0	5.2 ± 0.8	-	?
Eutectic	1.1 ± 0.1	93.7 ± 1.1	5.2 ± 1.1	-	-

Table 5.10. EDX phase analyses for nominal W_{25}:C_{25}:$Ni_{42.5}$:$Zn_{7.5}$ (at.%) in as-cast condition using a carbon standard derived from vanadium carbide (done at NMISA).

The solidification sequence was:

L → ~W_2C

L → (Ni)

L → ~W_2C + (Ni).

XRD analyses confirmed (Ni) and ~W_2C phases. Figure 5.8 shows the XRD pattern for the nominal as-cast sample W_{25}:C_{25}:$Ni_{42.5}$:$Zn_{7.5}$ (at.%). The pattern was good, with low background and sharp peaks, and had one unmatched peak (Table 5.11).

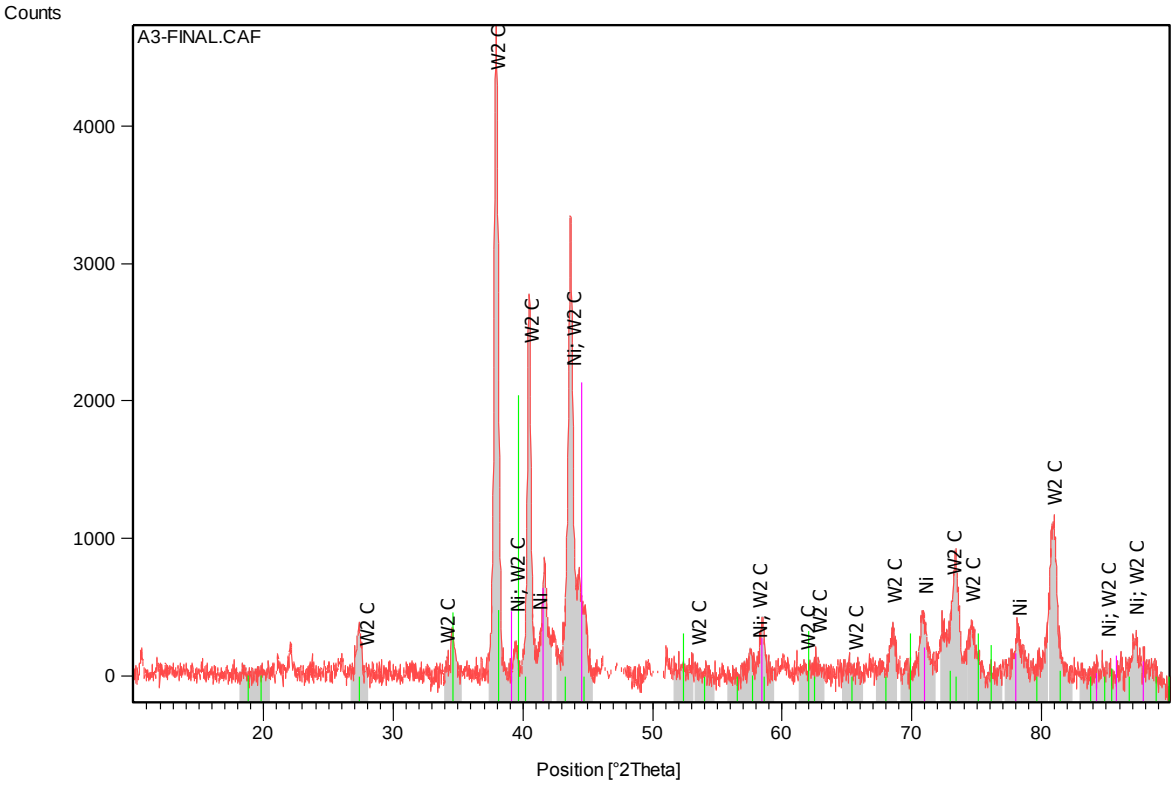


Figure 5.8. XRD pattern of nominal W_{25}:C_{25}:$Ni_{42.5}$:$Zn_{7.5}$ (at.%) in as-cast condition, showing ~W_2C and (Ni) peaks.

Peak No	2θ (degree)	d-spacing (Å)	Relative intensity (%)
1	21.89	3.44	1.86

Table 5.11. Unmatched XRD peak from nominal $W_{25}:C_{25}:Ni_{42.5}:Zn_{7.5}$ (at.%) in as-cast condition.

5.1.4 Nominal $W_{25}:C_{25}:Ni_{45}:Zn_5$ (at.%)

As-cast sample $W_{25}:C_{25}:Ni_{45}:Zn_5$ had two phases: light globular dendrites and a medium dark phase. There was a eutectic in the sample (Figure 5.9). The sample's microstructure was similar to as-cast $W_{25}:C_{25}:Ni_{42.5}:Zn_{7.5}$; they both had similar components but in different proportions, and this sample was fairly homogenous. There was no zinc found in the EDX data, which could be due to its evaporation during arc-melting.

Table 5.12 (UB) shows the phase analyses for nominal $W_{25}:C_{25}: Ni_{45}:Zn_5$ (at.%). The errors were larger for W and Ni in the eutectic; it could be due to contribution from the surrounding phases.

The light phase was assumed to be ~W_2C, as in the previous sample, because of its similar morphology and XRD pattern. The medium dark phase was confirmed to be (Ni) by the XRD (Figure 5.10) analysis.

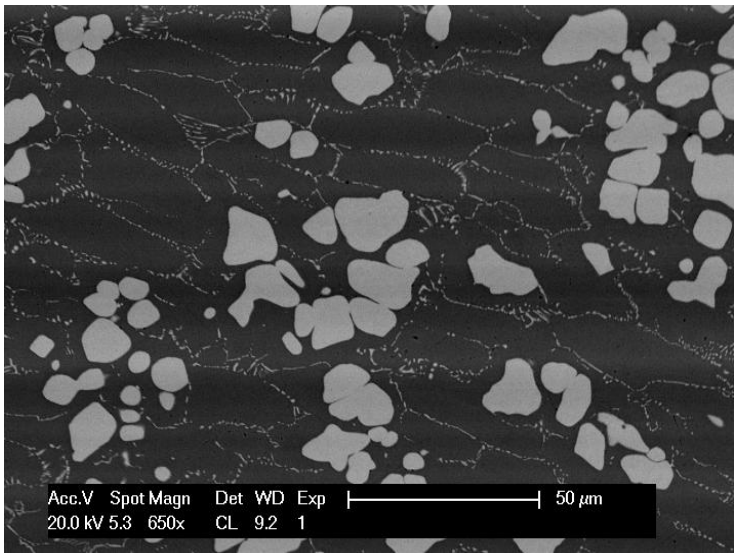


Figure 5.9. SEM-BSE image of nominal $W_{25}:C_{25}:Ni_{45}:Zn_5$ (at.%) in the as-cast condition: light ~W_2C; (Ni) medium grey; eutectic ~W_2C + (Ni).

Phase description	W	C	Ni	Zn	Phase deduced
Overall	24.6 ± 0.4	7.2 ± 0.5	68.2 ± 0.5	-	-
Dark	17.2 ± 0.2	6.4 ± 0.2	76.4 ± 0.3	-	(Ni)
Eutectic	25.1 ± 1.2	9.7 ± 0.6	65.2 ± 1.4	-	(Ni) + ~W_2C
Light	-	-	-	-	Could not be analysed

Table 5.12. EDX phase analyses for nominal W_{25}:C_{25}:Ni_{45}:Zn_5 (at.%) in the as-cast condition using standards made from the elements which samples were prepared (done at University of Botswana, UB).

The results obtained from samples analysed without standards are presented in Table 5.13 indicated some similarities in the tungsten compositions of results presented in Table 5.12, which were analysed with standards. Table 5.13 had much higher carbon content, whereas the nickel contents were lower than in Table 5.12.

Phase description	W	C	Ni	Zn	Phase deduced
Overall	20.8 ± 1.1	28.6 ± 3.9	50.6 ± 2.8	0.0 ± 0.0	-
Dark	14.0 ± 0.2	29.3 ± 1.1	56.7 ± 0.9	0.0 ± 0.0	(Ni) ?
Eutectic	19.0 ± 0.8	37.7 ± 1.8	43.3 ± 2.0	0.0 ± 0.0	(Ni) + ~WC/~W_2C?
Light	53.4 ± 2.0	45.4 ± 2.5	1.2 ± 0.9	0.0 ± 0.0	~WC/~W_2C?

Table 5.13. EDX phase analyses for nominal W_{25}:C_{25}:Ni_{45}:Zn_5 (at.%) in the as-cast condition without standards (done at UB).

Table 5.14 has results of the SEM at NMISA. The overall composition in Table 5.14 (from NMISA) was different from the results in Table 5.12 (University of Botswana) but had similar tungsten content. Carbon contents were high in all the phases in results from NMISA; and the eutectic did not reflect an average of the light and dark phases. These results were ignored.

The XRD pattern (Figure 5.10) was good, had sharp peaks and relatively low background. The nickel peaks slightly shifted, indicating a solid solution.

Phase description	W	C	Ni	Zn	Phase deduced
Overall	22.0 ± 0.8	60.9 ± 2.1	17.1 ± 1.4	0.0 ± 0.0	-
Dark	1.2 ± 0.2	76.6 ± 0.9	22.2 ± 0.7	0.0 ± 0.0	NiC_2 ?
Eutectic	7.6 ± 0.4	60.7 ± 1.3	31.7 ± 1.6	0.0 ± 0.0	?
Light	15.4 ± 2.1	83.7 ± 1.3	0.9 ± 0.5	0.0 ± 0.0	?

Table 5.14. EDX phase analyses for nominal $W_{25}:C_{25}:Ni_{45}:Zn_5$ (at.%) in the as-cast condition using pre-loaded standards (done at NMISA).

The solidification sequence was deduced as:

$L \rightarrow \sim W_2C$

$L \rightarrow (Ni)$

$L \rightarrow \sim W_2C + (Ni)$.

The solidification before the eutectic was probably due to the fast cooling after arc-melting.

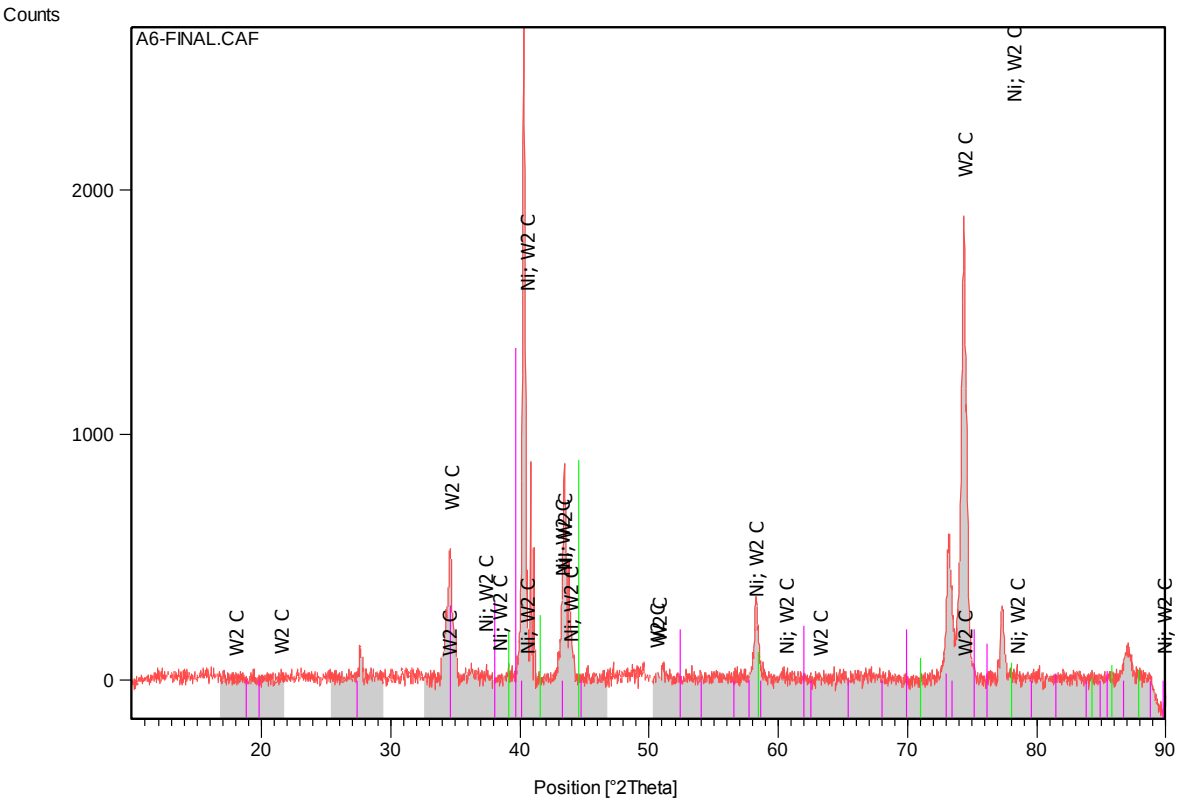


Figure 5.10. XRD pattern of nominal $W_{25}:C_{25}:Ni_{45}:Zn_5$ (at.%) in as-cast condition, showing $\sim W_2C$ and (Ni) peaks.

5.1.5 Nominal $W_{25}:C_{25}:Co_{30}:Mn_{20}$ (at.%)

The as-cast $W_{25}:C_{25}:Co_{30}:Mn_{20}$ sample was much more complex than the other previous samples. The sample had four different contrasts: they were the light, medium, medium dark and dark contrasts. The sample comprised medium contrast flakes forming the bulk of the alloy with lighter dendrites. The dendrites were ~WC (Figure 5.11 a), and were found with the medium flake phases forming on the outside. There was a peritectic relationship between the carbide and the medium contrast phase, followed by direct solidification of the medium phase. The composition of the medium phase showed it to be a ternary phase. It was either ~Co_7W_6 with C, or ~$(Co,W)_2C$. The ~$(Co,W)_2C$ phase could not be matched on the XRD pattern, since it was not available in the (ICDD) database [1991ICD]. However, Co_7W_6 matched very well on the XRD, the phase was assumed Co_7W_6 with C, ignoring the low content of Mn in the phase.

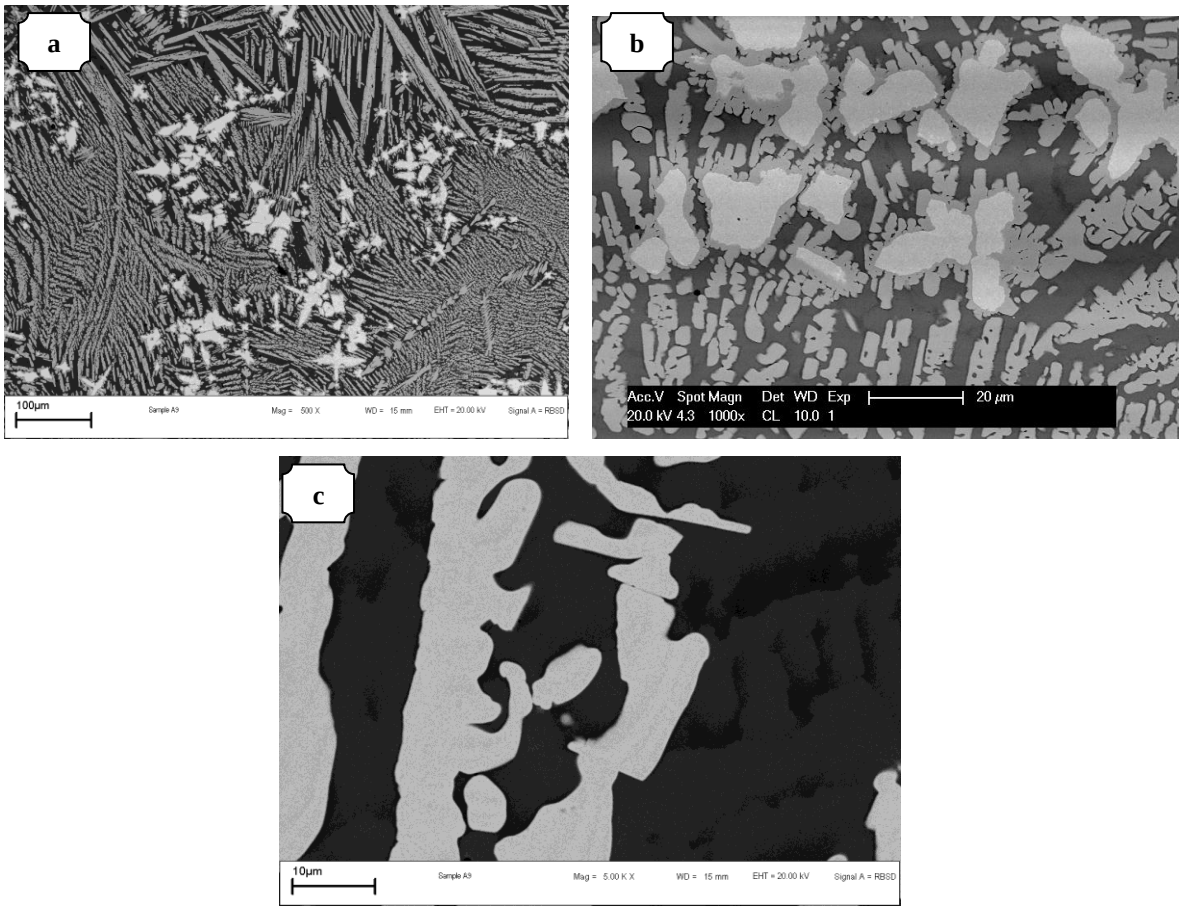


Figure 5.11. SEM-BSE images of nominal $W_{25}:C_{25}:Co_{30}:Mn_{20}$ in as-cast condition: showing a) the major medium flakes, b) light dendrites enclosed by flakes in dark cored matrix and c) dark phases in matrix at higher magnification.

The matrix (Figure 5.11b) was cored (Co), and the differences were only visible at high magnification (Figure 5.11c). The very dark component was less far less than 3µm across, and a few analyses were taken to observe the differences with the other phases. Tables 5.15 and 5.16 give EDX analyses from NMISA and UB respectively. The light phase from UB was ignored, but the medium phase analyses from both EDX sources were close to each other.

XRD also confirmed the WC and (Co) phases; this is shown in Figure 5.12. The XRD pattern had a high background, but had sharp peaks. All the unmatched peaks (Table 5.17) were patterns from the plasticine (Appendix A).

Phase description	**W**	**C**	**Mn**	**Co**	**Phase deduced**
Overall	23.2 ± 0.6	23.6 ± 1.7	6.8 ± 0.2	46.4 ± 0.9	-
Light	51.8 ± 0.7	45.4 ± 0.3	0.6 ± 0.5	2.2 ± 0.1	WC
Medium	30.2 ± 0.9	29.1 ± 1.1	5.6 ± 0.3	35.1 ± 0.7	Co_7W_6 with C / $(Co,W)_2C$
Dark	7.9 ± 0.4	19.8 ± 0.4	16.8 ± 0.6	55.5 ± 0.4	(Co) cored
Darker	7.9 ± 2.6	21.6 ± 3.5	16.0 ± 8.3	54.5 ± 3.1	(Co) cored

Table 5.15. EDX phase analyses for nominal $W_{25}:C_{25}:Co_{30}:Mn_{20}$ (at.%) in as-cast condition using pre-loaded standards (done at NMISA).

Phase description	**W**	**C**	**Mn**	**Co**	**Phase deduced**
Overall	27.1 ± 0.8	18.5 ± 1.5	6.9 ± 0.2	47.5 ± 0.7	-
Light	84.5 ± 14.3	12.2 ± 14.1	1.0 ± 0.2	2.3 ± 0.2	WC assumed from NMISA
Medium	35.9 ± 1.4	19.7 ± 3.0	3.7 ± 0.2	40.7 ± 1.6	Co_7W_6 with C / $(Co,W)_2C$
Dark	12.0 ± 1.1	20. 2 ± 1.6	8.5 ± 0.3	59.3 ± 1.3	(Co) cored
Darker	9.1 ± 0.8	23.4 ± 3.1	13.6 ± 1.6	53.9 ± 1.9	(Co) cored

Table 5.16. EDX phase analyses for nominal $W_{25}:C_{25}:Co_{30}:Mn_{20}$ (at.%) in as-cast condition without standards (done at University of Botswana, UB).

Solidification sequence was deduced to be:

$L \rightarrow \sim WC$

$L + \sim WC \rightarrow Co_7W_6$ with C / $(Co,W)_2C$

$L + Co_7W_6$ with C / $(Co,W)_2C \rightarrow$ (Co).

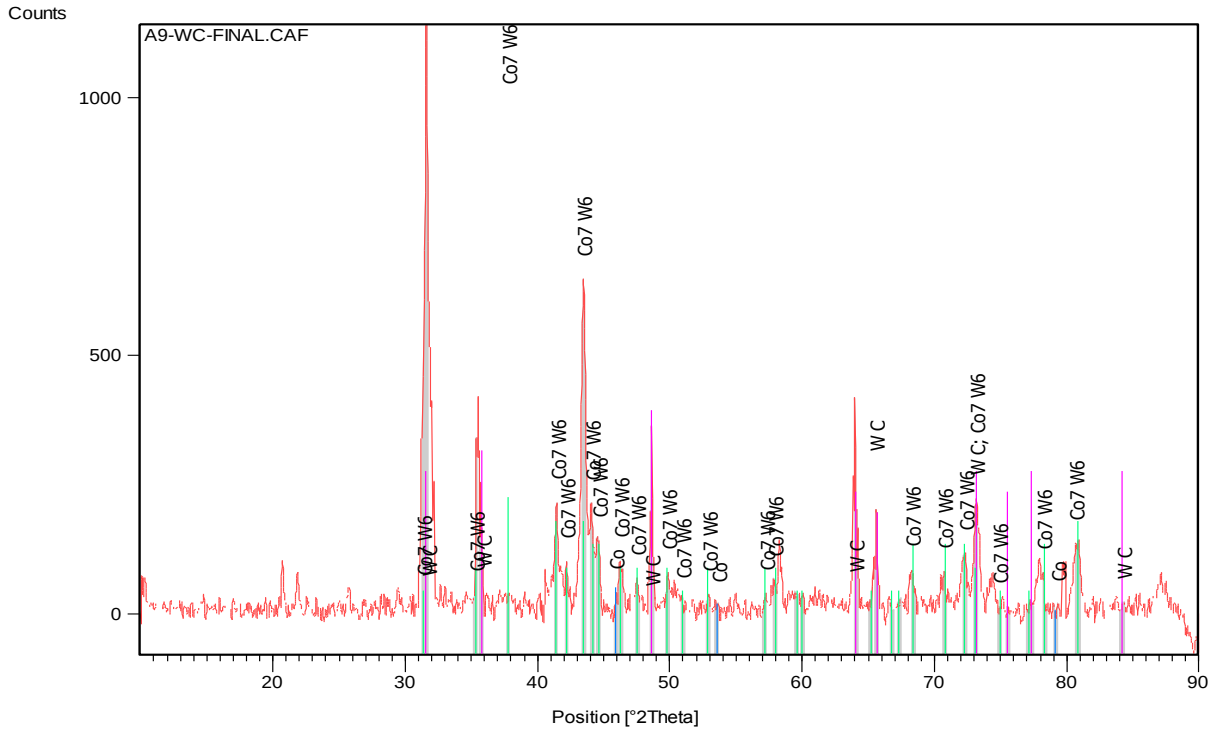


Figure 5.12. XRD pattern nominal W_{25}:C_{25}:Co_{30}:Mn_{20} (at.%) in as-cast condition showing ~WC (Co) and ~Co_7W_6.

Peak No	2θ (degree)	d-spacing (Å)	Relative intensity (%)
1	20.71	4.28	9.13
2	21.85	4.06	7.17
3	26.75	3.45	4.70

Table 5.17. Unidentified XRD peaks in nominal W_{25}:C_{25}:Co_{30}:Mn_{20} (at.%) in as-cast condition.

5.1.6 Nominal W_{25}:C_{25}:$Co_{12.5}$:$Mn_{37.5}$ (at.%)

The as-cast sample W_{25}:C_{25}:$Co_{12.5}$:$Mn_{37.5}$ (at.%) had two different regions, less and more dense areas (Figure 5.13). The denser area was made up of particles, mainly due to the sample not melting thoroughly (Figure 5.14). The less dense area looked much coarser, but there were some cracks too (Figure 5.15), which would be detrimental in service. Both regions had two phases: the light carbide phase was identified to be ~WC, while the dark phase was a solid solution of Mn with dissolved C and W (Figure 5.15).

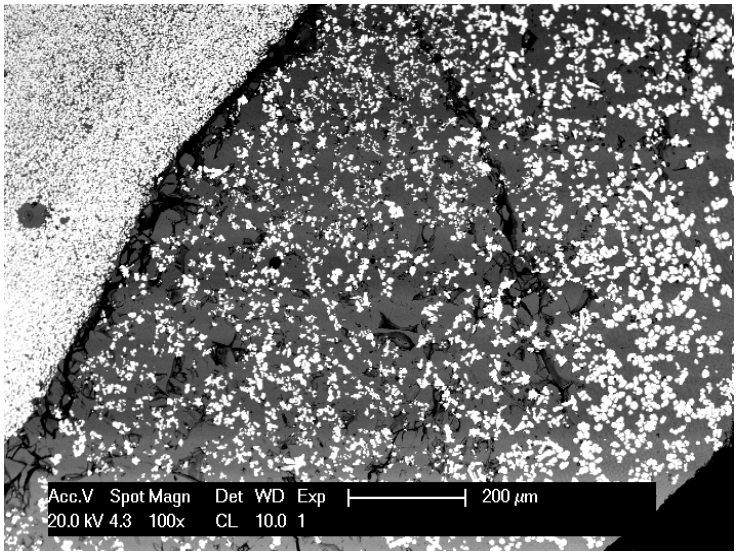


Figure 5.13. SEM-BSE image of nominal $W_{25}:C_{25}:Co_{12.5}:Mn_{37.5}$ (at.%) in as-cast condition, showing the two different regions of the sample with cracks in the dark phase of the less dense carbide portion.

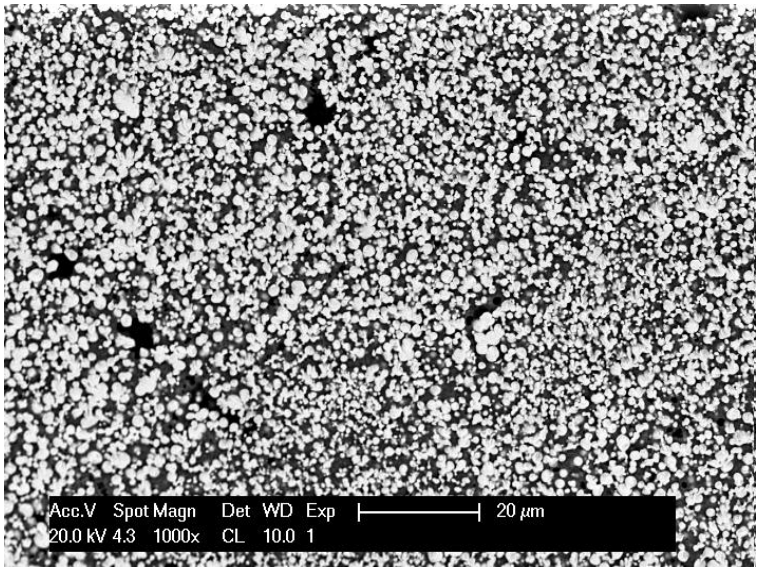


Figure 5.14. SEM-BSE image of nominal $W_{25}:C_{25}:Co_{12.5}:Mn_{37.5}$ (at.%) in as-cast condition showing: the denser region with light carbide particles and dark matrix.

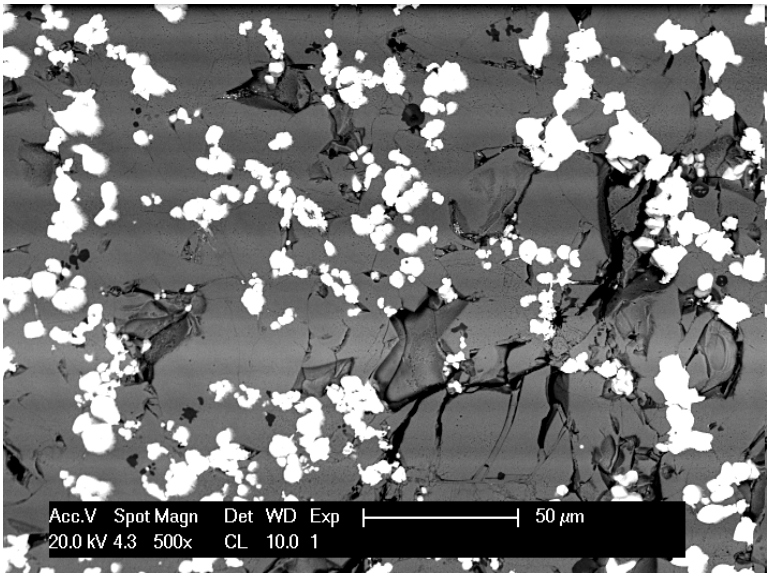


Figure 5.15. SEM-BSE image of nominal W_{25}:C_{25}:$Co_{12.5}$:$Mn_{37.5}$ in as-cast condition showing the less dense area with cracks, ~WC light phase and dark (Mn).

Tables 5.18 and 5.19 give the EDX phase analyses of the as-cast sample from NMISA, using preloaded standards and UB, without standards. Analysis was restricted to the less dense area because the particles in the denser area were far less than 3µm across, and so could not be analysed accurately. Table 5.19 are results from the UB SEM; they were not too different from analyses of NMISA's SEM, but the EDX results for the light phase looked more like ~W_2C than ~WC. XRD confirmed the presence of ~WC, agreeing with the results from UB.

Phase description	**W**	**C**	**Mn**	**Co**	**Phase deduced**
Overall	22.3 ± 0.3	28.2 ± 0.8	38.0 ± 0.4	11.5 ± 0.7	-
Medium	6.8 ± 0.9	17.6 ± 0.7	47.9 ± 0.4	27.7 ± 0.7	(βMn)
Light	52.8 ± 0.3	40.3 ± 1.0	4.4 ±0.9	2.5 ± 0.3	~WC

Table 5.18. EDX phase analyses for nominal W_{25}:C_{25}:$Co_{12.5}$:$Mn_{37.5}$ (at.%) in as-cast condition using pre-loaded standards (done at NMISA).

Phase description	**W**	**C**	**Mn**	**Co**	**Phase deduced**
Overall	29.7 ± 0.4	24.5 ± 1.3	38.0 ± 0.7	7.8 ± 0.7	-
Medium	1.3 ± 0.2	21.0 ± 5.5	51.7 ± 2.8	26.0 ± 3.1	(βMn)
Light	58.2 ± 2.1	37.5 ± 0.9	3.2 ± 1.4	1.1 ± 0.9	~W_2C?

Table 5.19. EDX phase analyses for nominal W_{25}:C_{25}:$Co_{12.5}$:$Mn_{37.5}$ (at.%) in as-cast condition without standards (done at University of Botswana, UB).

Figure 5.16 shows the XRD pattern for the nominal W_{25}:C_{25}:$Co_{12.5}$:$Mn_{37.5}$ (at.%) sample. The phases (Mn) and ~WC were confirmed by XRD, even though the EDX for (Mn) fell slightly out of the (Mn) range on the Co-Mn binary phase diagram. However, this is not surprising because the phase also had W and C. The pattern looked good with low background and had sharp peaks. All (Mn) peaks were slightly shifted and broadened, indicating it was a solid solution. Table 5.20 gives an unmatched XRD peak.

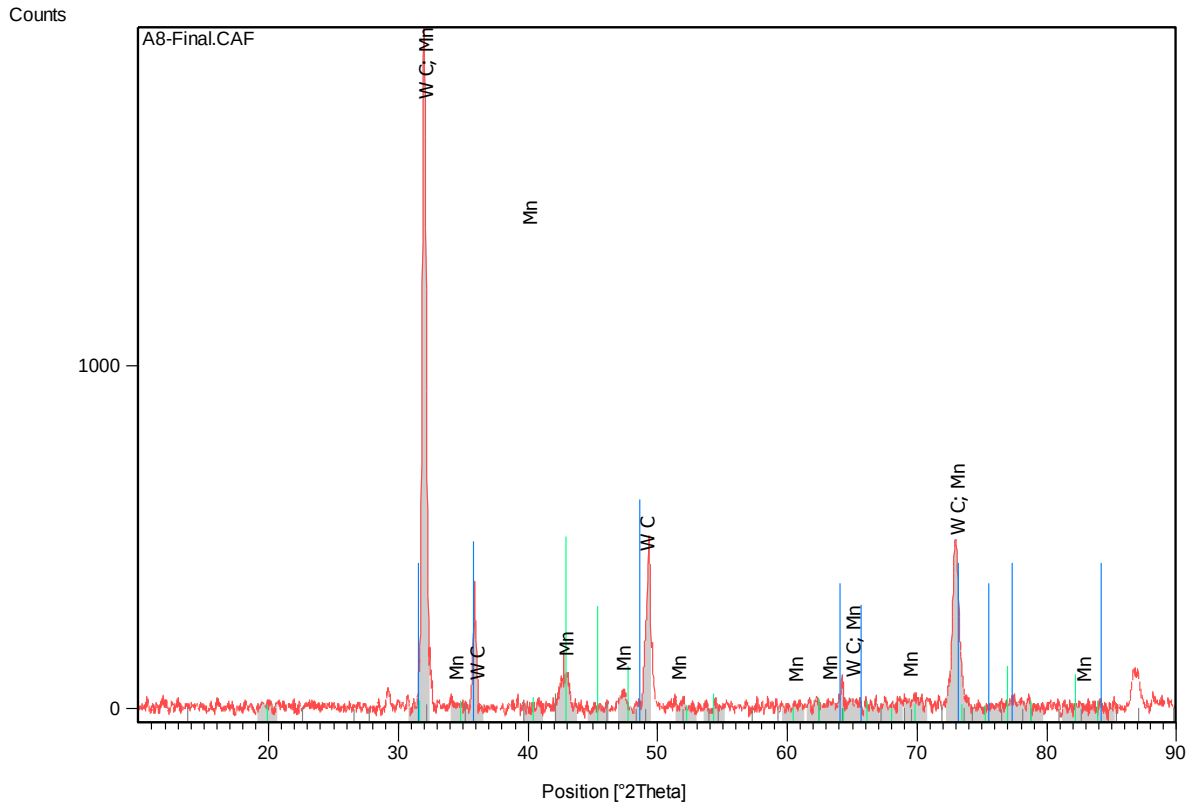


Figure 5.16. XRD pattern nominal W_{25}:C_{25}:$Co_{12.5}$:$Mn_{37.5}$ (at.%) in as-cast condition showing ~WC and (Mn).

Peak No	2θ (degree)	d-spacing (Å)	Relative intensity (%)
1	29.39	3.03	0.57

Table 5.20. Unidentified XRD peak in nominal W_{25}:C_{25}:$Co_{12.5}$:$Mn_{37.5}$ (at.%), in as-cast condition.

5.1.7 Nominal W_{25}:C_{25}:$Cu_{42.5}$:$Ni_{7.5}$ (at.%)

The as-cast sample W_{25}:C_{25}:$Cu_{42.5}$:$Ni_{7.5}$ (at.%) had four completely different regions, indicating the sample was inhomogeneous (Figure 5.17) and had not melted properly. There was a very light single phase region comprising only W (labelled 1 in Figure 5.17), indicating that W did not completely melt. There was another single phase region with a darker contrast (labelled 2 in Figure 5.17), comprising the (Cu,Ni) solid solution. Nearby, was a two–phase region with light carbide particles in (Cu,Ni) matrix (labelled 3 in Figure 5.17). The last region (labelled 4 in Figure 5.17) had two phases, with the bulk being the light globular dendrites in a sparse (Cu,Ni) medium dark matrix (Figure 5.18).

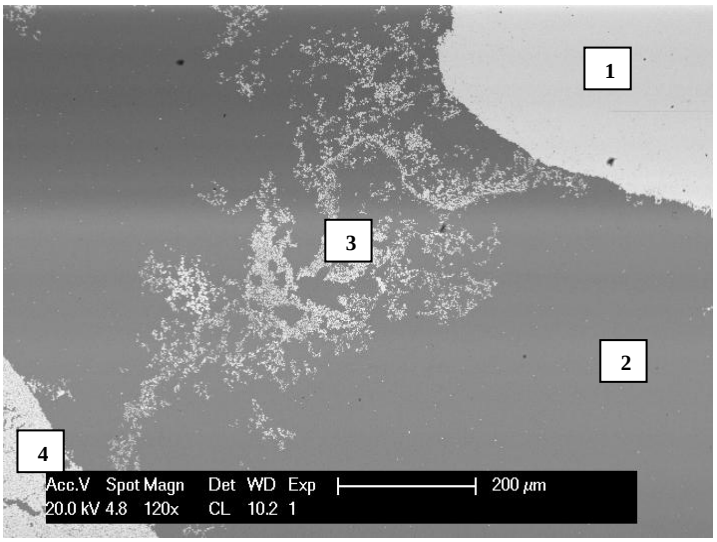


Figure 5.17. BSE-SEM image of nominal W_{25}:C_{25}:$Cu_{42.5}$:$Ni_{7.5}$ (at.%) in as-cast condition showing different regions*: *single phase W [1], dark (Cu,Ni) single phase [2], dark and lower carbide proportion [3] and the high proportion carbide region [4].

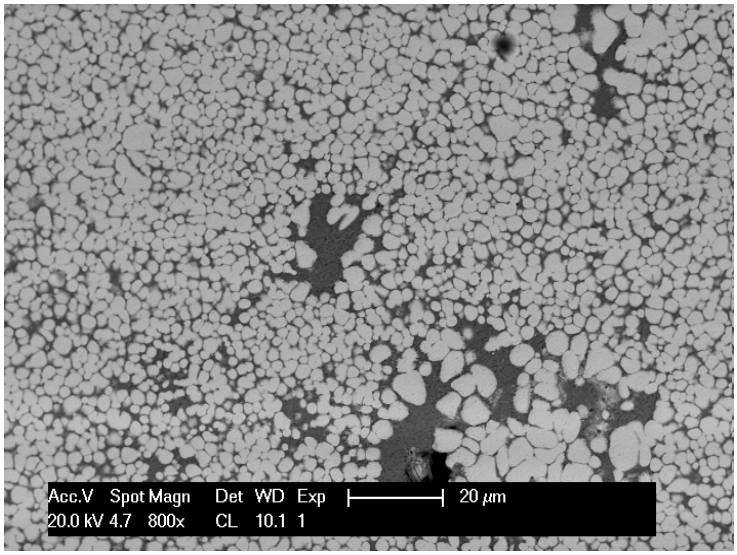


Figure 5.18. BSE-SEM image of nominal W_{25}:C_{25}:$Cu_{42.5}$:$Ni_{7.5}$ (at.%) in as-cast condition: light and medium dark phases.

Table 5.21 gives phase analyses of nominal W_{25}:C_{25}:$Cu_{42.5}$:$Ni_{7.5.}$ (at.%). The error was large for W in the overall analyses. Only one reading was done on the small W area. The (Cu,Ni) medium matrix in the WC-rich area had no dissolved W and a small amount of carbon (3.5 at.%). The light dendritic phase contained no Ni according to the EDX analyses. The analyses showed that carbon content in the light carbide phase (labelled 2 in Figure 5.17) was very low, assuming that it W_2C.

Phase description	**W**	**C**	**Cu**	**Ni**	**Phase deduced**
WC rich area					
Overall	50.8 ± 2.6	8.3 ± 0.4	33.6 ± 1.2	7.3 ± 0.4	-
Medium	0.0 ± 0.0	3.5 ± 1.4	81.6 ± 3.0	14.9 ±2.2	(Cu,Ni)
Light [4]	87.1 ± 0.8	10.5 ± 1.4	2.4 ± 1.3	-	~W_2C ?
Light [1]	100.0				W
Cu-Ni area					
Medium	-	-	83.5 ± 0.1	16.5 ± 0.1	(Cu,Ni)

Table 5.21. EDX phase analyses for nominal W_{25}:C_{25}:$Cu_{42.5}$:$Ni_{7.5}$ (at.%) in as-cast condition using standards made from the elements from which samples were prepared (done at University of Botswana, UB).

XRD confirmed the W and ~W_2C phases. Pure Cu was used in place of the (Cu,Ni) phase since the ICDD database had no (Cu,Ni) data, and the solid solution was at the Cu-rich end of

Cu-Ni binary phase diagram. Copper gave a very good match, but the peaks were slightly shifted, which implied the phase was a solid solution, agreeing with the EDX results. Figure 5.19 shows the XRD pattern for sample W_{25}:C_{25}:$Cu_{42.5}$:$Ni_{7.5}$ (at.%). The pattern had sharp peaks and a very low background as well. There was a small unidentified peak (Table 5.22).

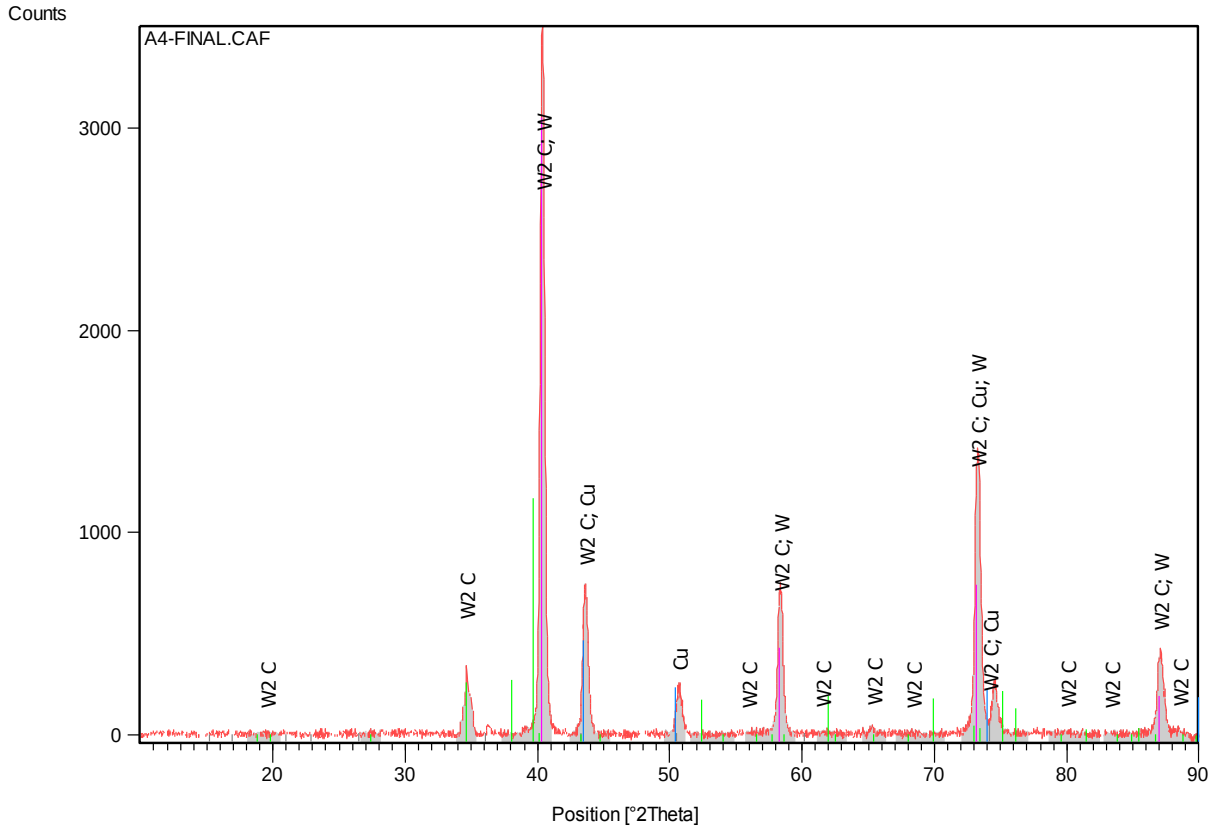


Figure 5.19. XRD pattern for nominal W_{25}:C_{25}:$Cu_{42.5}$:$Ni_{7.5}$ (at.%) in as-cast condition showing W, ~W_2C and (Cu).

Peak No	2θ (degree)	d-spacing (Å)	Relative intensity (%)
1	36.35	2.47	1.10

Table 5.22. Unidentified XRD peak in nominal W_{25}:C_{25}:$Cu_{42.5}$:$Ni_{7.5}$ (at.%), in as-cast condition.

5.1.8 Nominal W_{25}:C_{25}:Cu_{40}:Ni_{10} (at.%)

The as-cast sample W_{25}:C_{25}:Cu_{40}:Ni_{10} (at.%) showed a similar trend to the previous sample, containing copper (W_{25}:C_{25}:$Cu_{42.5}$:$Ni_{7.5}$ (at.%)), because of the inhomogeneity. There were

three different regions, and incomplete melting of the sample. There were two large two-phase regions (Figure 5.20, labelled A and B), with portion B showing porosity. These two-phase regions had more of the light carbide ~W_2C phase with the second phase (dark) showing only at higher magnification (Figure 5.21). The last region was single phase (Cu,Ni), and was dark in contrast (Figure 5.20, labelled C and Figure 5.22) and had some porosity.

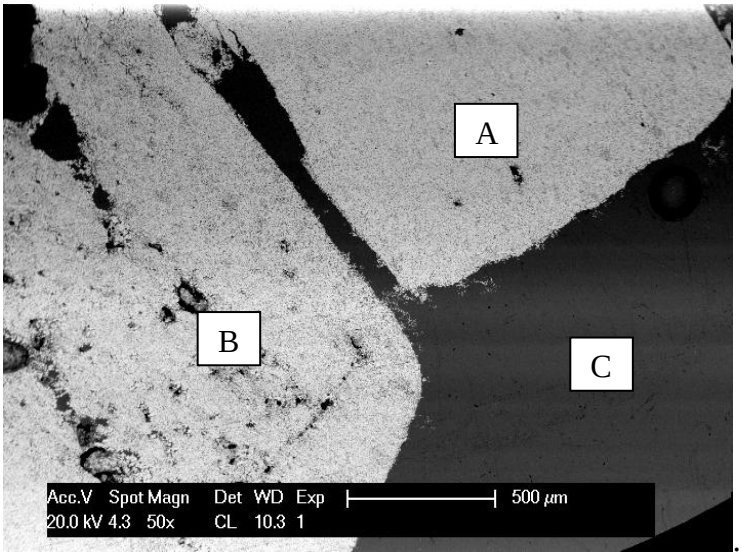


Figure 5.20. BSE-SEM image of nominal W_{25}:C_{25}:Cu_{40}:Ni_{10} (at.%) in as-cast condition showing different regions*: *two large mainly carbide two-phase regions [A,B] and the dark (Cu,Ni) single phase region [C].

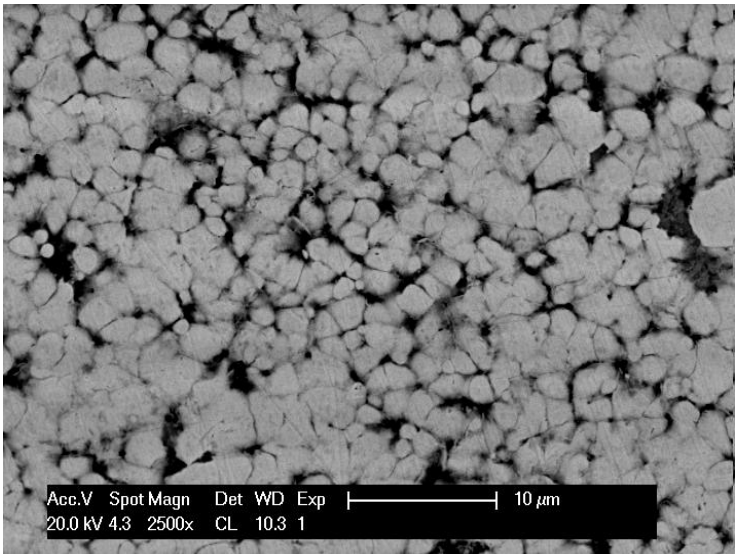


Figure 5.21. BSE-SEM image of nominal W_{25}:C_{25}:Cu_{40}:Ni_{10} (at.%) in as-cast condition showing the light ~W_2C carbide and dark (Cu,Ni).

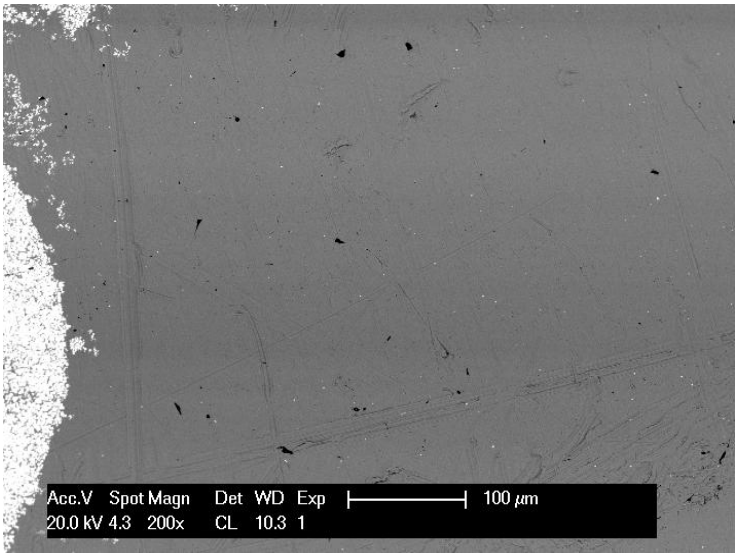


Figure 5.22. BSE-SEM image of nominal W_{25}:$C_{25}$$Cu_{40}$:$Ni_{10}$ (at.%) in as-cast condition showing the dark (Cu,Ni) single phase region with porosity and a portion of the light carbide.

Table 5.23 gives phase analyses of the as-cast sample W_{25}:C_{25}:Cu_{40}:Ni_{10} (at.%). A few analyses were taken at the two-phase regions to observe a trend only, since the carbide grains were less than 3µm across. The two-phase regions had very large errors, especially in portion A. This was due to the small sizes of the phases. The single (Cu,Ni) dark phase had no W; this could be poor solubility of Cu for W and poor melting. The carbon content in the medium (Cu,Ni) phase was high.

XRD identified ~W_2C and (Cu). The (Cu,Ni) phase was not available on the ICDD database. The peaks were sharp and the pattern had a low background. Figure 5.23 shows the pattern for nominal W_{25}:C_{25}:Cu_{40}:Ni_{10} (at.%). There were some unidentified peaks shown in Table 5.24.

Phase description	W	C	Cu	Ni	Phase deduced
Two-phase region [A] Figure 4.20					
Overall	50.7 ± 1.6	7.7 ± 3.6	36.6 ± 2.2	5.0 ± 0.4	-
Light phase	48.7 ± 15.0	33.3 ± 14.3	7.0 ± 5.0	11.0 ± 5.9	~W_2C
Medium	0.9 ± 0.9	16.3 ± 10.0	74.3 ± 8.3	8.5 ± 2.9	(Cu,Ni)
Two-phase region [B] Figure 4.20					
Overall	57.2 ± 4.2	7.1 ± 7.3	31.4 ± 3.5	4.3 ± 0.6	-
Light phase	76.6 ± 7.6	7.4 ± 6.8	12.7 ± 10.4	3.3 ± 0.8	~W_2C
Medium	0.6 ± 0.5	21.2 ± 5.4	70.3 ± 6.6	7.9 ±1.9	(Cu,Ni)
Single phase region [C] Figure 4.20					
Overall	-	24.4 ± 0.6	67.6 ± 0.6	8.0 ± 0.1	(Cu,Ni)

Table 5.23. EDX phase analyses for nominal W_{25}:C_{25}:Cu_{40}:Ni_{10} (at.%) in as-cast condition using standards made from the elements from which samples were prepared (done at University of Botswana, UB).

Peak No	2θ (degree)	d-spacing (Å)	Relative intensity (%)
1	26.52	3.36	4.11
2	36.48	2.72	3.85

Table 5.24. Unidentified XRD peaks in nominal W_{25}:C_{25}:$Cu_{42.5}$:$Ni_{7.5}$ (at.%), in as-cast condition.

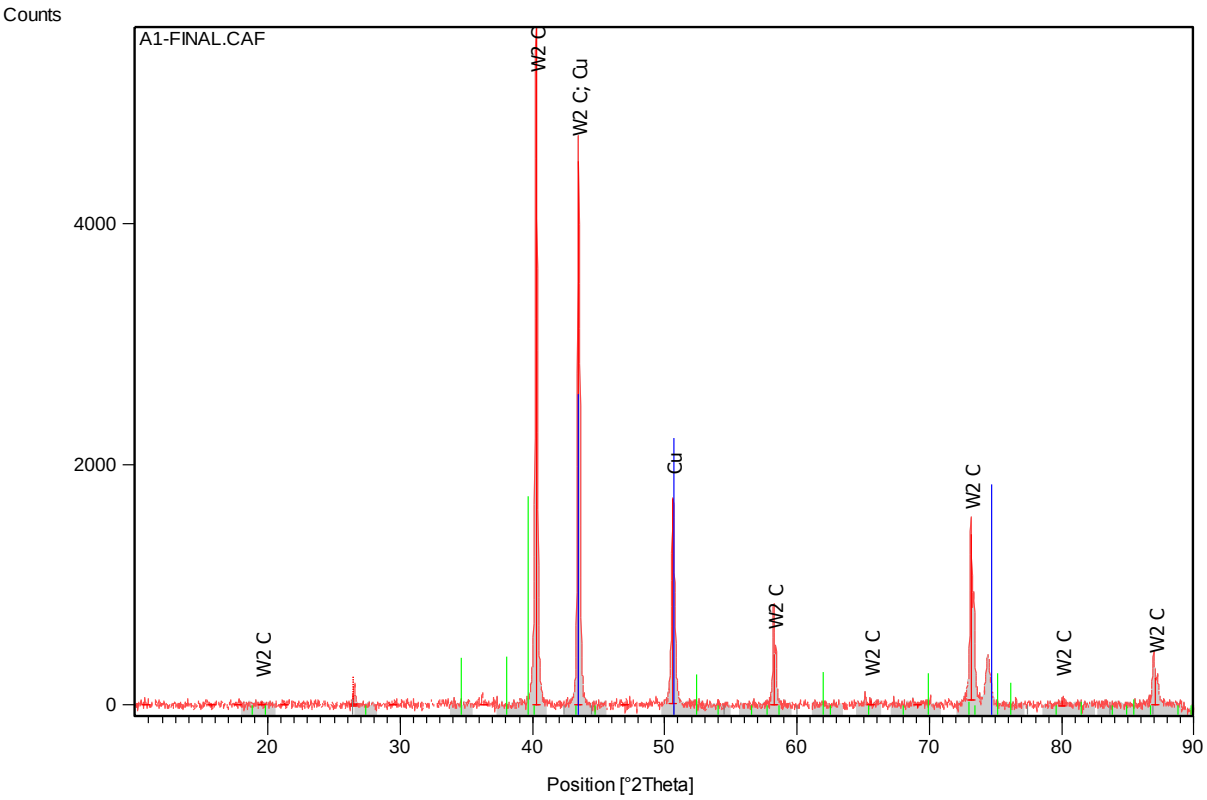


Figure 5.23. XRD pattern nominal W_{25}:C_{25}:$Cu_{42.5}$:$Ni_{7.5}$ (at.%) in as-cast condition showing ~W_2C, Cu and some unidentified peaks.

5.1.9 Nominal W_{25}:C_{25}:Mn_{25}:V_{25} (at.%)

Two different varying proportions of light dendrites were seen in the as-cast sample W_{25}:C_{25}:Mn_{25}:V_{25} (at.%), indicating the sample was inhomogeneous. Both regions had two phases. The light ~V_2C dendrites phase formed the bulk of the sample in both regions (Figure 5.24).

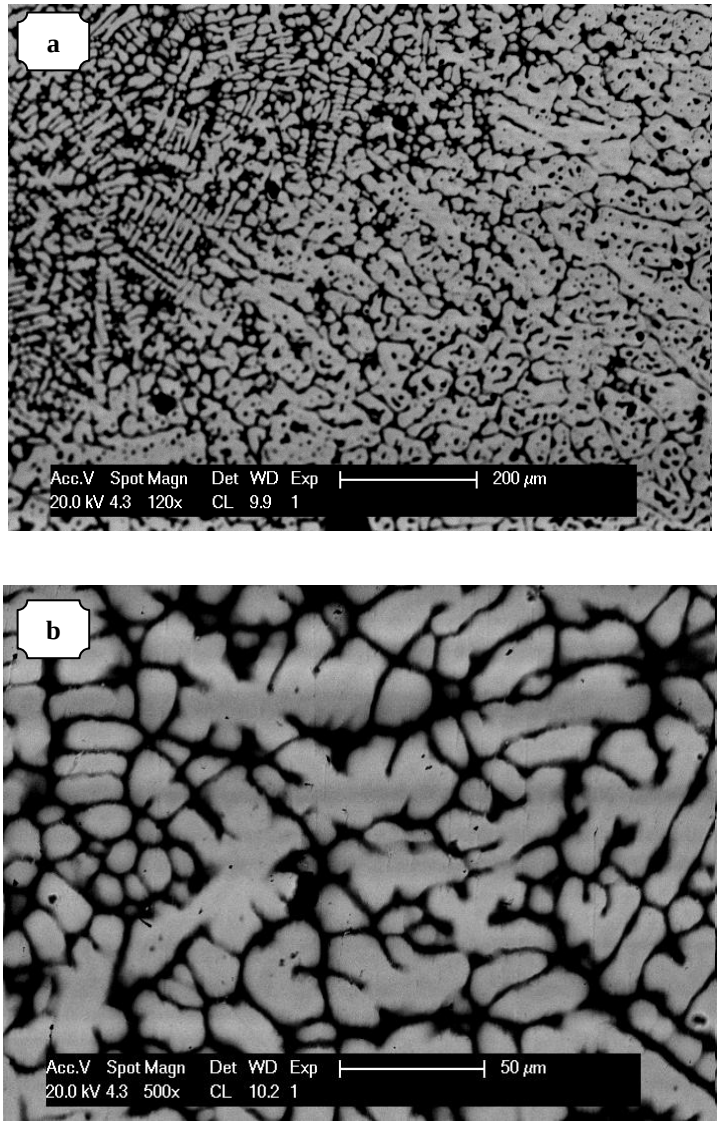


Figure 5.24. SEM-BSE images of nominal W_{25}:C_{25}:Mn_{25}:V_{25} in as-cast condition showing: a) overall view of the sample, light ~V_2C and dark (V) phase, b) higher magnification view.

Table 5.25 gives the EDX analyses of the as-cast sample. Missing in the analyses was manganese; this can be attributed to evaporation of lower melting pointing of manganese by the arc-melting.

XRD identified V_2C and confirmed the (V) phase as indicated by EDX analysis. Figure 5.25 shows the pattern for sample W_{25}:C_{25}:Mn_{25}:V_{25} (at.%). The (V) peaks were slightly shifted from the pure vanadium values, and were very broad, which was a good indication for a solid solution. However, the XRD pattern was poor, showing few high intensity peaks.

Phase description	W	C	Mn	V	Phase deduced
Low carbide proportion					
Overall	31.5 ± 1.0	25.6 ± 1.3	-	42.9 ± 0.7	-
Light	39.5 ± 0.5	26.4 ± 0.9	-	34.1 ± 0.5	~V_2C
Dark	5.7 ± 0.92	13.3 ± 0.3	0.2 ± 0.2	79.8 ± 0.6	(V)
High carbide proportion					
Overall	29.0 ± 0.2	24.2 ± 0.7	-	46.8 ± 0.9	-
Light	48.9 ± 0.9	21.7 ± 0.5	-	29.4 ± 0.6	~V_2C
Dark	6.1 ± 0.2	12.5 ± 0.5	-	80.4 ± 1.0	(V)

Table 5.25. EDX phase analyses for nominal W_{25}:C_{25}:Mn_{25}:V_{25} (at.%) in as-cast condition, without standards (done at University of Botswana, UB).

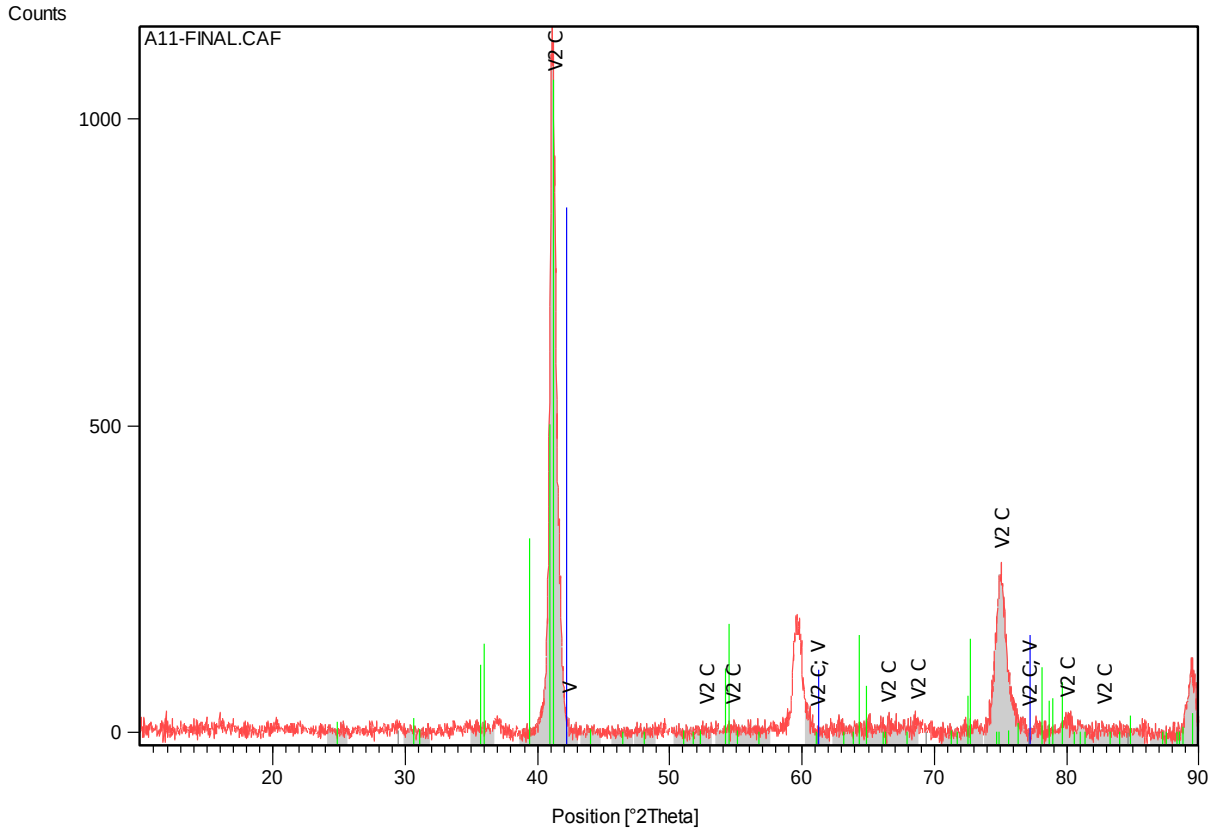


Figure 5.25. XRD pattern nominal W_{25}:C_{25}:Mn_{25}:V_{25} (at.%) in as-cast condition showing ~V_2C and (V).

5.1.10 Nominal W_{25}:C_{25}:$Cu_{47.5}$:$Mn_{2.5}$ (at.%)

The as-cast sample W_{25}:C_{25}:$Cu_{47.5}$:$Mn_{2.5}$ (at.%) was inhomogeneous and in layers, indicating improper melting. There were three notably different regions. A single medium dark phase (Cu,Mn) with a low carbide distribution formed a ring around a two-phase-region (1 in Figure 5.26) and had a crack and some porosity (Figure 5.28). The two-phase region comprised a light phase which formed the larger proportion and a dark phase, as shown in Figure 5.26 [region 2]. Figure 5.27 shows a higher magnification of the portion labelled 2 in Figure 5.26. This two-phase region also formed a ring around the innermost two-phase region in the centre. The innermost two-phase region had a lower proportion of the light phase and also a substantial amount of round porosity.

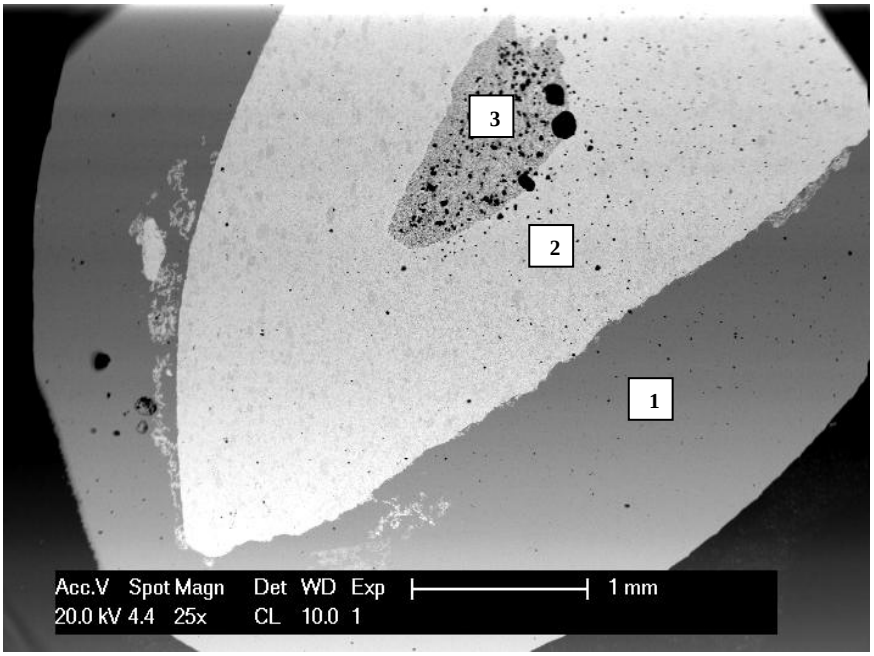


Figure 5.26. SEM-BSE image of nominal as-cast W_{25}:C_{25}:$Cu_{47.5}$:$Mn_{2.5}$ (at.%) showing the three different areas in the sample, (Cu,Mn) [1], the improperly melted light carbide grain region [2], and the innermost two-phase region [3].

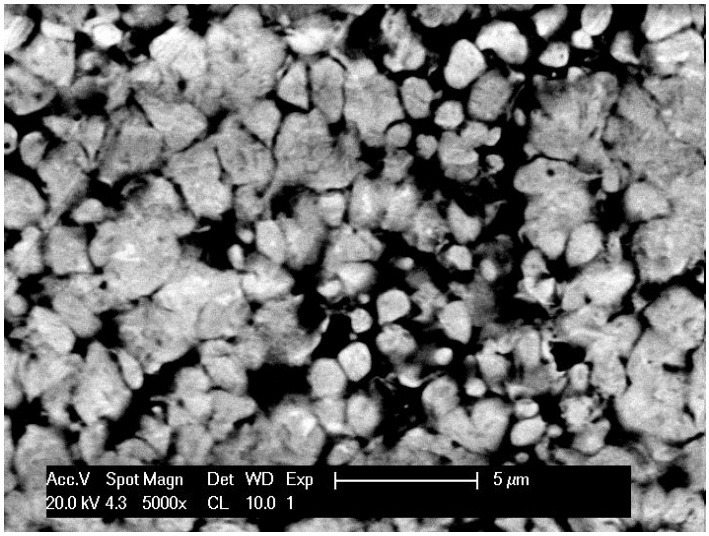


Figure 5.27. SEM-BSE image of nominal as-cast W_{25}:C_{25}:$Cu_{47.5}$:$Mn_{2.5}$ (at.%) showing middle two-phase region ([3] in Figure 5.26) comprising cored carbides.

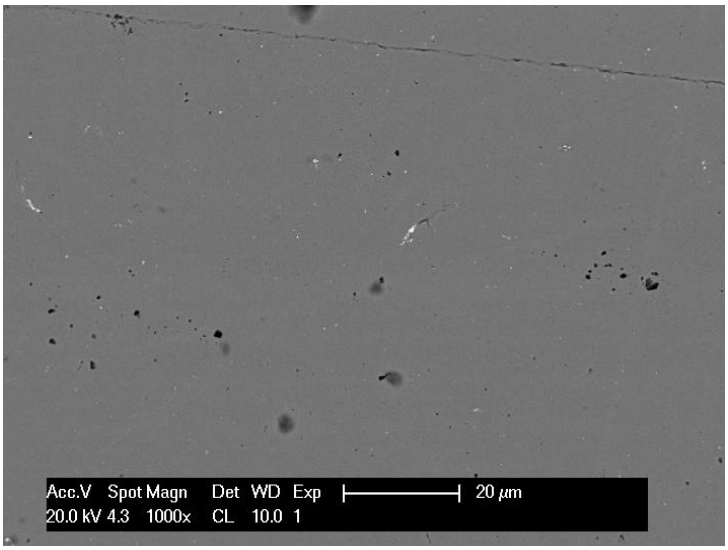


Figure 5.28. SEM-BSE image of nominal as-cast W_{25}:C_{25}:$Cu_{47.5}$:$Mn_{2.5}$ (at.%) showing the outermost dark single phase region ([1] in Figure 5.26) with a crack (top), few carbide patches and porosity.

Overall EDX analyses were taken at the carbide regions surrounding the central portion (2 in Figure 5.26), due the small phase sizes which were less than 3μm across. The EDX analyses of the nominal sample W_{25}:C_{25}:$Cu_{47.5}$:$Mn_{2.5}$ (at.%) are given in Table 5.26. The errors were huge in the analyses taken in the innermost two-phase region, due to the small phase sizes. The carbides in the innermost region were cored (Figure 5.26), which also explains the large errors. The overalls for the two two-phase regions were similar.

Phase description	W	C	Cu	Mn	Phase deduced
Two phase region ([2] in Figure 4.27)					
Overall	44.7 ± 1.6	31.4 ± 2.7	20.6 ± 2.2	3.3 ± 0.8	-
Two phase region ([1] in Figure 4.27)					
Overall	40.2 ± 3.7	32.5 ± 6.5	25.2 ± 2.8	2.1 ± 0.4	-
Light phase	63.2 ± 8.7	32.5 ± 8.8	4.3 ± 2.1	-	~W_2C
Medium	10.6 ± 7.0	5.2 ± 7.6	79.3 ± 12.9	4.9 ±0.6	(Cu,Mn)
Single phase region ([3] in Figure 4.27 Cu,Mn)					
Overall	-	18.8 ± 0.6	75.0 ± 0.6	6.2 ± 0.7	(Cu,Mn)

Table 5.26. EDX phase analyses for nominal W_{25}:C_{25}:$Cu_{47.5}$:$Mn_{2.5}$ (at.%) in as-cast condition without standards (done at University of Botswana, UB).

Figure 5.29 shows the XRD pattern for the nominal sample W_{25}:C_{25}:$Cu_{47.5}$:$Mn_{2.5}$ (at.%). XRD peaks matched very well with W_2C and give a good fit for (Cu) after shifting. There was an unmatched peak (Table 5.27). The XRD pattern had very sharp peaks and looked good, with a low background. All the peaks were fairly broad, indicating the presence of a solid solution.

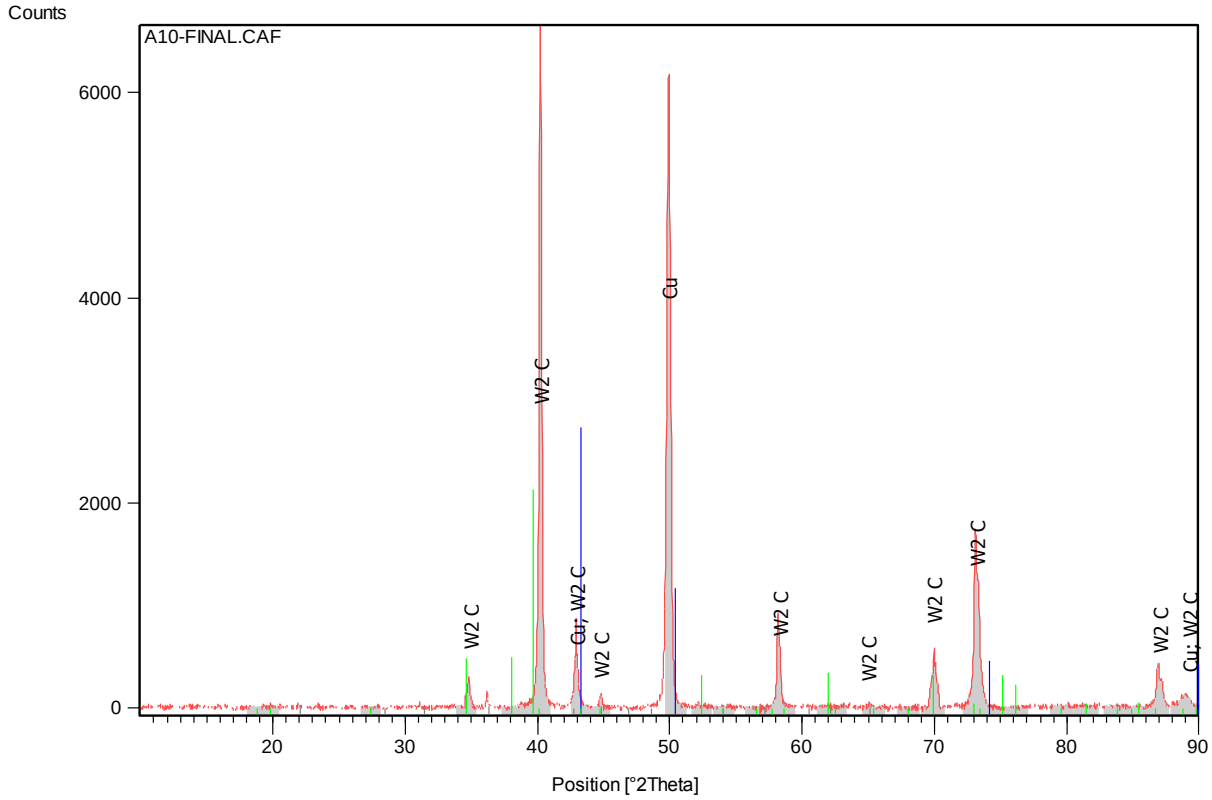


Figure 5.29. XRD pattern of nominal W_{25}:C_{25}:$Cu_{47.5}$:$Mn_{2.5}$ (at.%) in as-cast condition showing W_2C and (Cu).

Peak No	2θ (degree)	d-spacing (Å)	Relative intensity (%)
1	36.21	2.48	1.39

Table 5.27. Unidentified XRD peak in nominal W_{25}:C_{25}:$Cu_{47.5}$:$Mn_{2.5}$ (at.%), in as-cast condition.

5.1.11 Nominal W_{25}:C_{25}:Cu_{45}:Zn_5 (at.%)

The as-cast sample W_{25}:C_{25}:Cu_{45}:Zn_5 (at.%) did not melt properly and the largest portion which seemed to have melted better was selected, sectioned and prepared for analysis. This was a single carbide phase with much porosity (Figure 5.30).

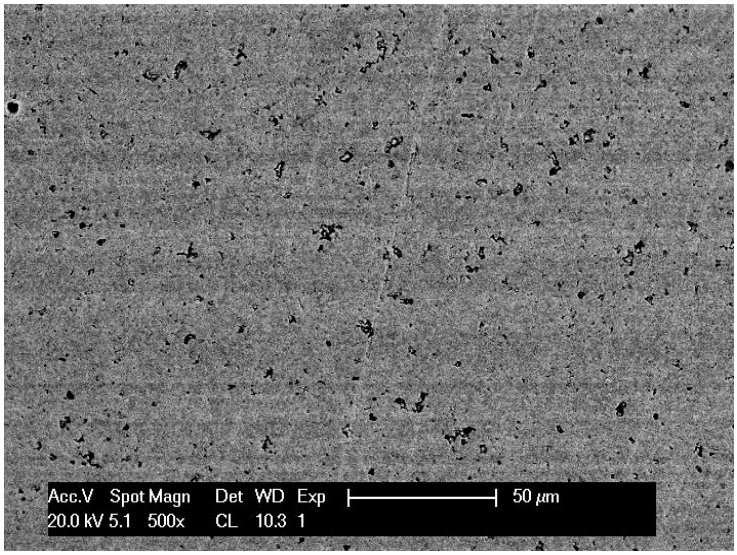


Figure 5.30. SEM-BSE image of nominal as-cast W_{25}:C_{25}:Cu_{45}:Zn_5 (at.%) showing the single carbide phase and irregular porosity.

Table 5.28 gives phase analyses for nominal W_{25}:C_{25}:Cu_{45}:Zn_5 (at.%). Although there was no discernable difference in the microstructure, the EDX analyses showed two different compositions: ~WC and ~W_2C. The different readings were then recorded separately in the Table 5.28 and were labelled 1 and 2. The errors were large, indicating coring.

Phase description	**W**	**C**	**Cu**	**Zn**	**Phase deduced**
Overall 1	71.9 ± 5.6	28.1 ± 5.6	-	-	~W_2C
Overall 2	52.6 ± 1.3	47.4 ± 1.3	-	-	~WC

Table 5.28. EDX phase analyses for a portion of nominal W_{25}:C_{25}:Cu_{45}:Zn_5 (at.%) in as-cast condition without standards (done at University of Botswana, UB).

The XRD pattern (Figure 5.31) confirmed the presence of ~W_2C and had a few WC peaks as well. The XRD pattern had relatively wide peaks, indicating coring. There was a very small unidentified peak as shown in Table 5.29.

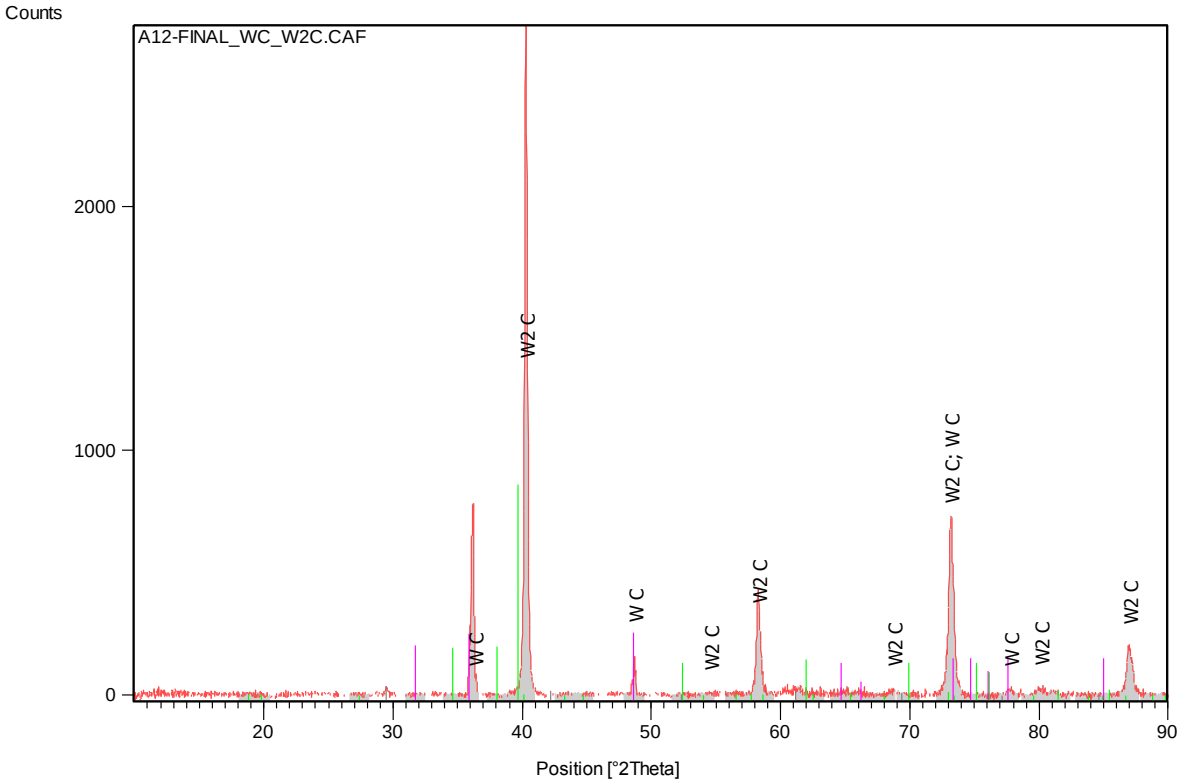


Figure 5.31. XRD pattern nominal W_{25}:C_{25}:Cu_{45}:Zn_5 (at.%) in as-cast condition showing both ~WC, ~W_2C and some small unidentified peaks.

Peak No	2θ (degree)	d-spacing (Å)	Relative intensity (%)
1	29.49	3.23	1.34

Table 5.29. Unidentified XRD peak in nominal W_{25}:C_{25}:Cu_{45}:Zn_5 (at.%) in as-cast condition.

5.1.12 Nominal W_{25}:C_{25}:Cu_{40}:Zn_{10} (at.%)

The nominal W_{25}:C_{25}:Cu_{40}:Zn_{10} (at.%) sample in the as-cast condition had two different regions (Figure 5.32), indicating incomplete melting (not melting uniformly or the sample being inhomogeneous). The middle part of the sample was a two-phase region with the bulk being light ~W_2C carbide particles in a dark (Cu,Zn) matrix (Figure 5.33). Surrounding the two-phase region was a dark single phase comprising a solid solution of copper and zinc as shown in (Figure 5.31b). The sample had round porosity.

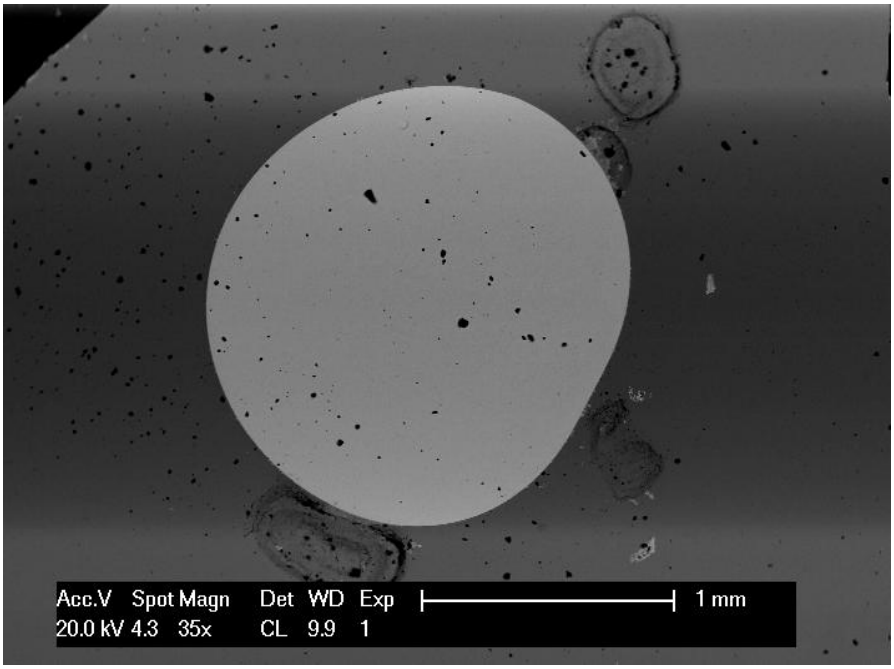


Figure 5.32. SEM-BSE image of nominal as-cast $W_{25}:C_{25}:Ni_{40}:Zn_{10}$ (at.%) showing an overall view, and the two phase-region in the middle surrounded by the dark (Cu,Zn) phase.

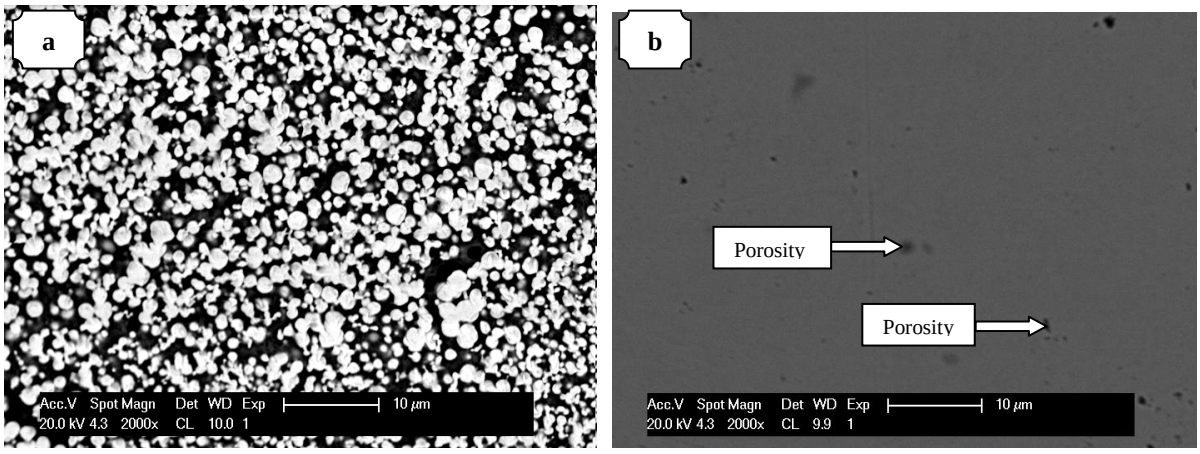


Figure 5.33. SEM-BSE images of nominal annealed $W_{25}:C_{25}:Ni_{40}:Zn_{10}$ (at.%) showing: a) light carbide phase in a dark matrix, b) a dark single phase with some round porosity.

Overall EDX analyses were taken of both regions. The light phase in the two-phase region was too small for accurate analyses, hence the measurements were restricted to overall analyses. Table 5.30 gives the phase analyses of the as-cast sample.

Phase description	W	C	Cu	Zn	Phase deduced
Dark single phase region					
Overall	-	-	97.3 ± 0.4	2.7 ± 0.1	(Cu,Zn)
Two-phase region					
Overall	60.8 ± 4.3	34.6 ± 4.3	4.4 ± 0.8	0.2 ± 0.4	~W_2C

Table 5.30. EDX phase analyses for a portion of nominal W_{25}:C_{25}:Cu_{40}:Zn_{10} (at.%) in as-cast condition without standards(done at University of Botswana, UB).

Figure 5.34 shows the XRD pattern for sample W_{25}:C_{25}:Cu_{40}:Zn_{10} (at.%). The pattern had sharp peaks with very low background. There were small peaks which could be not identified (Table 5.31).

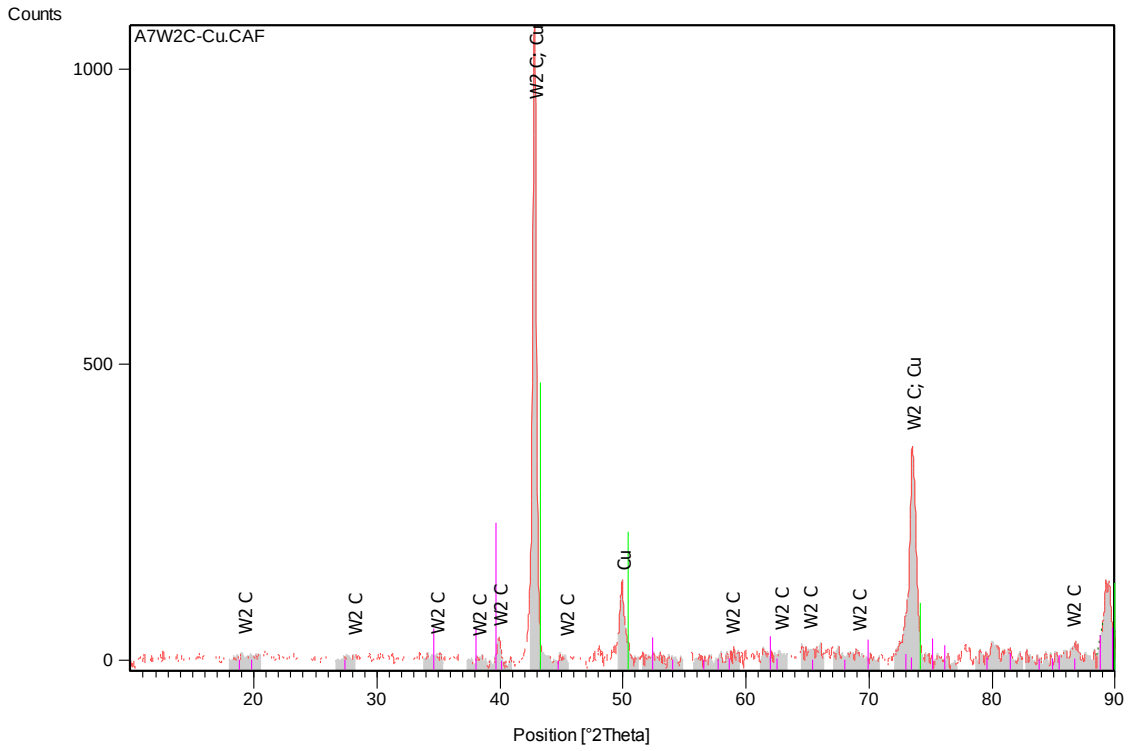


Figure 5.34. XRD pattern nominal W_{25}:C_{25}:Cu_{40}:Zn_{10} (at.%) in as-cast condition, showing ~W_2C and (Cu) peaks.

Peak No	2θ (degree)	d-spacing (Å)	Relative intensity (%)
1	39.00	3.23	1.34
2	77.67	1.20	1.01

Table 5.31. Unidentified XRD peaks in nominal $W_{25}:C_{25}:Cu_{40}:Zn_{10}$ (at.%) in as-cast condition.

5.2 Phase analysis of alloys – annealed at 1000 ºC for 168 hours

5.2.1 Nominal $W_{25}:C_{25}:Ni_{45}:V_{2.5}$ (at.%)

The microstructure of the alloy $W_{25}:C_{25}:Ni_{47.5}:V_{2.5}$ (at.%) after annealing for 168 hours at 100°C (Figure 5.35) was slightly different to the as-cast structure (Figure 5.1). The sample showed two distinct phases and had more eutectic (as shown in Figure 5.36) than the as-cast sample and it had coarsened.

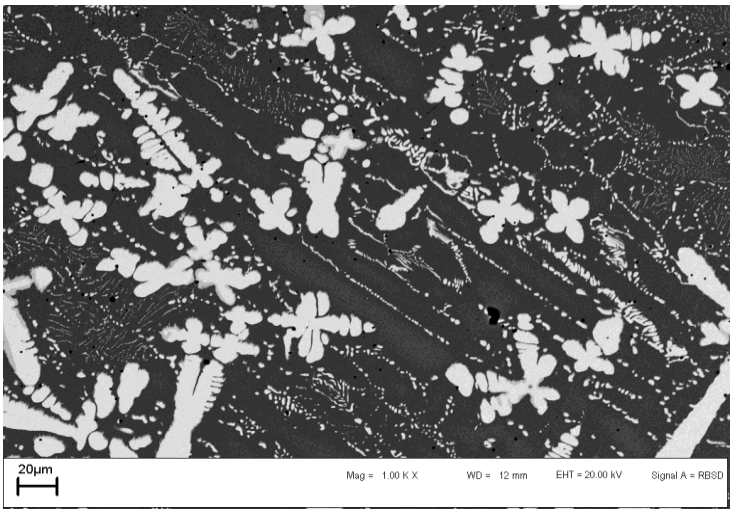


Figure 5.35. SEM-BSE image of nominal $W_{25}:C_{25}:Ni_{47.5}:V_{2.5}$ (at.%) after annealing at 1000ºC for 168 hours: light ~W_2C dendrites surrounded by medium dark ~Ni_2V and ~W_2C (light) + ~Ni_2V (dark) eutectic.

Some of the light dendrites had another phase on the outside; this could be a ternary phase. The ~Ni_2V dark phase was cored, but the eutectic component was not different in contrast, as seen in the as-cast (Figure 5.1).

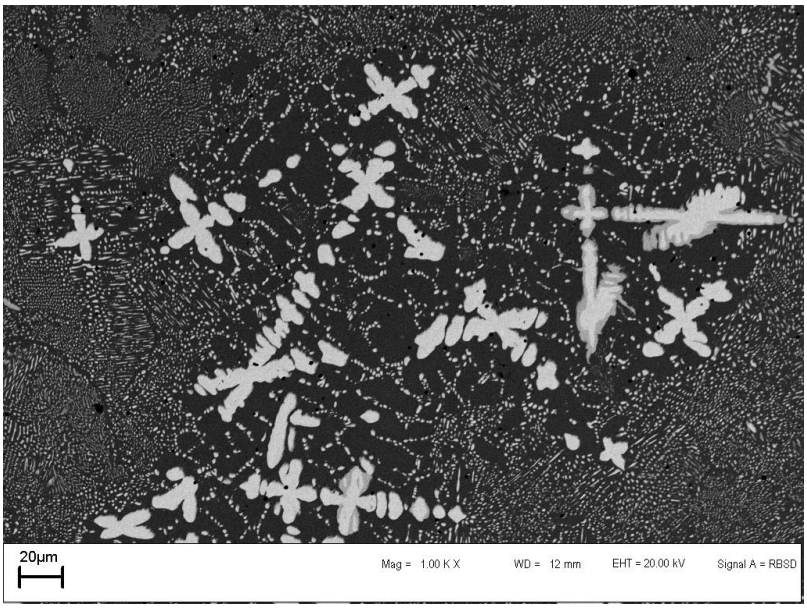


Figure 5.36. SEM-BSE image of nominal W_{25}:C_{25}:$Ni_{47.5}$:$V_{2.5}$ (at.%) after annealing at 1000ºC for 168 hours, showing large amounts of eutectic.

Table 5.32 gives the EDX phase analyses of the annealed W_{25}:C_{25}:$Ni_{47.5}$:$V_{2.5}$ (at.%) sample and the errors were reasonable, except for the medium edges of the dendrites. These regions were too small to analyse accurately.

The presence of ~W_2C and ~Ni_2V was identified using XRD; this is shown in Figure 5.37 which had a good pattern with sharp peaks and low background. The main carbide peak was slightly shifted; this could be due to other dissolved elements in it.

The EDX results from the different conditions (as-cast and annealed) generally looked slightly different. The tungsten content in the overall in the as-cast (18.8 ± 0.2 at.%) was slightly higher than in the annealed sample; carbon content in the overall was much higher in the annealed sample (29.3 ± 0.9 at.%) than in the as-cast sample which was 13.8 ± 0.5 at.%. Nickel content in the overall of the as-cast sample was 63.6 ± 0.6 at.%, which was much higher than in the annealed sample, whereas carbon and vanadium formed 3.8 ± 0.1 at.% of the overall composition in the as-cast sample and was 1.0 ± 0.1 at.% higher than the annealed sample.

The carbon contents in all the phases in the annealed condition were relatively higher than in the as-cast samples. EDX results for as-cast and annealed samples were taken from different SEMS.

Phase description	W	C	Ni	V	Phase deduced
Overall	16.3 ±0.3	29.3 ± 0.9	51.6 ± 0.7	2.8 ± 0.1	-
Dark	12.3 ± 0.1	30.5 ± 1.3	54.4 ± 0.6	2.8 ± 0.3	~Ni_2V
Light	48.3 ± 0.2	47.6 ± 0.9	3.7 ± 0.1	0.4 ± 0.1	~W_2C
Medium (edges of dendrites)	21.5 ± 5.9	33.6 ± 7.6	43.5 ± 17.1	1.4 ± 1.4	Ternary phase?
Eutectic	13.0 ± 2.4	29.6 ± 0.7	54.5 ± 0.8	2.9 ± 0.1	~Ni_2V+ ~W_2C

Table 5.32. Phase analyses for nominal W_{25}:C_{25}:$Ni_{47.5}$:$V_{2.5}$ (at.%) after annealing at 1000°C for 168 hours using pre-loaded standards (done at NMISA).

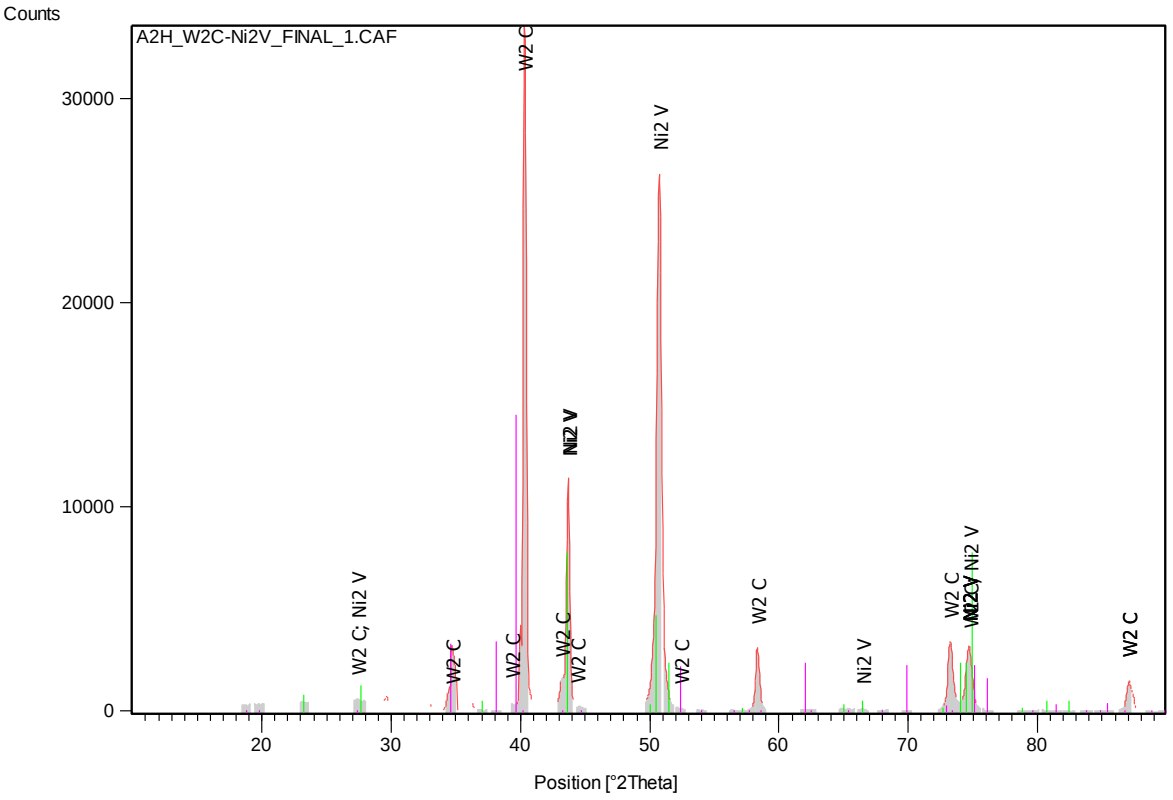


Figure 5.37. XRD pattern of nominal W_{25}:C_{25}:$Ni_{47.5}$:$V_{2.5}$ (at.%) in annealed condition, showing ~W_2C and ~Ni_2V peaks.

All peaks were identified in the as-cast condition, whereas some small peaks in the XRD pattern in the annealed sample were not identified (Table 5.33). The major XRD peaks in the annealed sample (Figure 5.37) were fewer than in the as-cast and the annealed sample had a lower background and a higher intensity than the as-cast. The peaks were for ~W_2C and ~Ni_3V in the as-cast sample, while the annealed sample had ~W_2C and ~Ni_2V. The unmatched peaks are likely to be peaks of the ternary phase.

Peak No	2θ (degree)	d-spacing (Å)	Relative intensity (%)
1	22.05	4.03	1.67
2	29.62	3.01	1.66
3	32.89	2.72	1.41
4	36.27	2.47	1.20
5	41.77	2.16	1.13
6	45.52	1.99	0.84
7	47.21	1.92	0.97

Table 5.33. Unidentified XRD peaks in nominal W_{25}:C_{25}:Ni_{45}:V_5 (at.%) in annealed condition.

5.2.2 Nominal W_{25}:C_{25}:Ni_{43}:V_7 (at.%)

Alloy W_{25}:C_{25}: Ni_{43}:V_7 (at.%) in the annealed condition (Figure 5.38) was very different from the as-cast alloy (Figure 5.4). The annealed sample had an apparent new phase; a new medium contrast phase had formed as coarse needles and light precipitates were found in both the medium and dark medium matrices. The light spots were too small to analyse. The light dendrites were much broader and had darker contrast edges as shown in Figure 5.39. There were some darker needles which might have formed on cooling.

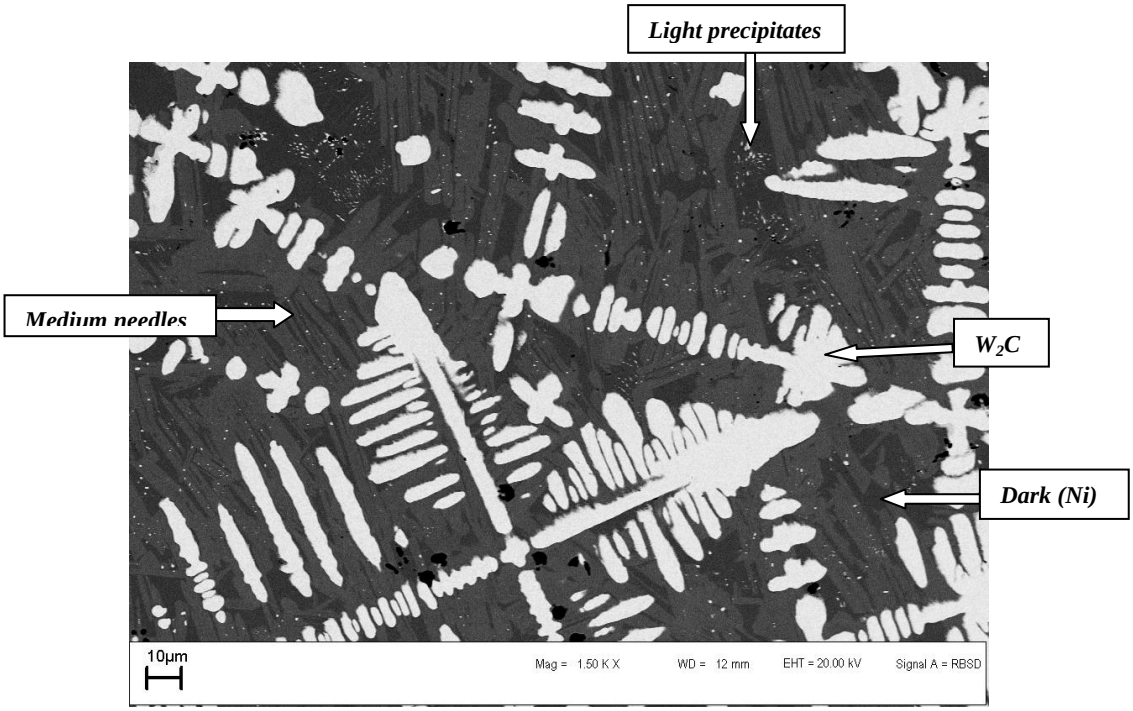


Figure 5.38. SEM-BSE image of nominal W_{25}:C_{25}:Ni_{43}:V_7 (at.%) in annealed condition showing ~W_2C dendrites, medium needles, light precipitates and dark (Ni).

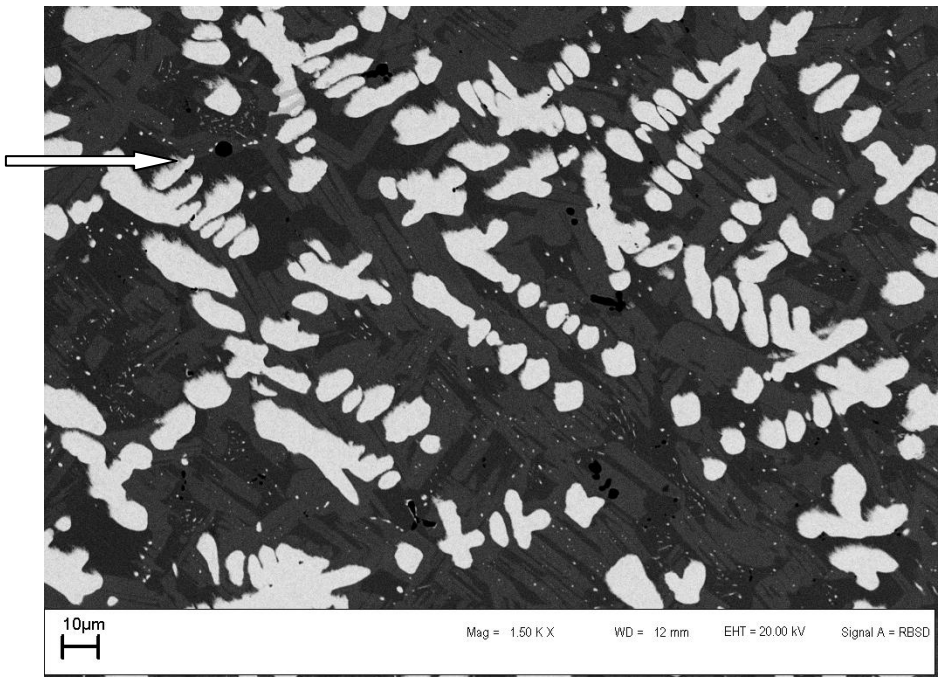


Figure 5.39. SEM-BSE image of nominal W_{25}:C_{25}:Ni_{43}:V_7 (at.%) in annealed condition showing ~W_2C dendrites with medium contrast dendrite edges (see arrow) and precipitation of a light phase (~W_2C).

Table 5.34 gives phase analyses of the annealed W_{25}:C_{25}:Ni_{43}:V_7 (at.%) sample. The medium and dark contrast regions had similar analyses, although they had distinct morphologies. The

errors were within accepted limits, except for the phase at the edges of the dendrites, which was too small to analyse accurately. There was no sign of the oxide after heat treatment, as in the as-cast sample. The EDX results of the as-cast were different the annealed sample. There was another phase present (Ni) in the annealed sample which was not found in the as-cast sample. The carbon and the nickel contents in the annealed sample were higher and lower respectively than in both overall and the matrix of the as-cast sample.

XRD identified three phases: ~W_2C, (Ni) and ~Ni_3V. The peaks matching for nickel were slightly shifted, indicating a solid solution. Figure 5.40 shows the pattern for the sample with low background and sharp peaks.

The as-cast XRD pattern looked slightly different and had a broad peak ~Ni_2V at $2\theta = 50$ which was absent in the annealed sample. The annealed sample had fewer peaks but slightly higher intensity peaks than the as-cast sample. The XRD pattern for the as-cast had two phases (~W_2C and ~Ni_2V) while the annealed sample pattern had three phases (~W_2C and ~Ni_2V and (Ni)).

Phase description	**W**	**C**	**Ni**	**V**	**Phase deduced**
Overall	16.8 ± 0.3	28.0 ± 1.6	47.5 ± 1.1	7.7 ± 0.2	-
Light phase	51.7 ± 0.6	44.1 ± 1.2	2.5 ± 0.8	1.7 ± 0.1	W_2C
Dark	7.7 ± 0.8	28.5 ± 1.3	55.8 ± 0.5	8.0 ± 0.1	(Ni)
Medium needles	6.8 ± 0.6	25.8 ± 0.9	59.5 ± 1.1	7.9 ± 0.2	~Ni_3V
Two-phase region	7.6 ± 0.1	27.0 ± 1.0	57.6 ± 0.9	7.8 ± 0.2	~W_2C + (Ni)
Light dendrite edge	46.7 ± 4.4	46.5 ± 4.8	4.5 ± 3.4	2.3 ± 1.1	~W_2C

Table 5.34. EDX phase analyses for nominal W_{25}:C_{25}:Ni_{43}:V_7 (at.%) in the annealed condition using pre-loaded standards (done at NMISA).

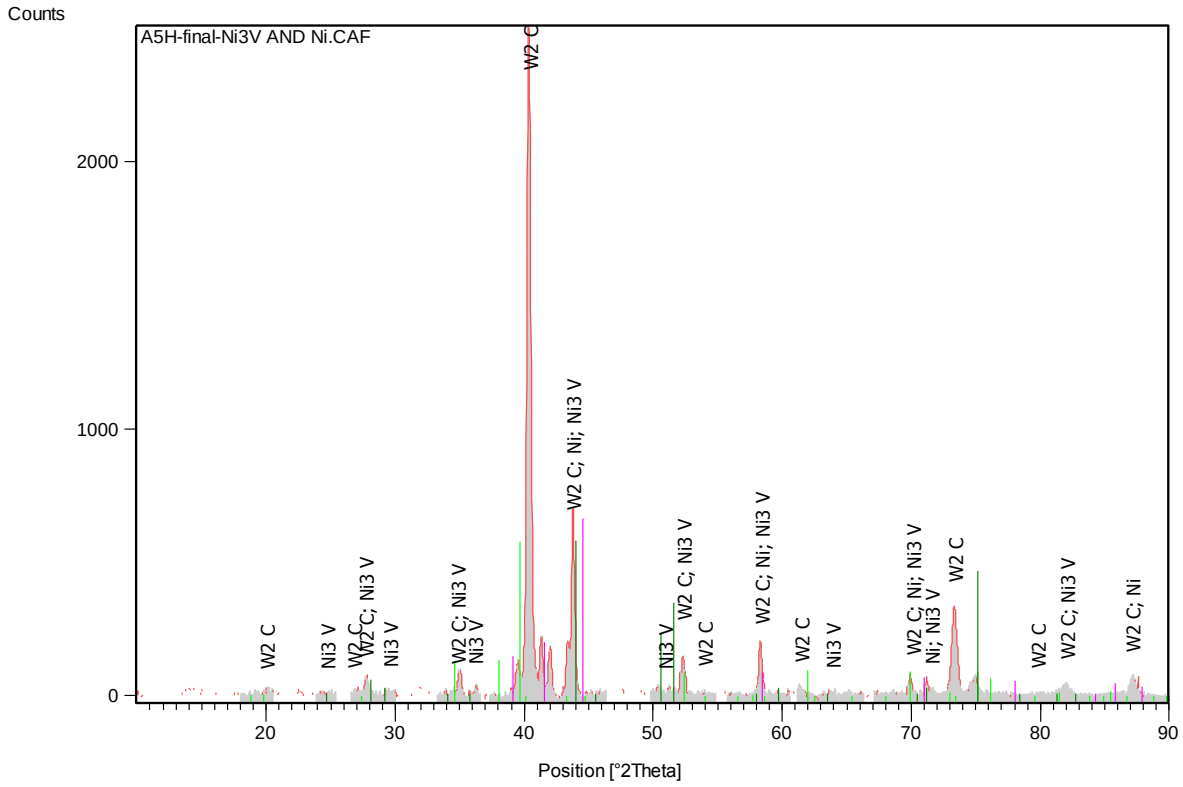


Figure 5.40. XRD pattern of nominal W_{25}:C_{25}:$Ni_{47.5}$:$V_{2.5}$ (at.%) in the annealed condition, showing ~W_2C, ~Ni_3V and (Ni) peaks.

5.2.3 Nominal W_{25}:C_{25}:$Ni_{42.5}$:$Zn_{7.5}$ (at.%)

The microstructure of the W_{25}:C_{25}:$Ni_{42.5}$:$Zn_{7.5}$ (at.%) sample in the annealed condition was the same as that of the as-cast sample, but the eutectic was coarsened as seen in Figure 5.41. The sample had varying proportions of the carbide, indicating inhomogeneity. The area with more carbide had two phases, the globular dendrites and a medium matrix with very little eutectic, while the region with fewer carbides also had two phases with similar looking globular light dendrites in a dark matrix and with much more eutectic. The annealed sample looked very similar to the as-cast sample.

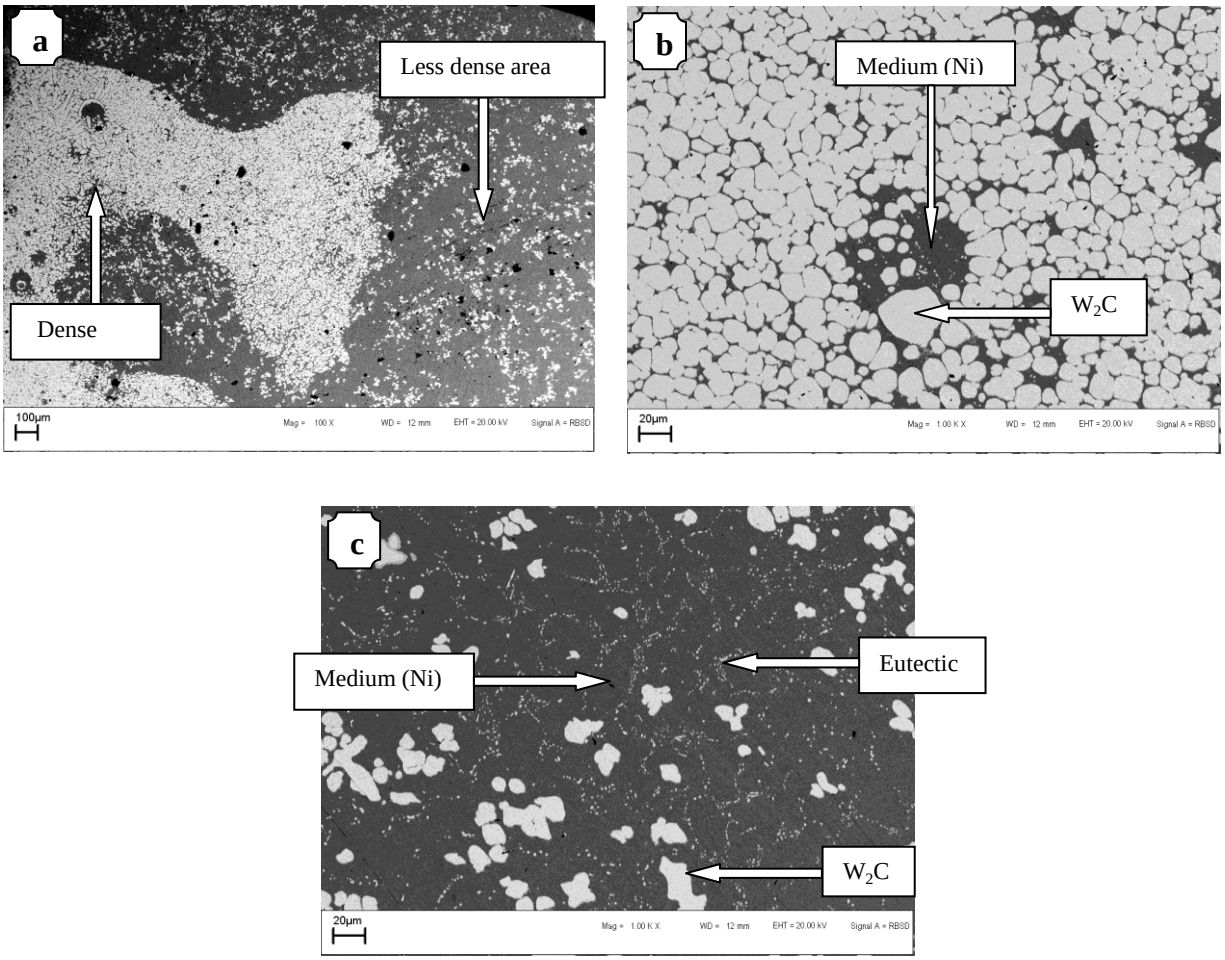


Figure 5.41. SEM-BSE images of nominal W_{25}:C_{25}:$Ni_{42.5}$:$Zn_{7.5}$ (at.%) in annealed condition: showing different regions with different proportions of phases, with light ~W_2C globules and dark matrix (Ni) and a ~W_2C (light) + (Ni) dark eutectic, a) the overall view of the sample, b) the high carbide proportion area c) lower carbide proportion area.

The phase analyses of the annealed sample W_{25}:C_{25}:$Ni_{42.5}$:$Zn_{7.5}$ (at.%) are given in Table 5.35. There was no zinc in the EDX analyses, as was also seen in the as-cast sample. The errors of the light phase in the lower carbide proportion were huge, due to inconsistency in the carbon which seemed to be over estimated. The analyses in the different regions were somehow different in the annealed samples, unlike in the as-cast sample.

Generally, the as-cast and annealed samples' EDX results were different. The overalls of both regions of different carbide proportions in the annealed and as-cast samples were not the same, although the two different carbide proportions were similar in the as-cast sample. Tungsten was 43.1 ± 1.1 at.% and 60.1 ± 5.1 at.% in the higher carbide proportion overall of the annealed and as-cast samples respectively. The carbon content was 44.7 at.% in the annealed sample and 21.6 ± 3.3 at.% in the as-cat sample. Nickel was 12.2 ± 0.5 at.% and

18.3 ± 7.7 at.% in annealed and as-cast samples of the higher carbide proportion regions respectively.

The EDX results of the as-cast were reasonable and were confirmed by XRD, whereas XRD was employed for phase identification in the annealed sample. The as-cast sample were analysed at UB and the annealed sample was analysed at NMISA.

Phase description	**W**	**C**	**Ni**	**Zn**	**Phase deduced**
Higher carbide proportion region					
Overall	43.1 ± 1.1	44.7 ± 1.6	12.2 ± 0.5	-	-
Medium	11.0 ± 0.4	40.6 ± 0.9	48.4 ± 0.4	-	(Ni)
Light phase	41.5 ± 0.4	57.4 ± 0.6	1.1 ± 0.2	-	~W_2C
Lower carbide proportion region					
Overall	49.6 ± 0.6	32.0 ± 0.7	18.4 ± 0.9	-	-
Medium	12.2 ± 0.5	37.2 ± 0.3	50.6 ± 0.1	-	(Ni)
Light	24.2 ± 4.8	63.7 ± 5.4	12.1 ± 0.5	-	~W_2C
Eutectic	14.2 ± 1.2	38.5 ± 2.5	47.3 ± 1.8	-	(Ni) + ~W_2C

Table 5.35. EDX phase analyses for nominal W_{25}:C_{25}:$Ni_{42.5}$:$Zn_{7.5}$ (at.%) in the annealed condition using pre-loaded standards (done at NMISA).

XRD was employed in phase identification because of the difficulty with EDX. The XRD pattern looked good with sharp peaks and low background shown in Figure 5.42. There were some unmatched peaks which were from the plasticine ($CaCO_3$) (Appendix A) used in holding the sample in the XRD sample holder. The (Ni) peaks were slightly shifted, indicating a solid solution.

The XRD peaks in the annealed sample had much lower background, and fewer and narrower peaks than in the as-cast sample. There were some unmatched peaks (Table 5.36) in the XRD pattern in the annealed sample, and none in the as-cast sample. Both spectra had similar intensity levels.

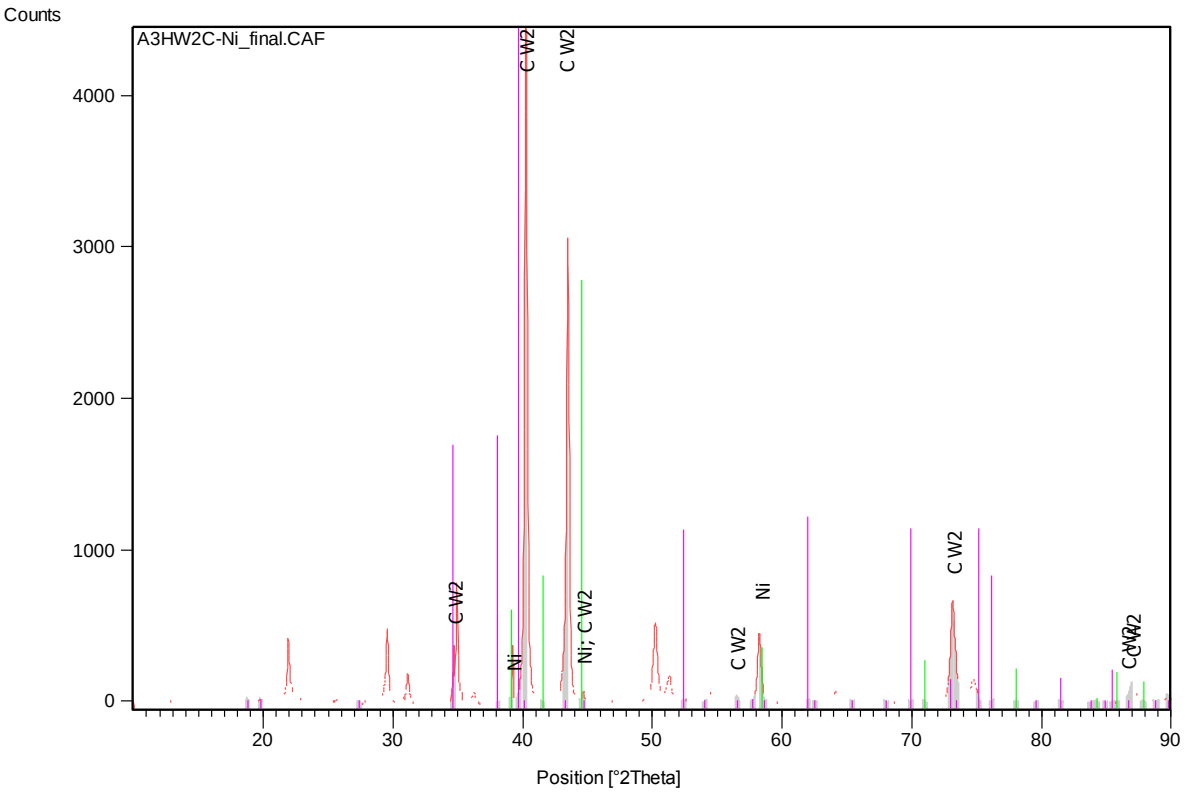


Figure 5.42. XRD pattern of nominal W_{25}:C_{25}:$Ni_{42.5}$:$Zn_{7.5}$ (at.%) in annealed condition, showing ~W_2C and (Ni) peaks.

Peak No	2θ (degree)	d-spacing (Å)	Relative intensity (%)
1	21.91	4.05	0.92
2	29.55	3.02	1.10
3	31.14	2.87	0.44
4	36.22	2.48	0.16
5	50.22	1.82	1.20
6	51.31	1.78	0.42
7	54.46	1.68	0.15
8	61.41	1.51	0.07
9	64.08	1.45	0.18

Table 5.36. Unidentified XRD peaks in nominal W_{25}:C_{25}:$Ni_{42.5}$:$Zn_{7.5}$ (at.%) in annealed condition.

5.2.4 Nominal $W_{25}:C_{25}:Ni_{45}:Zn_5$

The microstructure of the alloy $W_{25}:C_{25}:Ni_{45}:Zn_5$ (at.%) in the annealed condition appeared similar to the as-cast condition, although the eutectic had coarsened and reduced in amount considerably (Figure 5.43). There were two phases as seen in the as-cast sample: globular light dendrites in a dark matrix. The microstructure appeared to have coarse needles forming, as observed in Figures 5.38 and 5.39, although they were not so easy to see.

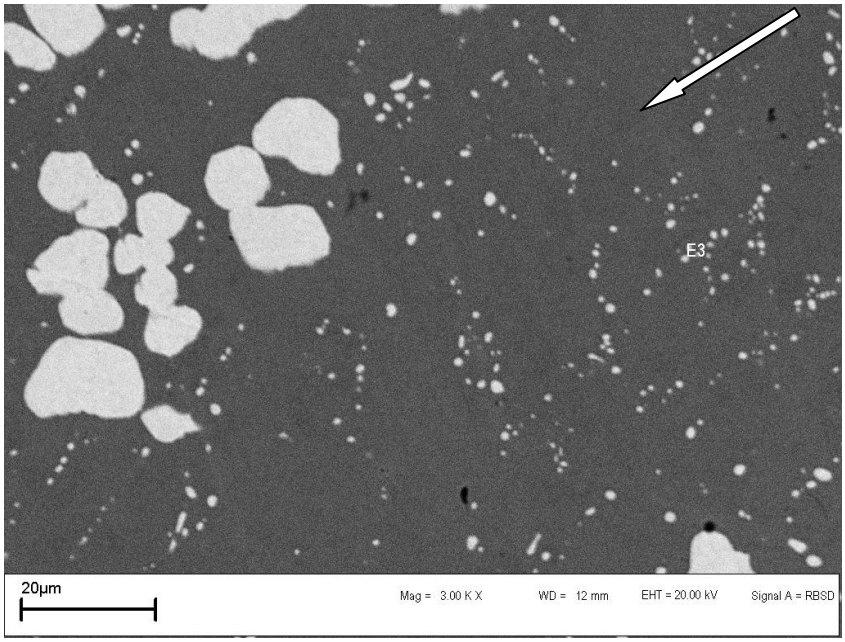


Figure 5.43. SEM-BSE image of nominal $W_{25}:C_{25}:Ni_{45}:Zn_5$ (at.%) in the annealed condition: light ~W_2C; (Ni) medium grey needles (see arrow); eutectic ~W_2C + (Ni).

Table 5.37 gives phase analyses of the annealed sample $W_{25}:C_{25}:Ni_{45}:Zn_5$ (at.%). Most of the phase errors were reasonable, except for the light phase in which EDX was believed to have overestimated carbon, and so led to inconsistencies. Again, no zinc was found, which agreed with the as-cast sample.

The annealed sample EDX generally did not look the same as the as-cast sample. Nickel was the major component in both conditions. Carbon compositions were far higher in all the phases in the annealed sample than in the as-cast sample. The light phase in the as-cast could not be analysed, hence could not be compared. The analyses were done on different SEMS: as-cast was done at UB, (with standards derived from elements from which samples were

prepared; these analyses seemed most accurate), while the annealed sample was done at NMISA (analysed with pre-loaded standards).

Phase description	W	C	Ni	Zn	Phase deduced
Overall	17 0 ± 0.6	35.6 ± 2.0	47.4 ± 1.8	-	-
Light phase	29.0 ± 7.7	69.7 ± 8.0	1.3 ± 0.5	-	~W_2C
Medium	10.7 ± 0.8	42.9 ± 1.8	48.4 ± 1.2	-	(Ni)
Eutectic	14.9 ± 0.5	36.1 ± 0.9	49.0 ± 0.9	-	~W_2C + (Ni)

Table 5.37. EDX phase analyses for nominal W_{25}:C_{25}:Ni_{45}:Zn_5 (at.%) in the annealed condition using pre-loaded standards (done at NMISA).

XRD identified two phases: ~W_2C and Ni. The peaks matching for nickel were slightly shifted, indicating a solid solution. Figure 5.44 shows the pattern for the sample, with a low background and sharp peaks. The peaks were narrower and had lower background in the annealed sample than in the as-cast.

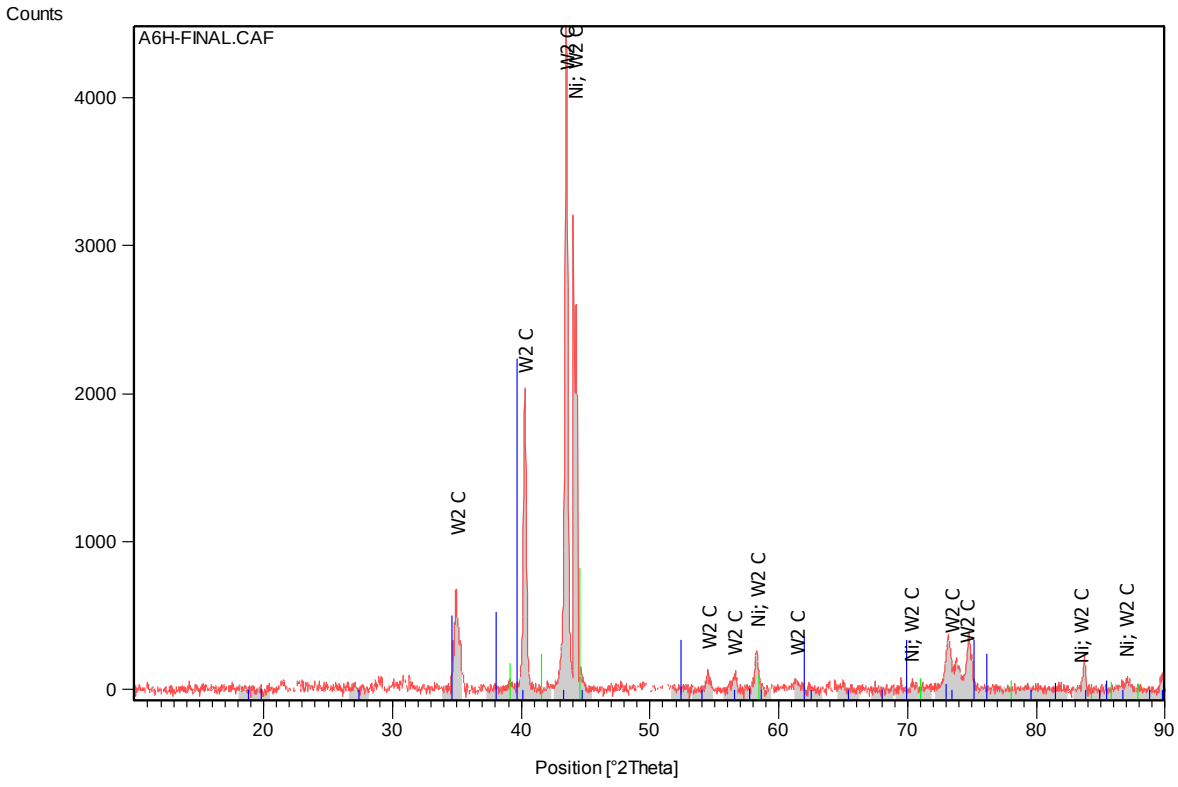


Figure 5.44 XRD pattern of nominal W_{25}:C_{25}:$Ni_{42.5}$:$Zn_{7.5}$ (at.%) in annealed condition, showing ~W_2C and (Ni) peaks.

5.2.5 Nominal W_{25}:C_{25}:Co_{30}:Mn_{20} (at.%)

The microstructure of the alloy W_{25}:C_{25}:Co_{30}:Mn_{20} (at.%) in the annealed condition (Figure 5.45) appeared very different from that in the as-cast condition (Figure 5.11). The annealed sample showed only two phases, whereas the as-cast sample had three phases. Annealing had removed the ternary phase. The needles had also coarsened. The bulk of the annealed alloy was the light phase, which formed as both needles, and flakes.

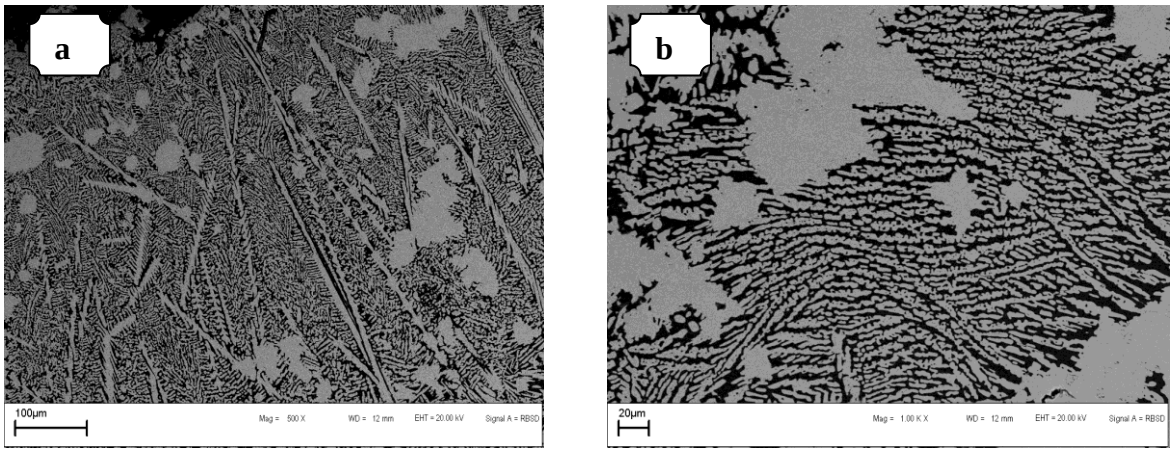


Figure 5.45. SEM-BSE images of nominal W_{25}:C_{25}:Co_{30}:Mn_{20} (at.%) in annealed condition: showing light needles and flakes in dark matrix.

Table 5.38 gives phase analyses of nominal W_{25}:C_{25}:Co_{30}:Mn_{20} (at.%) in annealed condition. EDX analyses showed that carbon content was high in the (Co), whereas the light ~W_2C had relatively higher cobalt content.

The EDX overall analyses showed that carbon was content was much higher in the annealed sample than the as-cast (8.0 ± 0.4 at.% higher), while tungsten was 3.5 ± 0.1 at.% higher in the as-cast sample than the annealed sample. The manganese was slightly higher in the annealed overall than the as-cast (1.2 ± 0.9 at.% higher), while cobalt content in the as-cast overall was 5.8 ± 0.2 at.% higher than the annealed sample.

Generally, the carbon content was higher in the annealed sample than the as-cast. The as-cast sample EDX had a ternary composition (~Co_7W_6 with C or $(Co,W)_2C$). The light phase was found to be ~W_2C in the annealed sample whereas it was ~WC in the as-cast sample.

Phase description	W	C	Mn	Co	Phase deduced
Overall	19.7 ± 0.5	31.6 ± 2.1	8.1 ± 1.1	40.6 ± 0.9	-
Light phase	23.0 ± 0.1	45.3 ± 0.4	2.9 ± 0.8	28.8 ± 1.0	~W_2C
Light (large regions)	24.3 ± 0.4	46.9 ± 0.6	3.3 ± 0.7	25.5 ± 0.9	~W_2C
Dark	21.3 ± 0.9	43.0 ± 0.7	4.8 ± 0.8	30.9 ± 0.7	(Co)

Table 5.38. EDX phase analyses for nominal W_{25}:C_{25}:Co_{30}:Mn_{20} (at.%) in the annealed condition using pre-loaded standards (done at NMISA).

The XRD pattern for the W_{25}:C_{25}:Co_{30}:Mn_{20} (at.%) sample shown in Figure 5.46 was good, and the existence of ~W_2C and (Co) was identified. There were a few small unmatched peaks and they are presented in Table 5.39.

There were fewer peaks in the XRD pattern of the annealed sample, which had two phases, than in the as-cast which also had a ternary phase (~Co_7W_6 with C or $(Co,W)_2C$).

Peak No	2θ (degree)	d-spacing (Å)	Relative intensity (%)
1	20.72	4.28	9.33
2	21.73	4.06	5.43
3	25.67	3.47	1.8
4	70.75	1.33	3.81
5	72.29	1.31	4.41

Table 5.39. Unidentified XRD peaks in nominal W_{25}:C_{25}:Co_{30}:Mn_{20} (at.%) in annealed condition.

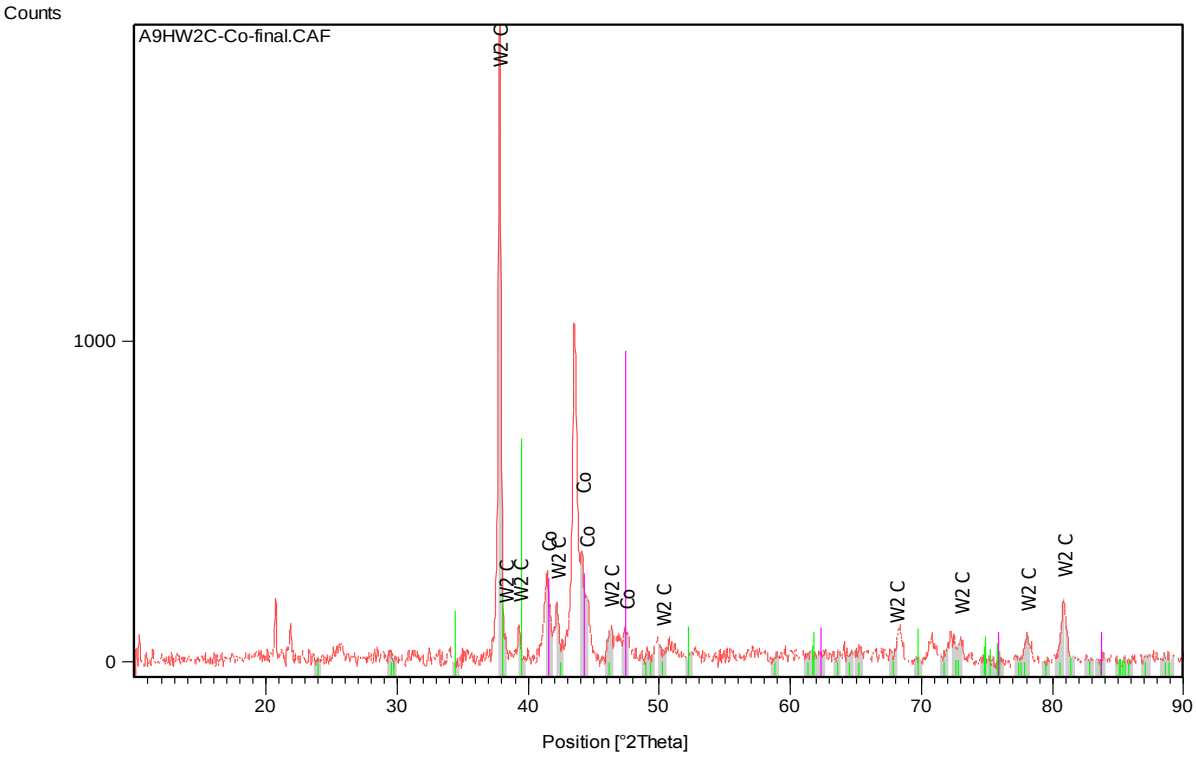


Figure 5.46. XRD pattern of nominal W_{25}:C_{25}:Co_{30}:Mn_{20} in annealed condition showing ~W_2C and (Co) with some unmatched peaks.

5.2.6 Nominal W_{25}:C_{25}:$Co_{12.5}$:$Mn_{37.5}$ (at.%)

The microstructure of the annealed sample W_{25}:C_{25}:$Co_{12.5}$:$Mn_{37.5}$ (at.%) (Figures 5.47 and 5.48) looked the same as the as-cast sample (Figure 5.13). The resemblance could be due to the short annealing time. They both had two phases and the coarse area showed cracks and with much porosity (Figures 5.47 and 5.48).

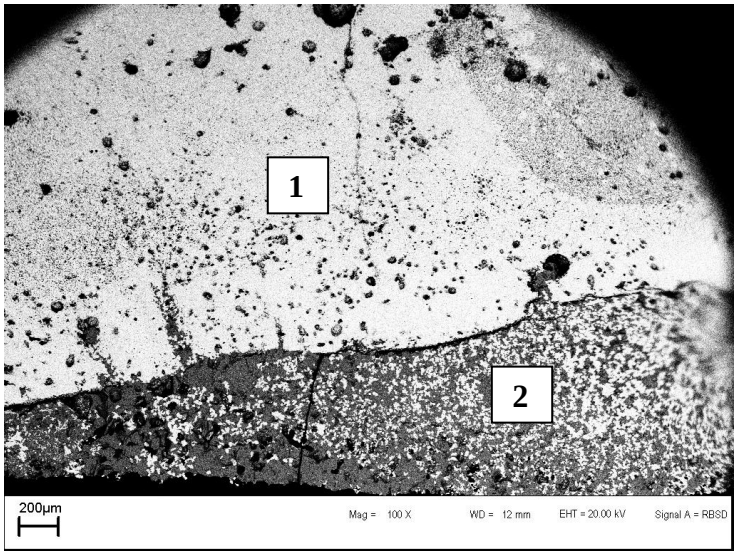


Figure 5.47. SEM-BSE image of nominal $W_{25}:C_{25}:Co_{30}:Mn_{20}$ (at.%) in annealed condition, showing overall view of the sample with finer [1] and coarser areas [2]: ~W_2C (light) and dark (Mn).

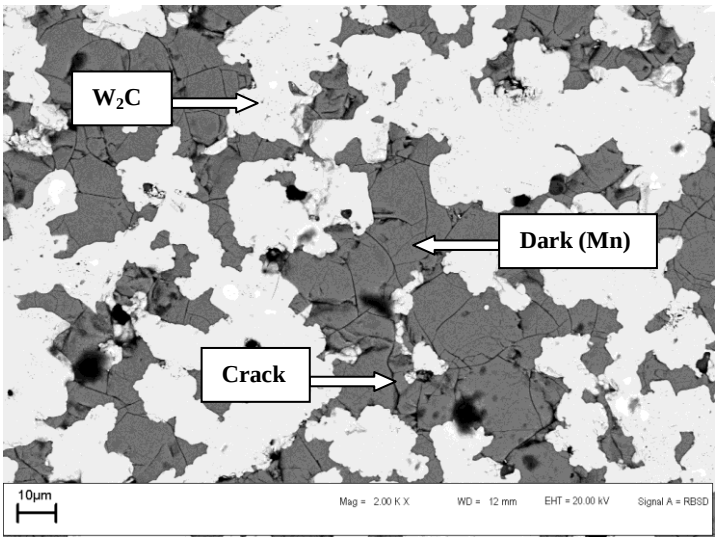


Figure 5.48. SEM-BSE image of nominal $W_{25}:C_{25}:Co_{30}:Mn_{20}$ (at.%) in annealed condition, showing with cracks in the dark phase: ~W_2C (light) and dark (Mn).

EDX readings were taken at the coarser area, since the regions in the fine area were less than 3µm across. These are given in Table 5.40.

The carbon composition in the overall was higher in the annealed than the as-cast sample (41.8 ± 1.3 at.% and 29.0 ± 0.9 at.%), the tungsten compositions were more similar in both as-cast and annealed samples (20.3 ± 0.5 at.% and 22.9 ± 0.3 at.% respectively in the

annealed and as-cast samples). The manganese content was much higher in the as-cast sample than was found the annealed sample.

Carbon contents were generally higher in the annealed sample than in the as-cast sample, except for the light phase, where it was almost 7 at.% less than in the as-cast sample. The cobalt contents were much higher in the annealed sample than the as-cast sample, especially in the matrix.

Phase description	**W**	**C**	**Mn**	**Co**	**Phase deduced**
Higher carbide proportion					
Overall	23.9 ± 0.7	38.0 ± 2.8	19.5 ± 0.8	18.6 ± 1.1	-
Lower carbide proportion					
Overall	20.2 ± 0.2	41.4 ± 1.2	19.4 ± 0.7	19.0 ± 1.0	-
Light	26.2 ± 1.8	32.8 ± 2.0	14.0 ± 0.9	22.0 ± 1.0	~W_2C
Medium	1.3 ± 0.1	24.2 ± 1.8	41.7 ± 0.6	32.8 ± 1.1	(βMn)

Table 5.40. EDX phase analysis of nominal W_{25}:C_{25}:Mn_{25}:V_{25} in annealed condition using pre-loaded standards (done at NMISA).

Figure 5.49 shows the XRD pattern for the annealed sample W_{25}:C_{25}:$Co_{12.5}$:$Mn_{37.5}$, and XRD identified ~W_2C and (βMn). The peaks were sharp and there was a low background. The as-cast sample had fewer peaks than the annealed. The peaks were better matched in the as-cast samples than in the annealed sample. There were some unmatched XRD peaks in the annealed sample and these are given in Table 5.41.

Peak No	**2θ (degree)**	**d-spacing (Å)**	**Relative intensity (%)**
1	20.68	4.29	7.13
2	21.82	4.07	4.60
3	25.64	3.47	4.37
4	34.98	2.56	0.37
5	35.97	2.49	0.18
6	36.66	2.45	6.09.
7	41.26	2.18	20.75
8	41.98	2.15	4.00
9	45.57	1.98	2.39
10	50.84	1.79	1.06

Table 5.41. Unidentified XRD peaks in nominal W_{25}:C_{25}:$Co_{12.5}$:$Mn_{37.5}$ (at.%) in annealed condition.

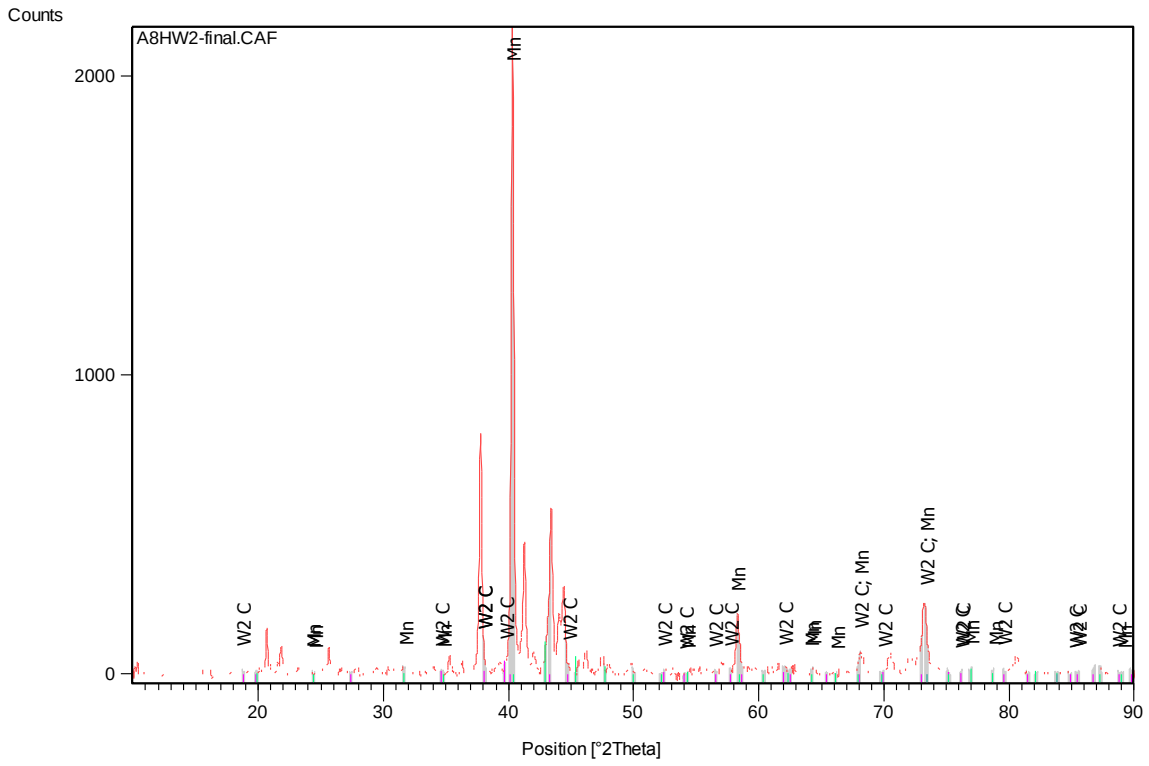


Figure 5.49. XRD pattern nominal W_{25}:C_{25}:$Co_{12.5}$:$Mn_{37.5}$ (at.%) in the annealed condition, showing ~W_2C and (Mn).

5.2.7 Nominal W_{25}:C_{25}:$Cu_{42.5}$:$Ni_{7.5}$ (at.%)

The W_{25}:C_{25}:$Cu_{42.5}$:$Ni_{7.5}$ (at.%) sample after annealing for 168 hours at 1000°C showed different portions of light carbide phase, indicating inhomogeneity was retained from the as-cast structure (Figure 5.50). The sample had two single phase regions, the dark (Cu,Ni) phase (labelled 2 in Figure 5.50) and a ~W_2C light phase (labelled 1 in Figure 5.50).

There were three different regions of the two phases with different carbide distributions. The part with higher proportion of the carbide had a dark interdendritic phase (labelled 3 in Figure 5.50) which was less than 3µm across. Only a few measurements were taken to observe the difference exhibited. The dark matrix in the two-phase regions (labelled 3 in Figure 5.50) was believed to be same as the dark single phase (Cu,Ni) (labelled 2 in Figure 5.50). The other small two-phase regions (labelled 4 and 5 in Figure 5.50) showed a similar trend, indicating light carbide dendrites with a (Cu,Ni) solid solution. The microstructure of the annealed sample was similar to the as-cast.

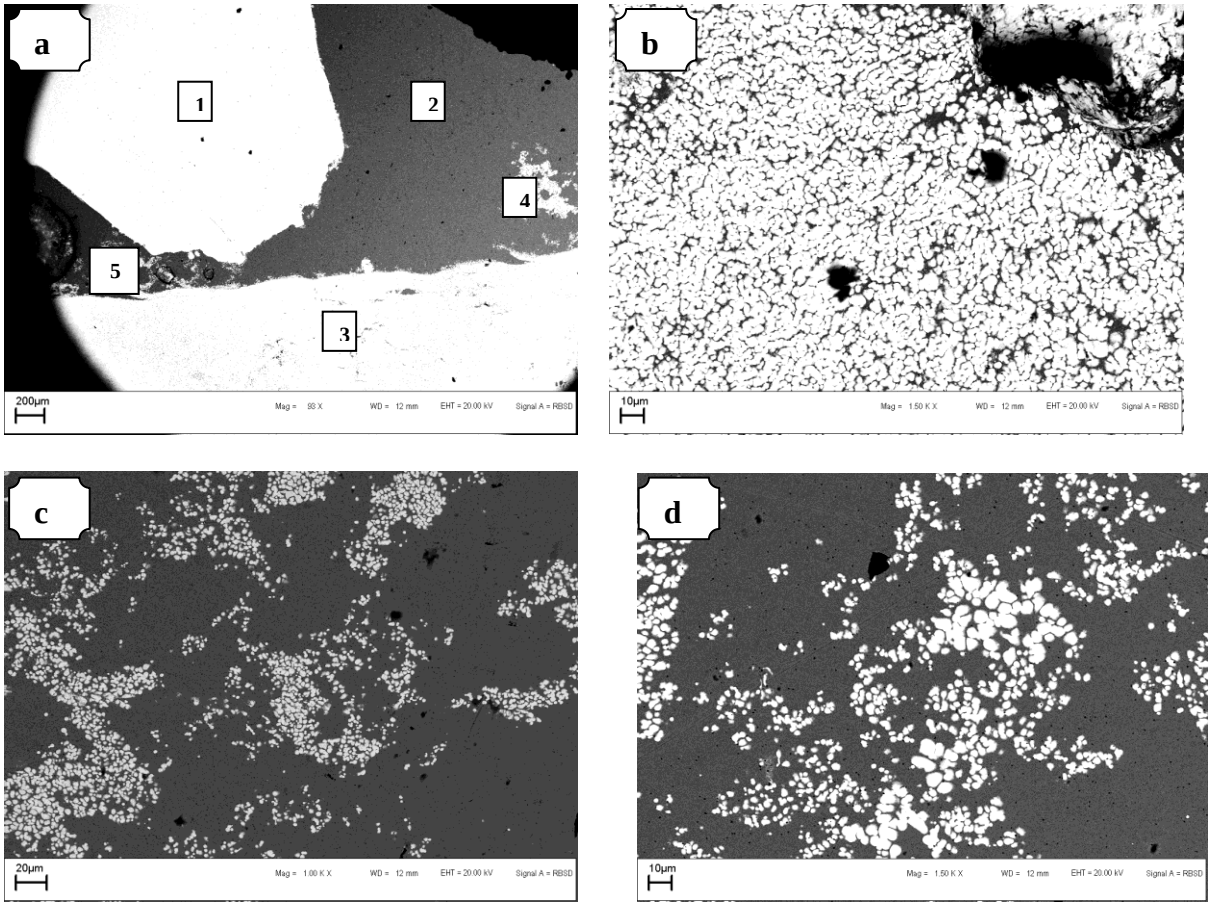


Figure 5.50. BSE-SEM images of nominal W_{25}:C_{25}:$Cu_{42.5}$:$Ni_{7.5}$ (at.%) in annealed condition showing: a) overview of the sample with single ~W_2C [1] and (Cu,Ni) [2], two-phase region with higher carbide [3] and the lower carbide two-phase regions [4] and [5], b) higher magnification of the denser carbide area [3], c) higher magnification of the less dense area with (~W_2C and (Cu,Ni)) [4], and d) two-phase region [5].

Table 5.42 gives the phase analyses of the sample. One overall EDX analyses was taken at the region labelled 5 in Figure 5.50a. Large errors were recorded in the portion labelled 3 in Figure 5.50a and b, this was because the phases were too small to be analysed accurately. There was some free tungsten in the as-cast, but was not in the annealed sample.

The overall compositions in the lower carbide areas (labelled 4 and 5 in Figure 5.50) were almost similar to the bulk of the composition, being copper. The overall composition in the higher carbide proportions regions in the annealed and as-cast samples were different. Carbon (37.7 ± 0.2 at.%) was the highest in the annealed sample, while tungsten was the highest in the as-cast (51.8 ± 3.5 at.%). The light phases were also different in both samples; the composition were 41.0 ± 7.1 at.% for tungsten, 50.8 ± 7.1 at.% for carbon, 6.3 ± 3.2 at.% for copper and 1.9 ± 0.7 at.% for nickel for the annealed sample and appeared to be ~WC, but the

XRD pattern had no major peak for WC and could indicate over estimation of the carbon. On the other hand, the as-cast composition for the light phase were 87.1 ± 0.8 at.% tungsten, 10.5 ± 1.4 at.% low carbon, 2.4 ± 1.3 at.% copper and no nickel.

Compositions were also different in dark single phase, (Cu,Ni). Tungsten was 0.27 ± 0.03 at.% and 26.7 ± 1.9 at.% carbon in the annealed sample, but tungsten and carbon were 0.0 ± 0.0 at.% in the as-cast. Both samples had copper as the major component. EDX analyses for annealed and as-cast samples were done at NMISA (analysed with pre-loaded standards) and UB (with standards, the most accurate analysis) respectively.

Phase description	**W**	**C**	**Cu**	**Ni**	**Phase deduced**
Light single phase ([1] in Figure 5.50)					
Overall	55.7 ± 0.4	44.3 ± 0.2	-	-	-
Single Dark phase ([2] Figure 5.50)					
Overall	0.3 ± 0.03	26.6 ± 1.9	60.0 ± 1.7	13.1 ± 0.2	-
Lower proportion carbide ([5] Figure 5.50)					
Overall	15.0	27.8	47.1	10.1	-
Lower proportion carbide ([4] Figure 5.50)					
Overall	10.7 ± 0.3	26.5 ± 0.3	50.9 ± 0.9	11.9 ± 0.2	-
Higher proportion carbide ([3] Figure 5.50)					
Overall	29.1 ± 0.6	37.7 ± 0.2	27.7 ± 0.1	5.5 ± 0.8	-
Light	41.0 ± 7.1	50.8 ± 7.1	6.3 ± 3.2	1.9 ± 0.7	~W_2C
Dark	1.4 ± 0.5	31.4 ± 1.4	55.8 ± 0.4	11.4 ± 0.1	(Cu,Ni)

Table 5.42. EDX phase analyses of the sample W_{25}: C_{25}:$Cu_{42.5}$:$Ni_{7.5}$ (at.%) in annealed condition using pre-loaded standards (done at NMISA).

XRD (Figure 5.51) confirmed the presence of (Cu) and ~W_2C. The pattern looked good and had sharp peaks. Copper was used in matching for (Cu,Ni) since the ICDD database had no data for (Cu,Ni). The peaks were narrower and had much higher intensities in the annealed sample than in the as-cast. They both had an unmatched peak at the same position, which was given in Table 5.43.

Peak No	**2θ (degree)**	**d-spacing (Å)**	**Relative intensity (%)**
1	36.35	3.44	1.86

Table 5.43. Unidentified XRD peak in nominal W_{25}:C_{25}:$Cu_{42.5}$:$Ni_{7.5}$ (at.%) in annealed condition.

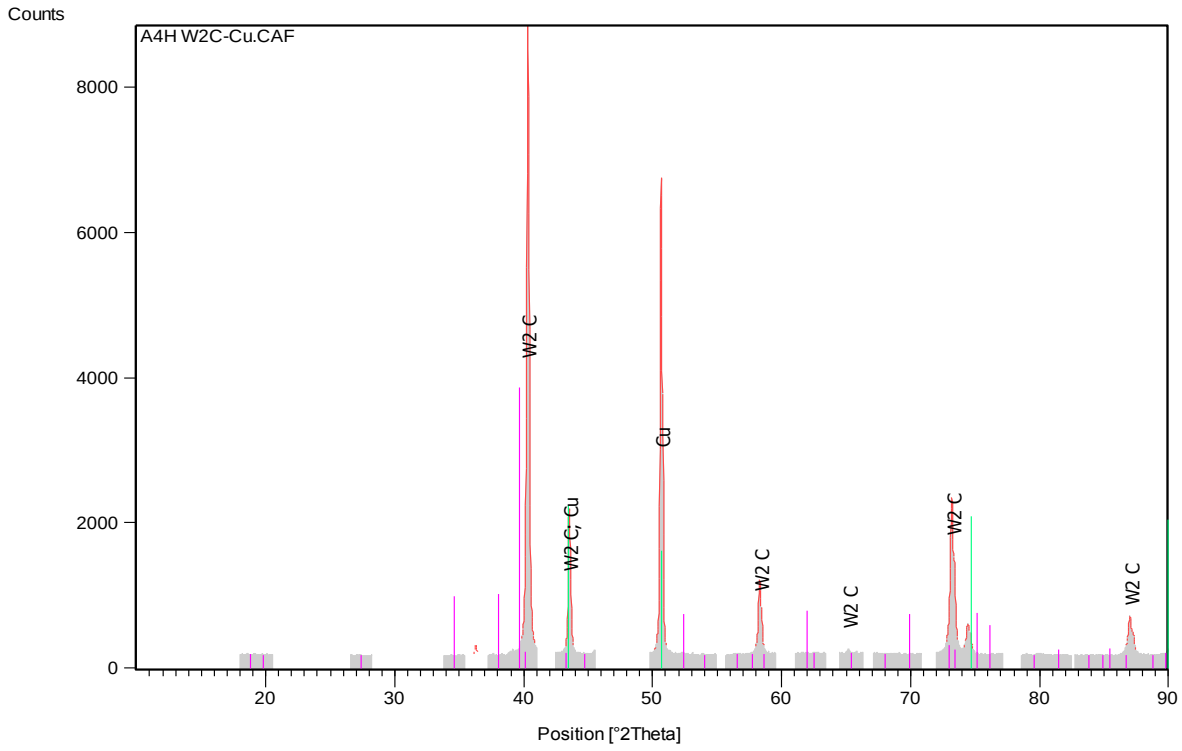


Figure 5.51. XRD pattern nominal W_{25}:C_{25}:$Cu_{42.5}$:$Ni_{7.5}$ (at.%) in annealed condition showing (Cu) and ~W_2C peaks.

5.2.8 Nominal W_{25}: C_{25}: Cu_{40}: Ni_{10} (at.%)

The annealed W_{25}:C_{25}:Cu_{40}:Ni_{10} (at.%) sample showed two regions with high proportions of the light carbide phase (labelled 1 in Figure 5.52), while there were other regions of low proportions of carbide phase (Figure 5.52, labelled 2). The was a single phase area comprising (Cu,Ni) (labelled 3 in Figure 5.52). The areas with high carbide proportions had two phases: light regions which looked like densely packed possibly unmelted carbide grains, with the dark phase between them (Figure 5.53). Close to the label 3 was a small portion which looked like it did not solidify the same as the surrounding regions. There was very little difference between the annealed sample and the as-cast.

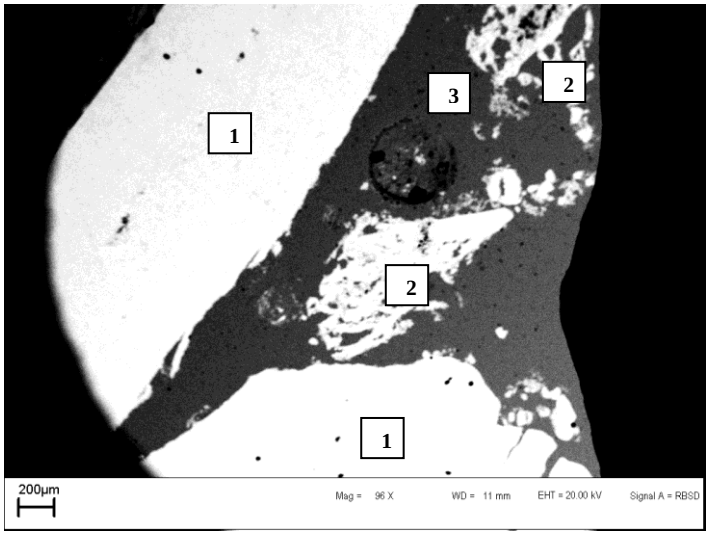


Figure 5.52. BSE-SEM image of nominal $W_{25}:C_{25}:Cu_{40}:Ni_{10}$ (at.%) in the annealed condition showing the different regions.

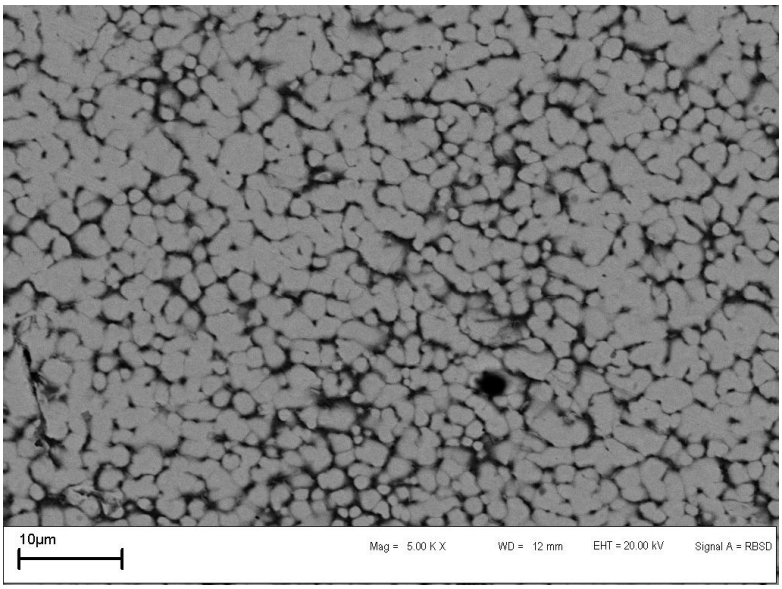


Figure 5.53. BSE-SEM image of nominal $W_{25}:C_{25}:Cu_{40}:Ni_{10}$ (at.%) in the annealed condition, showing light ~W_2C phase with dark (Cu,Ni) matrix in the high carbide proportion region.

The less dense carbide areas also had two phases; dark and light grains which were probably (Cu,Ni) and ~W_2C (Figure 5.54a). There was a single (Cu,Ni) phase with few carbides and which showed porosity (Figure 5.54b).

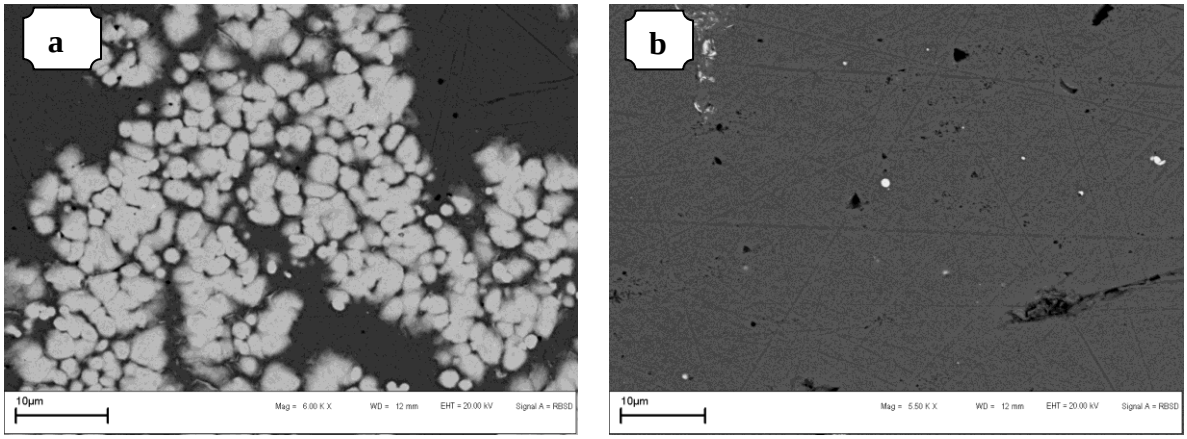


Figure 5.54. BSE-SEM image of nominal W_{25}:C_{25}:Cu_{40}:Ni_{10} (at.%) in annealed condition: a) light ~W_2C and dark (Cu,Ni), b) single dark phase (Cu,Ni) with few carbides and porosity.

Table 5.44 gives the phase analyses of nominal W_{25}:C_{25}:Cu_{40}:Ni_{10} (at.%) in the annealed condition. The errors were slightly higher in the light phase and the region labelled 1 in Figure 5.52. This was due to the smaller sizes of the light phase and probably uneven distribution of the phases in region 1. The carbide looked like ~WC from the EDX analyses, but XRD showed it was ~W_2C. This could be overestimation of the carbon, which was also seen in other samples.

The overalls of the high carbide regions in as-cast sample (labelled A and B in Figure 5.20) were different from those of the annealed sample (labelled 1 in Figure 5.52). The dark single phase (Cu,Ni) was similar in both, but contained a small amount of dissolved tungsten in the annealed sample. The dark (Cu,Ni) matrix in the two different two-phase regions were also very similar, with high carbon contents. The light phases were different in both samples, the carbon content was very high in the annealed sample, while it was very low in the as-cast. The as-cast and annealed samples analyses were done at UB (analysed with standards derived from elements from which the samples were made) and NMISA (analysed with pre-loaded standards) respectively.

XRD identified (Cu) with the peaks shifting slightly. The second phase identified by XRD was ~W_2C. The peaks were sharp and clear (Figure 5.55). Copper standards were employed in matching the (Cu,Ni), due to latter's absence of in the ICDD database [1991ICDD]. The peaks in the annealed sample were broader and with higher intensity. The copper peaks were more shifted (lower 2θ values), indicating more dissolved elements, which agrees with EDX.

Phase description	W	C	Cu	Ni	Phase deduced
Dark single phase Region ([3] in Figure 5.52)					
Overall	0.2 ± 0.4	23.3 ± 0.3	68.2 ± 0.1	8.3± 0.2	-
Higher carbide proportion ([1] in Figure 5.52)					
Overall	40.2 ± 1.2	43.0 ± 4.8	14.7 ± 2.9	2.1 ± 0.5	-
Lower carbide proportion ([2] in Figure 5.52)					
Overall	8.4 ± 0.5	50.2 ± 0.3	36.7 ± 0.1	4.7 ± 0.2	-
Light	42.6 ± 1.2	44.7 ± 1.2	8.2 ± 0.3	1.5 ± 0.2	~W_2C
Dark	0.2 ± 0.1	24.0 ± 0.3	67.7 ± 0.3	8.1 ± 0.1	(Cu,Ni)

Table 5.44. EDX phase analyses of nominal W_{25}:C_{25}:Cu_{40}:Ni_{10} (at.%) in annealed condition using pre-loaded standards (done at NMISA).

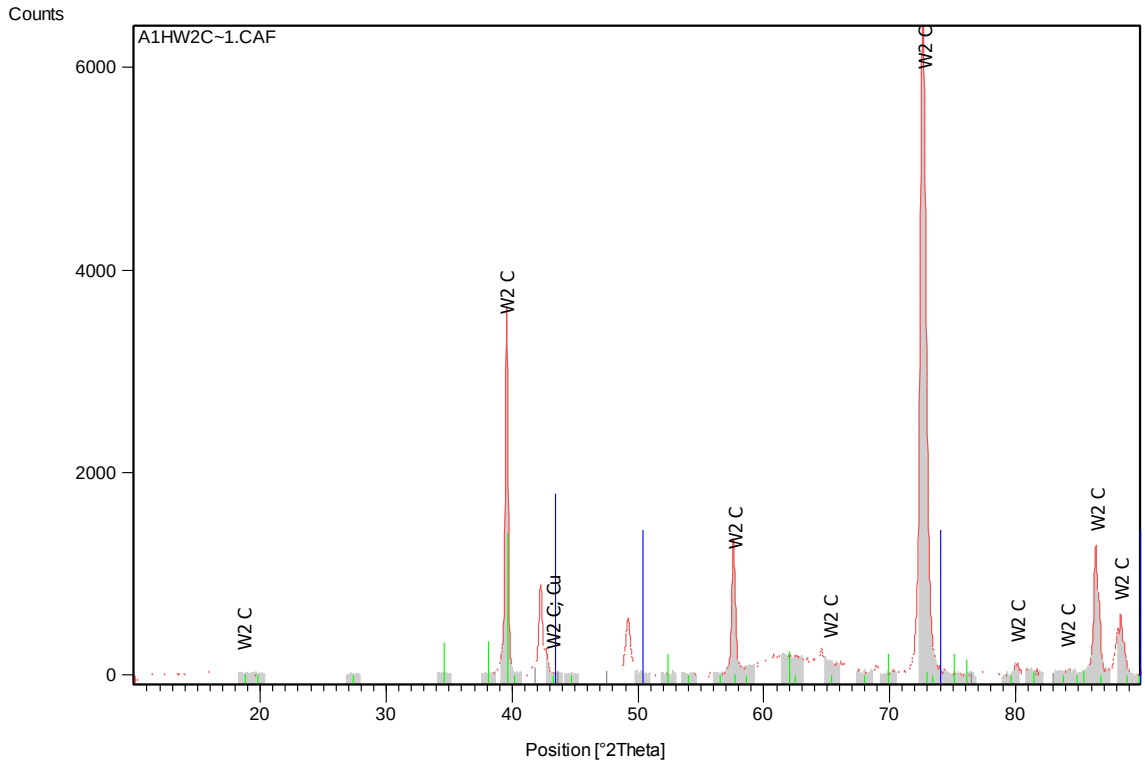


Figure 5.55. XRD pattern nominal W_{25}:C_{25}:Cu_{40}:Ni_{10} (at.%) in annealed condition, showing ~W_2C and (Cu) peaks.

5.2.9 Nominal W_{25}:C_{25}:Mn_{25}:V_{25} (at.%)

The annealed sample W_{25}:C_{25}:Mn_{25}:V_{25} (at.%) (Figure 5.56b) had two different proportions of the light dendrite phase, and looked similar to the as-cast sample (Figure 5.24), but was heavily cracked. The sample had three phases in the small area: light dendrites with a dark matrix and a medium dark phase, and had some porosity (Figure 5.56c). The medium dark phase was mostly found at the edges of the light dendrites (Figure 5.56b). The more dense carbide area had two phases, the dark interdendritic phase was smaller than 3μm across (and so could not be analysed accurately) and the light dendrites.

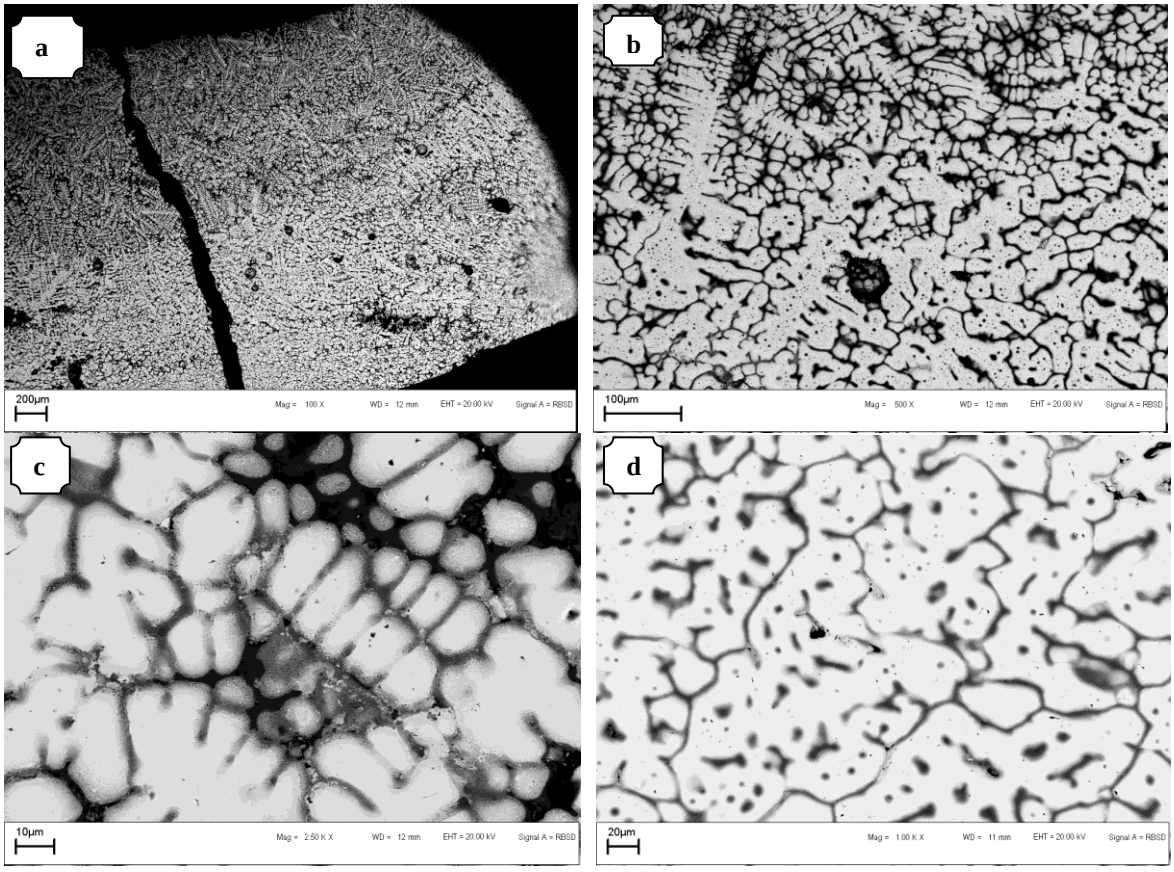


Figure 5.56. SEM-BSE images of nominal W_{25}:C_{25}:Mn_{25}:V_{25} (at.%) in annealed condition, a) overall view, b) varying proportions of carbide (top and bottom), c) less dense area with light dendrites, medium phase and porosity (dark contrast), and d) more dense area with light and dark interdendritic phase.

Table 5.45 gives EDX analyses of the annealed sample. A small amount of manganese was left after arc-melting the sample. The errors were all reasonable, except for the dark phase in

the densely packed carbide region; the dark interdendritic phase which was too small, and few measurements were taken, having large errors. The light ~V_2C had no manganese in both less dense and dense carbide proportion regions.

The overalls in the annealed and the as-cast samples looked similar, even though the as-cast contained no manganese. EDX results were similar for the light phase for the different regions in the annealed; the compositions were different from the as-cast sample, except for vanadium, which looked similar. The tungsten compositions in the matrix were similar, but the annealed sample had higher carbon than the as-cast sample, whereas the as-cast sample had slightly higher vanadium content than in the annealed sample. There was an apparent medium contrast phase present in the annealed sample which was not seen in the as-cast sample. However, the medium contrast phase in the annealed sample was found to be the same phase as the light phase, with a slightly different composition. The as-cast sample was analysed at UB (analysed without standards) while the annealed was done at NMISA (analysed with pre-loaded standards).

The XRD pattern (Figure 5.57) for sample W_{25}:C_{25}:Mn_{25}:V_{25} (at.%) looked poor with few high intensity peaks. XRD confirmed (V) and identified ~V_2C. The vanadium peaks were shifted from the pure values and the peaks were broad, both indicating a cored solid solution. The XRD pattern for the annealed sample looked very similar to the as-cast sample, but had the peak splitting at $2\theta = 60°$ and around 76°. There was an unmatched peak (Table 5.46).

Phase description	**W**	**C**	**Mn**	**V**	**Phase deduced**
Lower carbide proportion region					
Overall	20.0 ± 4.6	36.6 ± 5.5	0.3 ± 0.2	43.1 ± 3.7	-
Light	31.1 ± 0.9	36.3 ± 0.6	-	32.6 ± 0.7	~V_2C
Medium	29.7 ± 2.7	38.9 ± 3.7	-	31.4 ± 1.0	~V_2C
Dark	5.4 ± 0.4	24.6 ± 0.8	0.1 ± 0.1	69.9 ± 0.8	(V)
Higher carbide proportion region					
Overall	26.6 ± 0.5	25.4 ± 0.9	0.2 ± 0.2	47.8 ± 0.7	-
Light	28.7 ± 1.2	36.2 ± 0.8	-	35.1 ± 0.6	~V_2C
Dark	6.1 ± 1.3	25.3 ± 1.6	0.3 ± 0.2	68.3 ± 1.1	(V)

Table 5.45. EDX phase analysis of nominal W_{25}:C_{25}:Mn_{25}:V_{25} (at.%) in annealed condition using pre-loaded standards (done at NMISA).

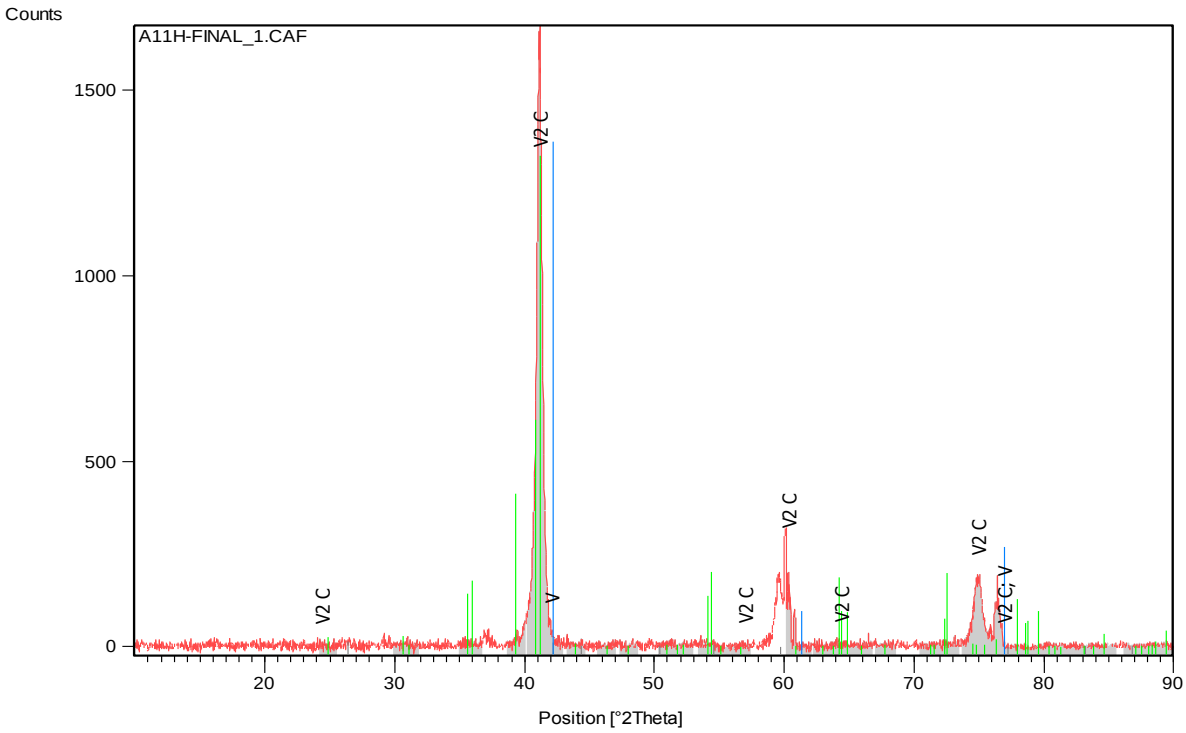


Figure 5.57. XRD pattern of nominal W_{25}:C_{25}:Mn_{25}:V_{25} (at.%) in annealed condition showing ~V_2C and (V).

Peak No	2θ (degree)	d-spacing (Å)	Relative intensity (%)
1	60.02	4.28	9.33

Table 5.46. Unidentified XRD peaks in nominal W_{25}:C_{25}:Co_{30}:Mn_{20} (at.%) in annealed condition.

5.2.10 Nominal W_{25}:C_{25}:Cu_{40}:Zn_{10} (at.%)

The sample annealed for 168 hours at 1000ºC was mainly a single phase with a very small patch of light phase (Figure 5.58a). Round porosity was seen a higher magnification near a small light carbide patch, near a "bubble" (Figure 5.58b and c), and was more noticeable in the annealed sample. Close to the edge of the sample was another area with some light phase, but the light phase was very small (less than 3µm across) (Figure 5.58c and d) and was not suitable for meaningful EDX analysis.

Table 5.47 gives the phase analyses of the annnealed W_{25}:C_{25}:Cu_{40}:Zn_{10} (at.%) sample. The sample still had a very small amount of Zn. The overall for the dark (Cu,Zn) region was differnt in the annealed sample than in the as-cast sample; the carbon content was very high in the annealed sample (33.3 ± 0.6 at.%) and had a small amount of tungsten, whereas no carbon or tungsten were found in the as-cast sample. The two-phase regions differed in compositions; the annealed sample had a high carbon content, while the as-cast had higher tungsten content.

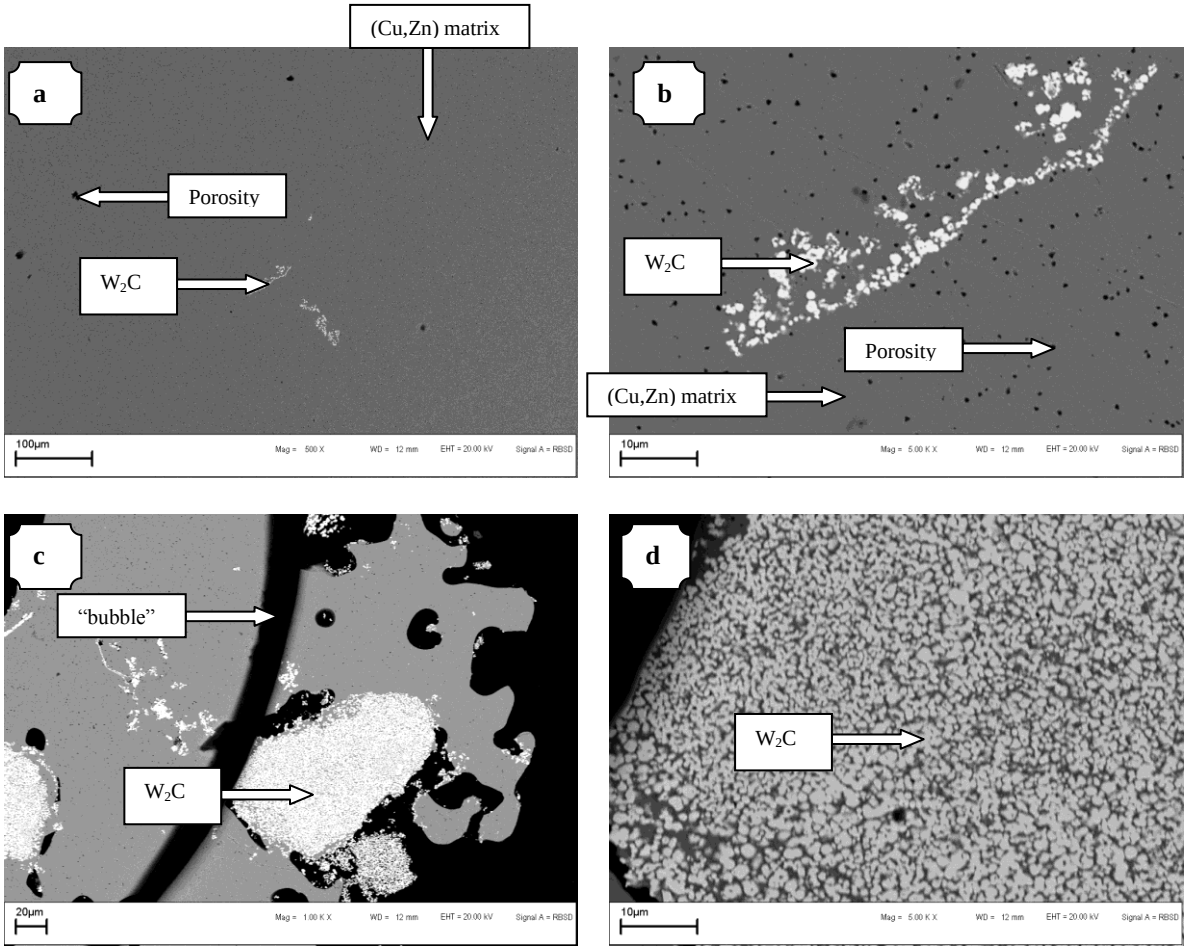


Figure 5.58. SEM-BSE images of nominal annealed W_{25}:C_{25}:Cu_{40}:Zn_{10} (at.%) showing: a) a single phase which formed the bulk of the alloy, b) porosity and the small amount of carbide phase, c) light carbide phase at the edge of the sample with a "bubble", and d) a portion at the edge with light phase and dark matrix.

Figure 5.59 shows the XRD pattern for the nominal W_{25}:C_{25}:Cu_{40}:Zn_{10} (at.%) sample in the annealed condition; the peaks were sharp and looked good. The single phase region was confirmed to be (Cu,Zn), while the carbide was found to be ~W_2C.

The XRD patterns for the as-cast and the annealed samples were fairly similar, but the annealed sample had lower intensity peaks.

Phase description	W	C	Cu	Zn	Phase deduced
Single Phase Region					
Dark	0.1 ± 0.0	33.3 ± 0.6	63.7 ± 0.6	2.9 ± 0.2	(Cu,Zn)
Edge of Sample (with carbide)					
Overall	16.0	60.8	22.4	0.8	-

Table 5.47. EDX phase analyses of the annnealed W_{25}:C_{25}:Cu_{40}:Zn_{10} sample (at.%) using pre-loaded standards (done at NMISA).

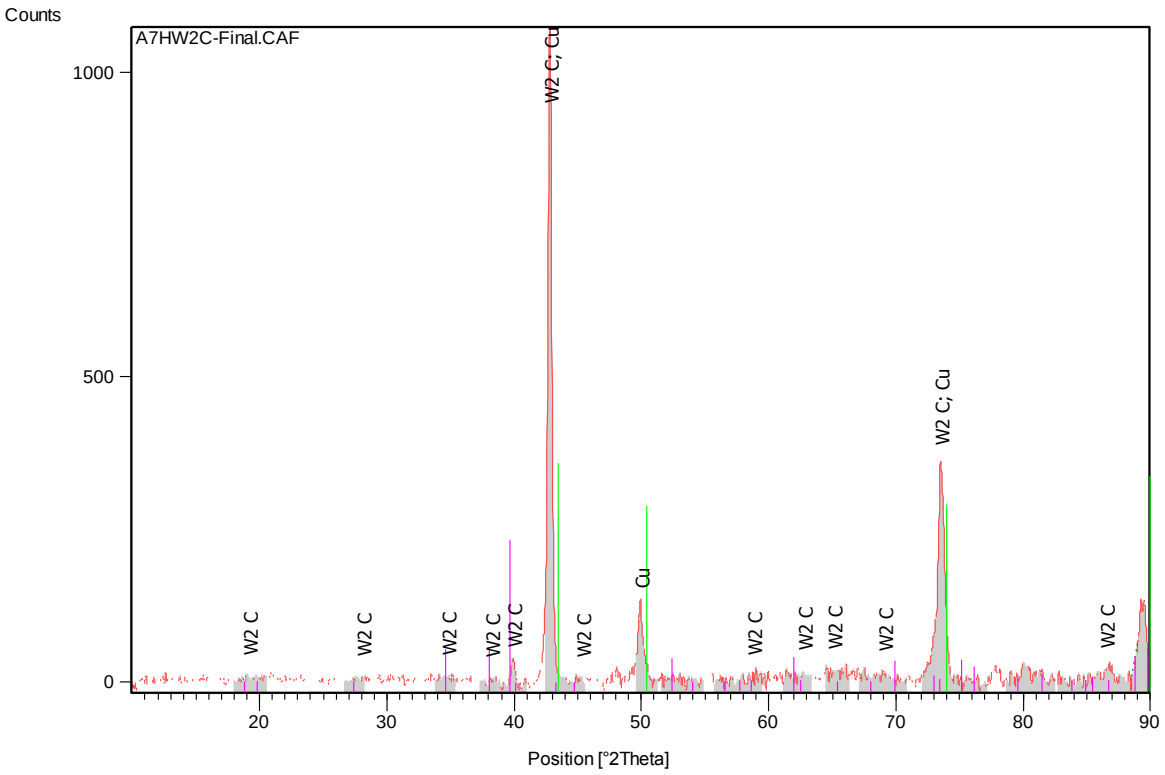


Figure 5.59. XRD pattern nominal W_{25}:C_{25}:Cu_{40}:Zn_{10} (at.%) in annealed condition, showing ~W_2C and (Cu) peaks.

5.2.11 Nominal W_{25}:C_{25}:Cu_{45}:Zn_5 (at.%)

The W_{25}:C_{25}:Cu_{45}:Zn_5 (at.%) sample (shown in Figure 5.60) was found to be a single phase after annealing at 1000ºC for 168 hours. The sample was also porous, and comprised mainly carbide, with a trace amount of copper, but had no zinc. The annealed sample did not look

very different from the as-cast sample, but had less porosity, which was more rounded. There was a dark blob which could be a stain.

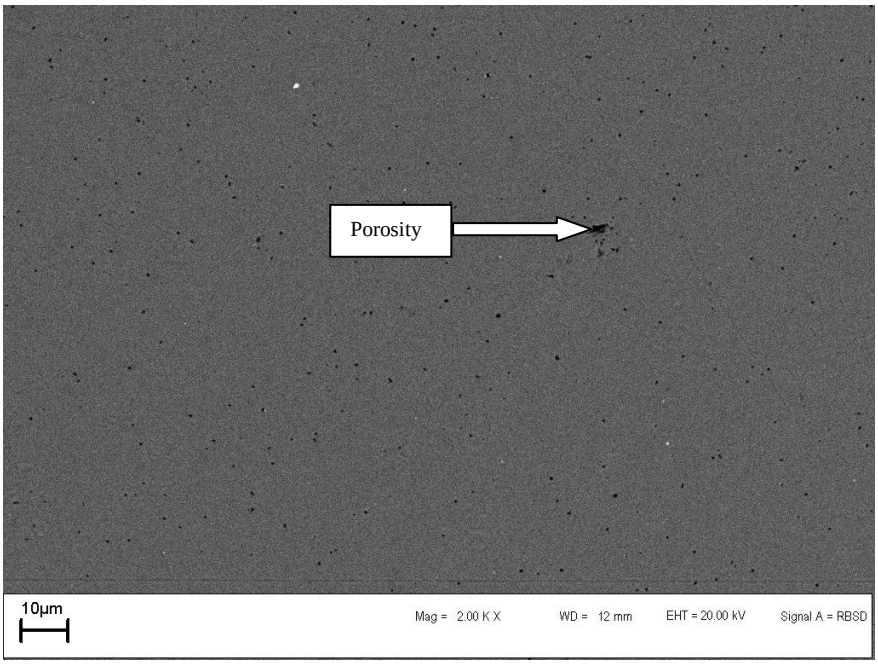


Figure 5.60. SEM-BSE image of nominal annealed W_{25}:C_{25}:Cu_{45}:Zn_5 (at.%) showing the single carbide phase with porosity.

Table 5.48 gives phase analyses of the sample W_{25}:C_{25}:Cu_{45}:Zn_5 (at.%) in the annealed condition. The EDX results looked like ~WC, but XRD had no major peaks for ~WC. The annealed sample had a small amount of copper, which was not found in the as-cast sample. This was because the sample did not melt properly on sample preparation and the larger portions were selected for analysis. The EDX analyses were taken from UB (analysed with no standards) and NMISA (analysed with pre-loaded standards) for as-cast and annealed samples respectively.

Figure 5.61 shows the XRD pattern obtained for the sample. XRD matched better with ~W_2C than ~WC. There were also unmatched peaks (Table 5.49). Although there was a trace amount of copper found by EDX, and ICDD data for Cu did not match any peak in the pattern. This is not surprising because at least 4% of a phase is needed to produce a noticeable XRD signal. Also, such a small amount of copper would be dissolved in another phase, here ~W_2C.

The XRD pattern looked similar but the peaks were broader in the annealed sample and had lower intensity than in the as-cast sample.

Phase description	W	C	Cu	Zn	Phase deduced
Single Phase Region					
Overall	50.4 ± 1.3	48.8 ± 1.0	0.8 ± 0.0	-	W_2C

Table 5.48. EDX phase analyses of the sample W_{25}:C_{25}:Cu_{45}:Zn_5 (at.%) in the annealed condition using pre-loaded standards (done at NMISA).

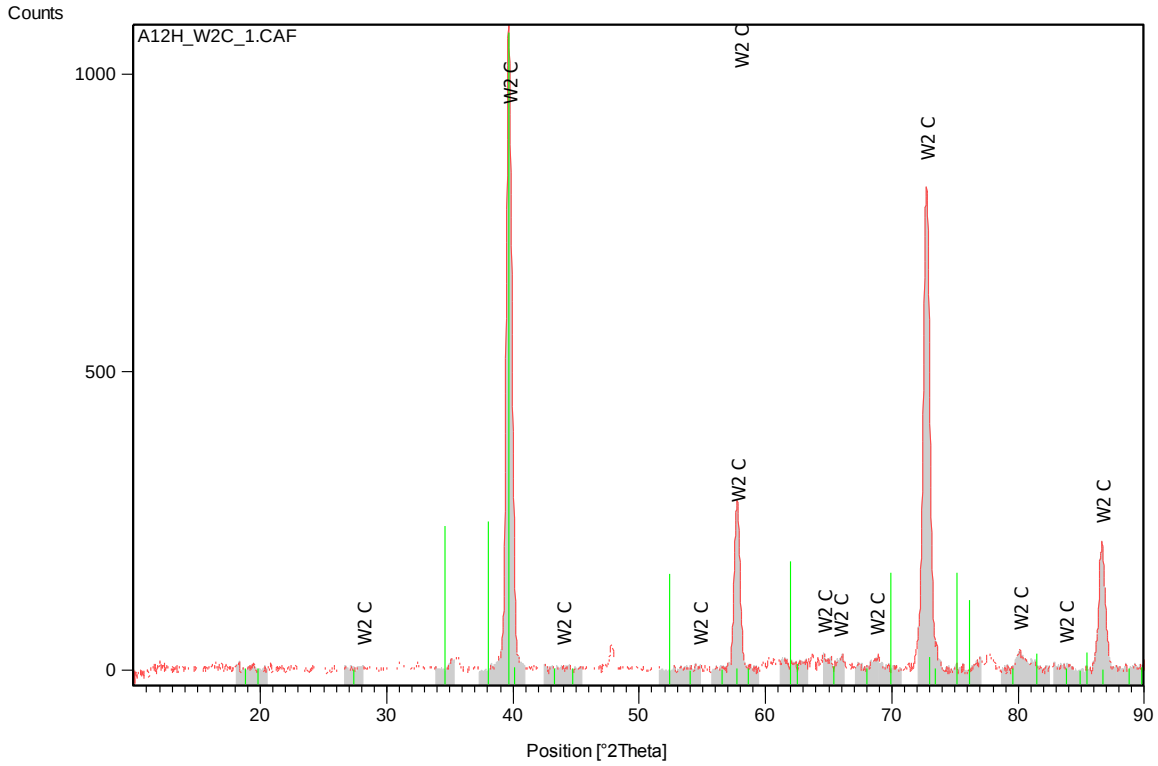


Figure 5.61. XRD pattern nominal W_{25}:C_{25}:Cu_{45}:Zn_5 (at.%) in annealed condition showing ~W_2C and some small unidentified peaks.

Peak No	2θ (degree)	d-spacing (Å)	Relative intensity (%)
1	35.61	4.21	5.45
2	47.79	5.01	9.33
3	77.70	4.06	5.43

Table 5.49. Unidentified XRD peaks in nominal W_{25}:C_{25}:Cu_{45}:Zn_5 (at.%) in annealed condition.

5.2.12 Nominal W_{25}:C_{25}:$Cu_{47.5}$:$Mn_{2.5}$ (at.%)

The nominal sample W_{25}:C_{25}:$Cu_{47.5}$:$Mn_{2.5}$ (at.%) after annealling for 168 hours at 1000ºC still had three different regions as was seen in the as-cast sample. One of the regions was a single phase comprising (Cu,Mn) (labelled 3 in Figure 5.62). The single-phase region surrounded a two-phase region which was mainly light carbide particles (labelled 2 in Figure 5.62). The last portion was a two-phase region in the innermost part of the sample (1 in Figure 5.62).

Figures 5.63 and 5.64 show the two-phase regions of the sample labelled 1 and 2 in Figure 5.62. The light carbides in Figure 5.63 were mostly particles instead of dendrites, and were coarsened in the innermost region (Figure 5.63).

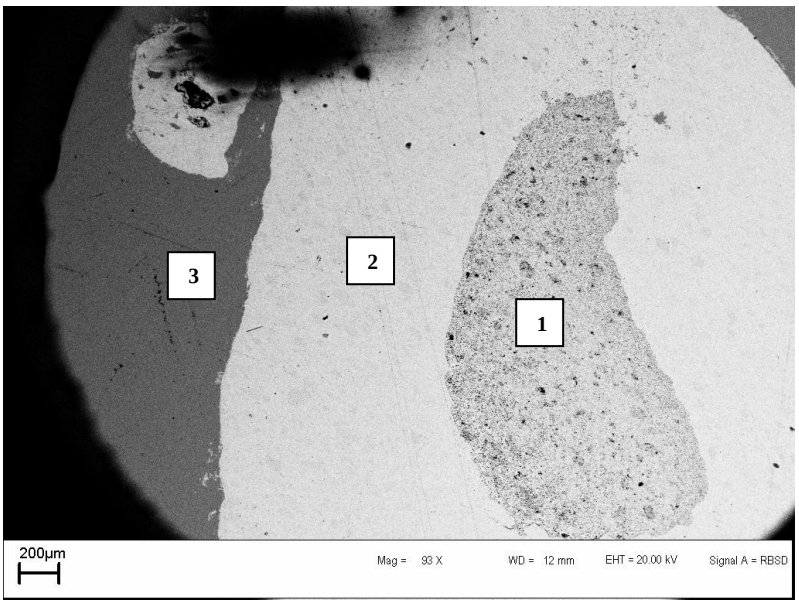


Figure 5.62. SEM-BSE image of nominal annealed W_{25}:C_{25}:$Cu_{47.5}$:$Mn_{2.5}$ (at.%) showing the three different areas in the sample: (Cu,Mn) [3], unmelted light carbide grain regions [2], and innermost two-phase region [1].

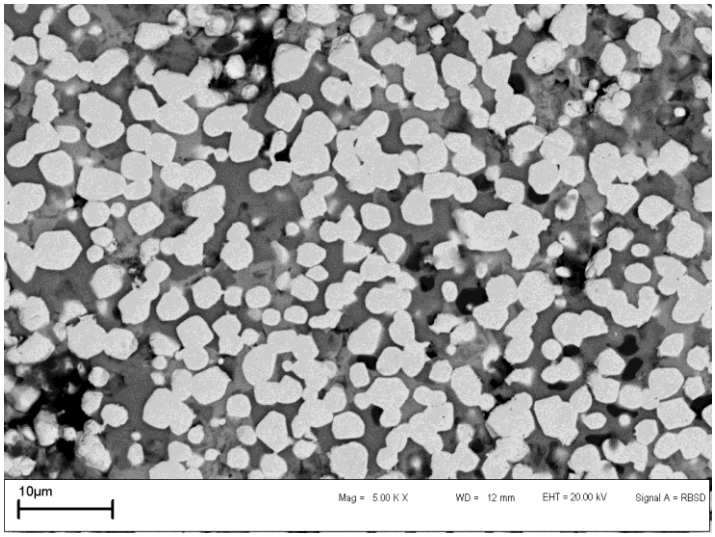


Figure 5.63. SEM-BSE image of nominal annealed W_{25}:C_{25}:$C_{47.5}$:$Mn_{2.5}$ (at.%) showing the innermost two-phase-region (labelled 1 in Figure .62).

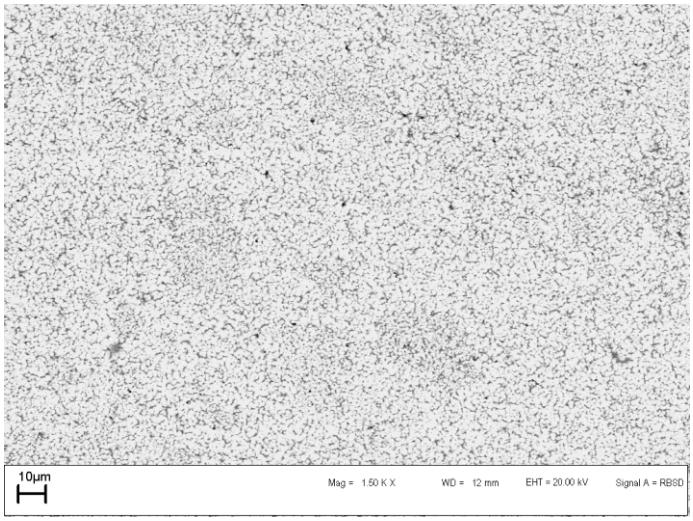


Figure 5.64. SEM-BSE image of nominal annealed W_{25}:C_{25}:$C_{47.5}$:$Mn_{2.5}$ (at.%) showing particles in middle two-phase-region (labelled 2 in Figure 5.62).

Table 5.50 gives phase analyses for nominal W_{25}:C_{25}:$Cu_{47.5}$:$Mn_{2.5}$ (at.%). Overall EDX analyses were taken from all the regions, rather than phase analysis due to the small particle sizes of the light phase (as shown in Figures 5.63 and 6.64). The dark single phase (Cu,Mn) region had no tungsten, while the innermost two-phase region also had no copper.

Phase description	W	C	Cu	Mn	Phase deduced
Single Phase Region (3 in Figure 5.62)					
Overall	-	19.1 ± 0.2	75.3 ± 1.4	5.6 ± 0.3	-
Two phase region (2 Figure 5.62)					
Overall	69.3 ± 0.6	12.8 ± 0.3	16.9 ± 0.8	1.0 ± 0.1	-
Two phase region (1 Figure 5.62)					
Overall	72.7 ± 0.2	15.2 ± 0.3	-	12.1 ± 0.5	-

Table 5.50. EDX phase analyses of the sample W_{25}:C_{25}:$Cu_{47.5}$:$Mn_{2.5}$ (at.%) in the annealed in condition using pre-loaded standards (done at NMISA).

Copper was used in matching for the dark (Cu,Mn) single phase region on the XRD (Figure 5.65), this was due to no (Cu,Mn) being in the database (ICDD). XRD identified the light phase as ~W_2C. The XRD patterns of the annealed and as-cast samples were very similar. A peak was not matched (Table 5.51).

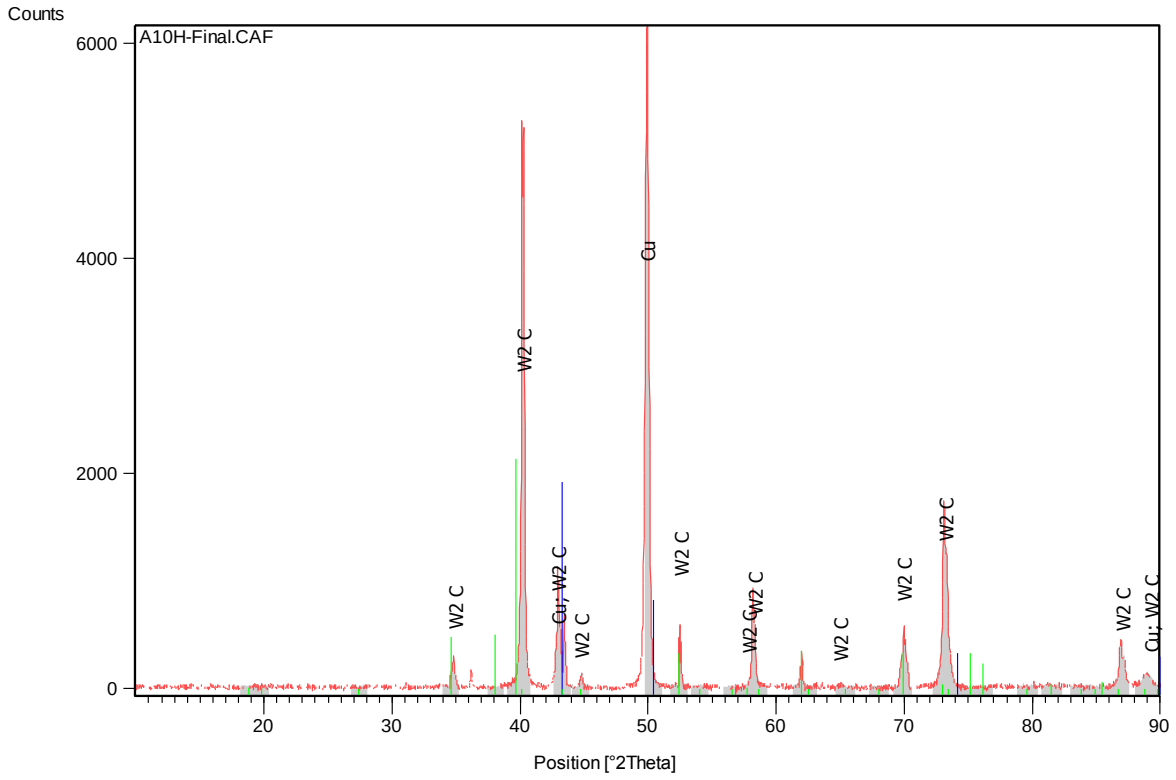


Figure 5.65. XRD pattern nominal W_{25}:C_{25}:$Cu_{47.5}$:$Mn_{2.5}$ (at.%) in annealed condition showing ~W_2C and (Cu) and unmatched peaks.

Peak No	2θ (degree)	d-spacing (Å)	Relative intensity (%)
1	36.24	4.28	9.33

Table 5.51. Unidentified XRD peaks in nominal $W_{25}:C_{25}:Cu_{47.5}:Mn_{2.5}$ (at.%) in annealed condition.

CHAPTER 6

CALCULATED RESULTS

6.1. Calculation of equilibrium phases

Thermo-Calc [2002And] uses internally-consistent thermodynamic datasets to carry out thermo-barometry and phase diagram calculations. Fundamentally, Thermo-Calc is a thermodynamic calculation program and it can be utilized to undertake a wide range of phase diagram calculations including *P-T* projections, *P-T, P-x* and *T-x* pseudo-sections,
compatibility diagrams μ-μ diagrams,
where:
P = Pressure,
T = Temperature,
x = Compositions, and
μ = Chemical potential.

In one way of representing data, the Thermo-Calc program shows the results as proportion diagrams where the proportions of each phase in the overall composition are plotted against the temperature. This is useful for multi-component systems, and the stabilities of the phases with temperature can be shown. These diagrams were calculated for each targeted composition of binder. Additionally, for each case, the phase compositions were calculated.

Two sets of calculations were done on the alloy compositions: the first set was the more realistic values to consider the replacement of cobalt, which was 10% composition binder. The second set calculated was for the 50% binder as studied experimentally. This was done to help interpret experimental results. (The experiments were done on 50:50 samples so that the phases could be more easily analysed, and the samples were easier to manufacture.)

6.1 90% Carbide-10% binder calculations

6.1.1 W_{45}:C_{45}:$Ni_{9.5}$:$V_{0.5}$ (at.%)

The calculated phase proportion diagram for nominal W_{45}:C_{45}:$Ni_{9.5}$:$V_{0.5}$ (at.%) is given in Figure 6.1. The stable phases in the diagram were FCC_A1#1, FCC_A1#2, MC_SHP and graphite. The graphite existed in the high temperature zone (above 2000°C) and solidified above 2600°C, likewise the MC_SHP phase solidified above 2600°C. The FCC_A#1 phase was stable over a temperature range below 800°C to 1400°C. This low temperature FCC_A1#1 was the last phase to emerge from the melt, and reached a maximum proportion on solidification.

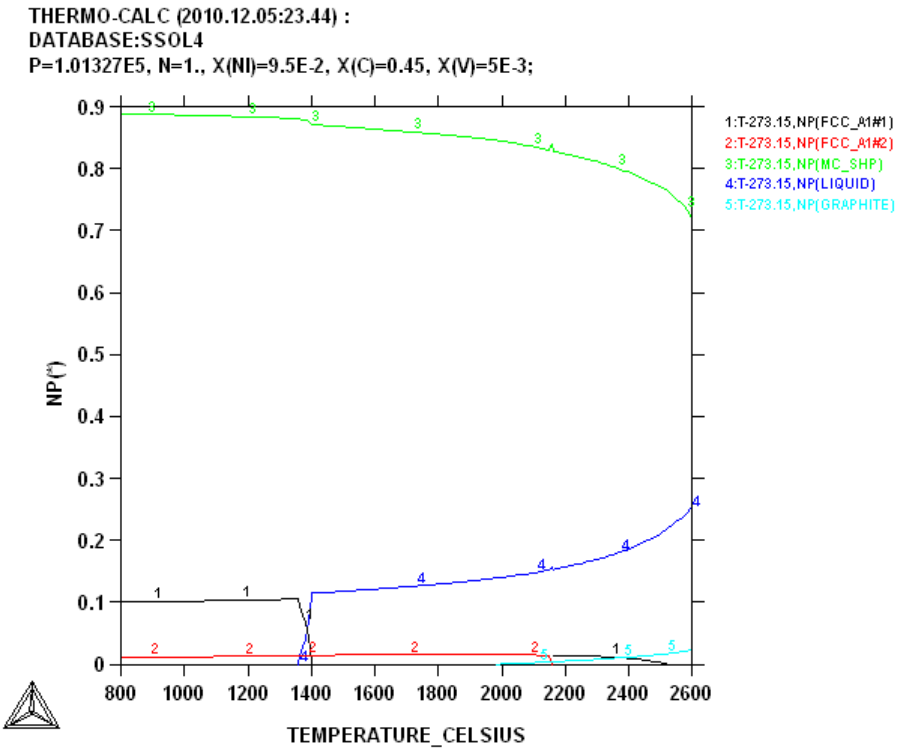


Figure 6.1. Phase proportion diagram of W_{45}:C_{45}:$Ni_{9.5}$:$V_{0.5}$ (at.%).

High temperature graphite and MC_SHP phases at 2600°C had proportions of ~2.6% and ~72.5% respectively. The graphite disappeared at 2000°C. The apparent high temperature FCC_A1#1 phase started forming at 2500°C and increased slightly to about ~1.5% at 1140°C, where it transformed to FCC_A1#2 and emerged again later at 1400°C. The FCC_A1#2 started forming at 1400°C and remained throughout the calculated temperature range. At 800°C, the FCC_A1#2 comprised 1.5% of the total alloy.

The MC_SHP phase (carbide), which formed the bulk of the alloy, increased from 72.5% at 2600°C to ~90.0% at 800°C. The summary of the property phase diagram for W_{45}:C_{45}:$Ni_{9.5}$:$V_{0.5}$ (at.%) is given in Table 6.1.

	Maximum stability (°C)	**Minimum stability (°C)**	**Maximum proportion**	**Minimum proportion**
FCC _A1#1	1400	<800	~0.10	0.00
FCC _A1#1	2500	1140	~0.01	0.000
FCC_A1#2	1150	<800	~0.01	~0.01
MC_SHP	>2600	<800	~0.89	~0.72
GRAPHITE	>2600	2000	~0.26	0.00

Table 6.1. Summary of phase proportions of W_{45}:C_{45}:$Ni_{9.5}$:$V_{0.5}$ (at.%).

Figure 6.2 shows composition of the carbide phase (MC_SHP), which comprised 50% W and 50% C (WC). There was negligible dissolved Ni and Zn.

Figure 6.3 shows the composition of the high temperature FCC_A1#1 which appears at 2500ºC and seemingly transforms at 2200ºC to FCC_A1#2. It was composed of carbon around 40%. The carbon content increased with decreasing temperature, and tungsten did the opposite. The carbon content at about 2353ºC was equal to tungsten. The vanadium content increased with decreasing temperature. This is thus a W,C,Ni ternary phase.

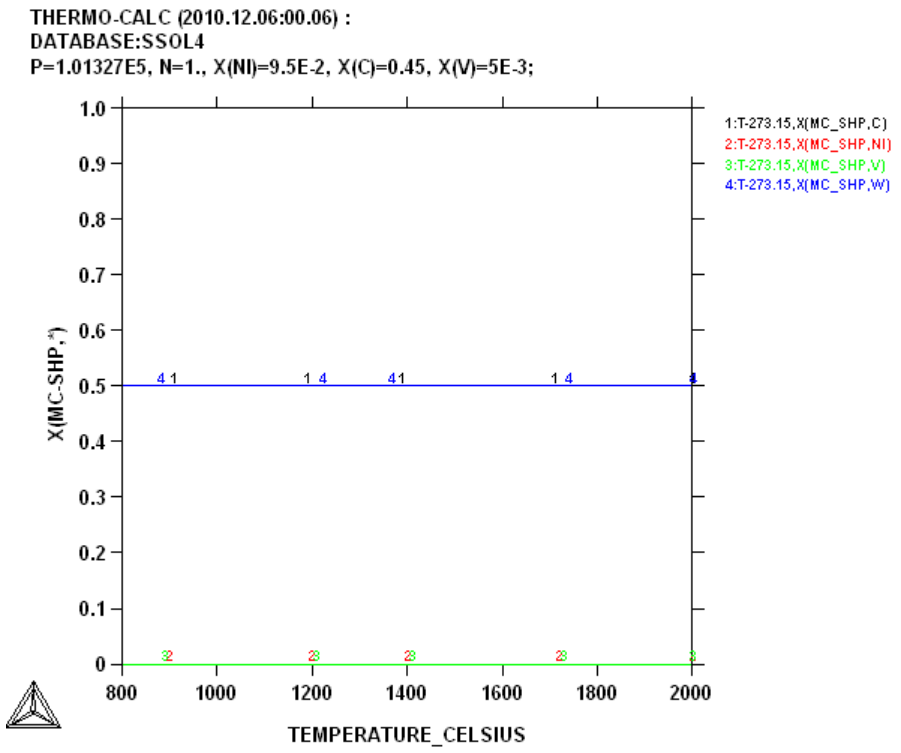


Figure 6.2. Composition of MC_SHP for W_{45}:C_{45}:$Ni_{9.5}$:$V_{0.5}$ (at.%).

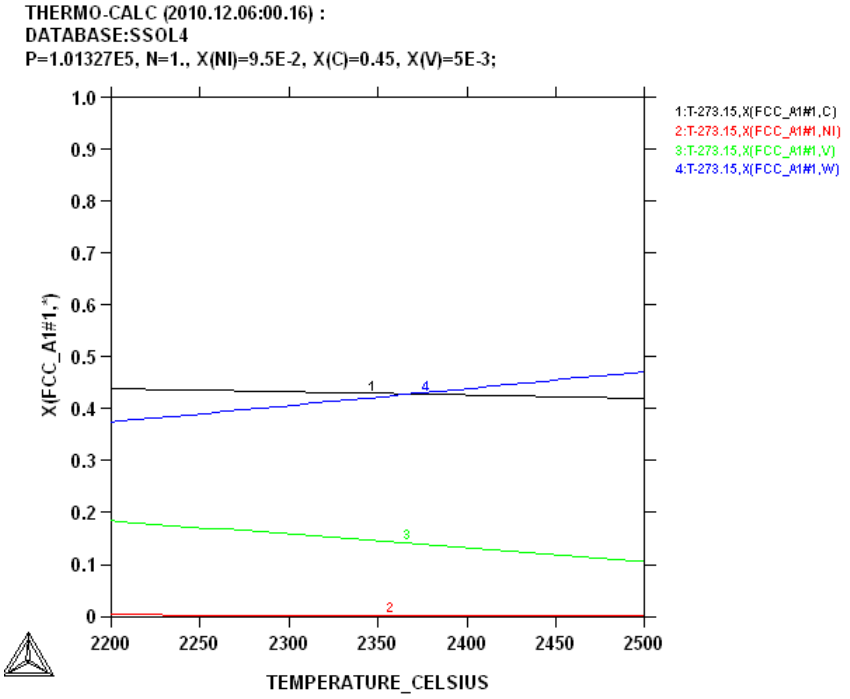


Figure 6.3. Composition of FCC_A1#1 at 2200-2500ºC for W_{45}:C_{45}:$Ni_{9.5}$:$V_{0.5}$ (at.%).

The low temperature FCC_A1#1 (Figure 6.4) was found to be (Ni) with about ~90 at.% nickel. This was confirmed with Ni-V binary phase diagram [1990Mas]. Tungsten was

between ~10% and ~6%, while carbon increased from ~2% at 1400ºC to a maximum of 4% at about 1370ºC. The vanadium was almost negligible.

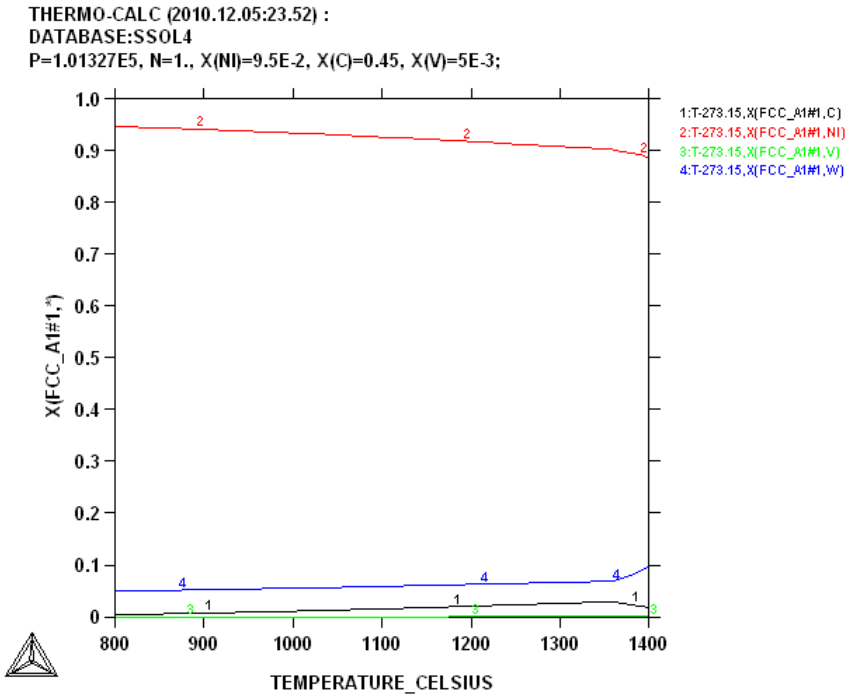


Figure 6.4. Composition of FCC_A1#1 at 800-1400ºC for W_{45}:C_{45}:$Ni_{9.5}$:$V_{0.5}$ (at.%).

The FCC_A1#2 phase composition is given in Figure 6.5. Carbon formed the highest proportion with ~45% and ~49% at 2000ºC and 800ºC, respectively. The second highest composition in this phase at 800ºC was vanadium, which was about ~22% at 2000ºC and gradually increased until there was a sudden increase up to ~38 at.% V at 1360ºC. After the sharp increase in V, the same earlier rate of increase continued up to 46% at 800ºC. Tungsten at 2000ºC was about 32%, it then gradually decreased until 1400ºC, then suddenly decreased to about 18% at 1360ºC, after which it decreased to ~8% at 800ºC. Nickel formed less than 1% of the phase.

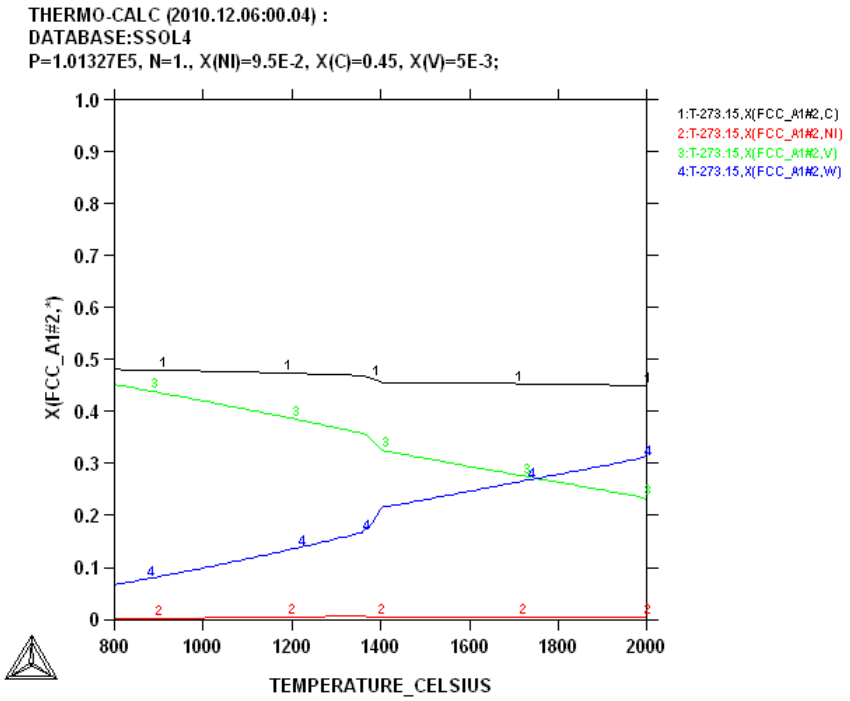


Figure 6.5. Composition of the FCC_A1#2 for W_{45}:C_{45}:$Ni_{9.5}$:$V_{0.5}$ (at.%).

The graphite phase (Figure 6.6) was composed of almost 100% carbon with negligible other dissolved elements.

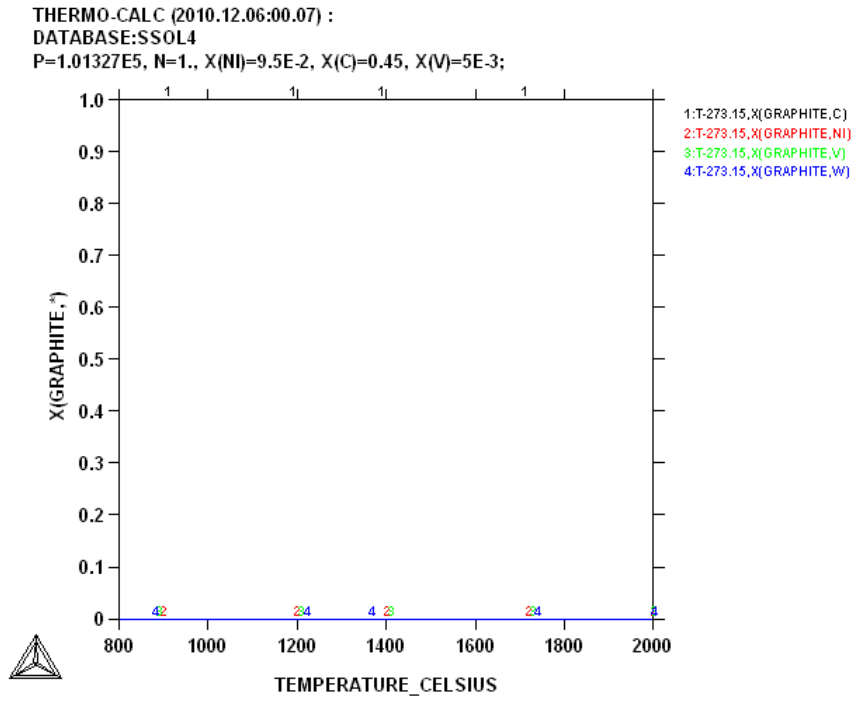


Figure 6.6. Composition of graphite for W_{45}:C_{45}:$Ni_{9.5}$:$V_{0.5}$ (at.%.).

6.1.2 W_{45}:C_{45}:$Ni_{8.6}$:$V_{1.4}$ (at.%)

The W_{45}:C_{45}:$Ni_{8.6}$:$V_{1.4}$ (at.%) phase proportion diagram (Figure 6.7) had the carbide (MC_SHP) forming the bulk of the material, and it solidified above 2600°C, while the graphite, which was only stable at high temperatures, solidified above 2600°C. The proportions of the stable phases and their temperature ranges are given in Table 6.2. At 1420ºC, liquid phase solidified to form FCC_A1#1 which was the last solid to emerge. The FCC_A1#2 was the last but one phase to solidify at 2340ºC, and attained a maximum of about ~8% then fell to about 5% at 800ºC. There was a high temperature FCC_A1#1 which solidified above 2600°C, but disappeared at 2340ºC and reappeared at 1420ºC. A summary of the property phase diagram is given in Table 6.2.

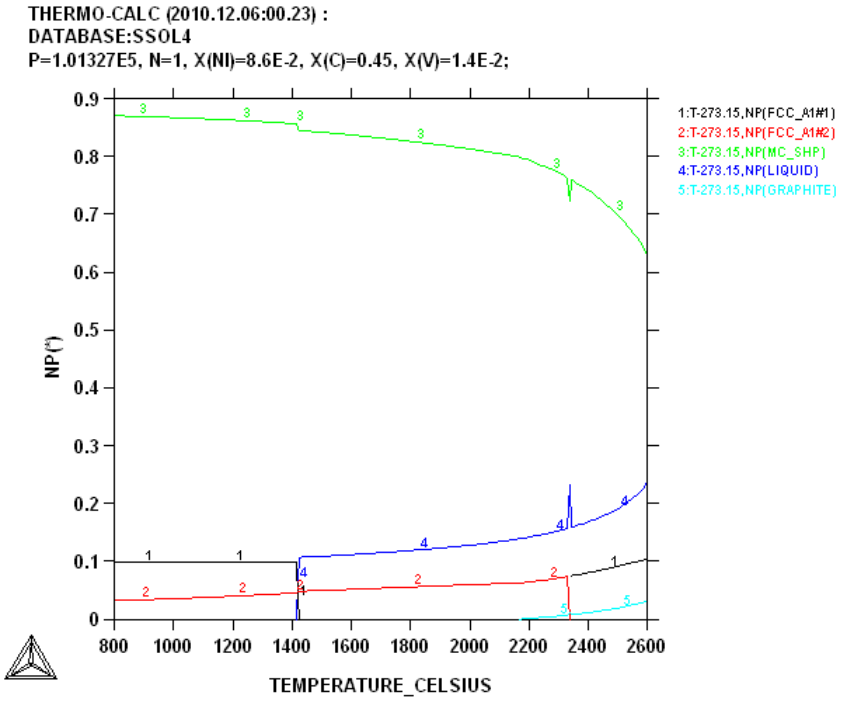


Figure 6.7. Phase proportions of W_{45}:C_{45}:$Ni_{8.6}$:$V_{1.4}$ (at.%).

	Maximum stability (°C)	Minimum stability (°C)	Maximum proportion	Minimum proportion
FCC_A1#1	1420	<800	~0.09	0.00
FCC_A1#1	>2600	1340	~0.11	0.04
FCC _A1#2	1340	<800	~0.08	~0.04
MC_SHP	>2600	<800	~0.87	~0.64
GRAPHITE	>2600	1380	0.04	0.00

Table 6.2. Summary of phase proportions of W_{45}:C_{45}:$Ni_{8.6}$:$V_{1.4}$ (at.%).

The MC_SPH phase calculated showed stoichiometric WC with negligible other elements. The plot was similar to Figure 6.2.

The nickel solid solution is the low temperature FCC_A1#1 phase; nickel comprised about 88%. Tungsten formed 10% of the phase, with the rest (carbon and vanadium) being less than 2% (Figure 6.8). The presence of the (Ni) was confirmed with Ni-V using the binary diagram [1990Mas].

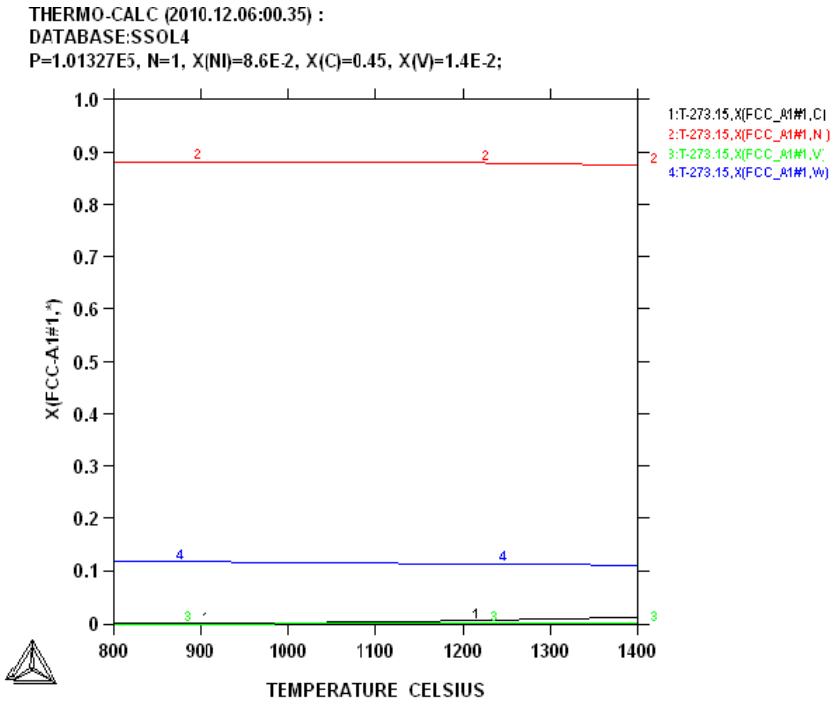


Figure 6.8. Composition of FCC_1A#1 for W_{45}:C_{45}:$Ni_{8.6}$:$V_{1.4}$ (at.%).

Figure 6.9 shows a calculation done for the FCC_A1#1 phase at an expanded scale, revealing more clearly the compositions of carbon and vanadium.

The FCC_A1#1 phase in Figure 6.10 shows a V,W ternary carbide. The tungsten steadily decreased with decreasing temperature, while vanadium increased. The amount of the nickel was very small, while carbon had the highest composition, ~47%.

The phase composition calculation shows that carbon forms 100% of the graphite phase, and was the same as in Figure 6.6.

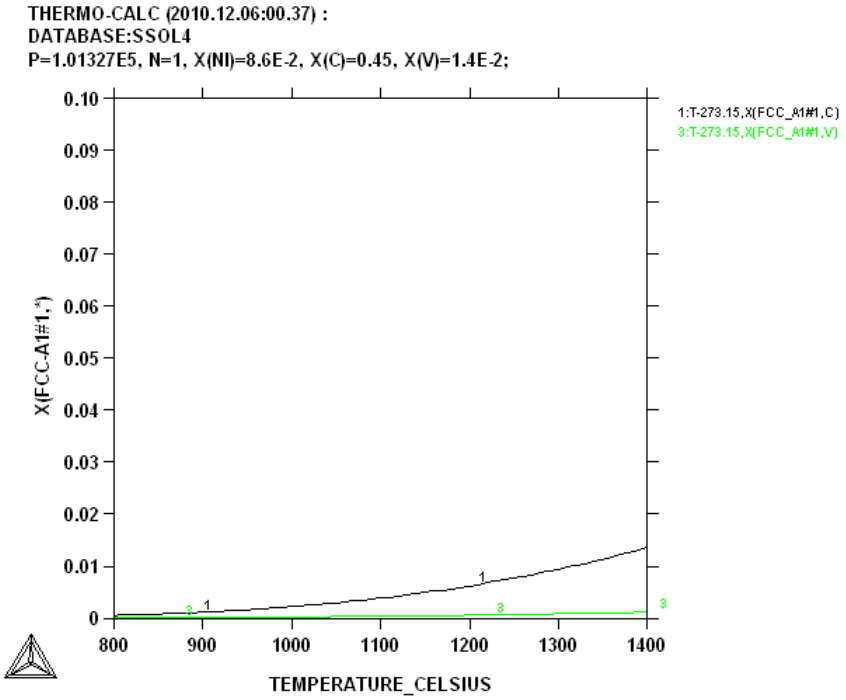


Figure 6.9. Composition diagram of the FCC_1A#1 for W_{45}:C_{45}:$Ni_{8.6}$:$V_{1.4}$ (at.%) showing carbon and vanadium.

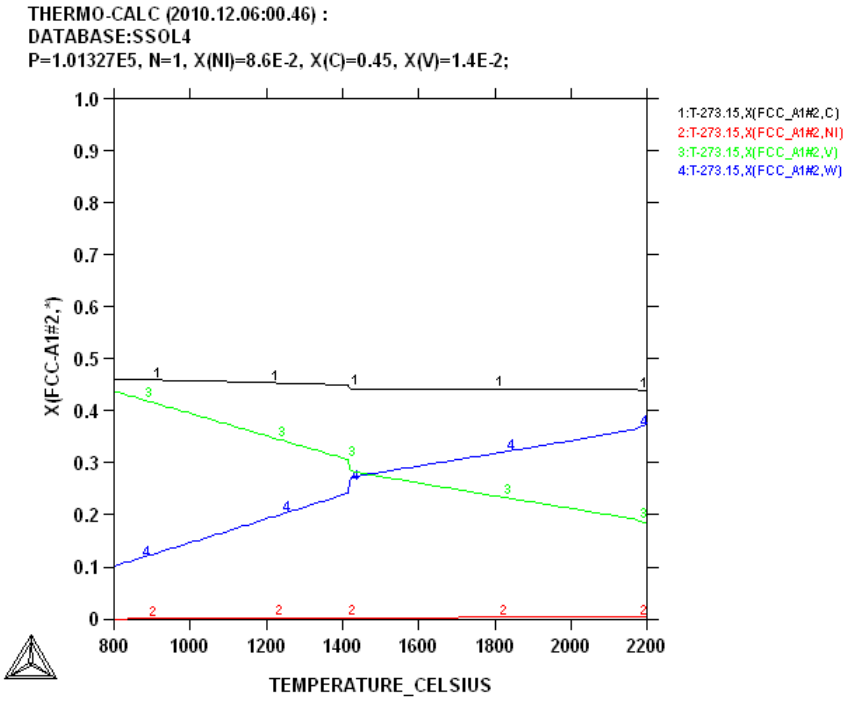


Figure 6.10. Composition of FCC_1A#2 for W_{45}:C_{45}:$Ni_{8.6}$:$V_{1.4}$ (at.%).

6.1.3 W_{45}:C_{45}:$Ni_{8.5}$:$Zn_{1.5}$ (at.%)

The calculation for W_{45}:C_{45}:$Ni_{8.5}$:$Zn_{1.5}$ (at.%) in Figure 6.11 showed three stable phases: MC_SHP, FCC_A1#1 and graphite. Graphite at 2600ºC was about ~25% and then disappeared at 1800ºC. Graphite then reappeared at about 1240ºC and was still present at 800ºC in a negligible proportion. The MC_SHP phase formed the bulk of the material and solidified above 2600°C. The binder FCC_A1 phase solidified last (1300°C). A summary of the phase proportions for W_{45}:C_{45}:$Ni_{8.5}$:$Zn_{1.5}$ (at.%) is given in Table 6.3.

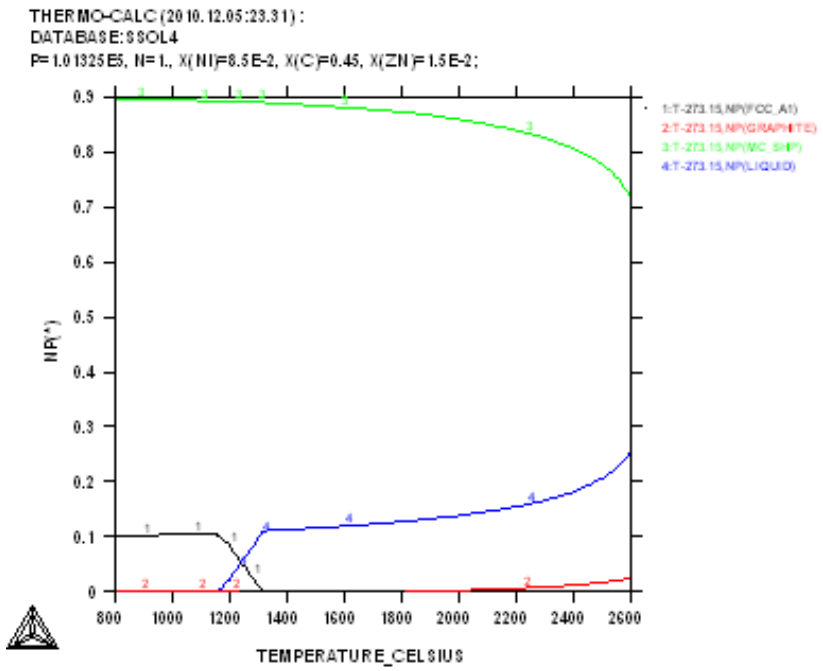


Figure 6.11. Phase proportions of W_{45}:C_{45}:$Ni_{8.5}$:$Zn_{1.5}$ (at.%).

	Maximum stability (°C)	**Minimum stability (°C)**	**Maximum proportion**	**Minimum proportion**
FCC_A1	1300	<800	~0.11	~0.10
GRAPHITE	1240	<800	~0.00	~0.00
GRAPHITE	>2600	1800	~0.03	~0.00
MC_SHP	>2600	<800	~0.89	~0.73

Table 6.3. Summary of phase proportions of W_{45}:C_{45}:$Ni_{8.5}$:$Zn_{1.5}$ (at.%).

Figure 6.12 shows the phase composition for FCC_A1. The tungsten decreased to a minimum, about 2%, while zinc increased steadily to about ~15% at 1150ºC, and then was constant. Nickel decreased about ~5% between 1300ºC and 1150ºC, and was the bulk of the phase, which implied a Ni solid solution. This was confirmed with Ni-Zn binary diagram [1990Mas].

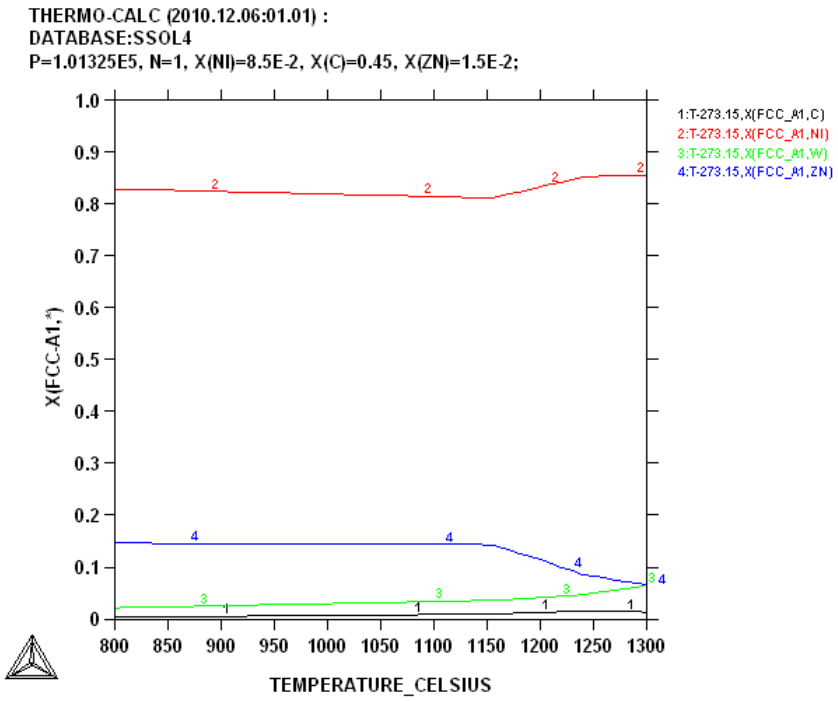


Figure 6.12. Composition of FCC_A1 for W_{45}:C_{45}:$Ni_{8.5}$:$Zn_{1.5}$ (at.%).

The graphite at low temperature, in the range 800ºC to 1200ºC, was 100% carbon. The plot looked the same as Figure 6.6.

The graphite phase at high temperatures, between the range 1800ºC to 2600ºC, was also calculated. The two graphite calculations were carried out to observe what happened when graphite disappeared at 1880ºC and reappearing at 1200ºC. No particular trend was observed. The graphite phase at high temperatures graphite phase was composed only of carbon, as in Figure 6.6.

The MC_SHP phase had 50 at.% W and 50 at.% C. This clearly indicated WC forming stoichiometrically, and the phase composition was the same as in Figure 6.2.

6.1.4 W_{45}:C_{45}:$Ni_{9.0}$:$Zn_{1.0}$ (at.%)

The calculated phase proportion for W_{45}:C_{45}:$Ni_{9.0}$:$Zn_{1.0}$ (at.%) is shown in Figure 6.13. There were three stable phases; FCC_A1, MC_SHP and graphite. At ~1260ºC, liquid solidified to form the FCC_A1 phase (the final phase), with a small amount of graphite, possibly as a eutectic reaction.

Graphite solidified above 2600ºC, forming ~2.6% of the material at 2600ºC. The graphite then disappeared at 1800ºC and reappeared around 1260ºC. It was negligible in proportion at the lower temperatures. Table 6.4 gives summary of the phases.

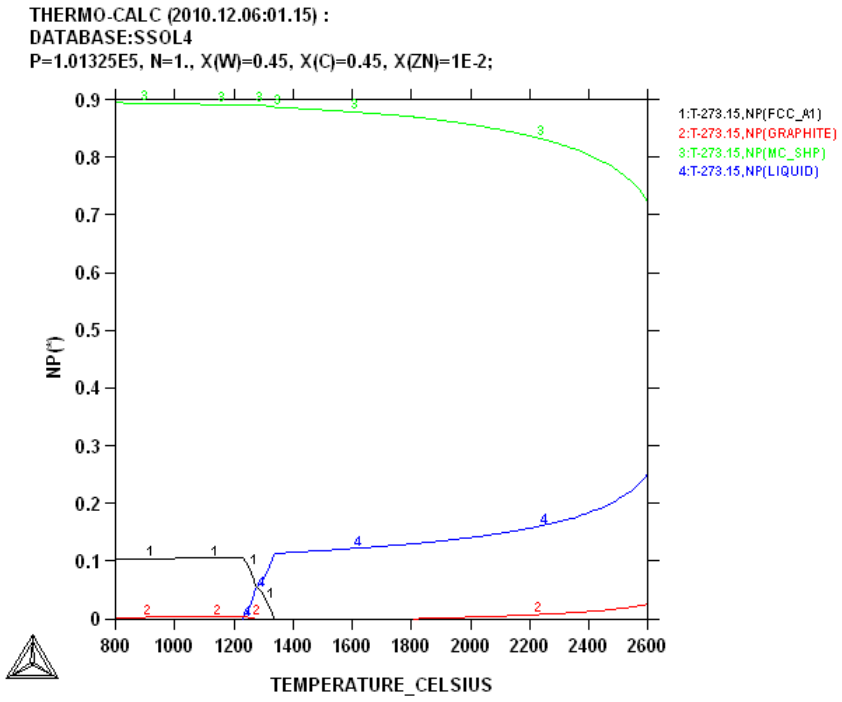


Figure 6.13. Phase proportions of W_{45}:C_{45}:$Ni_{9.0}$:$Zn_{1.0}$ (at.%).

	Maximum stability (°C)	**Minimum stability (°C)**	**Maximum proportion**	**Minimum proportion**
FCC_A1	1340	<800	~0.10	~0.10
GRAPHITE	1260	<800	~0.01	~0.00
GRAPHITE	>2600	1800	~0.03	~0.00
MC_SHP	>2600	<800	~0.89	~0.73

Table 6.4. Summary of phases proportions of W_{45}:C_{45}:$Ni_{9.0}$:$Zn_{1.0}$ (at.%).

Figure 6.14 shows the composition of FCC_A1#1, and nickel was the major component. At 1400ºC, the amount of Ni was about 88%. Zinc was at a relatively low composition (~5%), and increased steadily and attained its maximum proportion when Ni decreased to a minimum. The tungsten content decreased with decreasing temperature (8% to 2%).

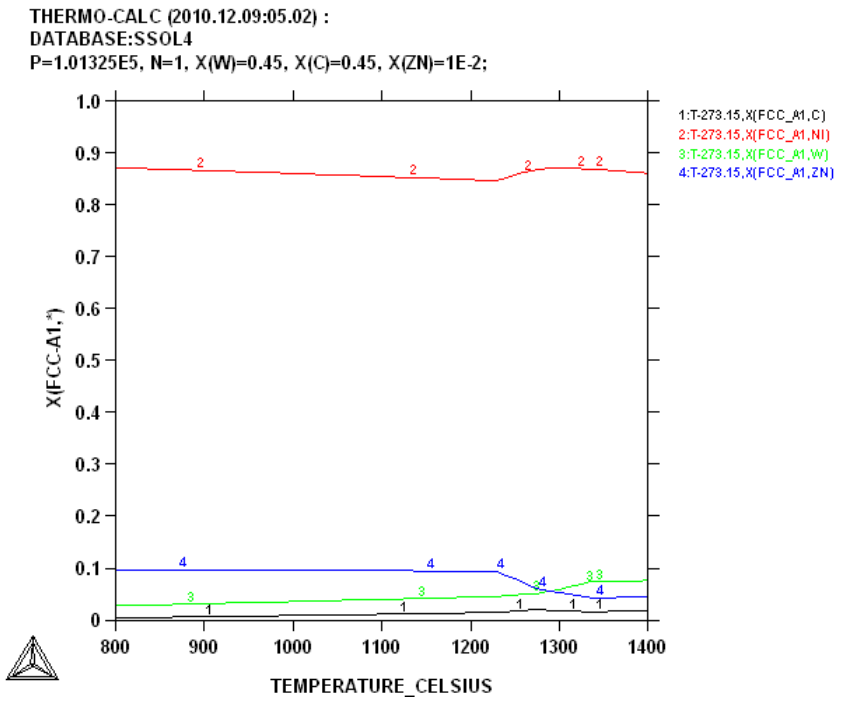


Figure 6.14. Composition diagram of the FCC_A1 for W_{45}:C_{45}:$Ni_{9.0}$:$Zn_{1.0}$ (at.%).

Calculations were done for the two sets of graphite phases (low and high temperature phases) to see if they were the same. The graphite was composed of only carbon, as seen in all the previous calculations. Graphite is known not to dissolve other elements to any extent [1990Mas]. The plots were similar to Figure 6.6.

The MC_SPH phase composition calculation showed stoichiometric WC with negligible other elements. The plot was similar to Figure 6.2.

6.1.5 W_{45}:C_{45}:Co_6:Mn_4 (at.%)

The phase proportion diagram for W_{45}:C_{45}:Co_6:Mn_4 (at.%) (Figure 6.15) reveals the solidification of the carbide at high temperatures and solidification of the binder phase HCP_A3, just above 1000ºC. The MC_SHP phase started solidification above 2600ºC and comprised ~90% of the material. Graphite at 2600ºC was about 8%, decreased with decreasing temperature and disappeared at the about 2300ºC.

A low temperature eutectic reaction also occurred at about 1000ºC to give the eta $M_{12}C$ carbide phase and HCP_A3 binder:

$$M_{12}C \leftrightarrow Liq + HCP_A3$$

Table 6.5 gives the summary of the phase proportions calculated.

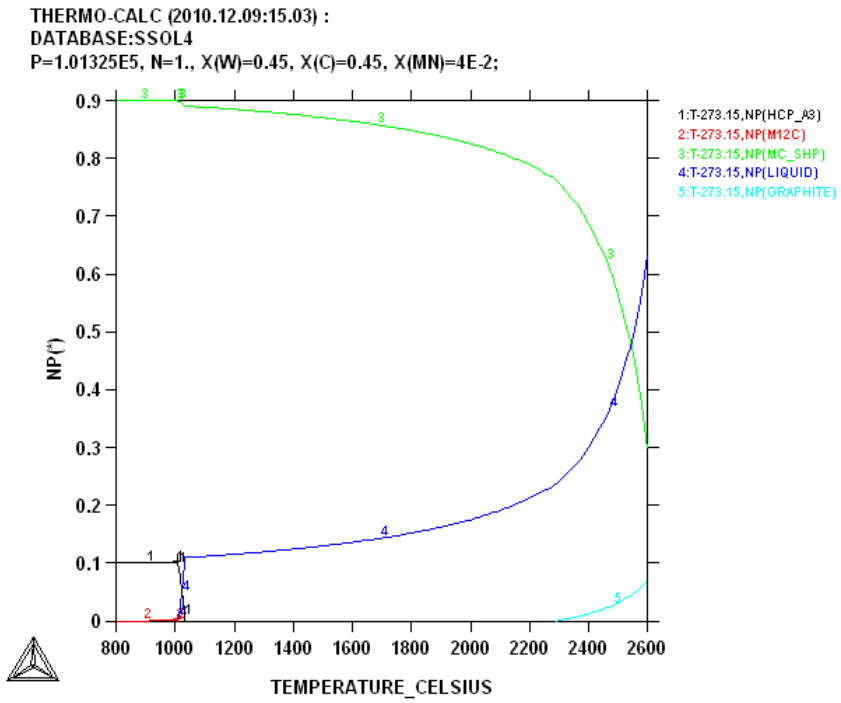


Figure 6.15. Phase proportions of W_{45}:C_{45}:Co_6:Mn_4 (at.%).

	Maximum stability (°C)	**Minimum stability (°C)**	**Maximum proportion**	**Minimum proportion**
HCP_A3	1120	<800	~0.10	~0.00
$M_{12}C$	1000	<800	~0.01	~0.00
GRAPHITE	>2600	2300	~0.08	~0.00
MC_SHP	>2600	<800	~0.90	~0.30

Table 6.5. Summary of phase proportions of W_{45}:C_{45}:Co_6:Mn_4 (at.%).

The HCP_A3 phase (Figure 6.16) had about 60% Co and almost 40% Mn, with the rest being C and W. The Mn increased to a maximum of ~40% at about 1010ºC, as the cobalt content decreased. The Mn proportion was about ~34% at 1040ºC, while Co was about ~64%. The proportions of cobalt and manganese indicated (Co); this was confirmed on the Co-Mn binary phase diagram [1990Mas].

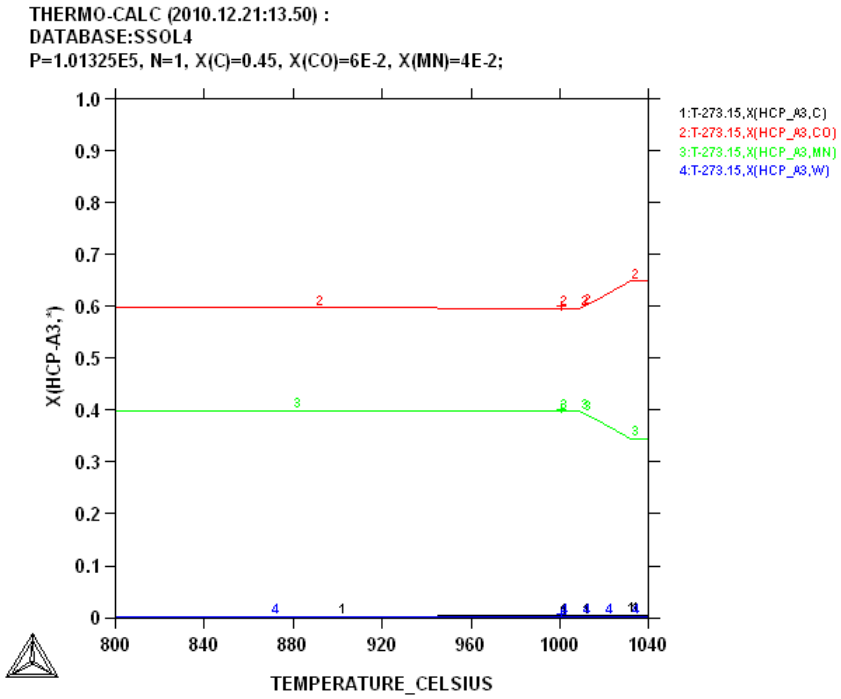


Figure 6.16. Composition diagram of the HCP_A3 for W_{45}:C_{45}:Co_6:Mn_4 (at.%).

The calculated $M_{12}C$ phase composition is shown in Figure 6.17. This phase is a ternary phase normally called eta phase. The $M_{12}C$ carbide has a fixed composition of Co_6W_6C [1965Kre].

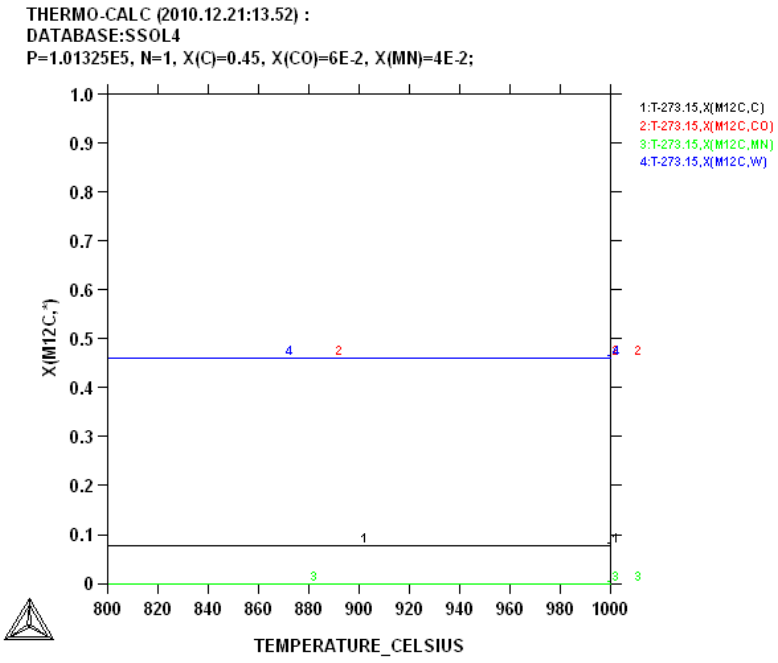


Figure 6.17. Composition of the $M_{12}C$ W_{45}:C_{45}:Co_6:Mn_4 (at.%).

The MC_SHP phase composition showed stoichiometric WC. The plot was the same as Figure 6.2.

The graphite phase calculated for this composition was similar to the other graphite compositions calculated, 100%. The graphite phase was only stable at high temperature, ranging between 2300ºC and 2600ºC. The plot was similar to Figure 6.6.

6.1.6 W_{45}:C_{45}:$Co_{2.5}$:$Mn_{7.5}$ (at.%)

Three stable phases were present in the calculation for W_{45}:C_{45}:$Co_{2.5}$:$Mn_{7.5}$ (at.%) (Figure 6.18). High temperature graphite was stable above 2200ºC. The bulk of the alloy was the MC_SHP phase, forming 90% at low temperatures.

A eutectic reaction occurred at about 1100ºC forming HCP_A3 and carbide $M_{12}C$. There was no (Mn) formed as a stable phase as expected, even though Mn was higher in content than cobalt; instead (Co) was predicted by Thermo-Calc, with some Mn in solution.

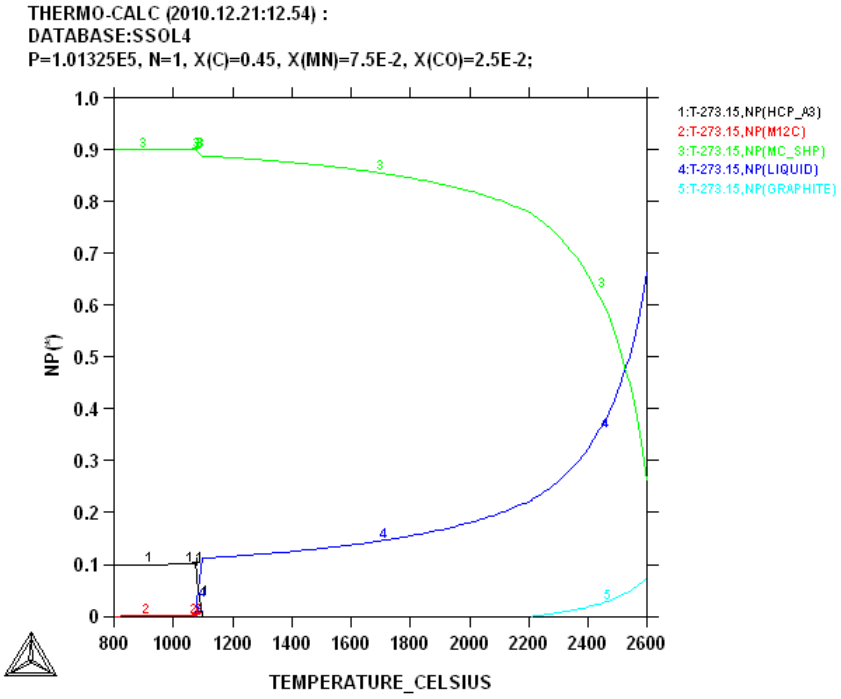


Figure 6.18. Phase proportions of W_{45}:C_{45}:$Co_{2.5}$:$Mn_{7.5}$ (at.%).

	Maximum stability (°C)	Minimum stability (°C)	Maximum proportion	Minimum proportion
HCP_A3	1100	<800	~0.10	~0.00
$M_{12}C$	1100	<800	~0.00	~0.00
GRAPHITE	>2600	2210	~0.08	~0.00
MC_SHP	>2600	<800	~0.90	~0.26

Table 6.6. Summary of phase proportions of W_{45}:C_{45}:$Co_{2.5}$:$Mn_{7.5}$ (at.%).

The phase composition for HCP_A3 is shown in Figure 6.19. Cobalt formed 75% of the phase, while Mn comprised about 25%. This composition was compared to the Co-Mn binary [1990Mas]; and agreed with the cobalt solid solution.

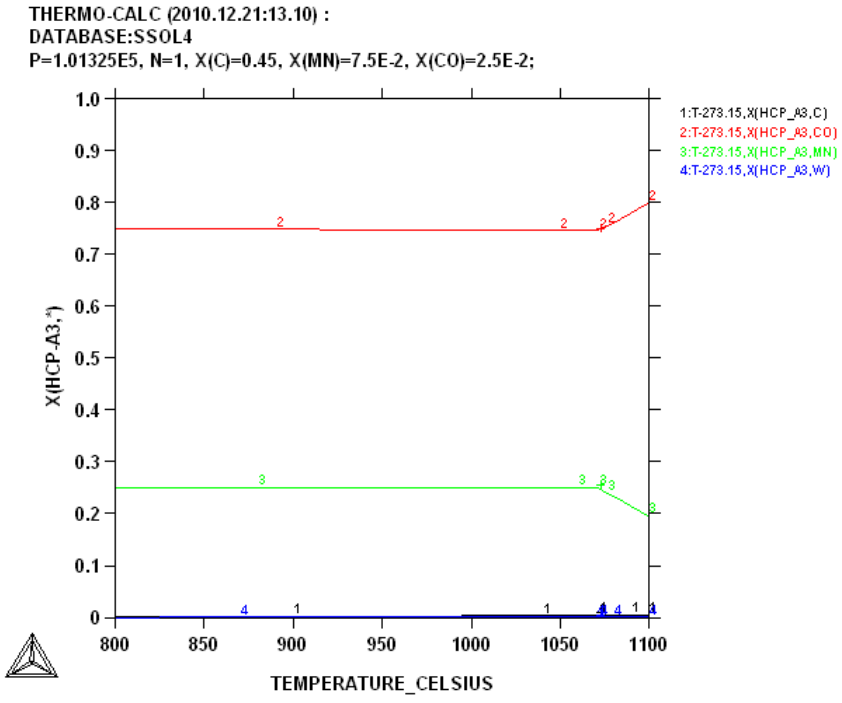


Figure 6.19. Composition of HCP_A3 in W_{45}:C_{45}:$Co_{2.5}$:$Mn_{7.5}$ (at.%).

The $M_{12}C$ phase consisted of about 46% cobalt and 46% tungsten with about 8% carbon (Figure 6.20). This composition suggested an eta phase with a composition of Co_6W_6C.

The MC_SHP phase composition showed stoichiometric WC. The phase composition plot was similar to Figure 6.2.

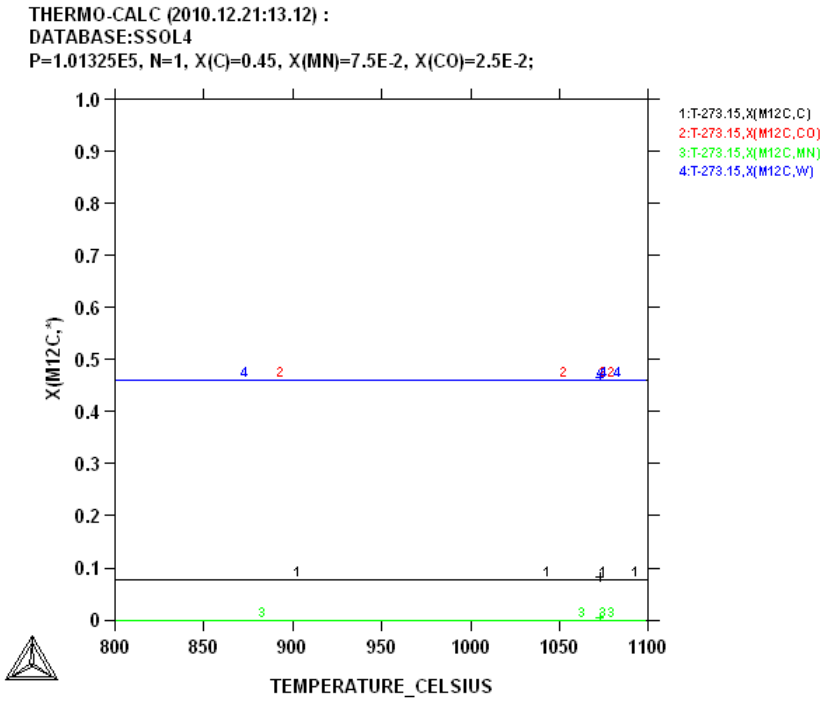


Figure 6.20. Composition of $M_{12}C$ W_{45}:C_{45}:$Co_{2.5}$:$Mn_{7.5}$ (at.%).

The graphite phase composition calculated for W_{45}:C_{45}:$Co_{2.5}$:$Mn_{7.5}$ (at.%) was found to be stable at high temperatures. Almost all the compoition was carbon with small disolved proportions of the other elements. The plot was similar to Figure 6.6.

6.1.7 W_{45}:C_{45}:$Cu_{8.5}$:$Ni_{1.5}$ (at.%)

The calculation for W_{45}:C_{45}:$Cu_{8.5}$:$Ni_{1.5}$ (at.%) shows three stable phases comprising FCC_A1, graphite and MC_SHP as shown in Figure 6.21. The MC_SHP formed the bulk of the alloy as expected. The carbide solidified above 2600ºC and was about 82% (2600ºC) and steadily increased over the stable temperature range to reach about 90% at 800ºC.

The solidification range of the binder was 1180°C-1140°C. The liquid phase finally solidified at about 1140ºC. The FCC_A1 phase at 800ºC formed 10% of the total composition of the system. Table 6.7 gives a summary of phases of W_{45}:C_{45}:$Cu_{8.5}$:$Ni_{1.5}$ (at.%).

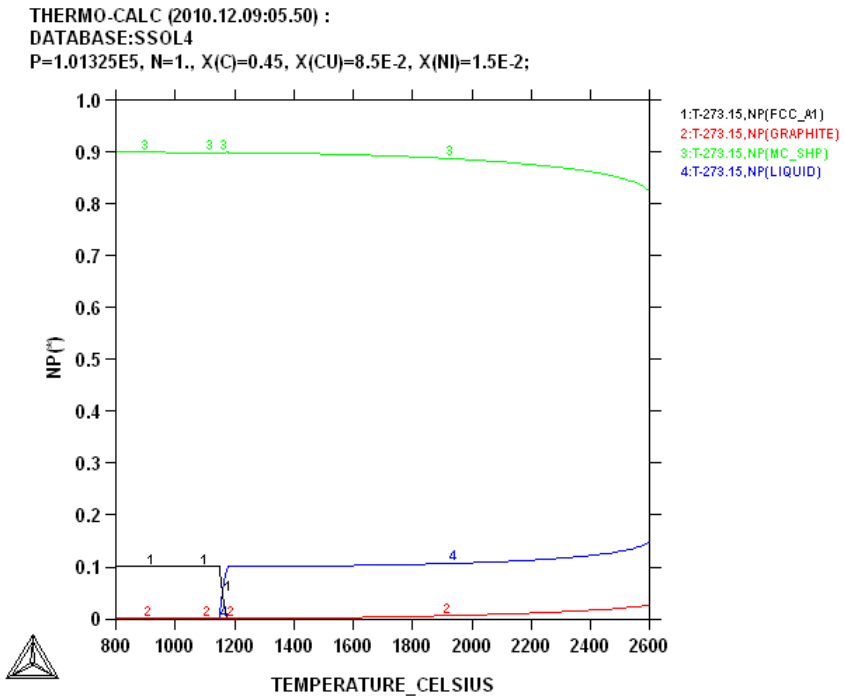


Figure 6.21. Phase proportion diagram of W_{45}:C_{45}:$Cu_{8.5}$:$Ni_{1.5}$ (at.%).

	Maximum stability (°C)	**Minimum stability (°C)**	**Maximum proportion**	**Minimum proportion**
FCC _A1	1800	<800	~0.10	~0.00
MC_SHP	>2600	<800	~0.90	~0.84
GRAPHITE	>2600	2000	~0.04	~0.01

Table 6.7. Summary of phase proportion of W_{45}:C_{45}:$Cu_{8.5}$:$Ni_{1.5}$ (at.%).

The FCC_A1 phase was mainly composed of Cu, this indicated a (Cu,Ni) solid solution at 800ºC with a total proportion of about 85%. At the same temperature, nickel formed almost 15% with tungsten and carbon dissolved in the (Cu,Ni) in an almost negligible amount. The concentration of copper at 2600ºC was about 78% and steeply increased to a maximum at about 1150ºC, while nickel at the same temperature was found to be ~22% but fell to its minimum and stayed constant to 800ºC. Figure 6.22 shows the composition for FCC_A1.

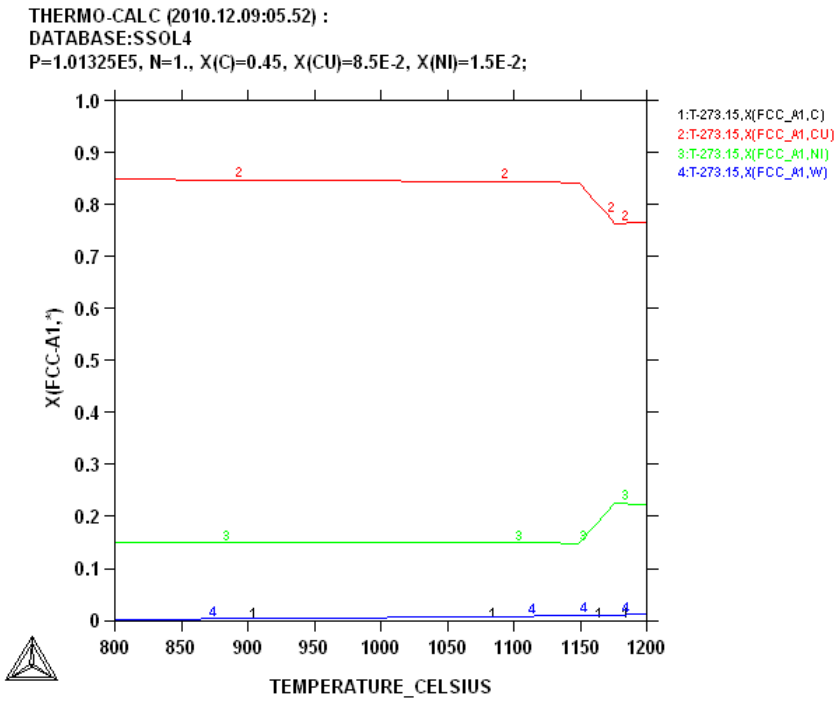


Figure 6.22. Composition of FCC_A1 in W_{45}:C_{45}:$Cu_{8.5}$:$Ni_{1.5}$ (at.%).

The MC_SHP phase had 50% W and 50% C, this clearly indicated stoichiometric WC. There was a negligible amount of dissolved copper and nickel in the phase. The plot for the graphite looked similar to Figure 6.2.

The graphite phase was basically composed of carbon with a negligible dissolved amount of the other elements. The plot was similar to Figure 6.6.

6.1.8 W_{45}:C_{45}:Cu_8:Ni_2 (at.%)

The calculation for W_{45}:C_{45}:Cu_8:Ni_2 (at.%) (Figure 6.23) looked similar to W_{45}:C_{45}:$Cu_{8.5}$:$Ni_{1.5}$ (at.%), but the solidification range for the FCC-A1 occurred at a slightly higher temperature, and was still the last phase to form. The MC_SHP phase solidified above 2600°C; it was about 81% at 2600ºC and then increased with decreasing temperature to about 90% at 800ºC. Summary of the phases proportions are given in Table 6.8.

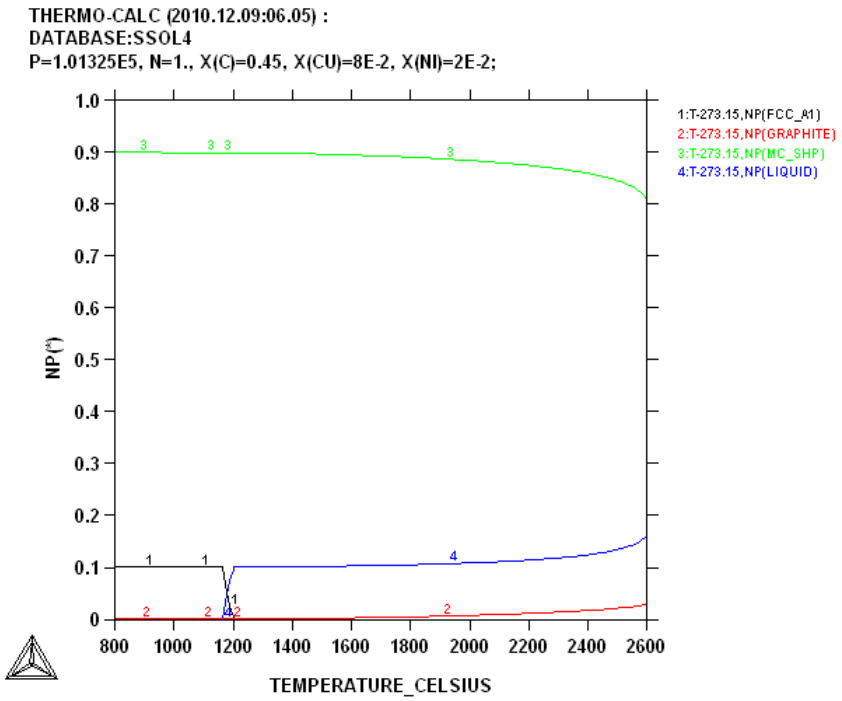


Figure 6.23. Phase proportion diagram of $W_{45}:C_{45}:Cu_8:Ni_2$ (at.%).

	Maximum stability (°C)	**Minimum stability (°C)**	**Maximum proportion**	**Minimum proportion**
FCC_A1	1200	<800	~0.10	~0.00
MC_SHP	>2600	<800	~0.90	~0.82
GRAPHITE	>2600	2000	~0.04	~0.00

Table 6.8. Summary of phase proportion of $W_{45}:C_{45}:Cu_8:Ni_2$ (at.%).

The FCC_A1 phase was identified as (Cu,Ni), and comprised ~80% copper at 800°C which formed the bulk of the phase (Figure 6.24). Nickel formed about 20% of the phase, with carbon and tungsten being negligible. At higher temperatures, the concentration of carbon and tungsten dissolved in the (Cu,Ni) increased to about 1%. This is also seen in the Cu-W binary phase diagram [1990Mas].

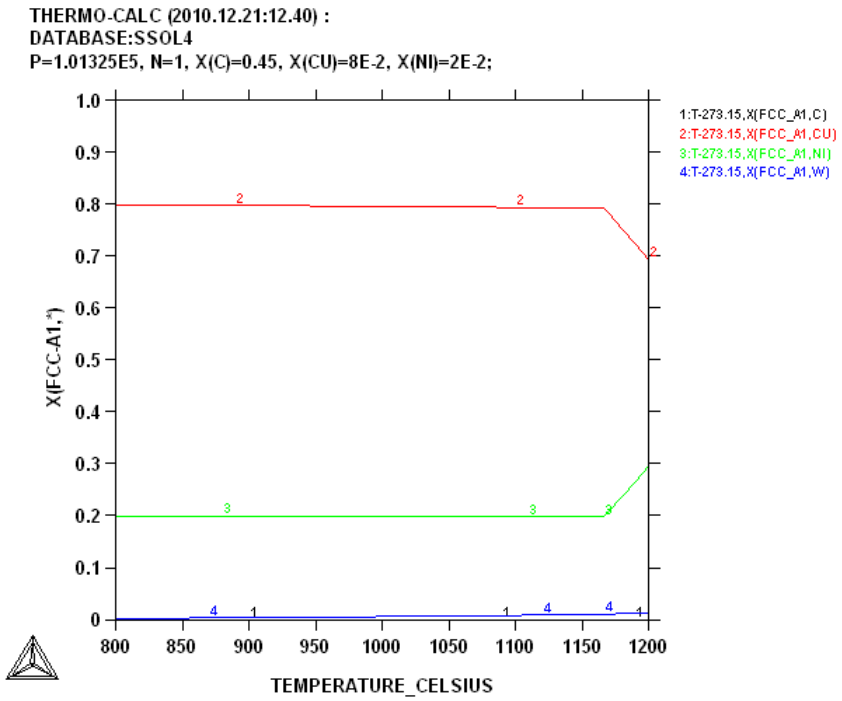


Figure 6.24. Composition diagram of the FCC_A1 for W_{45}:C_{45}:$Ni_{9.0}$:$Zn_{1.0}$ (at.%).

The graphite phase was 100% carbon. The phase was stable from 800ºC to 2600ºC, but formed a small proportion of the total. The phase composition plot for the graphite was similar to Figure 6.6.

The MC_SPH formed stoichiometric WC with negligible dissolved other elements, and was the same as Figure 6.2.

6.1.9 W_{45}:C_{45}:Cu_9:Zn_1 (at.%)

The sample had three stable phases. The major component of the calculated phase proportion for W_{45}:C_{45}:Cu_9:Zn_1 (at.%) was found to be the MC_SHP phase (Figure 6.25), while graphite formed the smallest amount. The MC_SHP phase comprised ~90% at 800°C, and graphite which solidified above 2600°C comprised a negligible proportion at 800°C. The FCC_A1 phase was last to solidify at about 1050ºC, and at formed ~10% at 800ºC. The summary of the phase proportion calculation is given in Table 6.9.

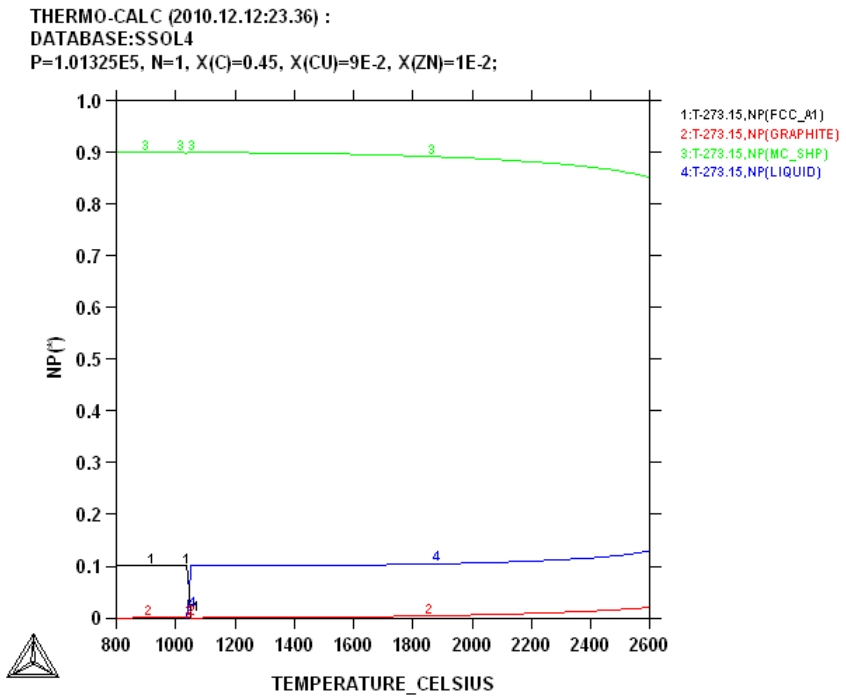


Figure 6.25. Phase proportion diagram of W_{45}:C_{45}:Cu_9:Zn_1 (at.%.).

	Maximum stability (°C)	**Minimum stability (°C)**	**Maximum proportion**	**Minimum proportion**
FCC_A1	1060	<800	~0.10	~0.00
MC_SHP	>2600	<800	~0.90	~0.86
GRAPHITE	>2600	2000	~0.02	~0.00

Table 6.9. Summary of phase proportion of W_{45}:C_{45}:Cu_9:Zn_1 (at.%).

The major component of FCC_A1 phase was copper, which was ~90% at 800ºC as shown in Figure 6.26. Nickel was the second highest, forming ~10% of the total composition of the phase. The other elements formed a very small percentages of the phase. The composition of the phase suggeseted (Cu,Ni), which was confirmed using the Cu-Ni binary phase diagram [1990Mas].

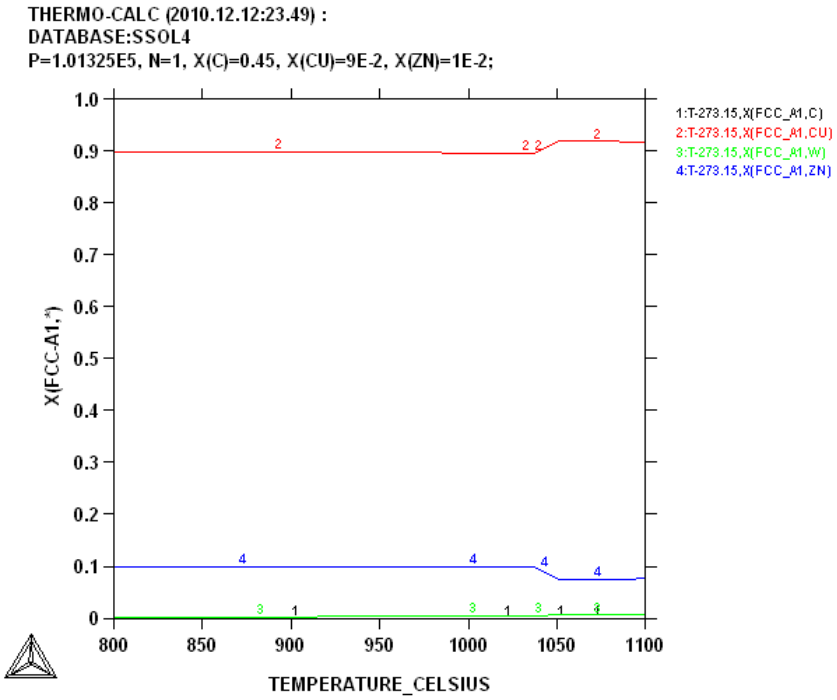


Figure 6.26. Composition diagram of the FCC_A1 for W_{45}:C_{45}:Cu_9:Zn_1 (at.%).

The MC_SHP phase which had the highest composition in the alloy was made up of 50 at.% W and 50 at.% C. These proportions in the MC_SHP phase indicated stoichiometric WC. The phase composition plot was similar to Figure 6.2.

The graphite phase was composed of 100% carbon with no discernable other elements. The diagram was similar to Figure 6.6.

6.1.10 W_{45}:C_{45}:$Cu_{9.5}$:$Zn_{0.5}$ (at.%)

The calculated phase proportion diagram for W_{45}:C_{45}:$Cu_{9.5}$:$Zn_{0.5}$ (at.%) is given in Figure 5.27. The composition had three stable phases which were FCC_A1, MC_SHP and graphite. The MC_SHP phase solidified above 2600°C; it was about 85% at 2600°C and slightly increased as temperature decreased and formed ~90% of the material at 800°C. The graphite similarly solidified above 2600°C where it was about 1% at 2600°C; it then fell to a negligible proportion at lower temperatures. The last phase to solidify was the binder FCC_A1, which started solidification at about 1080°C and formed almost 11% of the material. A summary of the phase proportions is given in Table 6.10.

	Maximum stability (°C)	Minimum stability (°C)	Maximum proportion	Minimum proportion
FCC_A1	1080	<800	~0.11	~0.00
MC_SHP	>2600	<800	~0.90	~0.85
GRAPHITE	>2600	2000	~0.01	~0.00

Table 6.10. Summary of phase proportion of W_{45}:C_{45}:$Cu_{9.5}$:$Zn_{0.5}$ (at.%).

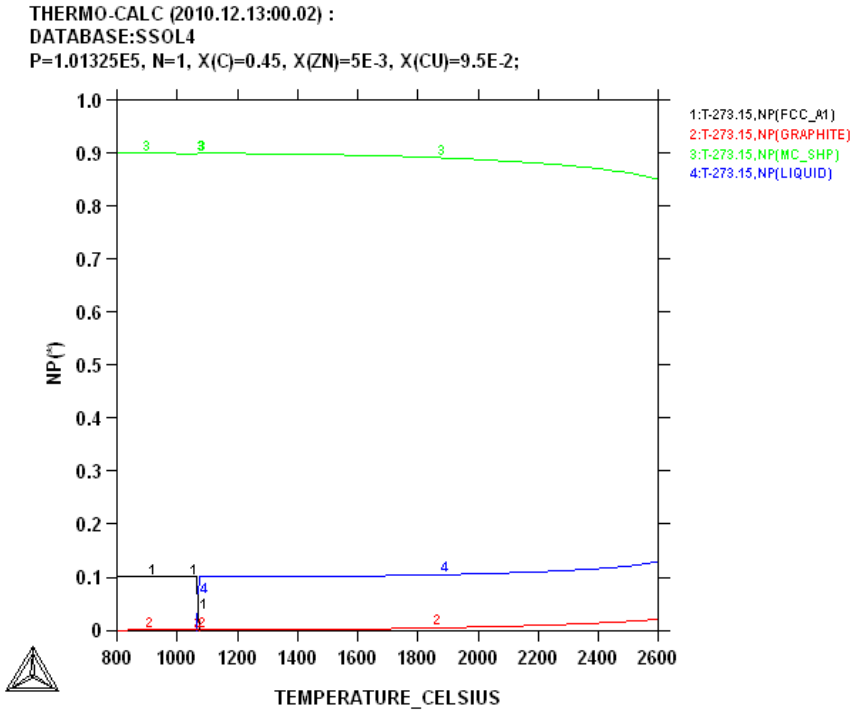


Figure 6.27. Phase proportions of W_{45}:C_{45}:$Cu_{9.5}$:$Zn_{0.5}$ (at.%).

The FCC_A1 phase (Figure 6.28) was mainly composed of copper, almost 95% at 800°C. The next highest composition of the phase was zinc which comprised ~6%. The other elements were at negligible amounts. The phase was identified as (Cu,Zn) solid solution, and was confirmed using the binary for Cu-Zn [1990Mas].

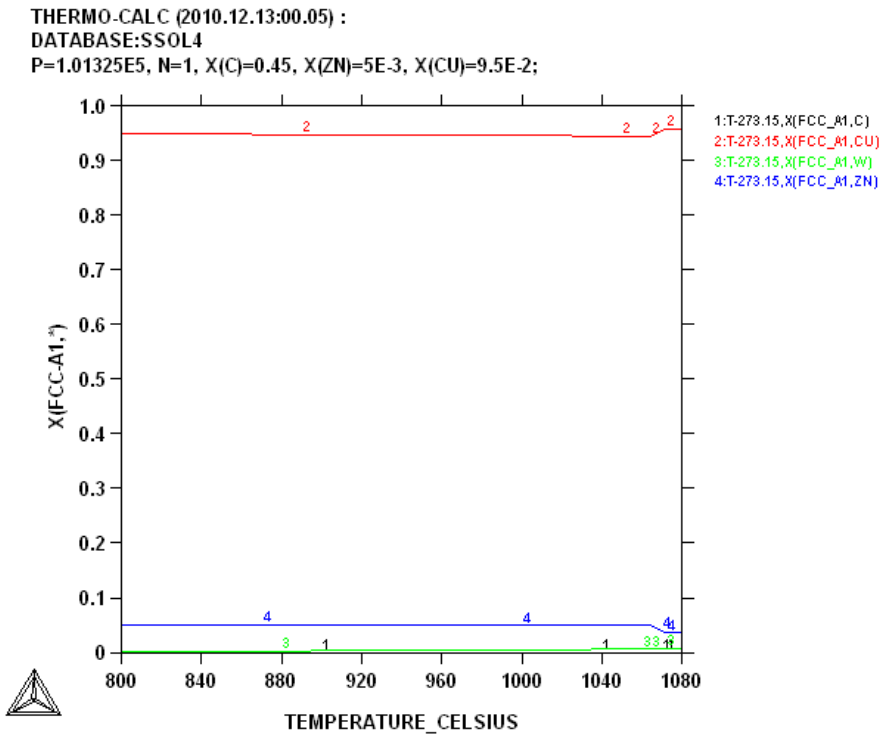


Figure 6.28. Composition diagram of the FCC_A1 for W_{45}:C_{45}:$Cu_{9.5}$:$Zn_{0.5}$ (at.%).

The calculation showed MC_SPH was stoichiometric WC, with negligible other elements. The diagram was the same as Figure 6.2.

The graphite phase was 100% carbon. This was similar to Figure 6.6.

6.1.11 W_{45}:C_{45}:Mn5:V_5 (at.%)

Four stable phases were present in W_{45}:C_{45}:Mn_5:V_5 (at.%) (Figure 6.29). The phases were BCC_A2, MC_SHP, V_3C_2 and graphite. The graphite and MC_SHP phases solidified above 2600°C, but the graphite phase existed only at high temperatures (2600°C to 2500°C) and had less than 10% proportion, while the MC_SHP phase spanned the entire temperature range of the calculation. The MC_SHP phase was ~40% at about 2600°C and later increased with decreased temperature, forming about 82% of the total at 800°C. The V_2C_3 phase was next to solidify at slightly above 2000°C. This phase formed ~10% of the composition at 800°C. The last phase to solidify was BCC_A2 and it was around 1860°C and also formed about 8% at 800°C. Table 6.11 gives a summary of the phase proportions calculated.

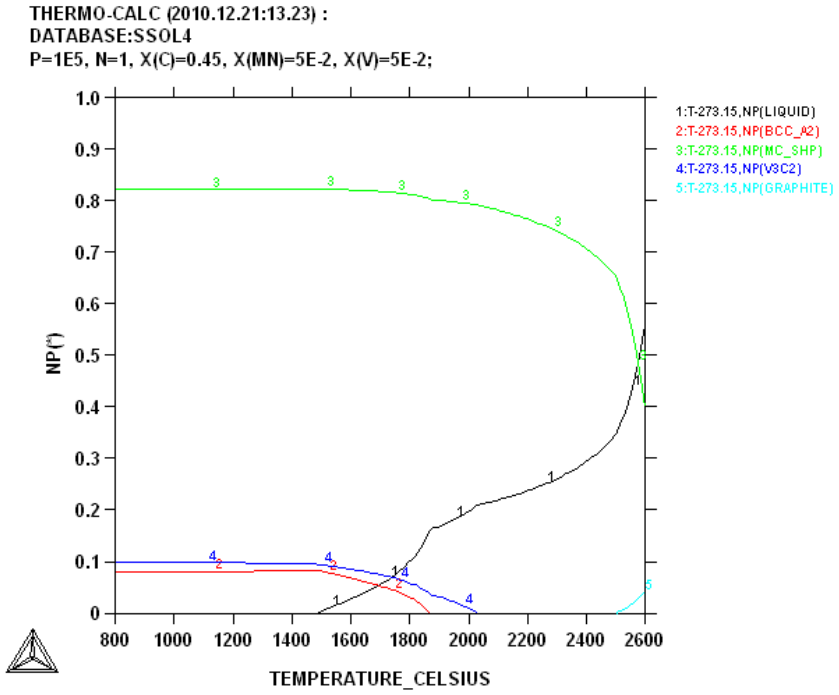


Figure 6.29. Phase proportion diagram of W_{45}:C_{45}:Mn_5:V_5 (at.%).

	Maximum stability (°C)	**Minimum stability (°C)**	**Maximum proportion**	**Minimum proportion**
BCC _A1	1860	<800	~0.08	~0.00
MC_SHP	>2600	<800	~0.82	~0.40
V_3C_2	2220	<800	~0.10	~0.00
GRAPHITE	>2600	2000	~0.01	~0.00

Table 6.11. Summary of phase proportion of W_{45}:C_{45}:Mn_5:V_5 (at.%).

The BCC_A1 phase shown in Figure 6.30 was composed of ~51% manganese and ~49% tungsten which could be a solid solution because of their similar bcc crystal structures. There was more tungsten than manganese at higher temperatures, but the opposite occurred at about 1600°C. The phase had about 3 at.% vanadium at 1500ºC, which increased at higher temperatures, but with negligible amounts at lower temperatures, as did carbon.

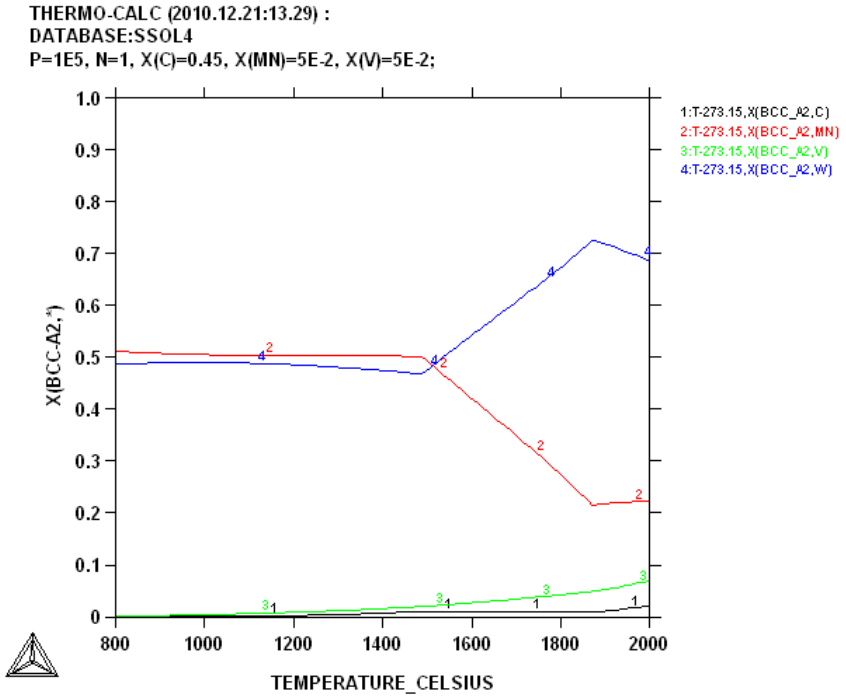


Figure 6.30. Composition of BCC_A2 for W_{45}:C_{45}:Mn_5:V_5 (at.%).

The carbide V_3C_2 phase (Figure 6.31) had vanadium as the major component, about 51% of the phase, below 1500°C, and carbon followed next which formed 40% through the entire phase range. There was dissolved manganese, which increased with decreasing temperature, forming almost 10% of the V_3C_2 phase.

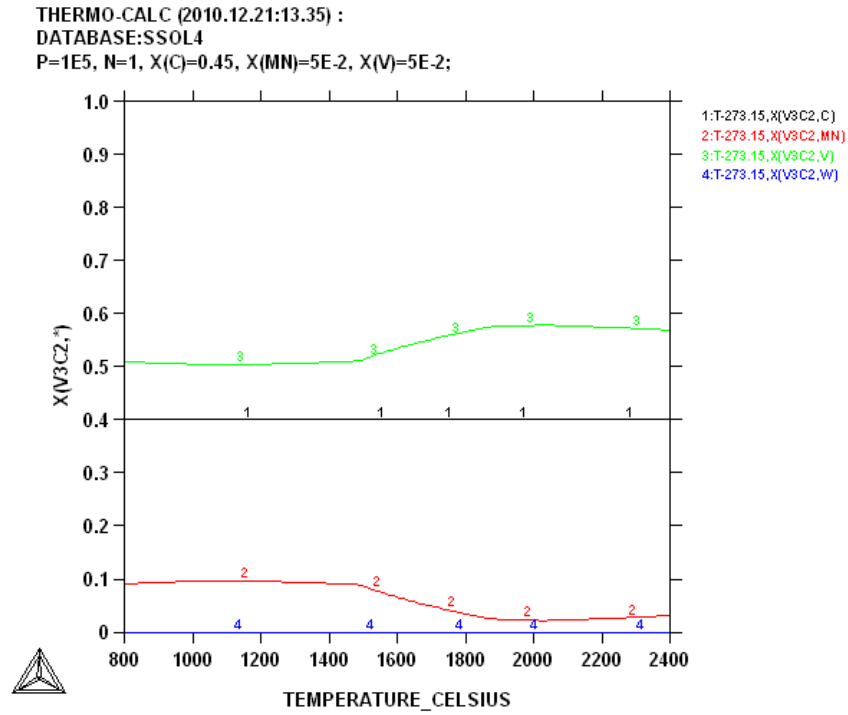


Figure 6.31. Composition of V_3C_2 for W_{45}:C_{45}:Mn_5:V_5 (at.%).

The calculation showed MC_SPH was stoichiometric WC, with negligible other elements. The diagram was the same as Figure 6.2.

The graphite phase was pure 100% carbon with negligible other elements. This was similar to Figure 6.6.

6.1.12 W_{45}:C_{45}:$Mn_{0.5}$:$Cu_{9.5}$ (at.%)

The calculation for W_{45}:C_{45}:$Mn_{0.5}$:$Cu_{9.5}$ (at.%) in Figure 6.32 had three stable phases which were: FCC_A1, graphite and MC_SHP. The graphite phase at 2600°C was about 11% in proportion but fell with decreasing temperature to a negligible amount. It solidified above 2600°C. The MC_SHP phase also solidified above 2600°C and was about ~24% at 2600°C and 50% at 800°C. The FCC_A1 phase solidified last, at about 1060°C, making it the last phase to form. The summary of the phase proportions are given in Table 6.12.

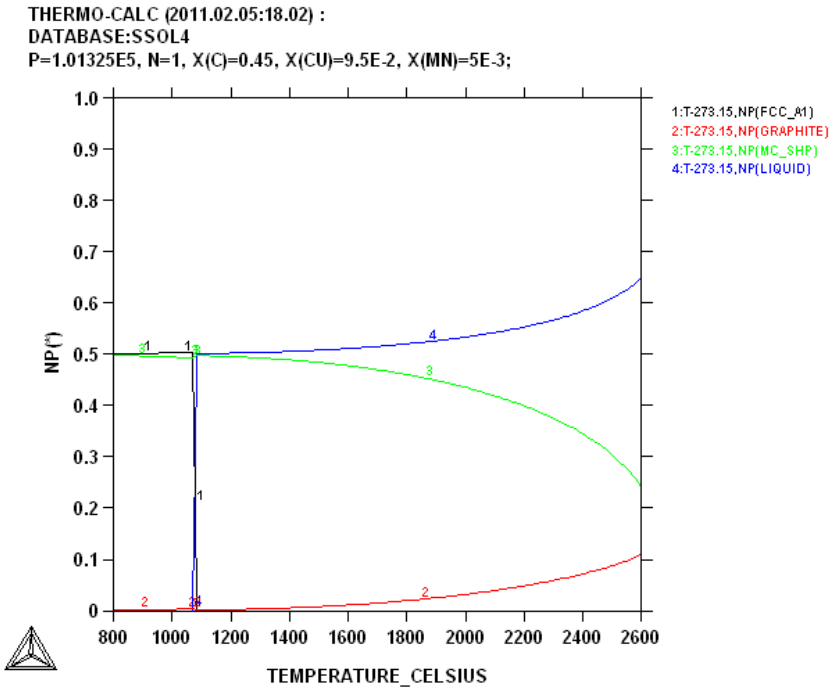


Figure 6.32. Phase proportion of W_{45}:C_{45}:$Mn_{0.5}$:$Cu_{9.5}$ (at.%).

	Maximum stability (°C)	Minimum stability (°C)	Maximum proportion	Minimum proportion
FCC_A1	1040	<800	~0.50	~0.00
MC_SHP	>2600	<800	~0.50	~0.24
GRAPHITE	>2600	<800	~0.12	~0.00

Table 6.12. Summary of phase proportion of W_{45}:C_{45}:$Mn0.5$:$Cu_{9.5}$ (at.%).

The FCC_A1 (Figure 6.33) was a (Cu) solid solution [1990Mas] which was composed of almost 99% copper with ~1% dissolved manganese, and neglegible tungsten and carbon.

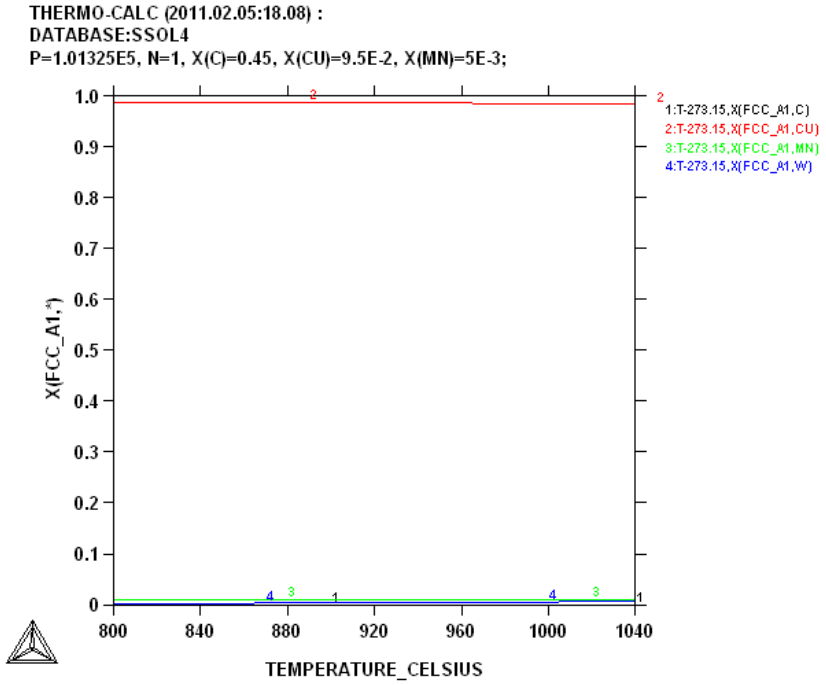


Figure 6.33. Composition diagram of the FCC_A1 for W_{45}:C_{45}:$Mn0.5$:$Cu_{9.5}$ (at.%).

The calculation showed MC_SPH was stoichiometric WC. The diagram was the same as Figure 6.2.

The graphite phase was pure 100% carbon. This was similar to Figure 6.6.

The temperatures for the solidifiation range of the binder phase are presented in Table 6.13. This could be useful for sintering of the various materails. The carbide phase is also included to verify that WC would be formed.

Sample	Binder	Binder composition (at.%)	Solidification range (°C)	Carbide phase
$W_{45}:C_{45}:Ni_{9.5}:V_{0.5}$	(Ni)	~10	1350-1400	WC
$W_{45}:C_{45}:Ni_{8.6}:V_{1.4}$	(Ni)	~9	1420-1440	WC
$W_{45}:C_{45}:Ni_{8.5}:Zn_{1.5}$	(Ni)	~10	1180-1310	WC
$W_{45}:C_{45}:Ni_{9.0}:Zn_{1.0}$	(Ni)	~10	1240-1340	WC
$W_{45}:C_{45}:Co_{6}:Mn_{4}$	(Co)	~10	1000-1020	WC and Co_6W_6C
$W_{45}:C_{45}:Co_{2.5}:Mn_{7.5}$	(Co)	~10	1080-1100	WC and Co_6W_6C
$W_{45}:C_{45}:Cu_{8.5}:Ni_{1.5}$	(Cu,Ni)	~10	1140-1180	WC
$W_{45}:C_{45}:Cu_{8}:Ni_{2}$	(Cu,Ni)	~10	1160-1200	WC
$W_{45}:C_{45}:Cu_{9}:Zn_{1}$	(Cu,Zn)	~10	1040-1060	WC
$W_{45}:C_{45}:Cu_{9.5}:Zn_{0.5}$	(Cu,Zn)	~10	1060-1070	WC
$W_{45}:C_{45}:Mn_{5}:V_{5}$	(Mn,W)?	~8	1300-1860	WC and V3C2
$W_{45}:C_{45}:Mn_{0.5}:Cu_{9.5}$	(Cu,Mn))	~50	1060-1080	WC

Table 6.13. Calculated solidification temperature ranges for all the binder phases, and carbide compositions.

6.2 50% Binder replacement

These calculations were done with the aim of understanding the experimental microstructure in terms of how they solidified. Thus, the phases that were formed on solidification and those that formed on heat treatment were identified.

6.2.1 $W_{25}:C_{25}:Ni_{45}:V_5$ (at.%)

The calculated phase proportion diagram for $W_{25}:C_{25}:Ni_{45}:V_5$ (at.%) is shown in Figure 6.34. The calculation showed four stable phases, namely: FCC_A1#1, FCC_A1#2, MC-SHP and graphite. Graphite exists in the high temperature region, and started solidification above 2600°C and disappeared by 2000°C. The FCC_A1#1 phase was second to solidify, at about 2450°C and transformed to FCC_A1#2 at about 2180°C. The liquid solidified to form FCC_A1#2. The FCC_A1#1 phase was in the highest proportion, the MC_SHP carbide

which started solidifying at about 2380°C was second highest in proportion forming ~44% at 800°C. The summary for the phase proportion diagram is given in Table 6.14.

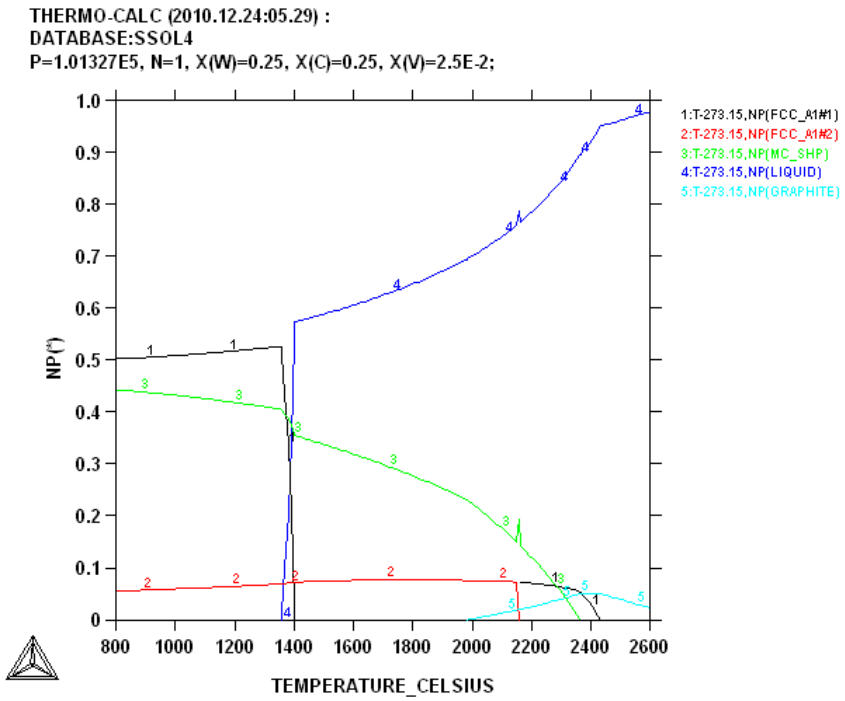


Figure 6.34. Phase proportions of W_{25}:C_{25}:Ni_{45}:V_5 (at.%).

	Maximum stability (°C)	Minimum stability (°C)	Maximum proportion	Minimum proportion
FCC _A1#1	1400	<800	~0.50	~0.00
FCC _A1#1	2450	2200	~0.08	~0.00
FCC_A1#2	2180	<800	~0.06	~0.07
MC_SHP	2420	<800	~0.45	~0.00
GRAPHITE	>2600	2000	~0.06	~0.00

Table 6.14. Summary of phase proportions of W_{25}:C_{25}:Ni_{45}:V_5 (at.%).

The low temperature FCC_A1#1 phase (Figure 5.35) appearing at 1400°C-800°C was mainly composed of nickel, which was about 95% of the phase at 800°C. Tungsten formed about 5% of the phase at 800°C. The carbon was a maximum of 4% and decreased to almost a negligible amount at 800°C. Vanadium was almost 5% with W and C being negligible. The

phase was identified to be (Ni), the solid solution based on nickel with less than 10% other elements [1990Mas].

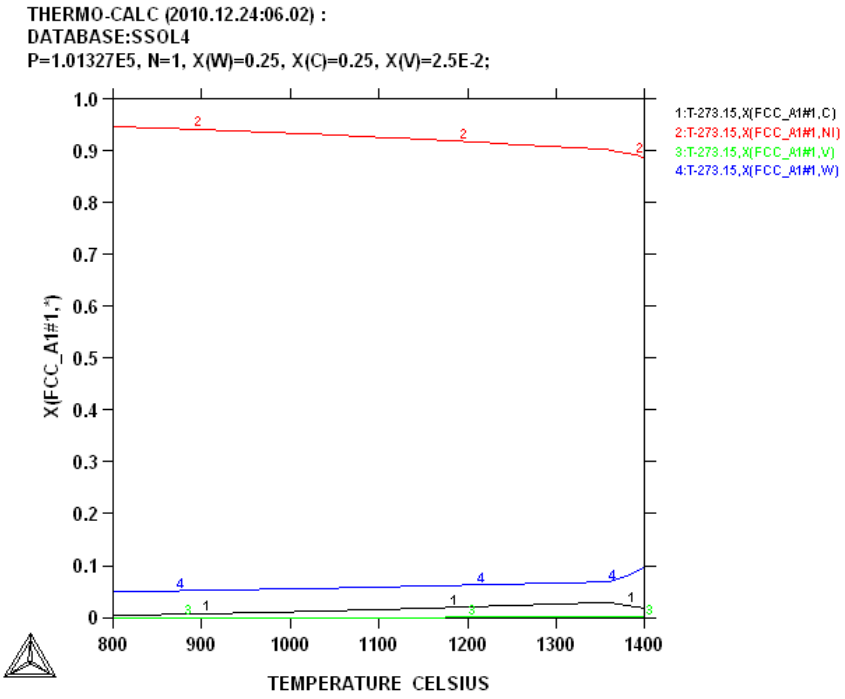


Figure 6.35. Composition of the FCC_A1#1 at 800-1400ºC for W_{25}:C_{25}:Ni_{45}:V_5 (at.%).

The high temperature FCC_A1#1 started solidification at about 2450°C, forming 8% soon after. The phase seemingly transformed to FCC_A1#2 at about 2200°C. Figure 6.36 shows the composition of the high temperature FCC_A1#1 phase. The composition of carbon and tungsten at 2370°C was about ~41%. A negligible amount of the nickel was present in the FCC_A1#1 phase at high temperature. The phase was identified as WC with V.

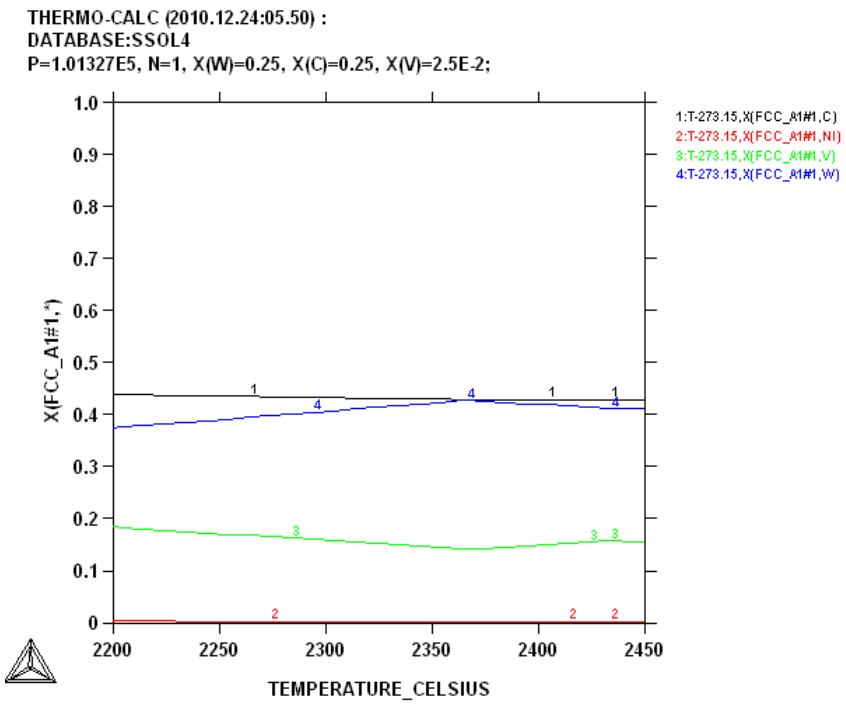


Figure 6.36. Composition of FCC_A1#1 at 2200-2450^{o}C for W_{25}:C_{25}:Ni_{45}:V_5 (at.%).

Figure 6.37 shows the phase composition of the FCC_A1#2 phase present at high temperatures. Carbon had the highest proportion of the phase with initial proportion of ~45% at 2000°C. Vanadium was next after the carbon, with a proportion of about 45%. The vanadium content increased with decreasing temperature, while tungsten decreased with decreasing temperature forming ~8% of the phase at 800°C. Nickel was about 0.01% in the phase. This was a carbide with W and V replacing each other (WC/VC).

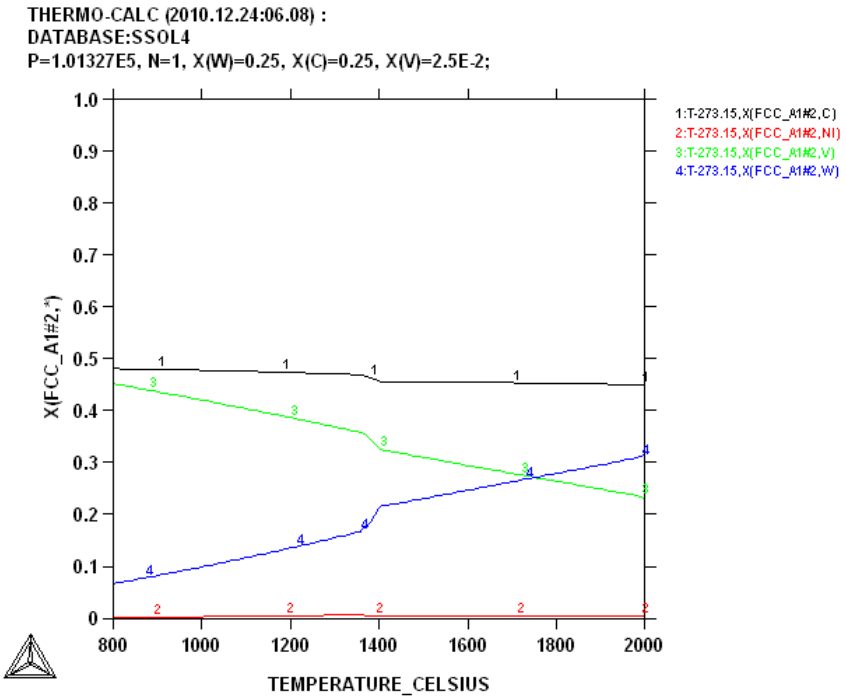


Figure 6.37. Composition of FCC_A1#2 for W_{25}:C_{25}:Ni_{45}:V_5 (at.%).

The graphite phase (Figure 6.38) was composed of almost 100% carbon with a negligible amount of the other elements.

Figure 6.39 indicates the MC_SHP phase which is stoichiometric WC, with negligible dissolved other elements.

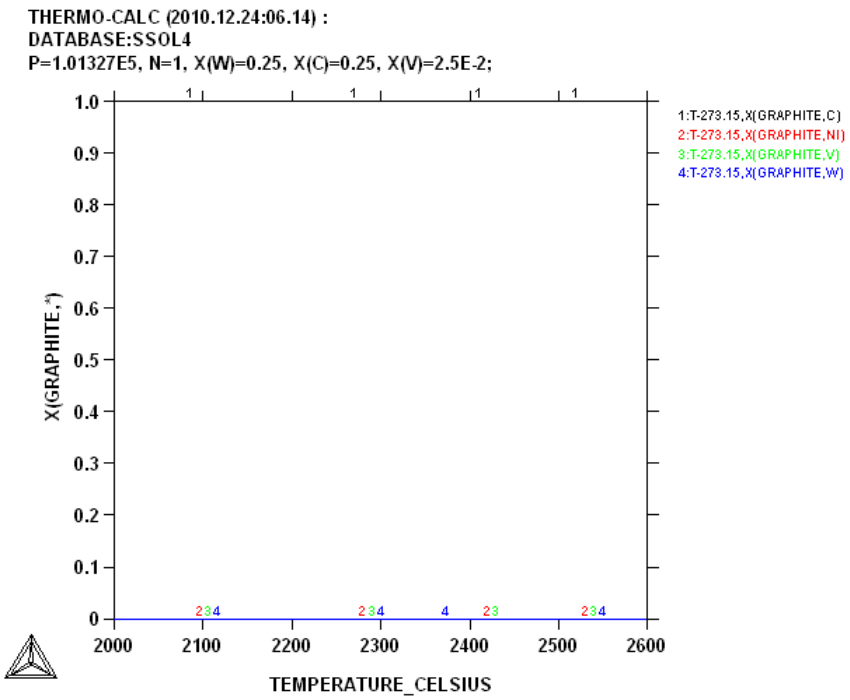


Figure 6.38. Composition of graphite for W_{25}:C_{25}:Ni_{45}:V_5 (at.%).

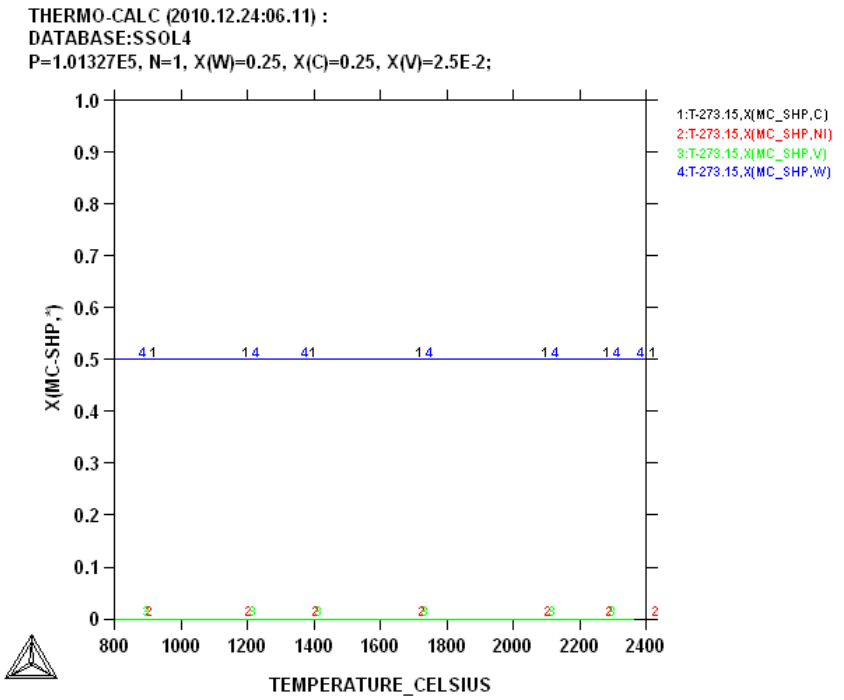


Figure 6.39. Composition of MC_SHP for W_{25}:C_{25}:Ni_{45}:V_5 (at.%).

The phases were studied at 1000ºC experimentally by heat treating and quenching in water. The phase proportions and compositions of all the stable phases at 1000ºC in the calculation were tabulated to see what the possible heat treated phases would be. Table 6.15 gives the three stable phases and their proportions at 1000ºC in nominal sample W_{25}:C_{25}:Ni_{45}:V_5 (at.%). The composition of the FCC_A1#1 and FCC_A1#2 phases differed slightly at 800ºC and 1000ºC. The MC_SHP and graphite were WC and carbon respectively (Table 6.15).

Phase description	**Compositions (at.%)**				**Phase deduced**	**Proportions (at.%) at 1000ºC**
	W	**C**	**Ni**	**V**		
FCC_A1#1	~5.0	~1.0	~94.0	~0.0	(Ni)	~52
MC_SHP	~50.0	~50.0	~0.0	~0.0	WC	~42
FCC_A1#2	~10.0	~48.0	~0.0	~42.0	VC with W	~6

Table 6.15. Phases, compositions and proportions at 1000ºC for W_{25}:C_{25}:Ni_{45}:V_5 (at.%).

6.2.2 W_{25}:C_{25}:Ni_{43}:V_7 (at.%)

The calculation of the phase proportions for W_{25}:C_{25}:Ni_{43}:V_7 (at.%) showed three stable phases, as shown in Figure 6.40. The FCC_A1#2 phase was the first to solidify at a very high temperature of about 2590°C. This phase attained a maximum proportion of ~32% at a temperature slightly below 2200°C. Graphite was next to solidify; the phase was only stable over a short temperature range (2210°C-2500°C) and formed a negligible amount. The next to solidify was the MC_SHP (carbide) phase at about 2150°C. The FCC_A1#1 phase started solidifying slightly above 1400°C and formed almost 49% of the total composition. A summary of the phase proportions is given in Table 6.16.

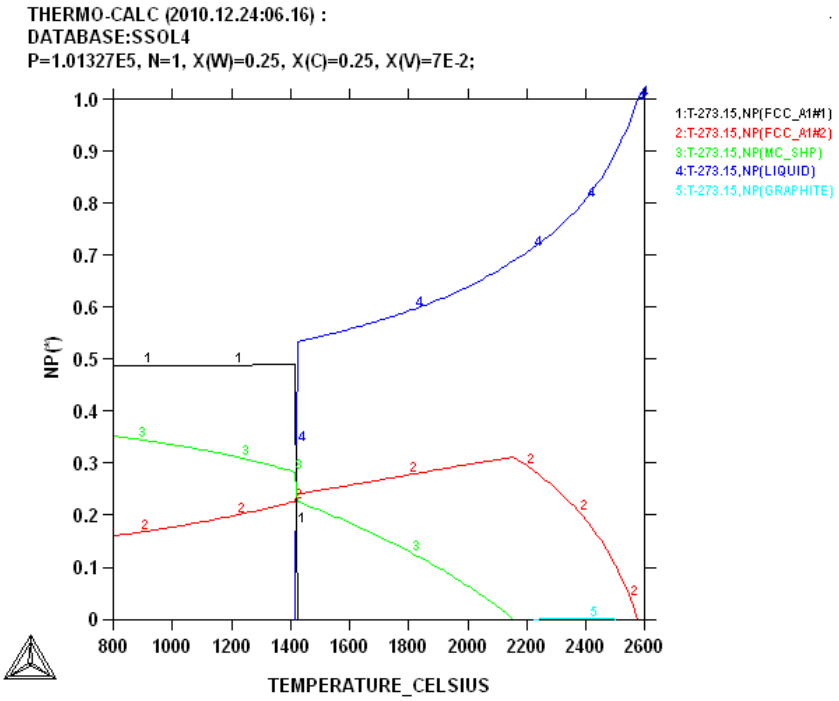


Figure 6.40. Phase proportions of $W_{25}:C_{25}:Ni_{43}:V_7$ (at.%).

	Maximum stability (°C)	Minimum stability (°C)	Maximum proportion	Minimum proportion
FCC _A1#1	1410	<800	~0.49	~0.00
FCC_A1#2	2580	<800	~0.32	~0.16
MC_SHP	2150	<800	~0.35	~0.00
GRAPHITE	2500	2210	~0.00	~0.00

Table 6.16. Summary of phase proportion of $W_{25}:C_{25}:Ni_{43}:V_7$ (at.%).

Figure 6.41 shows the composition of the FCC_A1#1 phase. Nickel formed about ~88% of the FCC_A1#1 phase at 800°C. Tungsten formed ~12% at the same temperature, and carbon and vanadium were almost negligible. Thus, FCC_A1#1 is (Ni), with some tungsten, carbon and vanadium.

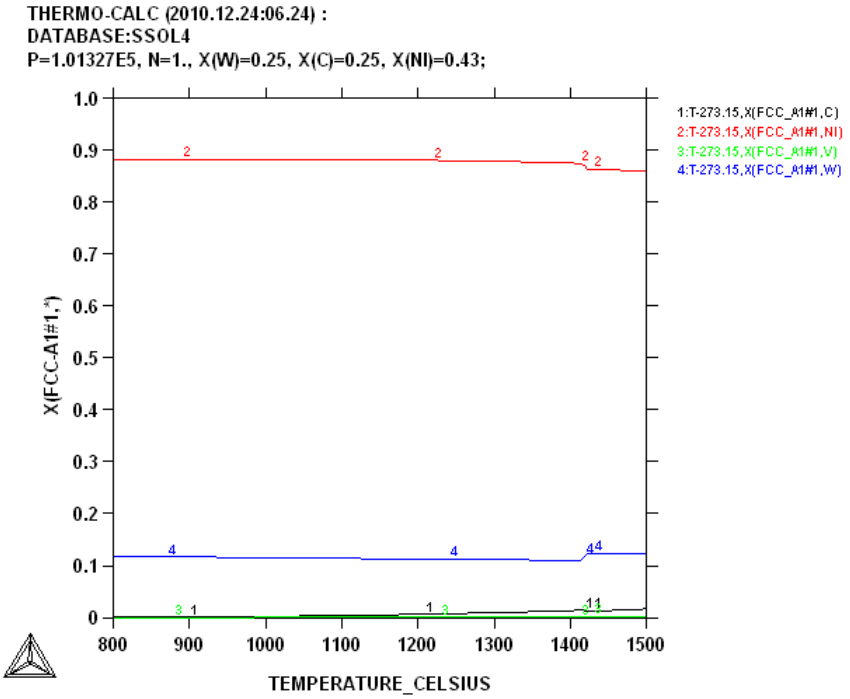


Figure 6.41. Composition of the FCC_A1#1 for W_{25}:C_{25}:Ni_{43}:V_7 (at.%).

The phase composition for FCC_A1#2 is shown in Figure 6.42. Carbon formed the major component of the phase at 800°C about ~46%. At about 2180°C, tungsten ~38%, and vanadium ~18% reached their maximum and minimum amounts respectively, and they substituted for each other. Nickel was around 1% of the phase. The phase was identified to be VC with W.

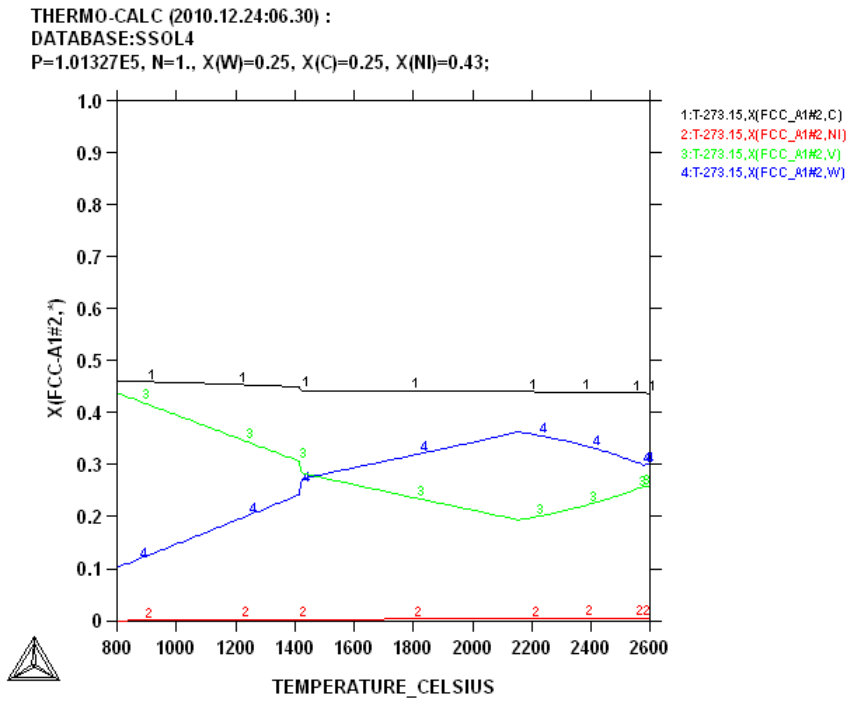


Figure 6.42. Composition of FCC_A1#2 at for W_{25}:C_{25}:Ni_{43}:V_7 (at.%).

The graphite phase was composed of pure carbon. The plot was similar to Figure 6.38.

The MC_SHP phase had 50 at.% W and 50 at.% C. This clearly indicated WC forming stoichiometrically, and the phase composition was the same as in Figure 6.39.

The alloy had three stable phases at 1000ºC. Their proportions slightly differed from the lower temperatures, and differed slightly in compostion from the phases at lower temperatures. The summary of the phase proportions, and their compositions with identified phases are given in Table 6.17.

Phase description	**Compositions (at.%)**				**Phase deduced**	**Proportions (at.%) at 1000ºC**
	W	**C**	**Ni**	**V**		
FCC_A1#1	~11.0	~0.0	~89.0	~0.0	(Ni)	~48
MC_SHP	~50.0	~50.0	~0.0	~0.0	WC	~18
FCC_A1#2	~14.0	~46.0	~0.0	~40.0	VC with W	~14

Table 6.17. Phases, compositions and proportions at 1000ºC for W_{25}:C_{25}:Ni_{43}:V_7 (at.%).

6.2.3 W_{25}:C_{25}:$Ni_{42.5}$:$Zn_{7.5}$ (at.%)

The W_{25}:C_{25}:$Ni_{42.5}$:$Zn_{7.5}$ (at.%) phase proportion calculation in Figure 6.43 showed three stable phases: FCC_A1, MC_SHP and the graphite phase. The liquid solidified to form FCC_A1 + graphite (sparse eutectic).

The high temperature graphite disappears at about 1800°C, falling from ~7%, the maximum proportion at 2410°C. The graphite reappears at about 1240°C, with a ~2% proportion down to 800°C. The MC_SHP increased with decreasing temperature as it solidified from the liquid; it formed ~47% at 800°C. The FCC_A1 phase was the last to solidify at about 1320°C. The FCC_A1 at 800°C had the highest proportion which was ~52%. Table 6.18 summarizes the phase proportions in Figure 6.43.

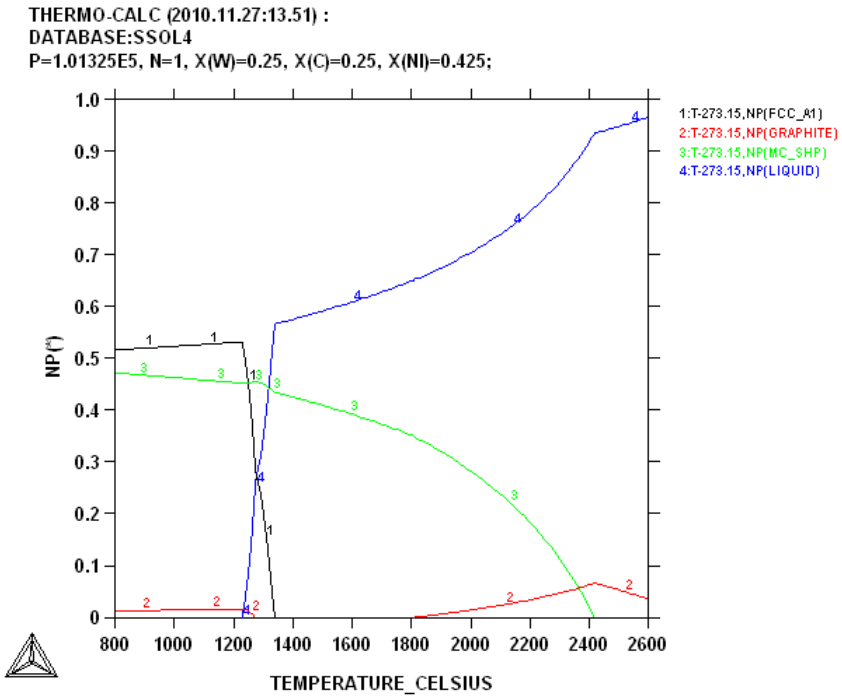


Figure 6.43. Phase proportions of W_{25}:C_{25}: $Ni_{42.5}$: $Zn_{7.5}$ (at.%).

	Maximum stability (°C)	Minimum stability (°C)	Maximum proportion	Minimum proportion
FCC_A1	1320	<800	~0.52	~0.00
GRAPHITE	1240	<800	~0.02	~0.00
GRAPHITE	>2600	1800	~0.07	~0.00
MC_SHP	2410	<800	~0.47	~0.00

Table 6.18. Summary of phase proportions of W_{25}:C_{25}: $Ni_{42.5}$: $Zn_{7.5}$ (at.%).

The FCC_A1 phase in Figure 6.44 shows nickel formed the bulk of the phase at 800°C, with a proportion of about ~87%. The zinc content was ~10% at 800°C. Tungsten formed only about 2% of the phase with carbon forming almost a negligible amount. The phase was identified as a solid solution of nickel, with dissolved amounts of the other elements; this was confirmed with the Ni-Zn binary phase diagram [1990Mas].

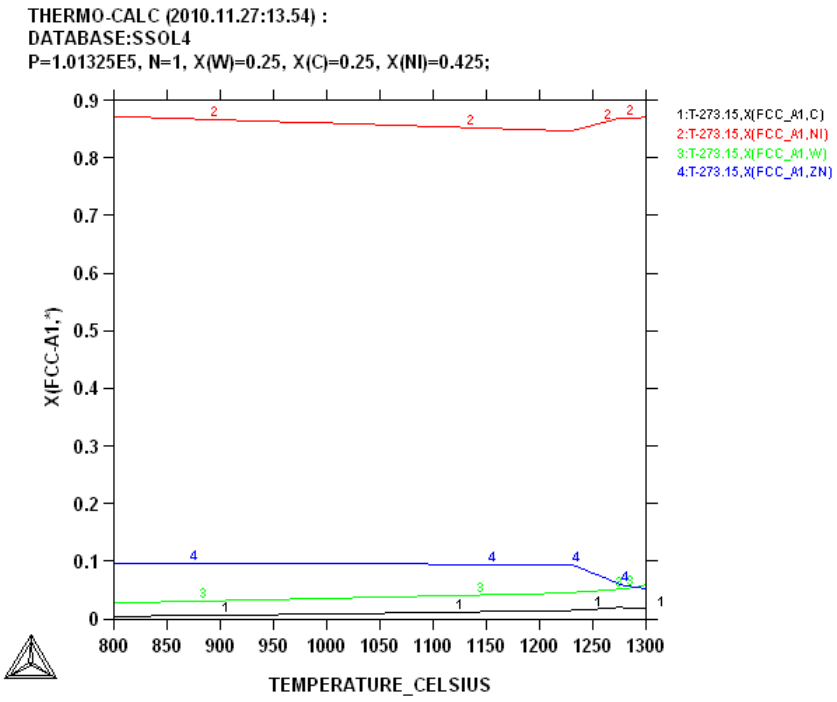


Figure 6.44. Composition of FCC_A1 for W_{25}:C_{25}: $Ni_{42.5}$: $Zn_{7.5}$ (at.%).

Two sets of calculations were done for the graphite phase; the high temperature graphite phase which disappeared at 1800°C and the low temperature graphite appearing at 1300°C. Both calculations showed that carbon was ~100%, with the other elements being negligible. The diagrams were similar to Figure.6.38.

The composition of the carbide phase (MC_SHP) comprised 50% W and 50% C (WC) and the plot was the same as Figure 6.39. There was a negligible nickel and zinc dissolved in the phase.

The FCC_A1, MC_SHP and graphite were the phases present at 1000ºC. The compositions of the graphite and the MC_SHP phases were similar throughout the entire temperature range of the calculations done, but the composition for the FCC_A1 phase slightly differed at 1000ºC and 800ºC. Table 6.19 gives summaries of the phase proportions, their compositions and the phases identified at 1000ºC.

Phase description	Compositions (at.%)				Phase deduced	Proportions (at.%) at 1000ºC
	W	C	Ni	Zn		
FCC_A1	~4.0	~1.0	~85.0	~9.0	(Ni)	~54
MC_SHP	~50.0	~50.0	~0.0	~0.0	WC	~45
Graphite	~0.0	~100.0	~0.0	~0.0	Graphite	~1

Table 6.19. Phases, compositions and proportions at 1000ºC for W_{25}:C_{25}:$Ni_{42.5}$: $Zn_{7.5}$ (at.%).

6.2.4 W_{25}:C_{25}:Ni_{45}:Zn_5 (at.%)

The phase proportion calculation for W_{25}:C_{25}:Ni_{45}:Zn_5 (at.%) in Figure 6.45 was similar to that of the nominal W_{25}:C_{25}:$Ni_{42.5}$:$Zn_{7.5}$ (at.%). This is due to the close compositions chosen. Three stable phases were revealed by the calculation. The graphite phase was the first to solidify, followed by the MC_SHP phase and the FCC_A1 phase was the last to solidify, starting at 1340°C. The summary of the phase proportion diagram is given in Table 6.20.

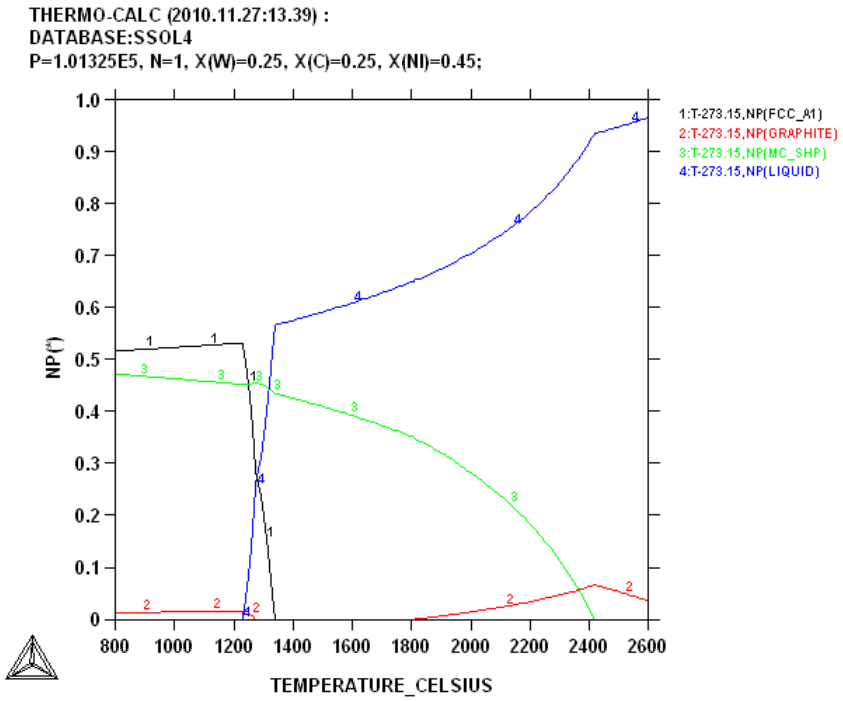


Figure 6.45. Phase proportions of W_{25}:C_{25}:Ni_{45}:Zn_5 (at.%).

	Maximum stability (°C)	Minimum stability (°C)	Maximum proportion	Minimum proportion
FCC_A1	1340	<800	~0.52	~0.00
GRAPHITE	1260	<800	~0.02	~0.00
GRAPHITE	>2600	1800	~0.07	~0.00
MC_SHP	2410	<800	~0.47	~0.00

Table 6.20. Summary of phase proportions of W_{25}:C_{25}:Ni_{45}:Zn_5 (at.%).

The FCC_A1 phase (Figure 6.46) comprised mainly nickel which formed close to 89% of the phase at 800°C, and zinc formed almost 10% of the phase. Tungsten and carbon comprised less than 5% of the phase. This phase was confirmed with Ni-Zn binary phase diagram [1990Mas] to be (Ni).

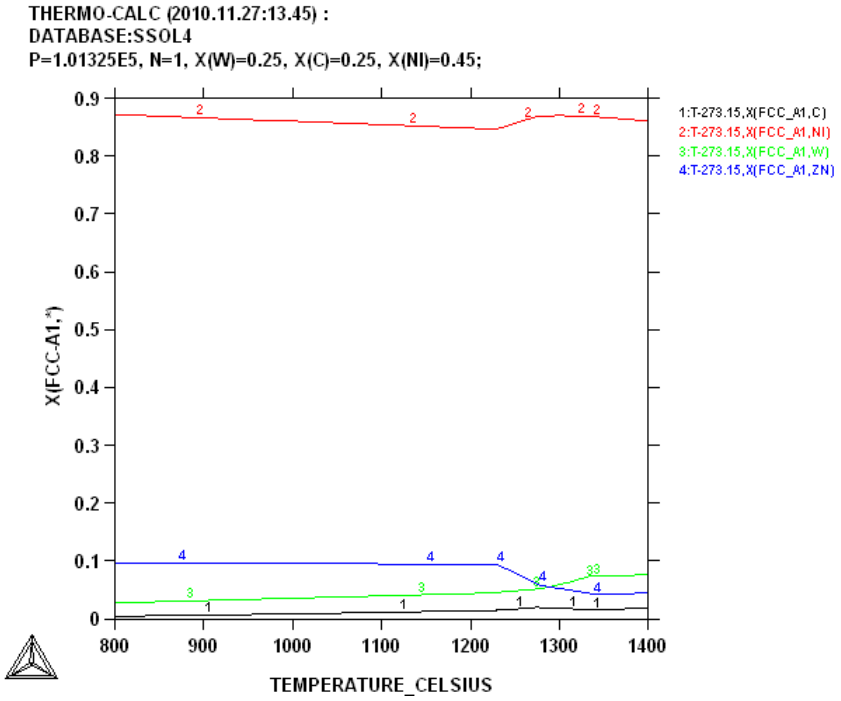


Figure 6.46. Composition of FCC_A1 for W_{25}:C_{25}:Ni_{45}:Zn_5 (at.%).

The MC_SHP phase had 50% W and 50% C. This clearly indicated WC forming stoichiometrically, and the phase composition was the same as in Figure 6.39.

The calculation for W_{25}:C_{25}:Ni_{45}:Zn_5 (at.%) showed three stable phases at 1000ºC, which are given in Table 6.21.

Phase description	Compositions (at.%)				Phase deduced	Proportions (at.%) at 1000ºC
	W	C	Ni	V		
FCC_A1	~4.0	~1.0	~86.0	~9.0	(Ni)	~53
MC_SHP	~50.0	~50.0	~0.0	~0.0	WC	~46
Graphite	~0.0	~100.0	~0.0	~0.0	Graphite	~1

Table 6.21. Phases, compositions and proportions at 1000ºC for W_{25}:C_{25}:Ni_{45}:Zn_5 (at.%).

6.2.5 W_{25}:C_{25}:Co_{30}:Mn_{20} (at.%)

The HCP_A3, MC_SHP and $M_{12}C$ phases were stable in the phase proportion calculation for W_{25}:C_{25}:Co_{30}:Mn_{20} (at.%), as shown in Figure 6.47. The MC_SHP phase was the first to solidify at about 2150°C; this phase increased gradually with decreasing temperature on solidification forming ~50% of the total composition at 800°C. The HCP_A3 phase solidified at a relatively lower temperature of about 1020°C and was also about ~50% at 800°C. The $M_{12}C$ phase was the last phase to solidify at around 1000°C and formed a very small proportion. Table 6.22 gives a summary of the phase proportions.

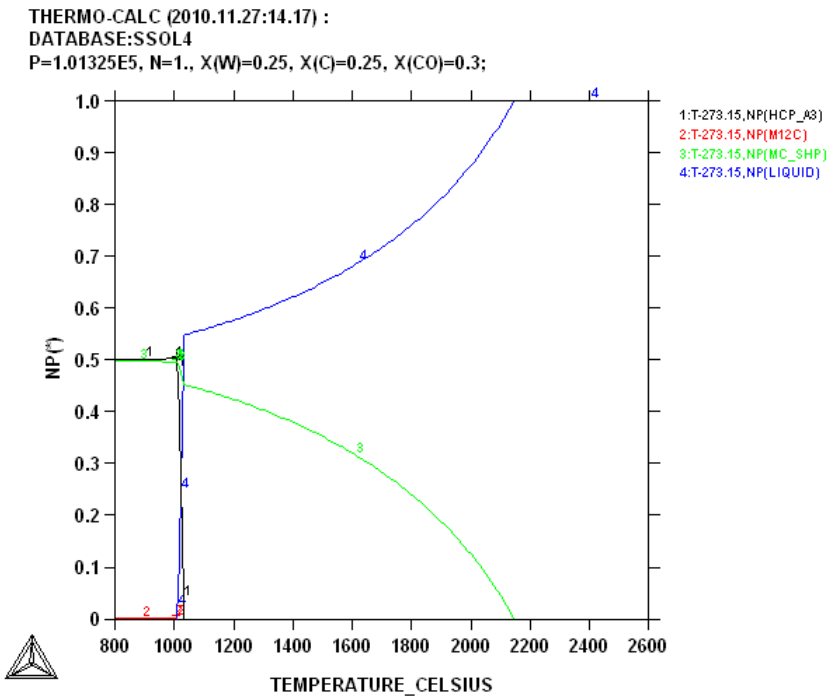


Figure 6.47. Phase diagram of W_{25}:C_{25}:Co_{30}:Mn_{20} (at.%).

	Maximum stability (°C)	Minimum stability (°C)	Maximum proportion	Minimum proportion
HCP_A3	1020	<800	~0.50	~0.00
$M_{12}C$	1000	<800	~0.00	~0.00
MC_SHP	2150	<800	~0.50	~0.30

Table 6.22. Summary of phase proportions of W_{25}:C_{25}:Co_{30}:Mn_{20} (at.%).

The HCP_A3 phase mainly comprised cobalt and manganese as shown in Figure 6.48. Cobalt formed ~60% of the phase at 800°C, while Mn formed almost ~40%. Cobalt increased to another ~5% at ~1040°C. Manganese decreased in proportion, simultaneously with cobalt increasing. The composition of the phase indicated a solid solution at the cobalt rich end, (Co). This was confirmed using the Co-Mn binary phase diagram [1990Mas].

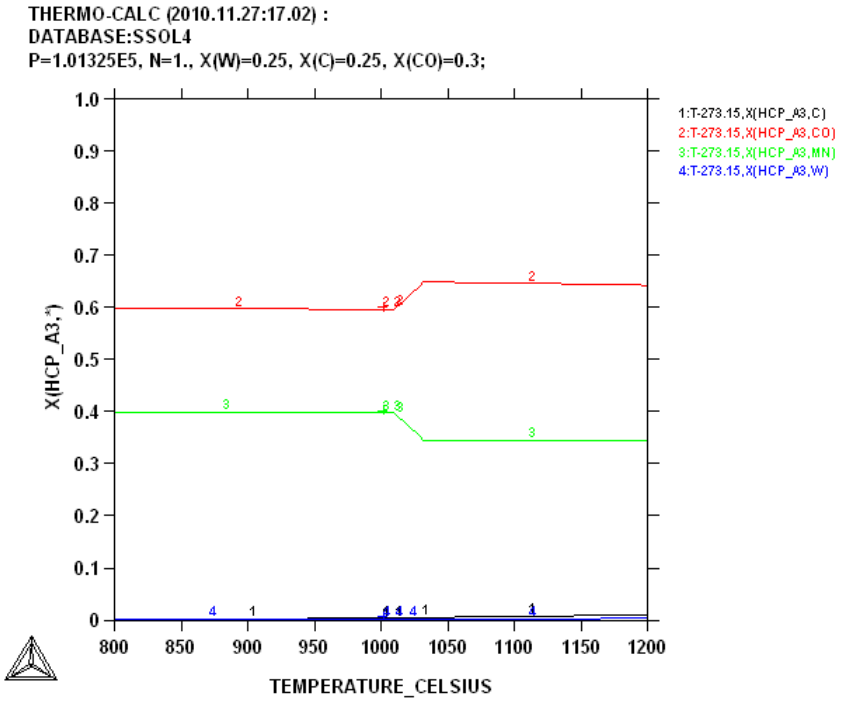


Figure 6.48. Composition of HCP_A3 for W_{25}:C_{25}:Co_{30}:Mn_{20} (at.%.).

The $M_{12}C$ phase was composed of the same amount of cobalt and tungsten, which was about ~45%, and carbon also formed about ~8% (Figure 6.49). The $M_{12}C$ carbide usually called eta phase and has a fixed composition of Co_6W_6C [1965Kre].

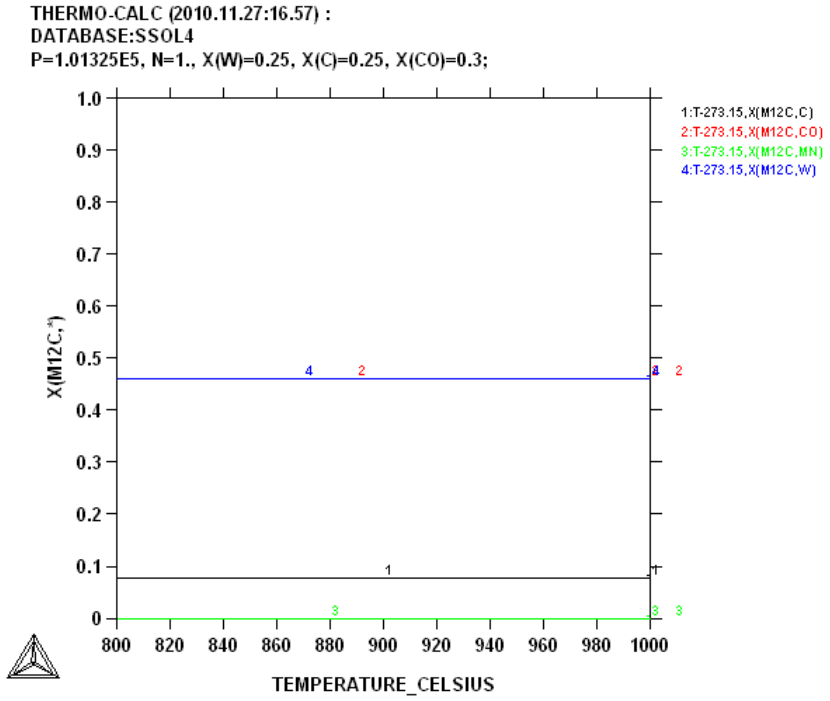


Figure 6.49. Composition of the $M_{12}C$ in W_{25}:C_{25}:Co_{30}:Mn_{20} (at.%).

The MC_SHP formed stoichiometric WC with negligible dissolved elements, and was the same as Figure 6.39.

The alloy at 1000ºC had three stable phases. Table 6.23 summarizes the phase proportions at 1000ºC.

Phase description	*Compositions (at.%)*				Phase deduced	Compositions (at.%) at 1000ºC
	W	C	Mn	Co		
HCP_A3	~0.0	~0.0	~40.0	~60.0	(Co)	~50
$M_{12}C$	~46.0	~8.0	~0.0	~46.0	Co_6W_6C	~0
MC_SHP	~50.0	~50.0	~0.0	~0.0	WC	~50

Table 6.23. Phases, compositions and proportions at 1000ºC for W_{25}:C_{25}:Co_{30}:Mn_{20} (at.%).

6.2.6 W_{25}:C_{25}:$Co_{12.5}$:$Mn_{37.5}$ (at.%)

The calculation for W_{25}:C_{25}:$Co_{12.5}$:$Mn_{37.5}$ (at.%) shows three stable phases comprising BCC_A2, HCP_A3 and MC_SHP as in Figure 6.50. The MC_SHP phase was the first to

solidify, at around 2190°C. The phase was about ~43% of the total composition of the system at 800ºC. Next to solidify was HCP_A3 phase, also around 1950°C; it increased until it attained a maximum of about ~39% and suddenly fell. The BCC_A2 phase was last phase to solidify around 1000°C. The reaction L + HCP_A3 → BCC + MC_SHP occurred at ~1000°C. It comprised almost 45% at 800°C. Table 6.24 gives a summary of the phase proportion diagram.

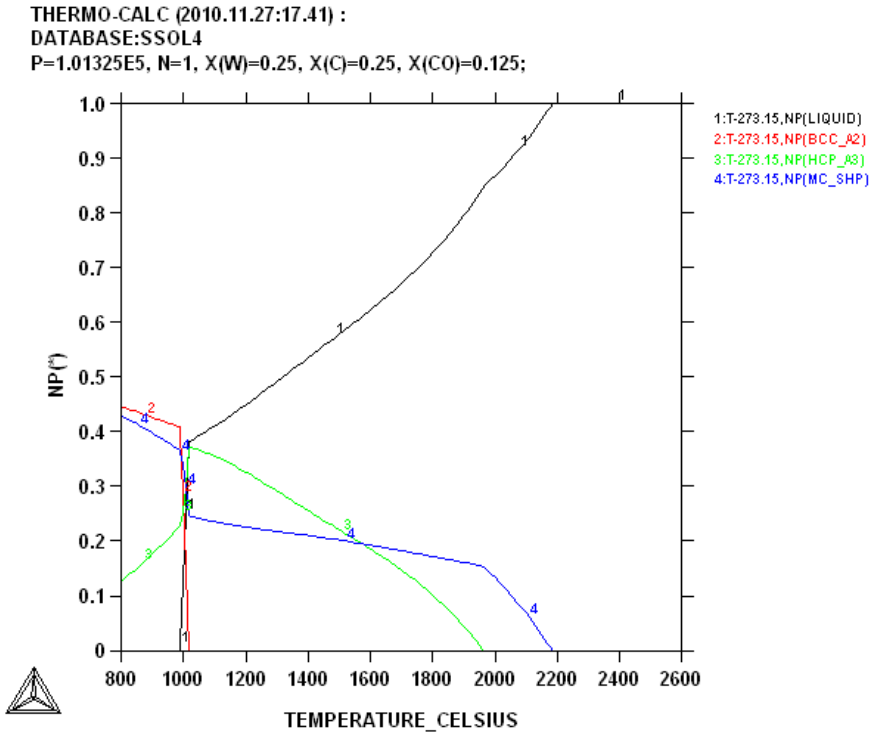


Figure 6.50. Phase proportions of $W_{25}:C_{25}:Co_{12.5}:Mn_{37.5}$ (at.%).

	Maximum stability (°C)	**Minimum stability (°C)**	**Maximum proportion**	**Minimum proportion**
BCC_A2	1020	<800	~0.45	~0.00
HCP_A3	1950	<800	~0.38	~0.00
MC_SHP	2190	<800	~0.43	~0.00

Table 6.24. Summary of phase proportions of $W_{25}:C_{25}:Co_{12.5}:Mn_{37.5}$ (at.%).

The bulk of the BCC_A2 phase was made up of manganese which formed almost 70% at 800°C as shown in Figure 6.51. Manganese was around 65% at 1040°C and gradually increased as the temperature decreased. Cobalt was next in proportion, and comprised about

~29% at 800°C, after falling from the maximum (~31%) at 1090°C. Tungsten and carbon formed less than 5% of the phase. The BCC_A2 phase was identified as a solid solution formed at the Mn rich end (Mn). This was confirmed by Co-Mn binary phase diagram [1990Mas].

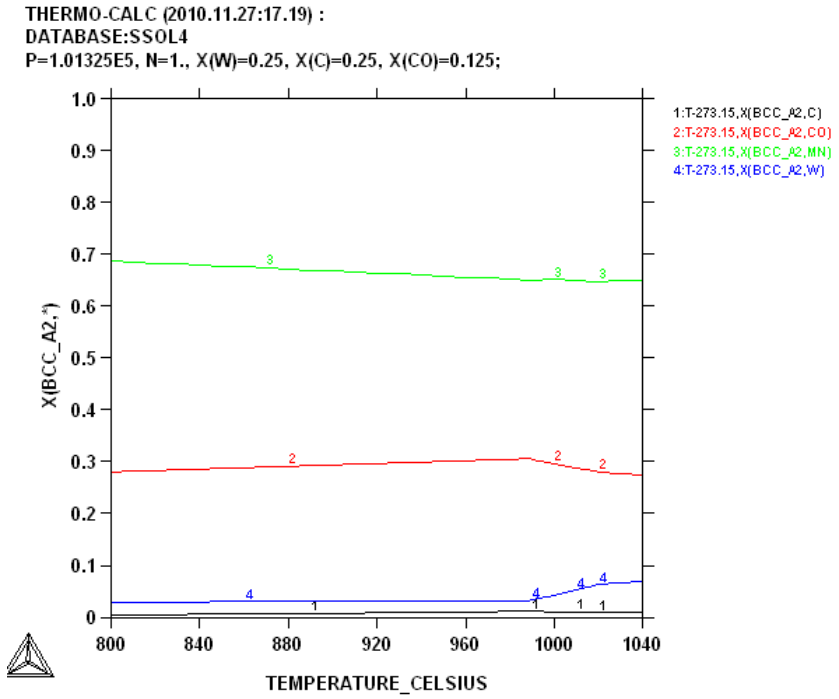


Figure 6.51. Composition of BCC_A2 for W_{25}:C_{25}:$Co_{12.5}$:$Mn_{37.5}$ (at.%).

Figure 6.52 shows the HCP_A3 composition with temperature. Tungsten had the highest proportion at 2000°C, which was about 55%, but decreased with decreasing temperature to about ~19% at 800°C, while manganese, which formed less than 15% of the phase at 2000°C, was about ~55% at 800°C. Carbon at 2000°C was about ~32% but slightly decreased as the temperature fell, to about ~27% at 800°C. Cobalt was present in the phase but was in a negligible proportion. This phase was a W and Mn carbide phase.

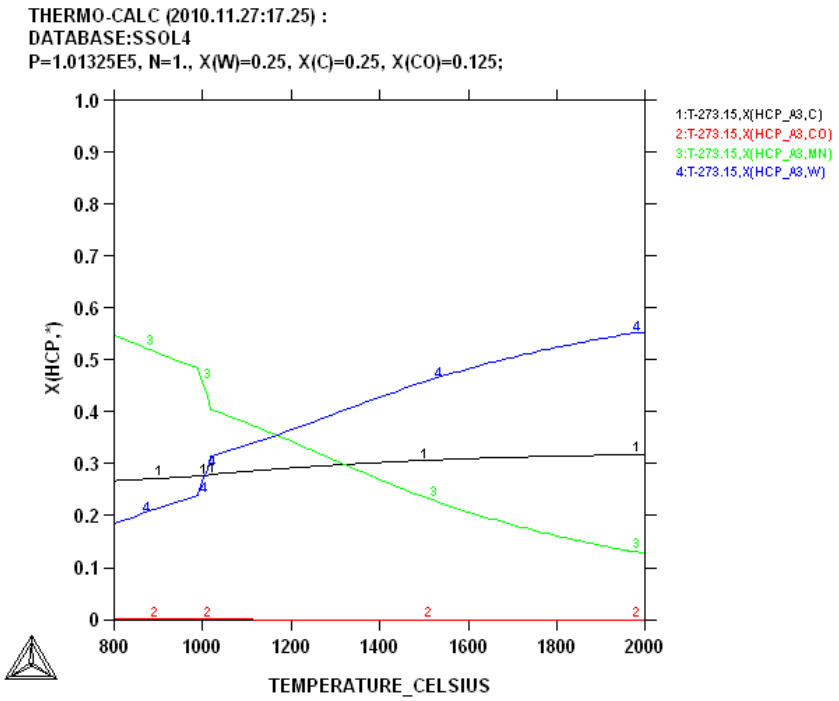


Figure 6.52. Composition diagram of HCP_A3 of W_{25}:C_{25}:$Co_{12.5}$:$Mn_{37.5}$ (at.%).

The calculation showed MC_SPH was stoichiometric WC, with negligible dissolved other elements. The diagram was the same as Figure 6.39.

Three phases: BCC_A2, HCP_A3 and MC_SHP were the stable phases in the material at 1000ºC. The phase proportions and their compositions are presented in Table 6.25.

Phase description	Compositions (at.%)				Phase deduced	Compositions (at.%) at 1000ºC
	W	C	Mn	Co		
BCC_A2	~5.0	~1.0	~64.0	~30.0	(Mn)	~42
HCP_A3	~24.0	~27.0	~49.0	~0.0	WMn_2C ?	~22
MC_SHP	~50.0	~50.0	~0.0	~0.0	WC	~36

Table 6.25. Phases, compositions and proportions at 1000ºC for W_{25}:C_{25}:$Co_{12.5}$:$Mn_{37.5}$ (at.%).

6.2.7 W_{25}: C_{25}:$Cu_{42.5}$:$Ni_{7.5}$ (at.%)

The calculated W_{25}:C_{25}:$Cu_{42.5}$:$Ni_{7.5}$ (at.%) phase proportions (Figure 6.53) showed that the MC_SHP phase and the graphite phase started solidification above 2600°C. Graphite and the MC_SHP phase were about 14% at 2600°C. The graphite proportion decreased as the

temperature fell and was almost zero at 800°C, while the MC_SHP phase increased with decreasing temperature and formed ~50% of the total composition at 800°C. The FCC_A1 phase started solidifying at ~1190°C, and formed about 50% at 800°C. Table 6.26 gives a summary of the phase proportion diagram.

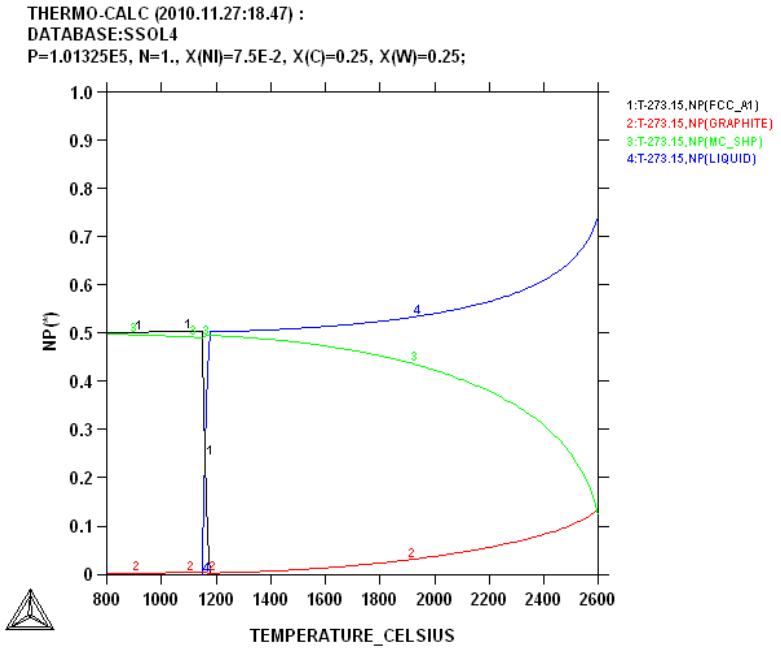


Figure 6.53. Phase proportions diagram of W_{25}: C_{25}:$Cu_{42.5}$:$Ni_{7.5}$ (at.%).

	Maximum stability (°C)	**Minimum stability (°C)**	**Maximum proportion**	**Minimum proportion**
FCC-A1	1190	<800	~0.50	~0.00
GRAPHITE	>2600	<800	~0.24	~0.00
MC_SHP	>2600	<800	~0.43	~0.24

Table 6.26. Summary of phase proportions of W_{25}:C_{25}:$Cu_{42.5}$:$Ni_{7.5}$ (at.%).

The phase composition calculation done for FCC_A1 shown in Figure 6.54 indicated a copper-nickel solid solution. Almost 85% of the phase was composed of copper at 800°C, and nickel comprised about ~15%. The copper and nickel contents were lower and higher respectively just after solidification. Tungsten and carbon formed almost a negligible amount of the phase.

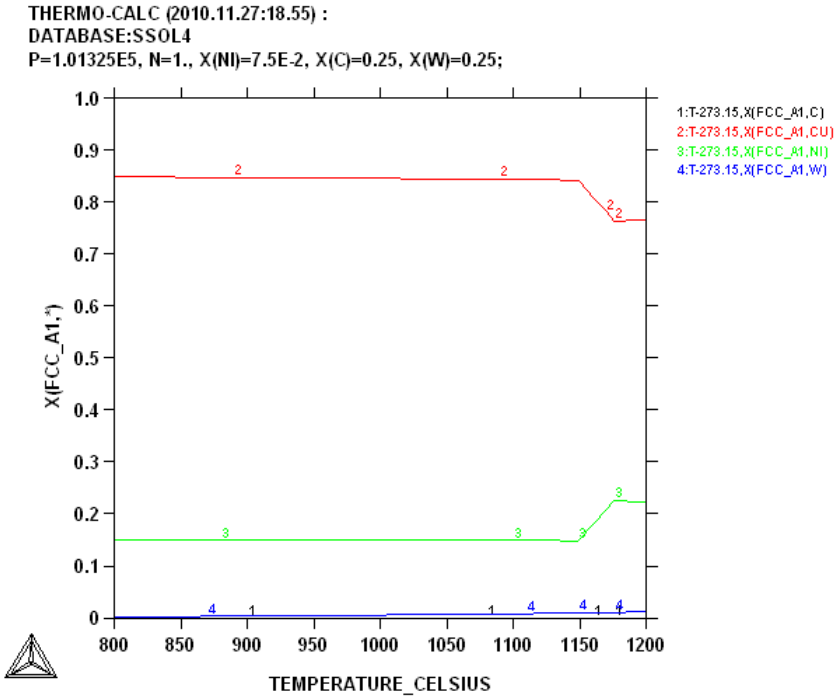


Figure 6.54. Composition of FCC_A1 for W_{25}: C_{25}:$Cu_{42.5}$:$Ni_{7.5}$ (at.%).

The graphite phase was composed of 100% carbon with no discernable other elements. The diagram was similar to Figure 6.38.

The MC_SHP was stoichiometric WC, and was the same as shown in Figure 6.39.

The calculation for the W_{25}:C_{25}:$Cu_{42.5}$:$Ni_{7.5}$ (at.%) composition showed three stable phases at 1000ºC. The last stable phase at 1000ºC was graphite, composed of carbon, which formed a negligible percentage of the material. The summary of the stable phases are given Table 6.27.

Phase description	**Compositions (at.%)**				**Phase deduced**	**Compositions (at.%) at 1000ºC**
	W	**C**	**Cu**	**Ni**		
FCC_A1#1	~0.0	~0.0	~85.0	~15.0	(Cu,Ni)	~51
MC_SHP	~50.0	~50.0	~0.0	~0.0	WC	~49
Graphite	~0.0	~100.0	~0.0	~0.0	Graphite	~0

Table 6.27. Phases, compositions and proportions at 1000ºC for W_{25}:C_{25}:$Cu_{42.5}$:$Ni_{7.5}$ (at.%).

6.2.8 W_{25}:C_{25}:Cu_{40}:Ni_{10} (at.%)

The FCC_A1, MC_SHP and graphite phases (Figure 6.55) were the stable phases present in the equilibrium calculation for nominal W_{25}:C_{25}:Cu_{40}:Ni_{10} (at.%). The graphite had a higher

proportion than MC_SHP at 2600ºC, but both solidified above 2600ºC. The FCC_A1 phase solidified last at about 1200ºC and formed ~50% of the alloy. The summary of the phase proportion is given in Table 6.28.

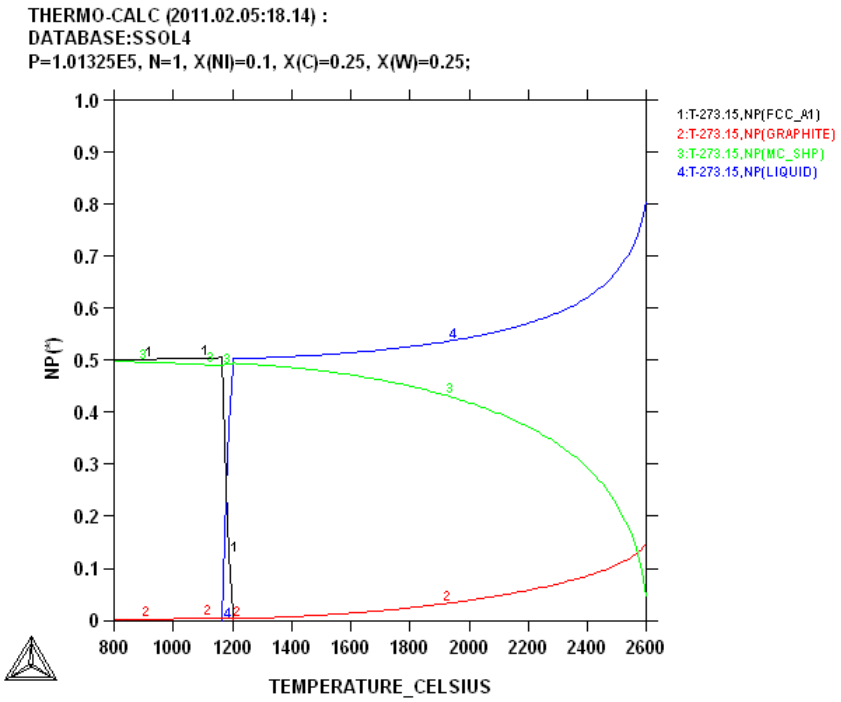


Figure 6.55. Phase proportions diagram of W_{25}:C_{25}:Cu_{40}:Ni_{10} (at.%).

	Maximum stability (°C)	**Minimum stability (°C)**	**Maximum proportion**	**Minimum proportion**
FCC-A1	1200	<800	~0.50	~0.00
GRAPHITE	>2600	< 800	~0.25	~0.00
MC_SHP	>2600	<800	~0.50	~0.05

Table 6.28. Summary of phase proportions of W_{25}:C_{25}:Cu_{40}:Ni_{10} (at.%).

At 1200°C, copper was about ~70% of the FCC_A1 phase; the proportion steadily increased to about ~80% and remained constant from about 1175°C to 800°C (Figure 6.56). The nickel, which was the second highest in the phase, decreased from about ~30% at 1200°C to a minimum ~20% at 1175°C. Nickel formed about ~20% of the FCC_A1 phase at 800°C. A very small percentage of carbon and tungsten was present. This phase was confirmed to be (Cu,Ni) using the Cu-Ni binary phase diagram [1990Mas].

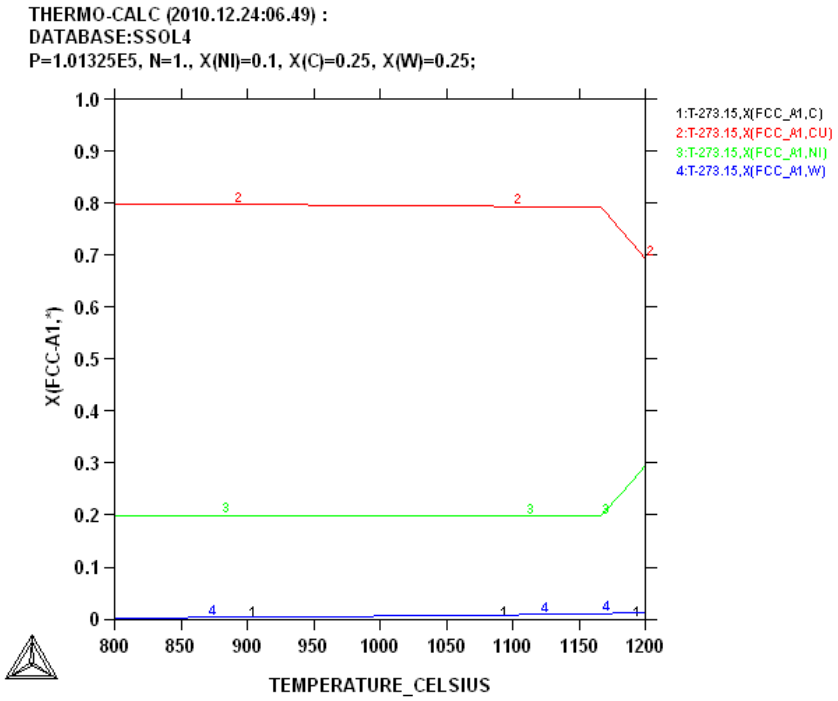


Figure 6.56. Composition of FCC_A1 for W_{25}:C_{25}:Cu_{40}:Ni_{10} (at.%).

The graphite phase was pure carbon, and the plot was the same as Figure 6.38.

The MC_SHP phase started solidifying above 2600°C and calculation of the phase composition for the nominal W_{25}:C_{25}:$Cu_{42.5}$:$Ni_{7.5}$ (at.%) revealed stoichiometric WC, the same as in Figure 6.39.

The FCC_A1, MC_SHP and the graphite were the phases present at 1000ºC. Table 6.29 gives summary of the phase proportions, and compositions and the phases identified at 1000ºC.

Phase description	**Compositions (at.%)**				**Phase deduced**	**Compositions (at.%) at 1000ºC**
	W	**C**	**Cu**	**Ni**		
FCC_A1	~0.1	~0.1	~79.9	~19.9	(Cu,Ni)	~51
MC_SHP	~50.0	~50.0	~0.0	~0.0	WC	~49
Graphite	~0.0	~100.0	~0.0	~0.0	Graphite	~0

Table 6.29. Phases, compositions and proportions at 1000ºC for W_{25}:C_{25}:Cu_{40}:Ni_{10} (at.%).

6.2.9 W_{25}:C_{25}:Cu_{40}:Zn_{10} (at.%)

The calculation for W_{45}:C_{45}:Ni_{40}:Zn_{10} (at.%) in Figure 6.57 had three stable phases, namely: MC_SHP, FCC_A1 and graphite. Graphite formed above 2600ºC and was about ~10% at 2600ºC. The graphite phase formed an insignificant proportion at 800ºC. The MC_SHP phase solidified above 2600ºC, and was 24% of phase proportions at 2600ºC. The MC_SHP and the FCC_A1 phase, which was last to start solidification (~1000°C), comprised almost ~50% of the total composition. Table 6.30 gives the summary of the phase proportions.

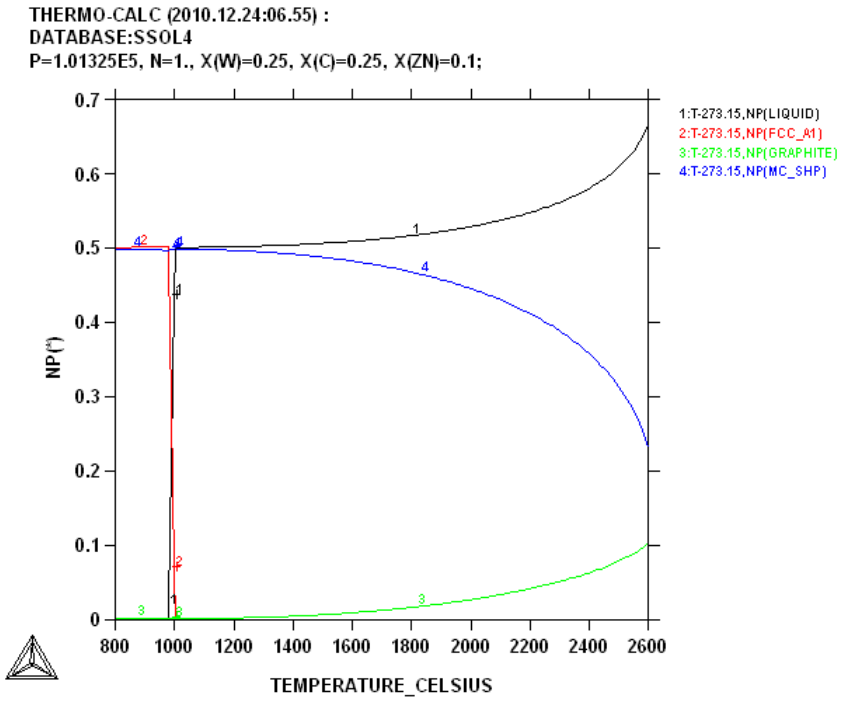


Figure 6.57. Phase proportions diagram of W_{25}:C_{25}:Cu_{40}:Ni_{10} (at.%).

	Maximum stability (°C)	**Minimum stability (°C)**	**Maximum proportion**	**Minimum proportion**
FCC-A1	1000	<800	~0.50	~0.00
GRAPHITE	<2600	<800	~0.20	~0.00
MC_SHP	<2600	<800	~0.50	~0.25

Table 6.30. Summary of phase proportions of W_{25}:C_{25}:Cu_{40}:Ni_{10} (at.%).

The FCC_A1 phase was composed of (Cu,Zn) with about 80% copper (Figure 6.58), while zinc formed almost 20%. Carbon and tungsten had negligible solubility in the (Cu,Ni) phase. This was confirmed by Cu-Zn binary phase diagram [1990Mas].

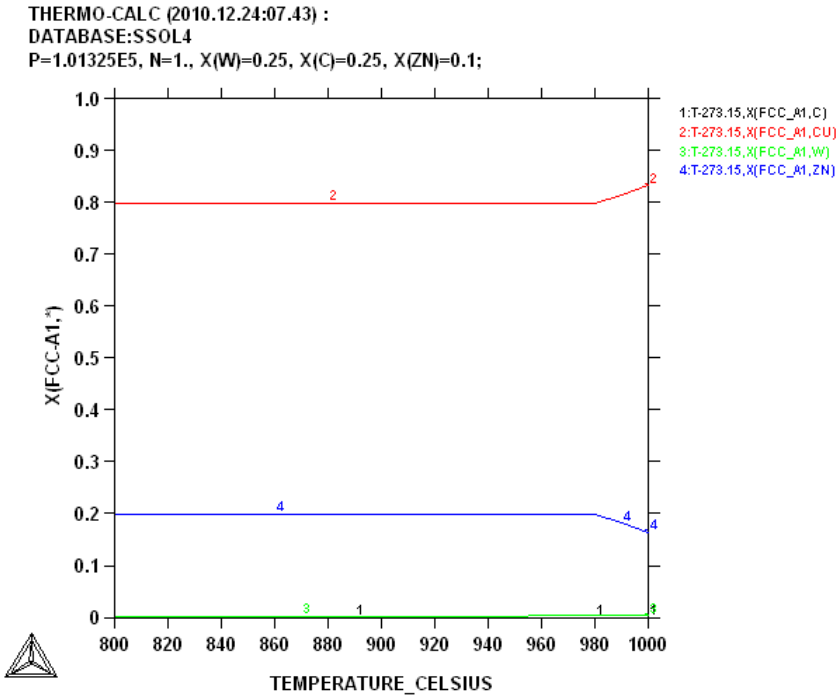


Figure 6.58. Composition of FCC_A1 for W_{25}:C_{25}:Cu_{40}:Zn_{10} (at.%).

Carbon was 100% of the graphite phase with the same plot as in Figure 6.38.

The MC_SHP phase was stoichiometric WC with negligible other elements, as in Figure 6.39.

The calculation for the nominal W_{25}:C_{25}:Cu_{40}:Zn_{10} (at.%) at 1000ºC revealed three stable phases. The summary of the stable phases are given Table 6.31.

Phase description	**Compositions (at.%)**				**Phase deduced**	**Compositions (at.%) at 1000ºC**
	W	**C**	**Cu**	**Zn**		
FCC_A1	~0.0	~0.0	83.0	~17.0	(Cu,Zn)	~50
MC_SHP	~50.0	~50.0	~0.0	~0.0	WC	~50
Graphite	~0.0	~100.0	~0.0	~0.0	Graphite	~0

Table 6.31. Phases, compositions and proportions at 1000ºC for W_{25}:C_{25}:Cu_{40}:Zn_{10} (at.%).

6.2.10 W_{25}:C_{25}:Cu:$_{45}$:Zn_5 (at.%).

The W_{25}:C_{25}:Cu:$_{45}$:Zn_5 (at.%) phase proportions calculated (Figure 6.59) had three phases, carbide (MC_SHP) and the graphite solidified above 2600ºC. The FCC_A1 phase, which was last to solidify at a much lower temperature (1020°C), formed ~50% at 800°C, just like MC_SHP. The proportions of the stable phases and their temperature ranges are given in Table 6.32.

The FCC_A1 phase (Figure 6.60) was mainly composed of copper which formed almost ~90%, with nickel following with a proportion of about ~10% at 800°C. Carbon and tungsten were present in the phase, but below 1%. The phase was identified as a solid solution of copper and zinc, from the Cu-Zn binary phase diagram [1990Mas].

The graphite phase was pure 100% carbon with no other elements. This was similar to Figure 6.38.

The MC_SHP phase had 50 at.% W and 50 at.% C; this clearly indicated WC forming stoichiometrically. The plot was the same as in Figure 6.39.

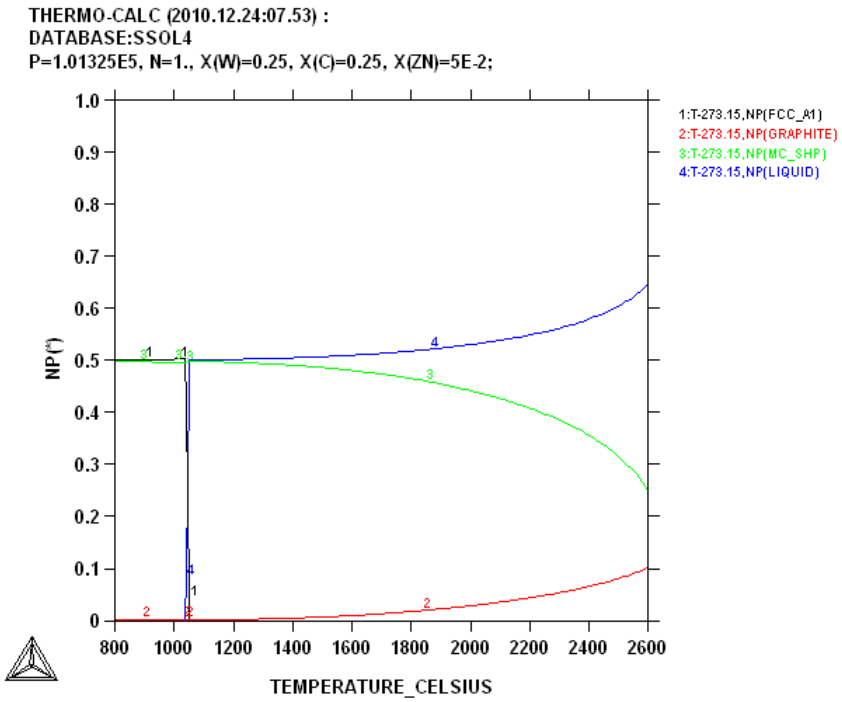


Figure 6.59. Phase proportions diagram of W_{25}:C_{25}:Cu:$_{45}$:Zn_5 (at.%).

	Maximum stability (°C)	Minimum stability (°C)	Maximum proportion	Minimum proportion
FCC-A1	1020	<800	~0.50	~0.00
GRAPHITE	>2600	<800	~0.21	~0.00
MC_SHP	>2600	<800	~0.50	~0.26

Table 6.32. Summary of phase proportions of W_{25}:C_{25}:$Cu_{:45}$:Zn_5 (at.%).

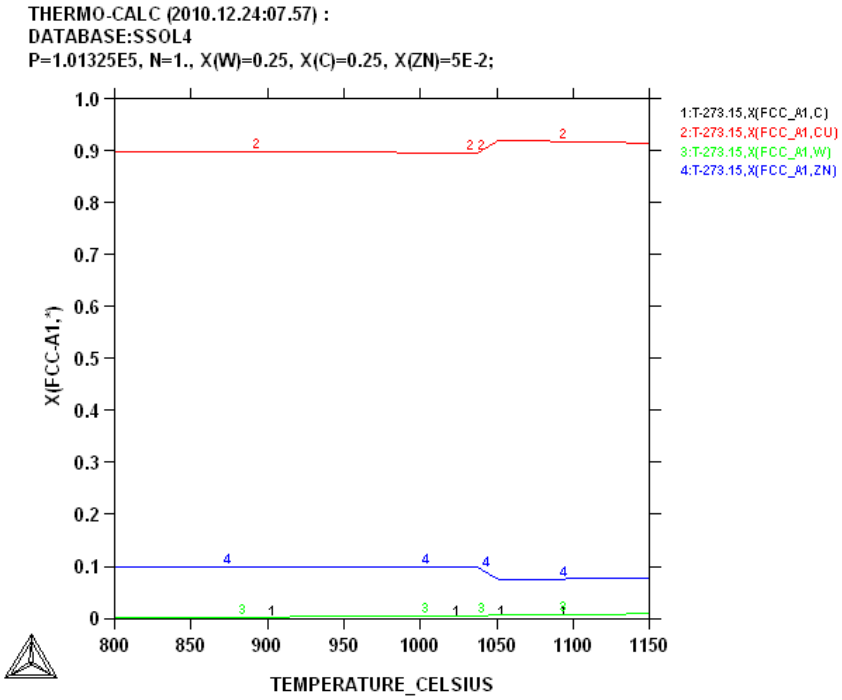


Figure 6.60. Composition of FCC_A1 for W_{25}:C_{25}:$Cu_{:45}$:Zn_5 (at.%).

The alloy at 1000ºC had three stable phases, including the binder FCC_A1 forming almost 50.1% of the alloy which was identified to be the (Cu,Zn) solid solution. Also present was the graphite phase, which formed a negligible proportion of the alloy, at 1000ºC. The MC_SHP phase which formed ~49.9% of the alloy was found to be WC. Table 6.33 summarises the phase proportions and the phase compositions at 1000ºC.

Phase description	Compositions (at.%)				Phase deduced	Compositions (at.%) at 1000°C
	W	C	Cu	Zn		
FCC_A1	~0.0	~0.0	~92.0	~8.0	(Cu,Zn)	~50
MC_SHP	~50.0	~50.0	~0.0	~0.0	WC	~50
Graphite	~0.0	~100.0	~0.0	~0.0	Graphite	~0.

Table 6.33. Phases, compositions and proportions at 1000°C for W_{25}:C_{25}:$Cu_{:45}$:Zn_5 (at.%).

6.2.11 W_{25}:C_{25}:Mn_{25}:V_{25} (at.%)

The calculation for W_{25}:C_{25}:Mn_{25}:V_{25} (at.%) in Figure 6.61 had three stable phases which were: V_3C_2, BCC_A2, and MC_SHP. The V_3C_2 formed the highest proportion of about 49% at 800°C, and was the first to solidify at slightly above 2000°C. The MC_SHP phase was next to solidify at about 1900°C, but formed the smallest proportion of the material. Shortly after the MC_SHP phase solidified, the BCC_A2 phase solidified at 1860°C. This shows that the binder phase solidifies at a very higher temperature, and so might not be appropriate for cobalt replacement cobalt since the sintering temperature will be very high for such a binder. This phase formed was ~40% at 800°C. The summary of the phase proportions is given in Table 6.34.

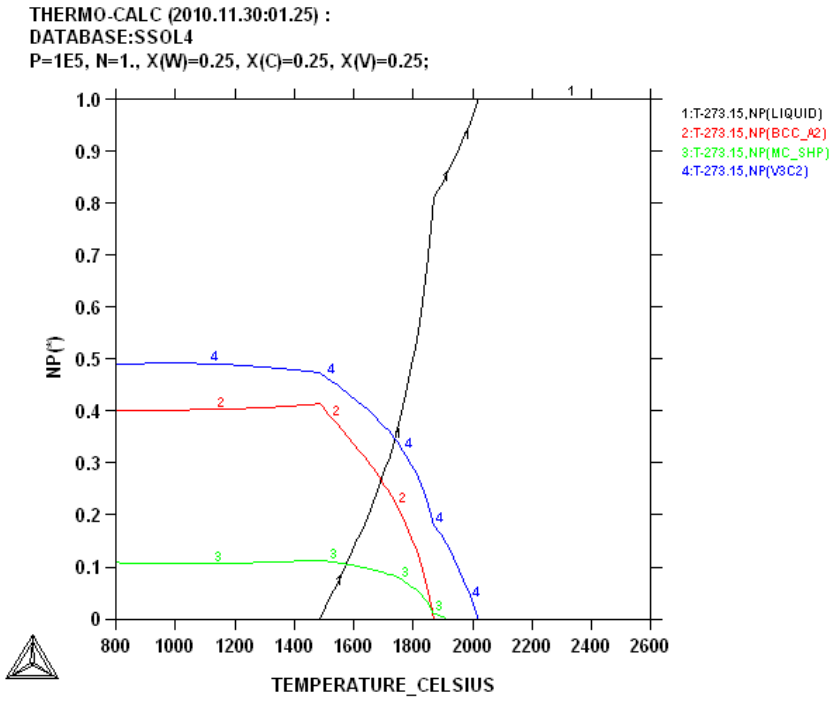


Figure 6.61. Phase proportions diagram of W_{25}:C_{25}:Mn_{25}:V_{25} (at.%).

	Maximum stability (°C)	Minimum stability (°C)	Maximum proportion	Minimum proportion
BCC-A2	1880	<800	~0.42	~0.40
V_3C_2	2010	<800	~0.49	~0.00
MC_SHP	1900	<800	~0.11	~0.00

Table 6.34. Summary of phase proportions of nominal W_{25}:C_{25}:Mn_{25}:V_{25} (at.%).

The BCC_A2 (Figure 6.62) phase comprised almost 51 at.% manganese and 49 at.% tungsten. The manganese had a lower proportion at higher temperatures, but increased with decreasing temperature, while the tungsten was the opposite. The phase contained vanadium and carbon above1600ºC, but they were negligible at 800ºC. This phase was assumed to be a solid solution of (Mn,W) since they both have similar crystal structure (BCC), although Miedema [Mie1976] deduced that no equilibrium phase was possible, and tungsten was found to be insoluble in liquid Mn [1901Sar, 1951Zwi].

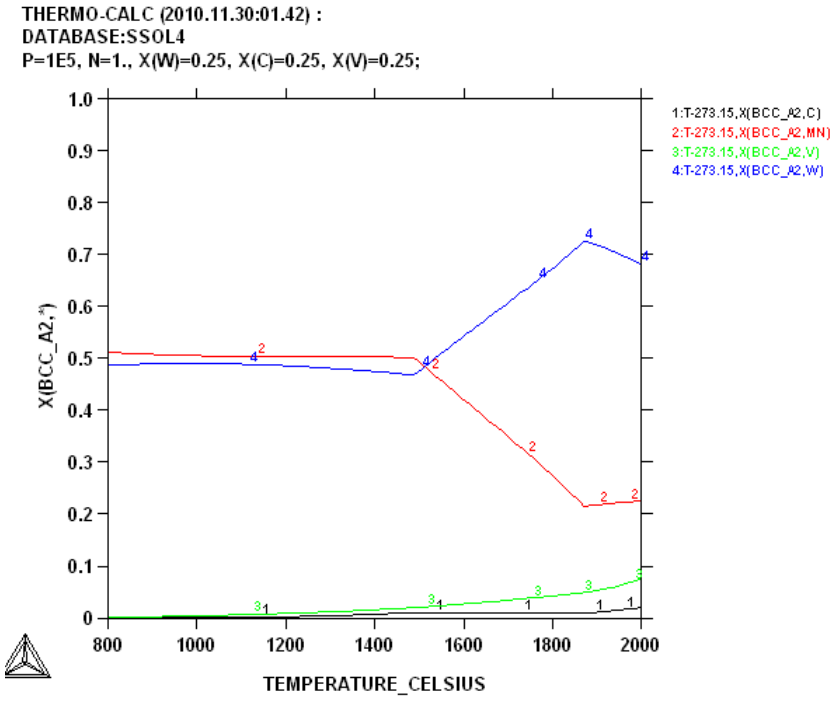


Figure 6.62. Composition of BCC_A2 for W_{25}:C_{25}:Mn_{25}:V_{25} (at.%).

The V_3C_2 phase was composed of vanadium, carbon, manganese and a negligible amount of tungsten (Figure 6.63). Vanadium was slightly above 50% of the phase, after decreasing in proportion at higher temperatures. The proportion of the carbon was constant, ~40%. The manganese increased as temperature decreased and was about 9% at 800ºC. The phase is suspected to be VC with of manganese.

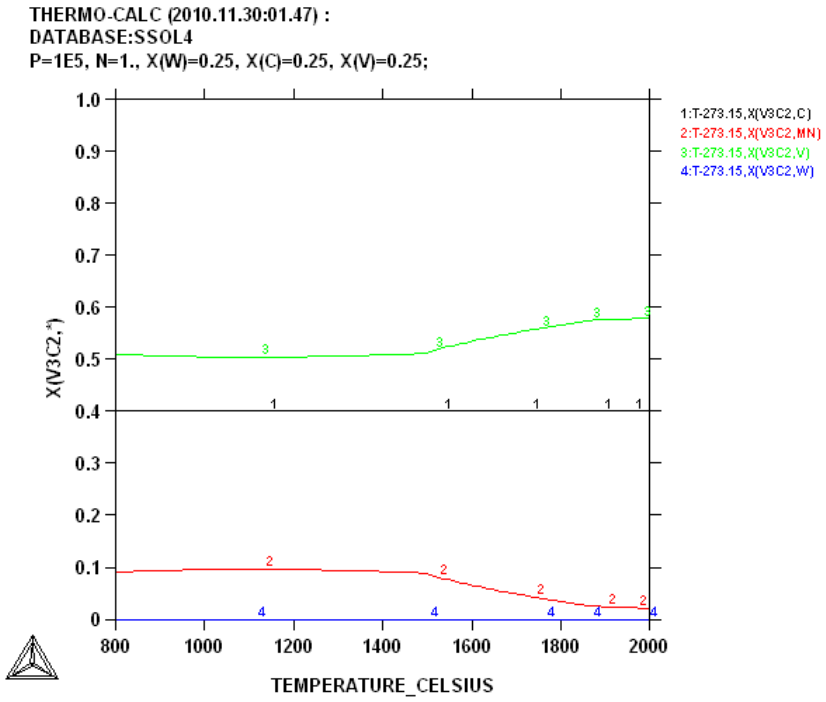


Figure 6.63. Composition of V_3C_2 for W_{25}:C_{25}:Mn_{25}:V_{25} (at.%).

The calculation showed MC_SPH was stoichiometric WC, with negligible dissolved other elements. The diagram was the same as Figure 6.39.

The BCC_A1, MC_SHP and V_3C_2 were the phases present at 1000ºC. The compositions of the MC_SHP phase was similar throughout the entire temperature range the calculations were done. The composition for the BCC_A1 phase slightly differed at 1000ºC and 800ºC, and was assumed to (Mn,W), as above. Table 6.35 gives summary of the phase proportions, and compositions and the phases identified at 1000ºC.

Phase description	Compositions (at.%)				Phase deduced	Proportions (at.%) at 1000ºC
	W	C	Mn	V		
BCC_A2	~49.0	~0.0	~51.0	~0.0	(Mn,W) ?	~40.
MC_SHP	~50.0	~50.0	~0.0	~0.0	WC	~12
V_3C_2	~0.0	~40.0	~9.0	~51.0	VC with Mn	~49

Table 6.35. Phases, compositions and proportions at 1000ºC for W_{25}:C_{25}:Mn_{25}:V_{25} (at.%).

6.2.12 W_{25}:C_{25}:$Mn_{2.5}$:$Cu_{47.5}$ (at.%)

The MC_SHP phase which formed ~50% of the alloy at 800ºC (Figure 6.64) was one of the three stable phases in the sample W_{25}:C_{25}:$Mn_{2.5}$:$Cu_{47.5}$ and it solidified above 2600ºC. The graphite also formed above 2600ºC but was in negligible proportion at 800ºC. The FCC_A1 phase solidified at a much lower temperature (1040ºC) and formed about 50% of the material. The summary of the phase proportions is presented in Table 6.36.

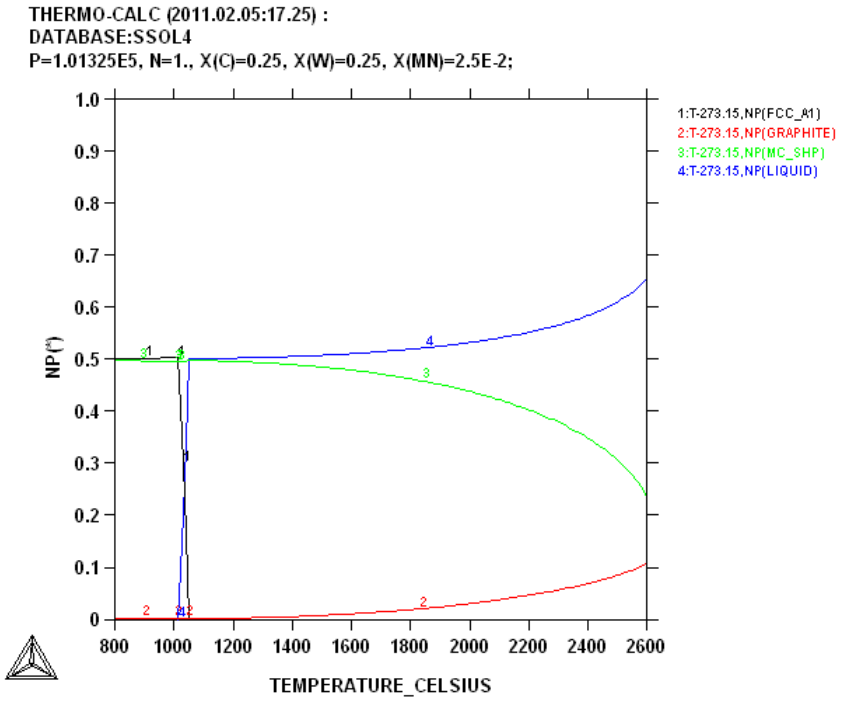


Figure 6.64. Phase proportions diagram of W_{25}:C_{25}:$Mn_{2.5}$:$Cu_{47.5}$ (at.%).

	Maximum stability (°C)	Minimum stability (°C)	Maximum proportion	Minimum proportion
FCC-A1	1040	<800	~0.51	~0.24
MC_SHP	>2600	<800	~0.50	~0.49
Graphite	>2600	<800	~0.11	~0.00

Table 6.36. Summary of phase proportions of W_{25}:C_{25}:$Mn_{2.5}$:$Cu_{47.5}$ (at.%).

The binder FCC_A1 (Figure 6.65) phase was identified as (Cu,Mn) [1990Mas]. Almost 95% of the phase was copper, while ~5% manganese was dissolved in the phase. The other elements formed a negligible portion of the phase.

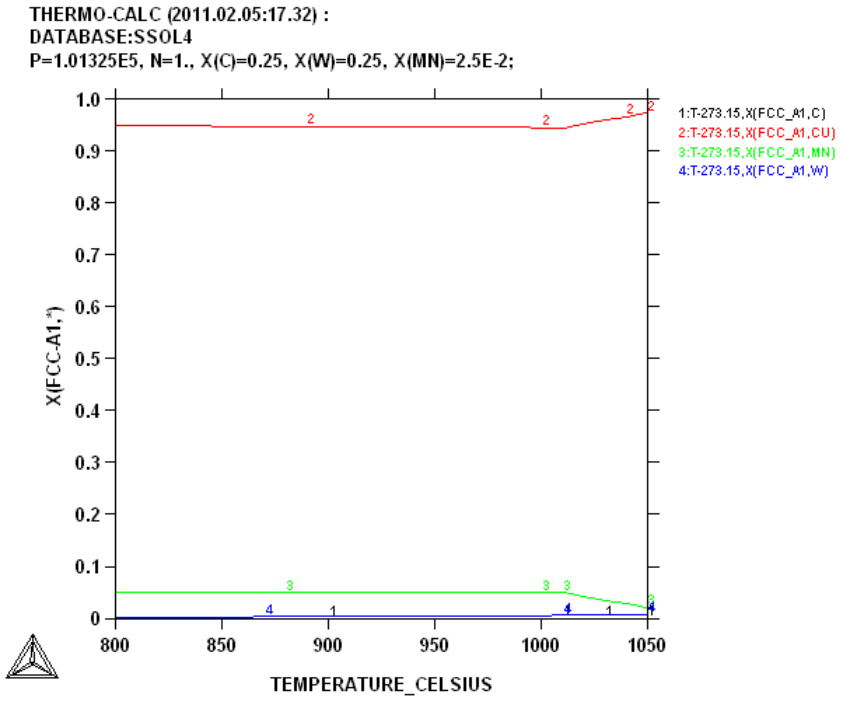


Figure 6.65. Composition of FCC_A1 for W_{25}:C_{25}:$Mn_{2.5}$:$Cu_{47.5}$ (at.%).

The graphite phase was pure 100% carbon. This was similar to Figure 6.38.

The MC_SHP phase had 50% W and 50% C; this clearly indicated WC forming stoichiometrically. The plot was the same as in Figure 6.39.

The calculation for the nominal W_{25}:C_{25}:$Mn_{2.5}$:$Cu_{47.5}$ (at.%) at 1000ºC revealed three stable phases. The summary of the stable phases are given Table 6.37.

Phase description	Compositions (at.%)				Phase deduced	Proportions (at.%) at 1000°C
	W	C	Cu	Mn		
FCC_A1	~0.0	~0.0	~95.0	~5.0	(Cu,Mn)	~50
MC_SHP	~50.0	~50.0	~0.0	~0.0	WC	~50
Graphite	~0.0	~100.0	~0.0	~0.0	Graphite	~0

Table 6.37. Phases, compositions and proportions at 1000ºC for W_{25}:C_{25}:$Mn_{2.5}$:$Cu_{47.5}$ (at.%).

Table 6.38 presents a summary of the solidification ranges for all the binder phases and the carbide formed.

Sample	Binder	Binder composition (at.%)	Solidification range (°C)	Carbide phase
W_{25}:C_{25}:Ni_{45}:V_5	(Ni)	50	1400-1360	WC
W_{25}:C_{25}:Ni_{43}:V_7	(Ni)	48	1420-1410	WC
W_{25}:C_{25}:$Ni_{42.5}$:$Zn_{7.5}$	(Ni)	52	1330-1220	WC
W_{25}:C_{25}:Ni_{45}:Zn_5	(Ni)	52	1340-1220	WC
W_{25}:C_{25}:Co_{30}:Mn_{20}	(Co)	50	1030-1010	WC and Co_6W_6C
W_{25}:C_{25}:$Co_{12.5}$:$Mn_{37.5}$	(Mn)	45	1020-990	WC and $WMnC_2$?
W_{25}:C_{25}:$Cu_{42.5}$:$Ni_{7.5}$	(Cu,Ni)	50	1180-1140	WC
W_{25}:C_{25}:Cu_{40}:Ni_{10}	(Cu,Ni)	50	1200-1140	WC
W_{45}:C_{45}:Ni_{40}:Zn_{10}	(Cu,Zn)	50	1010-980	WC
W_{25}:C_{25}:Cu:$_{45}$:Zn_5	(Cu,Zn)	50	1060-1040	WC
W_{25}:C_{25}:Mn_{25}:V_{25}	(Mn,W) ?	40	1880- 1490	WC and V_3C_2
W_{25}:C_{25}:$Mn_{2.5}$:$Cu_{47.5}$	(Cu,Mn))	50	1060-1010	WC

Table 6.38. Calculated solidification temperature ranges for all the binder phases and carbide compositions.

CHAPTER 7

DISCUSSION

7.1 Energy Dispersive Spectroscopy

Two different scanning electron microscopes, and hence energy dispersive spectroscopes (EDS) were used in these studies. These were the XL30 ESEM Philips SEM at the University of Botswana and LEO 1525 SEM at NMISA, Pretoria. A 20kV accelerating voltage was used in both SEMs and working distances between 9.2 mm and 16mm (for example, Figures 5.9 and 5.11a respectively) were used.

Standards for UB SEM-EDX were cut from the elements W, C, Ni, Cu and V from which samples were prepared. Tungsten carbide powder was compacted and used as a standard in the absence of pure carbide standards.

The first batch of as-cast samples were analysed with the XL30 ESEM Philips at UB suggested W_2C, which was confirmed by XRD. These were Samples $W_{25}:C_{25}:Ni_{45}:V_5$, $W_{25}:C_{25}:Ni_{43}:V_7$, $W_{25}:C_{25}:Cu_{42.5}:Ni_{7.5}$, $W_{25}:C_{25}:Ni_{43}:V_7$ and $W_{25}:C_{25}:Ni_{45}:Zn_5$. The second batch of samples analysed at UB (Samples $W_{25}:C_{25}:Cu_{40}:Ni_{10}$, $W_{45}:C_{45}:Ni_{40}:Zn_{10}$, $W_{25}:C_{25}:Co_{12.5}:Mn_{37.5}$, $W_{25}:C_{25}:Co_{30}:Mn_{20}$, $W_{25}:C_{25}:Mn_{2.5}:Cu_{47.5}$, $W_{25}:C_{25}:Mn_{25}:V_{25}$ and $W_{25}:C_{25}:Cu:_{45}:Zn_5$) were analysed with no standards; this was because the EDX was over-estimating carbon.

Some samples run at UB were also analysed at NMISA ($W_{25}:C_{25}:Ni_{45}:V_5$, $W_{25}:C_{25}:Ni_{42.5}:Zn_{7.5}$, $W_{25}:C_{25}:Ni_{43}:V_7$, $W_{25}:C_{25}:Ni_{45}:Zn_5$, $W_{25}:C_{25}:Co_{12.5}:Mn_{37.5}$, and $W_{25}:C_{25}:Co_{30}:Mn_{20}$) and most of the results were far apart from each other. The LEO 1525 SEM at NMISA was calibrated using a pure Ti standard; this was used in absence of pure W. The K line from Ti was used due to the fact that it had the least amount of errors, and the peak position was near the region of analysis close to W. The beam parameters, such as aperture size, were optimized to get good results for the analyses.

Two sets of analyses were done on the LEO 1525 SEM at NMISA, using preloaded carbon standards and also using a standard cut from VC for carbon. The carbon standard over-

estimated the carbon content extremely, while the pre-loaded standards, for which no information about conditions had been collected, gave many inconsistencies for carbon analyses. Thus, the EDX technique was not too reliable in these studies, due to the unavailability of good standards for the elements, especially carbon. However, XRD was used in most instances for the phase identification.

Table 7.1 gives the various EDX results from NMISA (pre-loaded standard and carbon standard) and EDX results from UB with standards derived from elements from which sample were made, and without standards.

Table 7.2 gives EDX analyses for the matrix from NMISA (pre-loaded standard and carbon standard) and EDX results from UB with standards derived from elements from which sample were made and without standards and analyses with standards.

The results in Tables 7.1 and 7.2 indicated analyses done at NMISA using pre-loaded standards had few of the phases been confirmed by XRD (e.g. W_{25}:C_{25}:$Co_{12.5}$:$Mn_{37.5}$, and W_{25}:C_{25}:Co_{30}:Mn_{20}). The carbon content seemed to be high, which made some of the EDX results doubtful.

Due to the inconsistencies observed in the carbon contents, a standard was made from VC (the only standard that became available) to correct the high carbon content, but the analyses done using a carbon standard from VC had extreme high carbon contents. Those results were completely ignored.

The EDX analysis in Table 7.1 done at UB using standards derived from elements from which samples were manufactured was much more reliable; most of the phases were confirmed by XRD. The second set of analyses done at UB without standards, were different from analyses which standards were used. There were many problems with the analyses, as shown in Appendix C (an e-mail from the scientist who runs the equipment).

Due to the various difficulties, not all samples were analysed for both conditions on both microscopes to select the most reliable results. In most cases, XRD was employed for phase identification. All heat treated samples were analysed at NMISA using pre-loaded standards.

The various analyses done showed that very good standards are needed for reliable EDX analyses. However, there were problems with both SEMs (Appendix C).

Sample	Condition	EDX results (at.%)				XRD
		UB (~WC-X)	Standards	NMISA (~WC-X)	Standards	
$W_{25}:C_{25}:Ni_{45}:V_5$	As-cast	$W_{72.4}:C_{23.8}:Ni_{2.9}:V_{4.1}$	From elements	$W_{23.5}:C_{75}:Ni_{1.2}:V_{0.3}$	Pre-loaded	W_2C
$W_{25}:C_{25}:Ni_{45}:V_5$	As-cast	$W_{57.2}:C_{39.8}:Ni_{2.1}:V_{0.9}$	No standards	Could not be analysed	No standards	W_2C
$W_{25}:C_{25}:Ni_{43}:V_7$	As-cast	$W_{0.0}:C_{0.0}:Ni_{0.0}:V_{0.0}$ (could not be analysed)	From elements	$W_{31.2}:C_{66.7}:Ni_{1.3}:V_{0.8}$	Pre-loaded	W_2C
$W_{25}:C_{25}:Ni_{43}:V_7$	As-cast	$W_{49.7}:C_{45.8}:Ni_{2.5}:V_{2.0}$	No standards	$W_{3.8}:C_{95.8}:Ni_{0.3}:V_{0.1}$	Carbon from VC	W_2C
$W_{25}:C_{25}:Ni_{42.5}:Zn_{7.5}$	As-cast	$W_{73.3}:C_{24.1}:Ni_{2.6}:Zn_{0.0}$ (high carbide proportion) $W_{69.4}:C_{28.2}:Ni_{2.4}:Zn_{0.0}$ (low carbide proportion)	From elements	$W_{31.3}:C_{67.3}:Ni_{1.4}:Zn_{0.0}$ (high carbide proportion)$W_{21.1}:C_{77.6}:Ni_{1.3}:Zn_{0.0}$ (low carbide proportion)	Pre-loaded	W_2C
$W_{25}:C_{25}:Ni_{42.5}:Zn_{7.5}$	As-cast	Could not be analysed	No standards	$W_{2.9}:C_{97.0}:Ni_{0.1}:Zn_{0.0}$ (high carbide proportion) $W_{1.9}:C_{97.8}:Ni_{0.3}:Zn_{0.0}$ (low carbide proportion)	Carbon from VC	W_2C
$W_{25}:C_{25}:Ni_{45}:Zn_5$	As-cast	Could not be analysed	From elements	$W_{15.4}:C_{83.7}:Ni_{0.9}:Zn_{0.0}$	Pre-loaded	W_2C
$W_{25}:C_{25}:Ni_{45}:Zn_5$	As-cast	$W_{53.4}:C_{45.4}:Ni_{1.2}:Zn_{0.0}$	No standards	Could not be analysed	No standards	W_2C
$W_{25}:C_{25}:Co_{30}:Mn_{20}$	As-cast	$W_{84.5}:C_{12.2}:Mn_{1.0}:Co_{2.3}$	No standards	$W_{51.8}:C_{45.4}:Mn_{0.6}:Co_{2.2}$	Pre-loaded	WC
$W_{25}:C_{25}:Co_{12.5}:Mn_{37.5}$	As-cast	$W_{58.2}:C_{37.5}:Mn_{3.2}:Co_{1.1}$	No standards	$W_{52.8}:C_{40.3}:Mn_{4.4}:Co_{2.5}$	Pre-loaded	WC

Table 7.1. EDX analyses of carbide phases showing results from UB, using standards made from elements which samples were prepared, UB analyses without standards, NMISA analyses using pre-loaded standards and NMISA analyses with carbon standard made from VC.

Sample	Condition	EDX results (at.%)				XRD
		UB (~WC-X)	Standards	NMISA (~WC-X)	Standards	
$W_{25}:C_{25}:Ni_{45}:V_5$	As-cast	$W_{17.2}:C_{0.0}:Ni_{78.7}:V_{4.1}$	From elements	$W_{5.5}:C_{62.8}:Ni_{30.2}:V_{1.5}$	Pre-loaded	Ni_3V
$W_{25}:C_{25}:Ni_{45}:V_5$	As-cast	$W_{14.5}:C_{21.6}:Ni_{60.8}:V_{3.1}$	No standards	Could not be analysed	No standards	Ni_3V
$W_{25}:C_{25}:Ni_{43}:V_7$	As-cast	$W_{10.1}:C_{7.1}:Ni_{73.1}:V_{9.7}$	From elements	$W_{6.4}:C_{60.2}:Ni_{31.2}:V_{2.2}$	Pre-loaded	Ni_2V
$W_{25}:C_{25}:Ni_{43}:V_7$	As-cast	$W_{8.2}:C_{29.5}:Ni_{55.2}:V_{7.1}$	No standards	$W_{0.9}:C_{90.5}:Ni_{7.5}:V_{1.1}$	Carbon from VC	Ni_2V
$W_{25}:C_{25}:Ni_{42.5}:Zn_{7.5}$	As-cast	$W_{16.3}:C_{11.3}:Ni_{72.4}:Zn_{0.0}$ (high carbide proportion) $W_{15.6}:C_{11.5}:Ni_{72.9}:Zn_{0.0}$ (low carbide proportion)	From elements	$W_{9.3}:C_{57.7}:Ni_{33.6}:Zn_{0.0}$ (high carbide proportion) $W_{7.7}:C_{58.4}:Ni_{33.9}:Zn_{0.0}$ (low carbide proportion)	Pre-loaded	(Ni)
$W_{25}:C_{25}:Ni_{42.5}:Zn_{7.5}$	As-cast	Could not be analysed	No standards	$W_{0.5}:C_{95.4}:Ni_{4.1}:Zn_{0.0}$ (high carbide proportion) $W_{1.9}:C_{93.9}:Ni_{5.2}:Zn_{0.0}$ (low carbide proportion)	Carbon from VC	(Ni)
$W_{25}:C_{25}:Ni_{45}:Zn_5$	As-cast	$W_{17.2}:C_{6.4}:Ni_{76.4}:Zn_{0.0}$	From elements	$W_{1.2}:C_{76.6}:Ni_{22.2}:Zn_{0.0}$	Pre-loaded	(Ni)
$W_{25}:C_{25}:Ni_{45}:Zn_5$	As-cast	$W_{14.0}:C_{29.3}:Ni_{56.7}:Zn_{0.0}$	No standards	Could not be analysed	No standards	(Ni)
$W_{25}:C_{25}:Co_{30}:Mn_{20}$	As-cast	$W_{12.0}:C_{20.2}:Mn_{8.5}:Co_{59.3}$	No standards	$W_{7.9}:C_{19.8}:Mn_{16.8}:Co_{55.5}$	Pre-loaded	(Co)
$W_{25}:C_{25}:Co_{12.5}:Mn_{37.5}$	As-cast	$W_{1.3}:C_{21}:Mn_{51.7}:Co_{26}$	No standards	$W_{6.8}:C_{17.6}:Mn_{47.9}:Co_{27.7}$	Pre-loaded	(Mn)

Table 7.2. EDX analyses of matrices showing results from UB, using standards made from elements which samples were prepared, UB analyses without standards, NMISA analyses using pre-loaded standards and NMISA analyses with carbon standard made from VC.

7.2 As-cast samples

The samples manufactured had 50% carbide and 50% binder alloy; this was done for easier melting and analysis. Most of the samples only had two phases as planned: carbide and matrix phases.

Alloy $W_{25:}C_{25}$:$Ni_{47.5}$:$V_{2.5}$ (at.%) had two types of dendrites, light ~W_2C carbides surrounded by ~Ni_3V (formerly (Ni)) dendrites. There were regions of eutectic ~W_2C + (Ni), and later the (Ni) transformed to ~Ni_3V on cooling. The eutectic ~Ni_3V had darker contrast than the ~Ni_3V dendrites. The differences in the phase compositions were small, and due to the difference in composition between a pro-eutectic solid and a eutectic component. Sample W_{25}:C_{25}:Ni_{43}:V_7 (at.%) differed a little in carbide proportions, but had the same elements. It had ~W_2C dendrites inside ~Ni_2V (originally (Ni)) dendrites, which was confirmed by XRD. The dark medium dendrites solidified as (Ni) and later transformed into ~Ni_2V, as shown by the Ni-V binary phase diagram [1990Mas]. The ~Ni_2V dendrites were cored due cooling in non-equilibrium conditions after arc-melting. Sample W_{25}:C_{25}:Ni_{43}:V_7 (at.%) had more vanadium, ~Ni_3V and no eutectic, whereas Sample $W_{25:}C_{25}$:$Ni_{47.5}$:$V_{2.5}$ (at.%) had less vanadium,~Ni_2V and a eutectic. The ~Ni_2V phase associated with the eutectic agrees with the phase diagram [1990Mas]. The ~Ni_3V in Sample $W_{25:}C_{25}$:$Ni_{47.5}$:$V_{2.5}$ (at.%) had no carbon, but had 17.2 at.% tungsten. Sample W_{25}:C_{25}:Ni_{43}:V_7 (at.%) had 6.8 at.% carbon in the Ni_2V, with 8.1 at.% tungsten.

Sample W_{25}:C_{25}:$Ni_{42.5}$:$Zn_{7.5}$ (at.%) and sample W_{25}:C_{25}:Ni_{45}:Zn_5 (at.%) lost Zn through evaporation. Zinc has a relatively low melting point compared to the other elements comprising the samples, therefore to attain complete melting, high temperatures were required, resulting in the evaporation of zinc. There could be a small amount of zinc left, but it was below the detection limit. Sample W_{25}:C_{25}:Ni_{45}:Zn_5 (at.%) had globular ~W_2C dendrites with medium (Ni) which was the bulk of the sample. Sample W_{25}:C_{25}:$Ni_{42.5}$:$Zn_{7.5}$ was inhomogeneous, with varying proportions of the globular carbide dendrites. The sample was treated as two separate regions for EDX analysis. Analyses were taken from both regions (high carbide proportion region and lower carbide proportion region). Both regions had ~W_2C and (Ni), the lower carbide region had more eutectic regions (~W_2C + (Ni)), but the dense carbide region had very few eutectic regions, and these were too small for accurate analyses. The higher carbide proportion had 16.3 ± 0.3 at.% tungsten and 11.3 ± 1.2 at.%

carbon dissolved in the (Ni) matrix. The lower carbide proportion region had 15.6 at.% tungsten dissolved, while carbon formed 11.5 ± 1.9 at.% of the binder phase. The tungsten content in the (Ni) matrix of Sample A6 was higher (17.2 ± 0.2 at.%) than in Sample W_{25}:C_{25}:$Ni_{42.5}$:$Zn_{7.5}$, while carbon dissolved in the binder phase was 6.4 ± 0.2 at.%, which was less than the carbon content in Sample W_{25}:C_{25}:$Ni_{42.5}$:$Zn_{7.5}$.

Nominal W_{25}:C_{25}:$Cu_{42.5}$:$Ni_{7.5}$ (at.%) was more complex, being more inhomogeneous than the other copper-containing samples, and with more phases. Pure tungsten, (Cu,Ni), and ~W_2C were the three phases found and confirmed with XRD and good XRD signals. Nominal W_{25}:C_{25}:Cu_{40}:Ni_{10} (at.%) had some mechanical damage from cutting of the sample, which was better revealed in the secondary electron mode. This would not be good for potential future replacement of cobalt. The ~W_2C did not appear fully melted. A solid solution of copper and nickel was the second phase in the sample.

Copper has very limited wettabilty to WC due to their mutual insolubility but alloying with another element with substantial solubility for tungsten, such as Fe, Mn, Ni, Zn etc., greatly improves wettability [2003Gua, 2003Cos]. The wettability of the binder phase was very poor in Samples W_{25}:C_{25}:$Cu_{42.5}$:$Ni_{7.5}$ (at.%) and W_{25}:C_{25}:Cu_{40}:Ni_{10} (at.%). There was no tungsten in the binder phase in the two-phase region of Sample W_{25}:C_{25}:$Cu_{42.5}$:$Ni_{7.5}$ (at.%), while copper formed a very small percentage of the light carbide phase (2.4 ± 1.3 at.%) and nickel was absent. Carbon was 3.5 ± 1.4 at.% in the (Cu,Ni) matrix. Tungsten and carbon were both absent in the dark single (Cu,Ni) phase, this indicated negligible solubility of the binder (Cu,Ni) phase for the carbide phase.

Sample W_{25}:C_{25}:Cu_{40}:Ni_{10} (at.%), which had more nickel in the binder alloy, showed a slight improvement in the dissolved amount of tungsten 0.9 ± 0.4 at.% and carbon16.3 ± 10.0 at.% in the matrix (the two-phase region A). The two-phase region labelled B in Figure 5.20 had 0.6 ± 0.5 at.% tungsten in the binder phase, while carbon was 21.2 ± 3.4 at.%, also indicated an improvement of the solubility. In the light carbide phase, the dissolved amount of copper and nickel was also significantly higher, indicating an improved in solubility (albeit with huge errors): copper was 7.0 ± 5.0 at.% and nickel 11.0 ± 5.9 at.% in portion A, while in portion B, the copper was 12.7 ± 10.4 at.% and nickel 3.3 ± 0.8 at.%. This improvement showed that increased nickel content increased mutual solubility between tungsten and copper, thereby increasing wettability of the matrix; this agreed with [2003Gua, 2003Cos].

Most of the samples containing copper showed inhomogeneity and had unmelted particles, indicating incomplete melting. Nominal compositions, $W_{25}:C_{25}:Cu_{42.5}:Ni_{7.5}$ (at.%), $W_{25}:C_{25}:Cu_{40}:Ni_{10}$ (at.%), $W_{25}:C_{25}:Cu_{45}:Zn_5$ (at.%), $W_{25}:C_{25}:Ni_{40}:Zn_{10}$ (at.%) and $W_{25}:C_{25}:Cu:_{47.5}:Mn_{2.5}$ (at.%) had their carbide phase in particles, rather than dendrites. This might have resulted from the use WC powder instead of WC lumps or pellets, even though it was compacted. It showed that WC powder probably did not melt correctly.

Nominal compositions for $W_{25}:C_{25}:Co_{30}:Mn_{20}$ (at.%) and $W_{25}:C_{25}:Co_{12.5}:Mn_{37.5}$ (at.%) alloys were selected from the solid solutions from both cobalt and manganese-rich ends on the Co-Mn binary phase diagram [1990Mas]. The nominal $W_{25}:C_{25}:Co_{30}:Mn_{20}$ (at.%) sample $W_{25}:C_{25}:Co_{30}:Mn_{20}$ (at.%) was fairly homogenous and the microstructure was more complex than the other samples. The sample had three phases comprising ~WC dendrites, dark (Co) and a medium contrast ternary phase. The latter was found at the boundaries of WC, and appeared to form peritectically. The ternary phase was believed to be either Co_7W_6 with C or $(Co,W)_2C$. The $(Co,W)_2C$ phase was not available on the ICCD database so it could not be matched on XRD, but it was identified by comparing the EDX analyses with the W-C-Co ternary diagram [1995Vil], ignoring the low manganese content. The ~Co_7W_6 phase matched very well. There was coring in the dark (Co) which was only visible at higher magnification. The dark cored (Co) contained 12.0 ± 1.1 at.% tungsten, while carbon comprised 20.2 ± 1.6 at.% (NMISA). The small darker phase was almost 3 at.% less in tungsten than in the dark phase, (9.1 ± 0.8 at.%) and the carbon in the darker phase was also almost 3 at.% higher than the dark phase (23.4 at.%).

The nominal $W_{25}:C_{25}:Co_{12.5}:Mn_{37.5}$ (at.%) sample was inhomogeneous. There were two different regions in the sample, with lower and higher carbide proportions. The portion with a high carbide proportion had two phases, ~W_2C carbide and (Mn). It had not properly melted; the ~W_2C were rounded particles, rather than dendrites. The portion with lower carbide also had two phases, and the light phase ~W_2C was much coarser which was much better for EDX analyses. These phases were identified as ~WC and (Mn), and (Mn) was identified by XRD to be (βMn). The (Mn) phase had cracks which might have resulted from the cutting of the sample for metallography. This would be detrimental for replacement of cobalt in commercial applications. The dark (Mn) matrix had 6.8 ± 0.9 at.% tungsten, which was lower than in Sample $W_{25}:C_{25}:Co_{30}:Mn_{20}$ (at.%), which had more manganese. The carbon content was 17.6 ± 0.7 at.%, also less than the carbon content in sample $W_{25}:C_{25}:Co_{30}:Mn_{20}$ (at.%).

The as-cast W_{25}:C_{25}:Cu_{45}:Zn_5 (at.%) sample showed that not all the compact melted; some ~WC powder from the compacted pieces was left, even after several attempts to melt the sample. Thus, complete melting was not achieved. The largest piece was selected, sectioned and prepared for analysis. For the portion analyzed, the overall EDX analyses showed that there was WC and ~W_2C. However, the XRD pattern had only a few ~WC peaks, while the rest were ~W_2C peaks. This confirmed ~WC is susceptible to decomposition to ~W_2C when overheated [2005Ser], especially in the fine powder state. There was no matrix to analyse.

Nominal samples W_{25}:C_{25}:$Ni_{47.5}$:$V_{2.5}$ (at.%), W_{25}:C_{25}: Ni_{43}:V_7 (at.%), W_{25}:C_{25}:$Ni_{42.5}$:$Zn_{7.5}$ (at.%), W_{25}:C_{25}:Ni_{45}:Zn_5 (at.%) and W_{25}:C_{25}:Co_{30}:Mn_{20} (at.%) completely melted and were fairy homogenous.

Nominal compositions W_{25}:C_{25}:$Co_{12.5}$:$Mn_{37.5}$ (at.%), W_{25}:C_{25}:$Cu_{42.5}$:$Ni_{7.5}$ (at.%), W_{25}:C_{25}:Cu_{40}:Ni_{10} (at.%), W_{25}:C_{25}:Cu_{45}:Zn_5 (at.%), W_{25}:C_{25}:Ni_{40}:Zn_{10} (at.%) and W_{25}:C_{25}:$Cu_{47.5}$:$Mn_{2.5}$ (at.%) had the light carbide phase incompletely melted; the carbides were mostly particles with some coarsening.

Nominal as-cast sample W_{25}:C_{25}:Mn_{25}:V_{25} (at.%) had a more dense side (high carbide content) and a less dense carbide region which could be due inhomogeneous melting. The microstructure showed coarse ~V_2C dendrites in the denser regions. Both regions of the sample had two phases: the ~V_2C carbides and a solid solution (V). The less dense carbide region had 5.7 ± 0.2 at.% tungsten and 13.3 ± 0.3 at.% carbon dissolved in the (V), whereas the denser region had slightly more dissolved tungsten (6.1 ± 0.2 at.%) and slightly less carbon (12.5 ± 0.5 at.%) than the low carbide region. No WC was formed, but rather ~V_2C, which probably means the binder could not be a replacement for Co, even though the matrix did not have high tungsten and carbon contents, which was beneficial.

7.3 Heat treated samples

The samples were annealed to give more equilibrium type conditions. It was expected that the annealed samples would be more indicative of liquid phase sintered materials.

The microstructure of the as-cast nominal sample W_{25}:C_{25}:$Ni_{47.5}$:$V_{2.5}$ (at.%) was slightly different after 168 hours at 1000ºC annealing. One significant feature in the microstructure was the higher proportion of the eutectic. The medium ~Ni_2V phase was still cored, even

after annealing, meaning the heat treatment time was not long enough to remove the coring. The edges of some the light carbide ~W_2C dendrites in the annealed sample were darker, and could be a ternary phase. The unmatched XRD peaks could be peaks for this ternary phase, although there was probably too small a proportion to be detected by XRD. These dark edges were too small for accurate analysis, hence they had large errors.

The medium dendritic phase in the as-cast sample W_{25}:C_{25}:$Ni_{47.5}$:$V_{2.5}$ (at.%) was found to be ~Ni_3V (after transforming from (Ni)) and the medium contrast phase of the annealed sample was ~Ni_2V. Although the phase identification in the annealed sample was done mainly using XRD, the ~Ni_3V phase had much more nickel than ~Ni_2V. The ~Ni_2V also had more carbon. There was more eutectic seen in the annealed sample, and it had coarsened.

The microstructure of nominal W_{25}:C_{25}: Ni_{43}:V_7 (at.%) was different after annealing for 1000ºC for 168 hours. Both the as-cast and annealed samples had ~W_2C as the light phase. There were darker edges on the ~W_2C phase as in sample W_{25}:C_{25}:$Ni_{47.5}$:$V_{2.5}$ (at.%), which were in too small a proportion to detect with XRD. There was another phase which might have formed on cooling, with light medium contrast, which appeared as coarse needles within the matrix. This phase was found to be ~4 at.% richer in Ni composition than the dark phase (Ni), with a slightly different composition of carbon too. This phase was identified with the aid of XRD as ~Ni_3V. The nickel content could not be correlated with contrast because of the different tungsten and carbon contents. There were very small light spots in the medium and dark phases, this indicated solid state precipitation (probably of the carbide, which did not occur in the as-cast sample) and they were too small for EDX analysis. However, this shows that there was less solubility of the carbide in the matrix at 1000ºC than at the casting (albeit under fast cooling).

Nominal W_{25}:C_{25}:$Ni_{42.5}$:$Zn_{7.5}$ (at.%) in the annealed condition, after annealing for 168 hours at 1000ºC, was not homogenous (as in the as-cast condition); there were two different portions, both of two phases, with varying proportions of the carbide. The portion with less carbide had more eutectic regions. No significant difference was seen between the as-cast and the annealed samples, and they both had (Ni) and ~W_2C. The compositions of zinc in both as-cast and annealed W_{25}:C_{25}:$Ni_{42.5}$:$Zn_{7.5}$ (at.%) samples were small. Due to zinc's relatively low melting point, the re-melting of the as-cast sample several times at high temperature led to the loss of zinc, to below the detection limit.

Nominal W_{25}:C_{25}:Ni_{45}:Zn_5 (at.%) in the annealed condition had two phases: ~W_2C and (Ni), the same as in the as-cast samples. There were eutectic regions which had coarsened. This sample had no zinc in the EDX analyses or in XRD. The phases in the annealed samples were mainly identified by XRD. The samples (as-cast and annealed) had no Zn, and that was attributed to the reasons explained above.

The annealed W_{25}:C_{25}:Co_{30}:Mn_{20} (at.%) sample had only two distinct phases, whereas the as-cast sample had a third phase, either Co_7W_6 with C or $(Co,W)_2C$. There was ~W_2C carbide, which was in the form of large needles or flakes with smaller irregular needles. The large needles could be a sectioning effect of the flakes. The matrix phase was (Co) with manganese, tungsten and carbon dissolved. The carbide phase in the as-cast sample was found to be ~WC (and was confirmed by XRD), whereas it was ~W_2C in the heat treated sample. This decomposition from ~WC to ~W_2C was reported by Schwarzkopf [1960Sch], Emeleus and Sharpe [1975Eme] and Sergei Zimakov [2005Ser]. Both samples had (Co) with 4.8 at.% manganese dissolved in the heat treated sample; the as-cast had 16.8 ± 0.6 at.% manganese in analyses done at NMISA using pre-loaded standards and 8.5 ± 0.3 at.% in the analyses done at UB without standards. The ternary phase, believed to be either Co_7W_6 with C or $(Co,W)_2C$ from the as-cast sample might have reacted with ~WC to form ~W_2C.

The microstructure of nominal W_{25}:C_{25}:$Co_{12.5}$:$Mn_{37.5}$ (at.%) in the annealed condition had two different portions: one portion with very small carbide particles. The second portion had less of the carbide phase, but it was coarsened. Both regions had two phases; ~W_2C carbide and dark (βMn) with dissolved cobalt. The dark (βMn) phase had cracks and also had porosity. The annealed and as-cast samples looked very similar. However, the carbide phase in the as-cast sample was identified as ~WC, while ~W_2C was found after annealing. This could be due to decomposition of the ~WC to ~W_2C [1960Sch, 1975Eme, 2005Ser].

The annealed sample W_{25}:C_{25}:Ni_{40}:Zn_{10} (at.%) was mainly composed of a single (Cu,Zn) phase with very small carbide particles. Close to the edge of the sample was an area with ~W_2C carbide. Small round porosity was visible at higher magnifications in the sample. The annealed sample looked completely different from the as-cast sample. The as-cast alloy had the carbide particles formed in the middle of the sample, surrounded by a single (Cu,Zn) phase. This clearly indicates the sample was inhomogeneous and experienced incomplete melting. This difference observed in the as-cast and the annealed samples was primarily due

to the sample not melting uniformly and the two cut halves were not the same. Surprisingly, compared to most of the nominal zinc-containing samples, there was some zinc left (~3.0 ± 0.2 at.%).

The W_{25}:C_{25}:Cu_{45}:Zn_5 (at.%) sample was single phase, as in the as-cast sample, after annealing, and the sample was porous. The sample comprised ~W_2C with a trace amount of copper, but had no zinc. Both as-cast and annealed samples were single phase.

The nominal sample W_{25}:C_{25}:$Cu_{47.5}$:$Mn_{2.5}$ (at.%) after annealing was not noticeably different from the sample in the as-cast condition. The sample was completely inhomogeneous and looked like unmelted carbide grains distributed in different proportions. The central portion of the samples (both annealed and as-cast) had carbide and (Cu) phases. The dark (Cu) single phase, which had a few carbide particle patches, surrounded the two-phase regions which were mainly carbide particles.

Nominal W_{25}:C_{25}:$Cu_{42.5}$:$Ni_{7.5}$ (at.%) in the annealed condition was inhomogeneous, similar to the as-cast sample, and had different regions with different proportions of the carbide, indicating that the annealing did not correct the incomplete melting. The annealed sample had some mainly single phase portions which were mainly (Cu,Ni) with some minor ~W_2C, as well as two-phase regions with varying proportions of carbides. Some free W, as well as ~W_2C, were found in the as-cast, whereas only the light contrast single phase ~W_2C was found in the annealed sample.

The annealed sample W_{25}:C_{25}:Cu_{40}:Ni_{10} (at.%) also showed that annealing could not compensate for the incomplete melting, which is not surprising for a short anneal (one week). The sample had regions with varying ~W_2C carbide proportions. There was a single phase region comprising (Cu,Ni). The annealed and the as-cast samples had reasonable resemblance. The similarity between the as-cast and annealed samples was probably due to the short time of the heat treatment.

Sample W_{25}:C_{25}:Mn_{25}:V_{25} (at.%) in the annealed condition had two different proportions of light dendrites, as seen in the as-cast sample. The annealed sample had three different contrasts: the light ~V_2C, the dark (V) matrix and the medium contrast, which was also identified to be ~V_2C. The medium contrast phase was mostly seen at the edges of the

carbide dendrites and was absent in the as-cast sample. All the phases, in both samples, had a very small amount of Mn left, and Mn could have been lost through evaporation in the arc-melting process, since it has a lower melting point compared to the other elements in the sample.

The matrix phases identified for all the alloys in both as-cast and annealed conditions are presented in Table 7.3.

Nominal $W_{25}:C_{25}:Ni_{47.5}:V_{2.5}$ (at.%)						
	W	**C**	**Ni**	**V**	**Phase deduced**	**XRD**
As-cast	17. 2 ± 0.6	0.0 ± 0.0	78.7 ± 0.5	4.1 ± 0.1	~Ni_3V	Ni_3V
Annealed	12.3 ± 0.1	30.5 ± 1.3	54.4 ± 0.6	2.8 ± 0.3	~Ni_2V?	~Ni_2V
Nominal $W_{25}C_{25}Ni_{43}:V_7$ (at.%)						
	W	**C**	**Ni**	**V**	**Phase deduced**	**XRD**
As-cast	10.1 ± 0.2	7.1 ± 0.3	73.1 ± 0.4	9.7 ± 0.1	~Ni_2V	~Ni_2V
Annealed	7.7 ± 0.8	28.5 ± 1.3	55.8 ± 0.5	8.0 ± 0.1	(Ni)/ ~Ni_3V?	(Ni) /~Ni_3V
Nominal $W_{25}:C_{25}:Ni_{42.5}:Zn_{7.5}$ (at.%)						
	W	**C**	**Ni**	**Zn**	**Phase deduced**	**XRD**
As-cast (more carbide)	16.3 ± 0.3	11.3 ± 1.2	72.4 ± 1.1	0.0 ± 0.0	(Ni)	(Ni)
As-cast (less carbide)	15.6 ± 0.5	11.5 ± 1.9	72.9 ± 1.6	0.0 ± 0.0	(Ni)	(Ni)
Annealed (more carbide)	11.0 ± 0.4	40.6 ± 0.9	48.4 ± 0.4	0.0 ±0.0	(Ni)?	(Ni)
Annealed (more carbide)	12.2 ± 0.5	37.2 ± 0.3	50.6 ± 0.1	0.0 ±0.0	(Ni)?	(Ni)
Nominal $W_{25}:C_{25}:Ni_{45}:Zn_5$ (at.%)						
	W	**C**	**Ni**	**Zn**	**Phase deduced**	**XRD**
As-cast	14.0 ± 0.2	29.3 ± 1.1	56.7 ± 0.9	0.0 ± 0.0	(Ni)	(Ni)
Annealed	10.7 ± 0.8	42.9 ± 1.8	48.4 ± 1.2	0.0 ± 0.0	(Ni)?	(Ni)
Nominal $W_{25}:C_{25}:Co_{30}:Mn_{20}$ (at.%)						
	W	**C**	**Mn**	**Co**	**Phase deduced**	**XRD**
As-cast (NMISA)	7.9 ± 0.4	19.8 ± 0.4	16.8 ± 0.6	55.5 ± 0.4	(Co) cored	(Co) cored
As-cast (UB)	12.0 ± 1.1	20. 2 ± 1.6	8.5 ± 0.3	59.3 ± 1.3	(Co)	(Co) cored
Annealed	21.3 ± 0.9	43.0 ± 0.7	4.8 ± 0.8	30.9 ± 0.7	(Co)	(Co)
Nominal $W_{25}:C_{25}:Co_{12.5}:Mn_{37.5}$ (at.%)						
	W	**C**	**Mn**	**Co**	**Phase deduced**	**XRD**
As-cast	6.8 ± 0.9	17.6 ± 0.7	47.9 ± 0.4	27.7 ± 0.7	(βMn)	(βMn)
Annealed	1.3 ± 0.1	24.2 ± 1.8	41.7 ± 0.6	32.8 ± 1.1	(βMn)	(βMn)

Table 7.3. The matrix compositions and the phases identified for samples in as-cast and annealed conditions.

Nominal $W_{25}:C_{25}:Mn_{25}:V_{25}$ (at.%)						
	W	**C**	**Mn**	**V**	**Phase deduced**	**XRD**
As-cast (less carbide)	5.7 ± 0.2	13.3 ± 0.3	0.2 ± 0.2	79.8 ± 0.6	(V)	(V)
As-cast (high carbide)	6.1 ± 0.2	12.5 ± 0.5	0.0 ± 0.0	80.4 ± 1.0	(V)	(V)
Annealed	5.4 ± 0.4	24.6 ± 0.8	0.1 ± 0.1	69.9 ± 0.8	(V)	(V)
Annealed	6.1 ± 1.3	25.3 ± 1.6	0.3 ± 0.2	68.3 ± 1.1	(V)	(V)
Nominal $W_{25}:C_{25}:Cu_{42.5}:Ni_{7.5}$ (at.%)						
	W	**C**	**Cu**	**Ni**	**Phase deduced**	**XRD**
As-cast	0.0 ± 0.0	3.5 ± 1.4	81.6 ± 3.0	14.9 ±2.2	(Cu,Ni)	(Cu,Ni)
As-cast (single phase)	0.0 ± 0.0	0.0 ± 0.0	83.5 ± 0.1	16.5 ± 0.1	(Cu,Ni)	(Cu,Ni)
Annealed	1.4 ± 0.5	31.4 ± 1.4	55.8 ± 0.4	11.4 ± 0.1	(Cu,Ni)	(Cu,Ni)
Annealed (Single phase)	0.3 ± 0.03	26.6 ± 1.9	60.0 ± 1.7	13.1 ± 0.2	(Cu,Ni)	(Cu,Ni)
Nominal $W_{25}:C_{25}:Cu_{40}:Ni_{10}$ (at.%)						
	W	**C**	**Cu**	**Ni**	**Phase deduced**	**XRD**
As-cast [A]	0.9 ± 0.9	16.3 ± 10.0	74.3 ± 8.3	8.5 ± 2.9	(Cu,Ni)	(Cu,Ni)
As-cast [B]	0.6 ± 0.5	21.2 ± 5.4	70.3 ± 6.0	7.9 ±1.9	(Cu,Ni)	(Cu,Ni)
As-cast (single phase)	0.0 ± 0.0	24.4 ± 0.6	67.6 ± 6.6	8.0 ± 0.1	(Cu,Ni)	(Cu,Ni)
Annealed	0.2 ± 0.1	24.0 ± 0.3	67.7 ± 0.3	8.1 ± 0.1	(Cu,Ni)	(Cu,Ni)
Annealed (single phase)	0.2 ± 0.4	23.3 ± 0.3	68.2 ± 0.1	8.3± 0.2	(Cu,Ni)	(Cu,Ni)
Nominal $W_{25}:C_{25}:Cu_{40}:Zn_{10}$ (at.%)						
	W	**C**	**Cu**	**Zn**	**Phase deduced**	**XRD**
As-cast (Overall)	0.0 ± 0.0	0.0 ± 0.0	97.3 ± 0.4	2.7 ± 0.1	(Cu,Zn)	(Cu,Zn)
Annealed (Overall)	0.1 ± 0.0	33.3 ± 0.6	63.7 ± 0.6	2.9 ± 0.2	(Cu,Zn)	(Cu,Zn)
Nominal $W_{25}:C_{25}:Cu_{45}:Zn_{5}$ (at.%)						
	W	**C**	**Cu**	**Zn**	**Phase deduced**	**XRD**
As-cast	0.0 ± 0.0	0.0 ± 0.0	0.0 ± 0.0	0.0 ± 0.0	-	-
Annealed	0.0 ± 0.0	0.0 ± 0.0	0.0 ± 0.0	0.0 ± 0.0	-	-

Table 7.3. (continued)The matrix compositions and the phases identified for samples in as-cast and annealed conditions.

Nominal $W_{25}:C_{25}:Cu_{47.5}:Mn_{2.5}$ (at.%)						
	W	**C**	**Cu**	**Zn**	**Phase deduced**	**XRD**
As-cast	10.6 ± 7.0	5.2 ± 7.6	79.3 ± 12.9	4.9 ±0.6	(Cu,Mn)	(Cu,Mn)
Annealed	0.0 ± 0.0	19.1 ± 0.2	75.3 ± 1.4	5.6 ± 0.3	(Cu,Mn)	(Cu,Mn)

Table 7.3. (continued)The matrix compositions and the phases identified for samples in as-cast and annealed conditions.

Table 7.4 gives carbide phases identified for all the alloys, in the as-cast and annealed samples.

Nominal $W_{25}:C_{25}:Ni_{47.5}:V_{2.5}$ (at.%)						
	W	**C**	**Ni**	**V**	**Phase deduced**	**XRD**
As-cast	72.4 ± 4.2	23.8 ± 5.3	2.9 ± 0.7	0.9 ± 0.7	~W_2C	~W_2C
Annealed	48.3 ± 0.2	47.6 ± 0.9	3.7 ± 0.1	0.4 ± 0.1	~WC?	~W_2C
Nominal $W_{25}C_{25}Ni_{43}:V_7$ (at.%)						
	W	**C**	**Ni**	**V**	**Phase deduced**	**XRD**
As-cast	-	-	-	-	Could not be analysed	W_2C
Annealed	51.7 ± 0.6	44.1 ± 1.2	2.5 ± 0.8	1.7 ± 0.1	WC?	W_2C
Nominal $W_{25}:C_{25}:Ni_{42.5}:Zn_{7.5}$ (at.%)						
	W	**C**	**Ni**	**Zn**	**Phase deduced**	**XRD**
As-cast (high carbide region)	73.3 ± 1.3	24.1 ± 1.8	2.6 ± 1.0	0.0 ± 0.0	~W_2C	W_2C
As-cast (low carbide region)	69.4 ± 2.7	28.2 ± 2.9	2.4 ± 0.5	0.0 ± 0.0	~W_2C	~W_2C
Annealed (high carbide region)	41.5 ± 0.4	57.4 ± 0.6	1.1 ± 0.2	0.0 ±0.0	~WC?	~W_2C
Annealed (low carbide region)	24.2 ± 4.8	63.7 ± 5.4	12.1 ± 0.5	0.0 ±0.0	~WC_2?	~W_2C

Table 7.4. Summary of carbide phases identified for as-cast and annealed samples.

Nominal $W_{25}:C_{25}:Ni_{45}:Zn_5$ (at.%)						
	W	**C**	**Ni**	**Zn**	**Phase deduced**	**XRD**
As-cast	-	-	-	-	could not be analysed	~W_2C
Annealed	29.0 ± 7.7	69.7 ± 8.0	1.3 ± 0.5	0.0 ± 0.0	~WC_2?	~W_2C
Nominal $W_{25}:C_{25}:Co_{30}:Mn_{20}$ (at.%)						
	W	**C**	**Mn**	**Co**	**Phase deduced**	
As-cast	51.8 ± 0.5	45.4 ± 0.6	0.6 ± 0.2	2.2 ± 0.3	WC	~WC
Annealed	23.0 ± 0.1	45.3 ± 0.4	2.9 ± 0.8	28.8 ± 1.0	?	~W_2C
Nominal $W_{25}:C_{25}:Co_{12.5}:Mn_{37.5}$ (at.%)						
	W	**C**	**Mn**	**Co**	**Phase deduced**	
As-cast	52.8 ± 0.7	40.3 ± 1.1	4.4 ±0.8	2.5 ± 0.6	~WC	~WC
Annealed	26.2 ± 1.8	32.8 ± 2.0	14.0 ± 0.9	22.0 ± 1.0	?	~W_2C
Nominal $W_{25}:C_{25}:Cu_{42.5}:Ni_{7.5}$ (at.%)						
	W	**C**	**Cu**	**Ni**	**Phase deduced**	**XRD**
As-cast	87.1 ± 0.8	10.5 ± 1.4	2.4 ± 1.3	0.0 ± 0.0	~W_2C?	~W_2C
Annealed	41.0 ± 7.1	50.8 ± 7.1	6.3 ± 3.2	1.9 ± 0.7	~WC?	~W_2C
Annealed [2]	42.6 ± 1.2	44.7 ± 1.2	8.2 ± 0.3	1.5 ± 0.2	~WC	~W_2C
Annealed [1]	40.2 ± 1.2	43.0 ± 4.8	14.7 ± 2.9	2.1 ± 0.5	-	~W_2C
Nominal $W_{25}:C_{25}:Cu_{40}:Ni_{10}$ (at.%)						
	W	**C**	**Cu**	**Ni**	**Phase deduced**	**XRD**
As-cast [A]	48.7 ± 15.0	33.3 ± 14.3	7.0 ± 5.0	11.0 ± 5.9	~WC	~W_2C
As-cast [B]	76.6 ± 7.6	7.4 ± 6.8	12.7 ± 10.4	3.3 ± 0.8	~W_2C	~W_2C
Annealed [1 overall]	40.2 ± 1.2	43.0 ± 4.8	14.7 ± 2.9	2.1 ± 0.5	-	~W_2C
Annealed [2]	42.6 ± 1.2	44.7 ± 1.2	8.2 ± 0.3	1.5 ± 0.2	~WC	~W_2C

Table 7.4. (continued) Summary of carbide phases identified for as-cast and annealed samples.

Nominal $W_{25}:C_{25}:Mn_{25}:V_{25}$ (at.%)						
	W	**C**	**Mn**	**V**	**Phase deduced**	**XRD**
As-cast (high carbide region)	39.5 ± 0.7	26.4 ± 0.8	0.0 ± 0.0	34.1 ± 0.3	?	~V_2C
As-cast (low carbide region)	48.9 ± 0.9	21.7 ± 0.5	0.0 ± 0.0	29.4 ± 0.6	?	~V_2C
Annealed (high carbide region)	31.1 ± 0.9	36.3 ± 0.6	0.0 ± 0.0	32.6 ± 0.7	?	~V_2C
Annealed (low carbide region)	28.7 ± 1.2	36.2 ± 0.8	0.0 ± 0.0	35.1 ± 0.6	?	~V_2C
Nominal $W_{25}:C_{25}:Cu_{47.5}:Mn_{2.5}$ (at.%)						
	W	**C**	**Cu**	**Mn**	**Phase deduced**	**XRD**
As-cast	63.2 ± 8.7	32.5 ± 8.8	4.3 ± 2.1	0.0 ± 0.0	~W_2C	~W_2C
Annealed	72.7 ± 0.2	15.2 ± 0.3	0.0 ± 0.0	12.1 ± 0.5	~W_2C	~W_2C
Nominal $W_{25}:C_{25}:Cu_{45}:Zn_5$ (at.%)						
	W	**C**	**Cu**	**Zn**	**Phase deduced**	
As-cast [overall 1]	71.9 ± 5.6	28.1 ± 5.6	0.0 ± 0.0	0.0 ± 0.0	-	~W_2C
As-cast [overall 1]	52.6 ± 1.3	47.4 ± 1.3	0.0 ± 0.0	0.0 ± 0.0	-	~WC
Annealed [overall]	50.4 ± 1.3	48.8 ± 1.0	0.8 ± 0.0	0.0 ± 0.0	-	~W_2C
Nominal $W_{25}:C_{25}:Cu_{40}:Zn_{10}$ (at.%)						
	W	**C**	**Cu**	**Zn**	**Phase deduced**	**XRD**
As-cast [overall 1	60.8 ± 3.4	34.6 ± 3.4	4.4 ± 0.8	0.2 ± 0.6	-	~W_2C
Annealed [overall	16.0	60.8	22.4	0.8	-	~W_2C

Table 7.3. (continued) Summary of carbide phases identified for as-cast and annealed samples.

7.4 Summary the calculation of equilibria phases (Thermo-Calc)

Two sets of calculations were done on the alloy compositions using the Thermo-Calc program. It should be noted that there are other programs which could be used for these calculations (e.g. Pandat), but were not available to the project, and there is also a proprietary WC-Co database, which was also not available, and could possibly have predicted the WC decomposition. The first set of calculations comprised 10% binder replacement and was a more realistic composition for possible replacement of Co. The second set of calculations was done to offer a better understanding of the experimental microstructure regarding the solidification sequence, phases that will form and possible phases that would be formed on heat treatment. They were for compositions of 50:50 at.% binder and WC, the same as the experimental compositions which was done for easy manufacturing and analyses.

All calculations were done within a temperature range of 800ºC-2600ºC, this was because the Thermo-Calc could not predict accurately at lower temperatures. The higher temperature limit was restricted to the melting point for tungsten.

The set of calculations involving 10% binder composition had the WC (MC_SPH) phase forming the bulk proportion, as expected, and it solidified at temperatures above 2600ºC. The second set of calculations with 50% binder composition showed that the binder compositions had reduced the high melting point of the WC (MC_SHP) phase. They solidified at a much lower temperature (~200°C) compared to the first set of calculations, but had a very similar solidification range for the binder phases for both set of calculations. The two sets of calculations had the MC_SHP carbide phase composed of WC for all samples. This implied Thermo-Calc was unable to predict WC decomposition at high temperatures.

7.4.1 90% Carbide 10% binder calculations

Compositions W_{45}:C_{45}:$Ni_{9.5}$:$V_{0.5}$ (at.%) and W_{45}:C_{45}:$Ni_{8.6}$:$V_{1.4}$ (at.%) had three phases at 800ºC. The bulk was the WC phase, followed by the (Ni) binder phase and a very small portion which was another carbide phase (WC/VC). The composition with higher vanadium content solidified slightly higher than for the sample with low vanadium content. This showed that increasing the vanadium content would possibly increase the melting point of the

binder phase and in effect increase sintering temperature. The (WC/VC) phase was much higher in proportion in the high vanadium content sample; this might be an unwanted phase for the target alloy and hence not be a choice for cobalt's replacement.

Compositions W_{45}:C_{45}:$Ni_{8.5}$:$Zn_{1.5}$ (at.%) and W_{45}:C_{45}:$Ni_{9.0}$:$Zn_{1.0}$ (at.%) had two main phases which were the WC and the (Ni) matrix. There was graphite which formed a negligible proportion and might not be a good indication for the target alloy since high graphite content will probably contribute to inferior mechanical properties of the alloy [2011Lan]. The composition with higher zinc content had solidified at a slightly lower temperature and a much narrower solidification range for the binder phase than the lower zinc content composition. This could be due to the influence of the low melting point of zinc.

The binder alloy composition for W_{45}:C_{45}:Co_6:Mn_4 (at.%) was chosen as the solid solution from the cobalt-rich end of the Co-Mn binary phase diagram, whereas W_{45}:C_{45}:$Co_{2.5}$:$Mn_{7.5}$ (at.%) was selected from the manganese-rich end of the same binary phase diagram.

The calculation showed that both compositions had eta (ternary phase-Co_6W_6C) [1965Kre], which occurred at lower temperature, <1000ºC. The phase is not desired in the alloy [1998Upa], due to its brittle nature. The solidification for W_{45}:C_{45}:Co_6:Mn_4 (at.%) was at a slightly lower temperature than W_{45}:C_{45}:$Co_{2.5}$:$Mn_{7.5}$ (at.%). Cobalt as a the traditional binder is normally sintered between 1300ºC-1490ºC depending on the cobalt content and its application. This shows alloying cobalt with manganese (solid solution of cobalt and manganese) may decrease the sintering temperature.

The calculations showed that compositions W_{45}:C_{45}:$Cu_{8.5}$:$Ni_{1.5}$ (at.%) and W_{45}:C_{45}:Cu_8:Ni_2 (at.%) had negligible graphite components, besides the main compositions (WC and (Cu)). Higher graphite proportion offers inferior mechanical properties to the target alloy [2011Lan]. The solidification range for sample W_{45}:C_{45}:Cu_8:Ni_2 (at.%) was slightly higher, which was probably due to the higher nickel content. The calculations of W_{45}:C_{45}:Cu_9:Zn_1 (at.%) and W_{45}:C_{45}:$Cu_{9.5}$:$Zn_{0.5}$ (at.%) were similar to the samples previously discussed.

Compositions W_{25}:C_{25}:Mn_{25}:V_{25} (at.%) had the BCC_A2 binder phase solidifying at 1860°C. This indicated the binder phase solidified at a very high temperature and might not be appropriate for cobalt replacement since the sintering temperature will be very high for such a

binder. Also, the binder is a BCC_A2 might not have such good properties as the usual FCC cobalt, because of its different structure. There were two carbides present in the alloy, which were V_2C and WC. This might also not be a good indication for the target alloy.

The sample W_{25}:C_{25}:Mn_{25}:V_{25} (at.%) had three phases at 800°C. The WC and (Ni) formed the bulk of the sample, with a negligible graphite proportion.

7.4.2 90% Carbide-10% binder calculations

Composition W_{25}:C_{25}:Ni_{45}:V_5 (at.%) had the WC (MC_SHP) phase forming about 44% proportion at 800ºC. This could be due the formation of the other carbide phase (WC/VC which replaced each other at different temperatures) at 800ºC. The (Ni) matrix had a solidification range (1360ºC-1400ºC) similar to the compositions with 10% binder (W_{45}:C_{45}:$Ni_{9.5}$:$V_{0.5}$ (at.%)), even though the binder compositions were different in the two samples. The phases at 1000ºC for the composition W_{25}:C_{25}:Ni_{45}:V_5 (at.%) were the same, but had slightly different in compositions, from those at 800ºC. The phase at 1000ºC was observed to see what phases were likely to form on heat treatment, as was studied experimentally.

The calculation of the phase proportions for W_{25}:C_{25}:Ni_{43}:V_7 (at.%) showed that there were two carbides present. The WC (MC_SHP) phase was lower in proportion than expected (50% which formed the starting material); this indicates that, portions of the W and C carbon were lost to the formation of the other carbide. The other carbide (VC+W) was in a significant amount (forming almost 18% of the total proportion). This carbide phase could probably be an unwanted phase in the target alloy. The binder had a very narrow solidification range and was also similar to that of the (W_{45}:C_{45}:$Ni_{8.6}$:$V_{1.4}$ (at.%)) composition with 10% binder alloy composition. The phases at 1000ºC were the same as that identified at lower temperature (800ºC).

The W_{25}:C_{25}:$Ni_{42.5}$:$Zn_{7.5}$ (at.%) phase proportions showed that the WC (MC_SHP) phase was just a little less than 50%, while the binder phase was also slightly above 50% of the total. There was a graphite phase at 800ºC, which might have been originated from the WC (MC_SHP) phase. The binder phase, which formed the bulk of the sample, had a wider solidification range than the previous composition and was similar to what was observed in

the calculation for the 10% binder composition. The phases were similar at 1000ºC and 800ºC.

The sample W_{25}:C_{25}:Ni_{45}:Zn_5 (at.%) had no significant difference from the previous sample: W_{25}:C_{25}:$Ni_{42.5}$:$Zn_{7.5}$ (at.%). This was due to the small differences in their compositions.
The sample W_{25}:C_{25}:Co_{30}:Mn_{20} (at.%) was composed of almost 50% of the (Co) binder (HCP_A3) phase and also about 50% carbide (WC). There was a ternary (Co_6W_6C) phase, believed to have formed by a eutectic reaction, that occurred at a much lower temperature (<1000ºC). The ternary eta phase is a brittle unwanted phase [1998Upa], which formed a negligible proportion of the alloy. The binder phase solidified at a very low temperature and had a very narrow solidification range (1010ºC-1030ºC). The phases at 1000ºC were WC, (Co) and the ternary (Co_6W_6C).

W_{25}:C_{25}:$Co_{12.5}$:$Mn_{37.5}$ (at.%) had same elements as the previous composition but had different proportions. The binder alloy was selected from Mn-rich end of the Co-Mn binary phase diagram. This sample (50:50 binder composition calculation) had a different matrix from the calculation involving 10% binder; the binders were BCC_A2, which was (Mn), and HCP_A3 (Co) respectively. The binder phase for W_{25}:C_{25}:$Co_{12.5}$:$Mn_{37.5}$ (at.%) solidified at a much lower temperature, but had a slightly wider solidification range (1020-990ºC) than W_{45}:C_{45}:$Co_{2.5}$:$Mn_{7.5}$ (at.%) for 10% binder. This was attributed to the difference in binder compositions. The W_{25}:C_{25}:$Co_{12.5}$:$Mn_{37.5}$ (at.%) composition had another carbide phase believed to be ternary WMn_2C. This phase had a significant proportion, and might not be a desirable phase for the target alloy. The phases present at 1000ºC were WC, WMn_2C and (Mn).

The calculated phase proportions for samples W_{25}:C_{25}:$Cu_{42.5}$:$Ni_{7.5}$ (at.%) and W_{25}:C_{25}:Cu_{40}:Ni_{10} (at.%) showed WC and (Cu,Ni) as the main components, but had graphite that formed a negligible proportion at 800ºC. The calculation with higher nickel content (W_{25}:C_{25}:Cu_{40}:Ni_{10} (at.%)) had a slightly wider solidification range and solidified at much higher temperature than the low nickel content composition. This indicated that nickel content could regulate sintering temperature range depending on its proportion.

The calculations for W_{45}:C_{45}:Ni_{40}:Zn_{10} (at.%) and W_{25}:C_{25}:Cu:$_{45}$:Zn_5 (at.%) had phases similar to the previously-discussed samples. The binder phase for the composition with low

zinc content solidified at a slightly higher temperature and had a wider solidification range than the high content zinc calculation. This is because zinc has a lower melting point, and alloying zinc with copper probably increases the solidification temperatures for the binder phase.

Sample W_{25}:C_{25}:Mn_{25}:V_{25} (at.%) had two carbides, V_3C_2 and WC; this might be a deviation from the target alloy. The binder BCC_A2 solidified at a much higher temperature (1860ºC). This indicated that the binder might not be appropriate for cobalt replacement since the sintering temperature will be very high for such a binder. Also, the binder is BCC, which might have less good properties. This phase formed was ~40% at 800ºC.

The calculation for the W_{25}:C_{25}:$Mn_{2.5}$:$Cu_{47.5}$ (at.%) revealed two main phases: the carbide (WC) and the binder phase (Cu,Mn) with a negligible proportion of graphite.

Table 7.5 summarizes the phases identified by experimental studies and by the phase proportions calculation.

Sample	**Calculated Phases**		**Experimental phases**	
	Binder	**Carbide phase**	**Binder**	**Carbide**
W_{25}:C_{25}:Ni_{45}:V_5	(Ni)	WC	~Ni_3V	~W_2C
W_{25}:C_{25}:Ni_{43}:V_7	(Ni)	WC	~Ni_2V	~W_2C
W_{25}:C_{25}:$Ni_{42.5}$:$Zn_{7.5}$	(Ni)	WC	(Ni)	~W_2C
W_{25}:C_{25}:Ni_{45}:Zn_5	(Ni)	WC	(Ni)	~W_2C
W_{25}:C_{25}:Co_{30}:Mn_{20}	(Co)	WC and Co_6W_6C	(Co)	~W_2C Co_7W_6 + C / $(Co,W)_2C$
W_{25}:C_{25}:$Co_{12.5}$:$Mn_{37.5}$	(Mn)	WC and $WMnC_2$?	(Mn)	~WC
W_{25}:C_{25}:$Cu_{42.5}$:$Ni_{7.5}$	(Cu,Ni)	WC	(Cu,Ni)	~WC
W_{25}:C_{25}:Cu_{40}:Ni_{10}	(Cu,Ni)	WC	(Cu,Ni)	~W_2C
W_{45}:C_{45}:Ni_{40}:Zn_{10}	(Cu,Zn)	WC	(Cu,Zn)	~W_2C
W_{25}:C_{25}:Cu:$_{45}$:Zn_5	(Cu,Zn)	WC	(Cu,Zn)	~W_2C
W_{25}:C_{25}:Mn_{25}:V_{25}	(Mn,W) ?	WC and V_3C_2	(V)	~V_2C
W_{25}:C_{25}:$Mn_{2.5}$:$Cu_{47.5}$	(Cu,Mn)	WC	(Cu,Mn)	~W_2C

Table 7.4. Phases identified experimentally and by calculation.

The phases as summarized in Table 7.5 showed that there were some similarities and differences in the binder phase obtained by experiment and by calculations. While all the carbides obtained from calculation were found to be WC, only samples W_{25}:C_{25}:Co_{30}:Mn_{20} and W_{25}:C_{25}:$Co_{12.5}$:$Mn_{37.5}$ had WC as the carbide phase. Thermo-Calc did not show that WC can decompose to W_2C. This decomposition occurred at the high temperatures used in the arc-melting used in making the experimental samples, because a dark soot-like layer was noticed in the upper chamber of the arc-melter after arc-melting of the samples. This could be carbon been lost from the sample, causing carbon deficiency, which resulted in WC. Under normal hard metal manufacture, only liquid phase sintering of the binder is done. Thus, the decomposition is unlikely to happen in normal circumstances.

The most probable binder that can replace cobalt based on this study is from the Ni-V binder alloy in the W_{25}:C_{25}:Ni_{43}:V_7 sample. This is because the microstructure (two phases with no eutectics) was good, it had moderate solubility for tungsten and carbon, and finally it would be economical to produce due to the abundance of vanadium in South Africa.

CHAPTER 8

8.1 Conclusions

Twelve samples with different binder compositions were studied using SEM with EDX and XRD. EDX analyses were not completely successful, due to the lack of a reliable carbon standard, and it was difficult to compare the results between the different microscopes and sample conditions. The Thermo-Calc program was used to calculate equilibrium phases as well.

The phases identified for the as-cast samples were:

- $W_{25}:C_{25}:Ni_{45}:V_5$ (at.%) sample: ~W_2C and ~Ni_3V
- $W_{25}:C_{25}:Ni_{43}:V_7$ (at.%) sample: ~W_2C and ~Ni_2V
- $W_{25}:C_{25}:Ni_{42.5}:Zn_{7.5}$ (at.%) sample: ~W_2C and (Ni)
- $W_{25}:C_{25}:Ni_{45}:Zn_5$ (at.%) sample: ~W_2C and (Ni)
- $W_{25}:C_{25}:Co_{30}:Mn_{20}$ (at.%) sample: ~WC, (Co) and ~Co_7W_6 with C / ~$(Co,W)_2C$
- $W_{25}:C_{25}:Co_{12.5}:Mn_{37.5}$ (at.%) sample: ~WC and (Mn)
- $W_{25}:C_{25}:Cu_{42.5}:Ni_{7.5}$ (at.%): sample ~W_2C and (Cu,Ni)
- $W_{25}:C_{25}:Cu_{40}:Ni_{10}$ (at.%) sample: ~W_2C and(Cu,Ni)
- $W_{45}:C_{45}:Ni_{40}:Zn_{10}$ (at.%) sample: ~W_2C and (Cu,Zn)
- $W_{25}:C_{25}:Cu_{45}:Zn_5$ (at.%) sample: ~W_2C and WC
- $W_{25}:C_{25}:Mn_{2.5}:Cu_{47.5}$ (at.%) sample: ~W_2C and (Cu,Mn)
- $W_{25}:C_{25}:Mn_{25}:V_{25}$ (at.%) sample: ~V_2C and (V).

The phases identified after annealing were:

- $W_{25}:C_{25}:Ni_{45}:V_5$ (at.%) sample: ~W_2C and ~Ni_2V
- $W_{25}:C_{25}:Ni_{43}:V_7$ (at.%) sample : ~W_2C, (Ni) and ~Ni_3V
- $W_{25}:C_{25}:Ni_{42.5}:Zn_{7.5}$ (at.%) sample: ~W_2C and (Ni)
- $W_{25}:C_{25}:Ni_{45}:Zn_5$ (at.%) sample: ~W_2C and (Ni)
- $W_{25}:C_{25}:Co_{30}:Mn_{20}$ (at.%) sample: ~W_2C, (Co)
- $W_{25}:C_{25}:Co_{12.5}:Mn_{37.5}$ (at.%) sample: ~W_2C and (Mn)
- $W_{25}:C_{25}:Cu_{42.5}:Ni_{7.5}$ (at.%) sample: ~W_2C and (Cu,Ni)

- $W_{25}:C_{25}:Cu_{40}:Ni_{10}$ (at.%) sample: ~W_2C and(Cu,Ni)
- $W_{45}:C_{45}:Ni_{40}:Zn_{10}$ (at.%) sample: ~W_2C and (Cu,Zn)
- $W_{25}:C_{25}:Cu_{45}:Zn_5$ (at.%) sample: ~W_2C and (Cu,Zn)
- $W_{25}:C_{25}:Mn_{2.5}:Cu_{47.5}$ (at.%) sample: ~W_2C and (Cu,Mn)
- $W_{25}:C_{25}:Mn_{25}:V_{25}$ (at.%) sample: ~V_2C and (V).

The phases obtained from 50% binder calculations:

- $W_{25}:C_{25}:Ni_{45}:V_5$ (at.%) composition: ~WC and ~Ni_2V
- $W_{25}:C_{25}:Ni_{43}:V_7$ (at.%) composition: ~WC, (Ni) and ~Ni_3V
- $W_{25}:C_{25}:Ni_{42.5}:Zn_{7.5}$ (at.%) composition: ~WC and (Ni)
- $W_{25}:C_{25}:Ni_{45}:Zn_5$ (at.%) composition: ~WC and (Ni)
- $W_{25}:C_{25}:Co_{30}:Mn_{20}$ (at.%) composition: ~WC, (Co) and Co_6W_6C
- $W_{25}:C_{25}:Co_{12.5}:Mn_{37.5}$ (at.%) composition: ~WC , (Mn) and $WMnC_2$?
- $W_{25}:C_{25}:Cu_{42.5}:Ni_{7.5}$ (at.%) composition: ~WC and (Cu,Ni)
- $W_{25}:C_{25}:Cu_{40}:Ni_{10}$ (at.%) composition : ~WC and (Cu,Ni)
- $W_{25}:C_{25}:Cu_{40}:Zn_{10}$ (at.%) composition: ~WC and (Cu,Zn)
- $W_{25}:C_{25}:Cu_{45}:Zn_5$ (at.%) composition: ~WC and (Cu,Zn)
- $W_{25}:C_{25}:Mn_{2.5}:Cu_{47.5}$ (at.%) composition: ~WC and (Cu,Mn)
- $W_{25}:C_{25}:Mn_{25}:V_{25}$ (at.%) composition: ~V_3C_2, ~WC and (V).

The phases obtained from 10% binder calculations:

- $W_{45}:C_{45}:Ni_{9.5}:V_{0.5}$ (at.%) composition: ~WC and ~Ni_2V
- $W_{45}:C_{45}:Ni_{8.6}:V_{1.4}$ (at.%) composition: ~WC, (Ni) and ~Ni_3V
- $W_{45}:C_{45}:Ni_{8.5}:Zn_{1.5}$ (at.%) composition: ~WC and (Ni)
- $W_{45}:C_{45}:Ni_{9.0}:Zn_{1.0}$ (at.%) composition: ~WC and (Ni)
- $W_{45}:C_{45}:Co_6:Mn_4$ (at.%) composition: ~WC, (Co) and Co_6W_6C
- $W_{45}:C_{45}:Co_{2.5}:Mn_{7.5}$ (at.%) composition: ~WC, and (Co)
- $W_{45}:C_{45}:Cu_{8.5}:Ni_{1.5}$ (at.%) composition: ~WC and (Cu,Ni)
- $W_{45}:C_{45}:Cu_9:Ni_1$ (at.%) composition: ~WC and(Cu,Ni)
- $W_{45}:C_{45}:Cu_9:Ni_1$ (at.%) composition: ~WC and (Cu,Zn)
- $W_{45}:C_{45}:Cu_{9.5}:Zn_{0.5}$ (at.%) composition: ~WC and (Cu,Zn)
- $W_{45}:C_{45}:Mn_{0.5}:V_{9.5}$ (at.%) composition: ~WC and (Cu,Mn)
- $W_{45}:C_{45}:Mn_5:V_5$ (at.%) composition; ~V_3C_2, ~WC and (V).

Most samples had two phases: the binder phase and carbide phase. The carbides decomposed from WC to W_2C in most of the samples. This was attributed to the powder used and mainly the high temperature arc-melting. Thermo-Calc could not predict the decompositions of the carbide, because equilibrium conditions were calculated.

All samples containing copper did not melt properly, and were inhomogeneous with very low solubility for the carbide. Almost all nominal zinc-containing samples had the zinc evaporated to below EDX detection limits. This was not predicted by Thermo-Calc, due to the reasons given above. The nominal as-cast W_{25}:C_{25}:Co_{30}:Mn_{20} (at.%) sample with a binder selected from the cobalt-rich end had a ternary phase (~Co_7W_6 with C / ~$(Co,W)_2C$).

The most promising sample was W_{25}:C_{25}:Ni_{43}:V_7 (at.%) from the experiments. The W_{25}:C_{25}:$Co_{12.5}$:$Mn_{37.5}$ sample had a matrix of (Mn) solid solution with a moderate solubility for W and C, but experienced cracking, so would not be suitable. The sample W_{25}:C_{25}:Ni_{43}:V_7 (at.%) initially solidified as (Ni) and later transformed into ~Ni_2V on cooling. This sample looked promising from the microstructure and economic viewpoint. Further studies need to be done on these samples, especially sintering realistic compositions and carrying out hardness and abrasion tests.

The calculations for compositions W_{25}:C_{25}:Ni_{45}:V_5 (at.%) W_{25}:C_{25}:Ni_{43}:V_7 (at.%), W_{25}:C_{25}:$Ni_{42.5}$:$Zn_{7.5}$ (at.%) and W_{25}:C_{25}:Ni_{45}:Zn_5 (at.%) were the most promising obtained for both sets of calculations (10 at.% and 50 at.% binder). Their binders all formed solid solutions and had small or negligible proportions of graphite at lower temperatures. However, W_{25}:C_{25}:Ni_{45}:V_5 (at.%) had some eutectic which is undesirable, and the zinc-containing samples lost their zinc on sample manufacture.

8.2 Recommendations for future work

- Pure WC standards should be used to analyse samples with EDX in the future.
- WC lumps / pellets, or any form besides powder, should be used for further studies to see if WC will not decompose.
- Another method should be employed in manufacturing nominal compositions containing zinc, since zinc could not withstand the high arc-melt temperature.

- Hardness tests could be undertaken on the samples to verify and hardening in the binder, especially for the manganese-containing alloys.

- The Ni-V and Ni-Zn systems should be explored further in the future by manufacturing a more realistic composition such as W_{45}:C_{45}:$Ni_{8.8}$:$V_{1.2}$ (with the binder being 88 at.% Ni-12 at.% V) and W_{45}:C_{45}:$Ni_{7.5}$:$Zn_{2.5}$ (with the binder being 75 at.% Ni-25 at.% Zn).

REFERENCES

[1921Hau] Haughton J.L. and Bingham, K.E., *Proc. R. Soc. (London), Series A*, Vol. 99, p. 46-69 (1921).

[1922Ima] Imai, H., *Sci. Rep*. Tôhoku Imp. Univ., Vol. 11, No. 1, pp. 313-332 (1922).

[1926Wes] Westgren, A. and Phargmen, G. Z., *Anorg. Chem*., Vol. 156, p. 27 (1926).

[1925Dix] Dix, E.H., Proc. ASTM, Vol. 25, No. 2, pp. 120-136 (1925).

[1925Gen] Genders, R. and Bailey, G.L., *J. Inst. Met*., Vol. 33, pp. 213-223 (1925).

[1927Bau] Bauer O. and Hansen, M., *Z. Metallkde*., Vol. 19, pp. 423-434 (1927).

[1927Gwy] Gwyer, A.G.C. and Phillips, H.W.L., *J. Inst. Met*., Vol. 38, pp. 29-83 (1927).

[1928Beck] Becker, K., *Z. Physik*, Vol. 51, pp. 481-482 (1928).

[1929Rue] Ruer R. and Kremers, K., *Z. Anorg*. Chem., Vol. 184, pp. 193-231 (1929).

[1931Tak1] Takeda, S., *Technical Rep*., Tohoku Univ., Vol. 9, p. 483 (1931).

[1931Tak2] Takeda, S., *Technical Rep.,* Tohoku Univ., Vol. 9, p. 627 (1931).

[1935Mar] Marsh, J.S., *Principles of Phase Diagrams*, McGraw-Hill, (1935).

[1935Sch1] Schramm, J., *Metallwirtschaft*., Vol. 14, 995-1001, (1935).

[1935Sch2] Schramm, J., *Metallwirtschaft*., Vol. 14, pp.1047-1050 (1935).

[1936Tak] Takeda, S., *Sci. Rep. Res. Inst. Tohoku Univ., Honda Anniv.* No. 864 (1936).

[1937Mar] Marian, V., *Ann. Phys*., Vol. 7, pp. 459-527 (1937).

[1938Sch] Schramm, J., *Z. Metallkde*., Vol. 30, pp. 122-135 (1938), in German.

[1944Ray] Raynor, G.V., *Annotated Equilibrium Diagram Series*, No. 3, Institute of Metals, London (1944).

[1952Hes] Hess, J.B. and Barret, C.S., *Trans. AIME*, Vol. 194, p. 645 (1952).

[1952Pea] Pearson, W.B. and Hume-Rothery, W., *J. Inst. Met*., Vol. 80, pp. 641-648 (1952).

[1953Kuo] Kuo, K., *J. Iron and Steel Inst.*, Vol. 173, p. 363 (1953).

[1954Pfe] Pfey, P. and Rix, W., *Z. Metallkde*, Vol. 45, p. 116 (1954).

[1954Whi] Whitehead, K. and Brownlee, L. D., *Res. Rep* 5006, (Metrovickers Electrical Co.Ltd.) (1954).

[1955Nev] Nevitt, M.V. and Beck, P.A., *Trans. AIME*, Vol. 203, p. 669-674 (1955).

[1957Hel] Hellawell, A. and Hume-Rothery, W., *Philos. Trans. R. Soc. (London), Series A*, Vol. 249, pp. 417-459 (1957).

[1957Mei] Meijering, J.L., *Acta Metall*., Vol. 5, pp. 257-264 (1957).

[1958Han] Hansen, M. and Anderko, K., *Constitution of Binary Alloys*, McGraw-Hill, New York, 1958.

[1958Lan] Lander, J. L. and Gemer, L. J., *Trans AIME*, Vol. 175, p. 648 (1958).

[1959Agt] Agte, C., *Neue Hutte*, Vol. 2, p. 537. (1959).

[1959Hor] Hornbogen, E., *Z. Metallkde*., Vol. 50, pp. 70-74 (1959).

[1960But] Butorina, L. N. and Piskner, Z. B., *Kristallografya*, Vol. 5, p. 585 (1960).

[1960Lee] Lee, J.R., *J. Iron Steel Inst*., Vol. 194, pp. 222-224 (1960).

[1960Sch] Schwarzkolpf, P., Leszynsti, W., Benesousky, F., *Cemented Carbides*, New York, Macmillan, (1960).

[1961Hin] Hinnuber, J., Rudiger, O. and Kinna, W., *Powder Metall.*, Vol. 5, No. 8, p. 1 (1961).

[1962Gla] Glaiser, M. and Chipman, J., *Trans. AIME*, Vol. 224, pp. 1278-1279 (1962).

[1962Mas] Massalski T.B. and King, H.W., *Acta Metall*., Vol. 10, pp. 1171-1181 (1962).

[1962Kun] Kunze, G., *Z. Metallkde*., Vol. 53, pp. 329-341 (1962).

[1962Par] Parthe, E. and Sadagopan, V., *Montash. Chem*., Vol. 93, p. 263 (1962).

[1962Wat] Waterstrat, R.M., *Trans. AIME*, Vol. 224, pp. 240-243 (1962).

[1963Jol] Jolley, W. and Hull, D., *J. Inst. Met*., Vol. 92, pp. 129-135 (1963/64).

[1964Cha] Chaporova, I. N., Tretyakov, V. I., Shchetling E. A. and Makarenko, T. G., in S. I. Bashkirov (ed.), *Hardmetals Production Technology and Research in USSR*, Pergamon, Oxford, p. 172 (1964).

[1964Edw] Edwards, R. and Raine, T., *Proc. 1st Plansee Semin.*, Metallwerk Plansee, Reutte, 1953, p. 232, Pergamon, Oxford, p. 172, (1964).

[1965Fis] Fischmeiter, H.F. and Exner, H. E., *Planseeber Pulvermet.*, Vol. 13, p.17 (1965).

[1965Sar] Sara, R.W., *J. Am. Cerm. Soc*., Vol. 48, p. 251 (1965).

[1965Sch] Schumann, H., *Wiss. Z. Uni. Rostoct*, Vol. 19, pp.685-693 (1978)

[1965Wil] Willens, R. and Behier, E., *Appl. Phys. Let*., Vol. 7, p. 25 (1965).

[1966Geb] Gebhradt, E., Fromm, E. and Roy, U., *Z. Metallkde*, Vol. 57, p. 732 (1966).

[1966Rud] Rudy. E., Windisch, S. and Hoffman, J. R., *Report AFML-TR-65-2*, Part 1, Vol. 6, Wright-Patterson, Air Force Base, Ohio (1966).

[1967Gol] Goldschmitdt, H.J., *Interstitial Alloys*, Butterworth, London (1967).

[1967Roc] Rocquet, P., Jegaden, G. and Petit, J.C., *J. Iron Steel Inst*., Vol. 205, pp. 437-441 (1967).

[1967Kra] Krainer E. and Robitsch, J., *Planseeber Pulvermet*., Vol. 15, p. 27 (1967).

[1967Neu] Neumeier, L.A. and Holman, J.L., *U.S. Bur. Mines Rep. Invest*., p. 6956 (1967).

[1967Rud] Rudy, E. and Holffman, J.R., *Planseeber Pulvermet*., Vol. 15, p. 174 (1967).

[1967Sch] Schumann, H., *Trans. Metallography*. Vol. 4, pp. 275-383 (1967).

[1967Tan] Tanaka, M., Suzuki T. and Komura, J., *Bull. Tokyo Inst. Technol.*, Vol. 82, p.65 (1967).

[1967Tel] Telegus, V.S., Gladyshevskiy, Yu.I. and Kripyakevich, P.I., *Kristallografya*, Vol. 2, pp. 936-940 (1967).

[1968Fil] Filimonenko, V.N. and Pivovarov, L., *Metallovedeniye i Teximicheskaya Obrabotka Metallove*., Vol. 9, p. 58 (1968).

[1968Jel] Jellinghuas, W., *Arch Eisenhuttenwesen*, Vol. 39, p.705 (1968).

[1968Yvo] Yvon, K., Nowotny, H. and Benesovsky, F., *Monastsh. Chem*., Vol. 99, pp. 726-731 (1968).

[1968Nag] Nagakur, S. and Oketani, S., *Trans. Iron Steel Instit.* (Japan), p. 256 (1968).

[1969Hum] Hume-Rothery, W., *Atomic Theory for Students of Metallurgy*, The Institute of Metals, London, 1969 (fifth reprint).

[1970Mos] Moskowitz, D., Ford N.J. and Humenik, M., Jr., *Int. J. Powder Metall.*, Vol. 6, No. 4, p.55. (1970).

[1970Ste] Stevens, E.R. and Carlson, O.N., *Metall. Trans*., Vol. 1, pp. 1267-1271 (1970).

[1970Pal] Pallock, C.B. and Stadelmair, H.H., *Metall. Trans*. Vol. 1, p. 767 (1970).

[1971Arb] Arbuzov, M.B. and Kayenko, B.V., *UZFh.*, Vol. 16, pp. 1421-1427 (1971).

[1971Bas] Bastow, B.D. and Kirkwood, D.H., *J. Inst. Met*., 99, 277-283 (1971).

[1971Fee] Feest E.A. and Doherty, R.D., *J. Inst. Met*., Vol. 99, pp. 102-103 (1971).

[1971Gre] Greenbank, J.C., J. Iron and Steel Inst., Vol. 205, p. 986 (1971).

[1971Lug] Lugscheider E. and Ettmayer, P., *Monatsh. Chem*., Vol. 102, pp. 1234-1244 (1971).

[1971Tsi] Tsioplakis, K. and Gödecke, T. *Z., Metallkde*, Vol. 62, pp. 680-681 (1971), in German.

[1972Lia] Liang, W.W., Franks, J.W. and Chang, Y.A., *Metall. Trans*., Vol. 3, pp. 2555-2556 (1972).

[1972Wag] Wagner, C., *Act. Metall.*, Vol. 20, p. 803 (1972).

[1973Bar] Barrat, C.R., Nix, W.D. and Tetelman, A.S., *The Principles of Engineering Materials*, p. 72, Prentice Hall, NJ, USA (1973).

[1973Hul] Hulgren, H., Desai, P., Hawkins, D., Gleiser, M. and Kelley, K., *Properties of Binary Alloys*, ASM, Metals Park, p. 536 (1973).

[1973Kuh] Kuhlmann, H.H., *Tech. Wiss. Abhand. Osram Ges*., Vol. 11, p. 328 (1973).

[1974Bud] Budurov, S., Vasilev, G. and Nenchev, N., *Z. Metallkde*, Vol. 65, No. 11, pp. 681-683 (1974), in German.

[1975All] Allen, S.M. and Cahn, S.M. *Acta Metall*., Vol. 23, pp. 1017-1026 (1975).

[1975Suz] Suzuki T. and Hagiwara, M. *Trans. Jpn. Inst. Met*., Vol. 16, pp. 473-479 (1975).

[1975Bar] Barlow, G., Presented at *Proc. 4th Eur. Powder Metallurgy Symp., Grenoble, May 1975*, Société Franqaise de Métallurgie, Paris.

[1975Eme] Emeleus, H.J. and Sharpe, A.G. *Advances in Inorganic Chemistry and Radiochemistry*, Vol. 17, Academic Press Inc. (1975).

[1975Fie] Fiedler, M.L. and Stadelmaier, H.H., Z. *Metallkde*, Vol. 66, p. 402. (1975).

[1977Ber] Bergstrom, M., *Mater. Sci. Eng*., Vol. 4, p.257 (1977).

[1977Mos] Moskowitz, D., in Hausner, H. H. and Taubenblat, P. V., *Modern*

Developments in Powder Metallurgy, Vol. 10, Metal Powder Industries Federation, Princeton, NJ, p. 543 (1977).

[1977Pra] Prakash, L, *KfK-Ext., 6/77-1,* p. 52 (Kernforschungs zentrum Karlsruhe GmbH), (1977).

[1977Uhr1] Uhrenius, B. and Harvig, H., *Met. Sci.*, Vol. 9, p. 67 (1977).

[1977Uhr2] Uhrenius, B. and Frondell, S., *Met. Sci.*, Vol. 11, p.73 (1977).

[1978Kau] Kaufman, L. and Nesor, H., *Calphad*, Vol. 2, pp. 81-108 (1878).

[1978Pra] Prakash, L, *KfK-Ext., 6/78-1,* p. 87 (Kernforschungszentrum Karlsruhe GmbH), (1978).

[1978She] Shevchuk, L.A., Dudetskaya, L.R., Gurinovich, V.I. and Tkacheva, V.A., *Vestsi Akad. Navuk BSSR, SER, FIZ-TEKH NAVUK*, Vol.1, p. 43 (1978).

[1978Shi] Shimizu, K. and Tanaka, Y., *Trans. Jpn. Inst. Met*., Vol. 19, pp. 685–93. (1978).

[1979Fre] Freytag, J., *Ph.D. Thesis*, Universitat Stuttgart, 1977, (cited by H.E. Exner, *Int. Metals. Rev.*, No. 4, p.149 (1979)).

[1979Yih] Yih, S.W.H. and Wang, C.T., T*ungsten: Sources, Metallurgy, Properties, and Applications*, 1st Edn, Plenum Publishing Corporation, New York (1979).

[1979Mor] Morton, A.H., *Acta Metall*., Vol. 27, No. 5, pp.863-867 (1979).

[1980Kos] Koester, W. and Goedecke, T., *Z. Metallkde*, Vol. 71, pp. 765-769 (1980), in German.

[1980Sch] Schuermann, E. and Kaiser, H.-P. *Arch Eisenhüttenwes*, Vol. 51, pp. 325-327 (1980), in German.

[1980Sch] Schmid-Fetzer, R., *Beitrag zur thermodynamic der Komponenten in Mehrstoffleggieurungen angewandt auf metallische systeme*, Habillitationsschrift Technishe Universitat Clausthal (1980).

[1981Hol] Holleck, H., *Binare, und ternar Carbide und Nitride der Ubergangsme talle und ihre Phasenbenziehungen,* KFK 3087B, Institut fur Material und Festkorperforschung, Kernforchungszentrum, Karlruhe (1981).

[1982Bet] Betteridge, W., *Cobalt and its Alloys*, John Wiley and Sons, New York (1982).

[1982Has] Hasebe, M., Oikawa, K. and Nishizawa, T., *J. Jpn. Inst. Met*., Vol. 46, pp. 577-583 (1982), in Japanese.

[1982Smi] Smith, J.F. and Carlson, O.N., The (Manganese-Vanadium) system, *J. Phase Equilibria*, Vol. 2, No. 4, pp. 473-478 (1982).

[1983Col] Coltters, R.G. and Belton, G.R., *Metall. Trans*., Vol. 14A, p. 1915 (1983).

[1984Gab] Gabriel, A., *Thesis,* Institut National Polytechnique de Grenoble (1984).

[1984Mur] Murakami, Y., Kachi, S. and Nakanishi, N., *Trans. Jpn. Inst. Met*., Vol. 25, No.1, pp. 19-22 (1984).

[1984Oha] Ohtani, H., Hasebe, M. and Nishizawa, T., *Trans. ISIJ*, Vol. 24, pp. 857-862 (1984).

[1984Upa] Upadhyaya, G.S., (Ed.), *Sintered Metal-Ceramic Composites*, Elsevier, Amsterdam, p. 41. (1984).

[1985Ger] German, R.M., *Liquid Phase Sintering*, Plenum, New York 1985.

[1985Has] Hasebe, M., Ohtani, H. and Nishizawa, T., *Met. Trans*., Vol. 16A, pp. 913-916 (1985).

[1985Mio] Miodownik, A.P., *J. Less-Common Met*., Vol. 114, No.1, pp. 81-88 (1985).

[1986Gab] Gabriel, A., Pastor, H., Deo, D.M., Basu, S. and Allibert, C.H., *Int. J. Ref. Hard Mater.* Vol. 5, p. 215 (1986).

[1986Gri] Griger, A., Stefaniay, V. and Turmezey, T., *Z. Metallkde*, Vol. 77, pp. 30-35 (1986).

[1986Gus] Gustafson, P., *Mater. Sci. and Tech*. Vol. 2, p. 653 (1986).

[1986Kaj] Kajihara, M., Kikachi, M. and Tanaka, R., Tetsu-to-Hagneé, *J. Iron Steel* Inst., Japan, Vol. 72, No. 7, p. 862 (1986).

[1986Sch] Schmidt, I., *Proceedings of the International Conference on Martensitic Transformations.* The Japan Institute of Metals, Nara, Japan p. 497– 502. (1986).

[1987Gul] Guillermet, A.F., *Z. Metallkde*, Vol. 78, p. 7007 (1987).

[1987Gus] Gustafson, P., Gabriel, A. and Ansara, I., Z. *Metallkde.*, Vol. 78, p. 15 (1987).

[1987Rud] Rud, A.D., Ustinov, A.I. and Chuistov, K.V., *Metallofizika*, Vol. 9, p. 56 (1987).

[1987Wac] Wachtel E. and Bahle, J., *Z. Metallkde.*, Vol. 78, pp. 229-232 (1987), in German.

[1988Ho] Ho-Yi, L. and Jinghui, Y., *Mod. Dev. In P/M*, (P.U. Gummeson and D.A. Gustafuson, Eds.), Metal Powder Industries Federation, NJ, USA, Vol. 19, p. 25 (1988).

[1988Pen] Penrice, T.W., *Carbide Tool J*., Vol. 20, No. 4, pp. 12–15 (1988).

[1988Upa] Upadhyaya, G.S. and Bhaumik, S.K., *Mat. Sci. and Eng.,*Vol. 231, pp. 249-256 (1988).

[1989Ant] Anton, D.L., Shah, D.M., Duhl, D.N. and Giamei, A.F., *J.O.M.,* Vol. 41, p.12 (1989).

[1989ASM] ASM International, *ASM Eng. Mat. Ref. Book*, p. 182 (1989).

[1989Fle] Fleischer, R.L., Dimidick, D.M. and Lipsitt, H.A., *Ann. Rev. Mater. Sci*., Vol. 19, p. 231 (1989).

[1989Gar] Gardon, M., Etienne, S. and Fantozzi, G., *Euro-Ceramics*, (G. de With, R.A. Terpstra and R. Metselaar, Eds.), Elsevier Applied Science, New York, Vol. 3. p. 3356 (1989).

[1989Gui] Guillermet, A.F., *Z. Metallkde.*, Vol. 80, p. 83 (1989).

[1989Smi] Smith, J.F., Carlson O.N. and Nash, P.G., in J.F. Smith (Ed.), *Phase Diagrams of Binary Vanadium Alloys,* American Society for Metals, Metals Park, OH, (1989).

[1990Mas] Massalski, T.B., *Binary Alloy Phase Diagrams*, ASM International, (1990), Ohio, USA.

[1991Cha] Chakrabarti, D.J., Laughlin. D.E., Chen. S.W. and Chang Y.A. *Phase Diagrams of Binary Nickel Alloys,* (P. Nash, Ed.), ASM International, Materials Park, OH, pp. 85-95 (1991).

[1991Far] Farroq, T. and Davies, T.J., *Int. J. Powder Metall*., 27, Vol. 4, pp. 347–355 (1991).

[1991Nas] Nash, P. and Pan Y.Y., in *Phase Diagrams of Binary Nickel Alloys*, (P. Nash, Ed.), ASM Intl., Materials Park, OH, 1991, pp. 382-390.

[1990Lar] Larsen-Basse, J., *Scripta Metallurgica et Materialia*, Vol. 24, No. 5, pp. 821-826 (1990).

[1991ICD] International Centre for Diffraction Data, Powder Diffraction Search Manual, *Hanawalt Method Inorganic*, Swarthmore, PA USA (1991).

[1991Ish] Ishida, K. and Nishizawa T., *J. Phase Equilibra*, Vol. 12, pp. 417-411 (1991).

[1991Kak] Kakeshita, T., Wayman, C.M., *Mater. Sci. Eng*., Vol. A 141, pp. 209–219 (1991).

[1992Tra] Tracey, V.A., *Int. J. Refract. Metals Hard Mater*., Vol. 11, pp.137–149 (1992).

[1992Uhr] Uhrenius, B., *Powder Metall*. Vol. 35 No. 3, p. 203–210 (1992).

[1993Kat] Kattner, U.R. and Burton B.P., Al-Fe (Aluminum-Iron), Phase Diagrams of Binary Iron Alloys, *ASM International*, Materials Park, OH, USA (1993).

[1995Bro] Brookes, K.J.A., *Metal Powder Report*, Vol. 50 (12), p. 22 (1995).

[1994McH] McHale, A.E., *Phase Equilibria Diagrams – Phase Diagrams for Ceramists*, Vol. 10, p. 8969, The American Ceramic Society, Westerville, OH, USA (1994).

[1994Tel] Telle, R., *Boride and Carbide Ceramics, in Structure and Properties of Ceramics*, Vol. 11, Ed. M. V. Swain, VCH, New York (1994).

[1995Vil] Villars, P., Prince, A. and Okomoto, H., *Handbook of Ternary Alloy Phase Diagrams, ASM International*, USA (1995).

[1996OQu] O'Quigley, D., *MSc dissertation*, University of Witwatersrand, Johannesburg, (1996).

[1996Sto] Stoloff, N.S. and Davis, R.G., *Prog. Mater. Sci*., Vol. 13, p.1 (1996).

[1997Mun] Munroe, P.R., *Mater. Forum*, Vol. 21, p. 79 (1997).

[1997Sch] Schneibel, J.H., *Intermetallics*, Vol. 5, p. 61 (1997).

[1998Bro] Brooks, K.J.A., *Hardmetals and Other Hard Materials*, 3rd edition, International Carbide Data, East Barnet, Hertfordshire, England (1998).

[1998Upa] Upadhyaya, S.G., *Cemented Tungsten Carbides, Properties, Properties and Testing*, Noyes, NJ, USA, p. 13 (1997).

[1999Bha] Bhaumik, S.K., *Mater. Sci. Tech.*, Vol. 7, p. 723 (1999).

[2001And] Andren, H.O., *Mater. and Design*, Vol. 22, No. 6, pp. 491-498 (2001).

[2001Han] Hanyaloglu, C., Aksakal, B. and Bolton, J.D., *Materials Characterization*, Vol. 47, pp. 315– 322 (2001).

[2003Cos] Costa, F.A., Silva, A.G.P., Gomes, U.U., *Powder Technol*., Vol. 134, pp. 123–132 (2003).

[2003Gua] Gauthier, V., Robaut, F., Upadhyaya, A. and Allibert, C.H., *J. Alloys Compd*., Vol. 36, pp. 222–226 (2003).

[2003Sud] Sudaprasert, T., Shipway, P.H. and McCartney, D.G., *WEAR*, Vol. 255 pp. 943–949 (2003).

[2005Mos] Mosbah, A.Y., Wexler, D. and Calka, A., *Wear*, Vol. 258, pp. 1337–1341 (2005).

[2005Zim] Zimakov, S. Priit, K., Goljandin, D. and Peetsalu, P., *Welding & Powder Metallurgy*, Proceedings of the Jurmala International Conference Welding and Powder Metallurgy: April 28-29, Jurmala, Latvia (2005).

[2009Fer] Fernandes, C.M., Popovich, V., Matos, M., Senos A.M.R. and Vieira M.T., *Ceramics International*, Vol. 35, pp.369–372 (2009).

APPENDICES

A. XRD pattern for plasticine matched with $CaCO_3$.

B. XRD reference peaks for identified phases, from the International Centre for Diffraction Data, Powder Diffraction Search Manual.

C. E-mail describing the different standards used in analyzing the as-cast samples (UB).

D. Presentation during the course of this study.

E. Codes for the samples.

APPENDIX A: XRD PATTERN FOR PLASTICINE MATCHED WITH $CaCO_3$

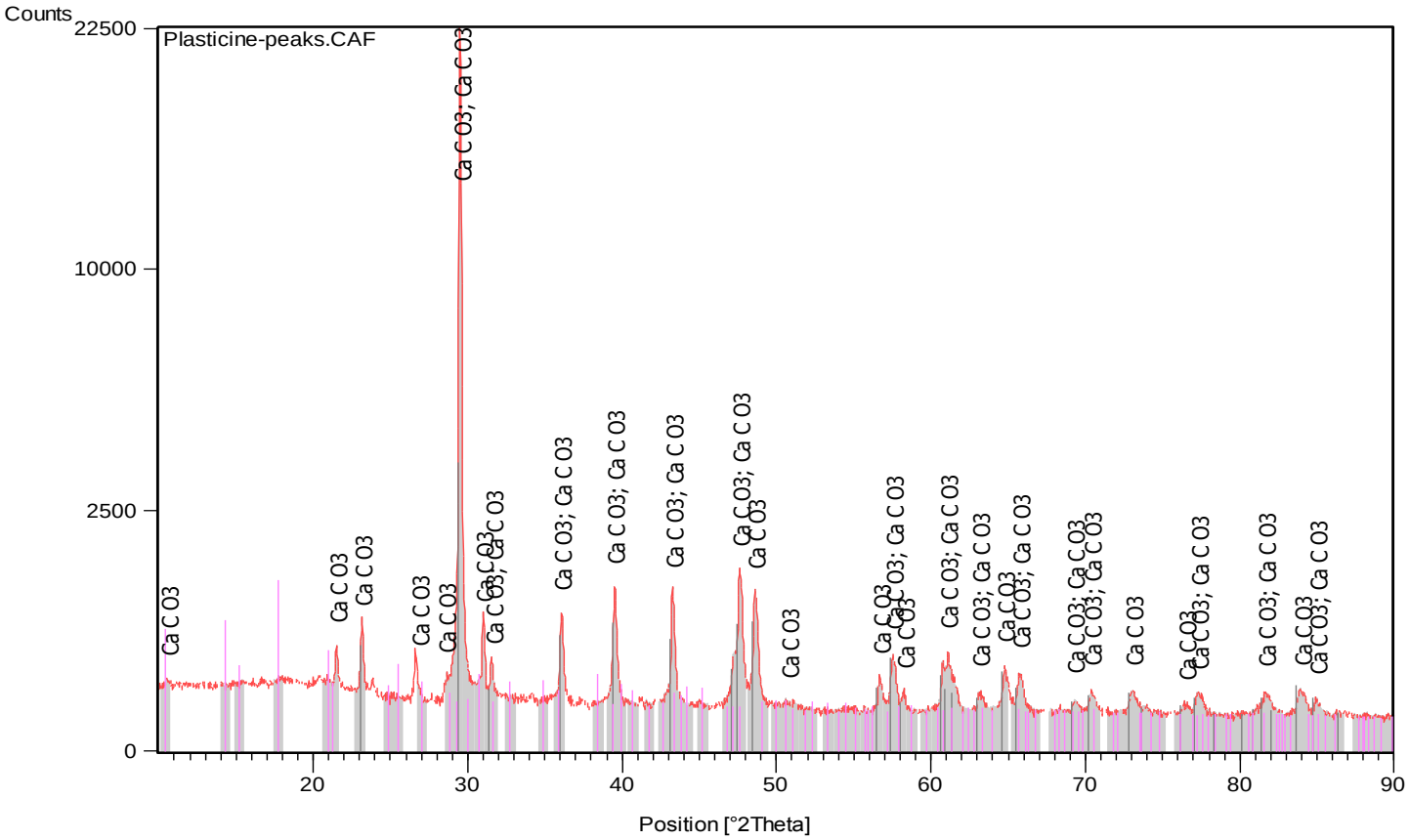


Figure A1. XRD pattern for plasticine matched with $CaCO_3$.

APPENDIX B: XRD REFERENCE PEAKS FOR IDENTIFIED PHASES, FROM THE INTERNATIONAL CENTRE FOR DIFFRACTION DATA, POWDER DIFFRACTION SEARCH MANUAL

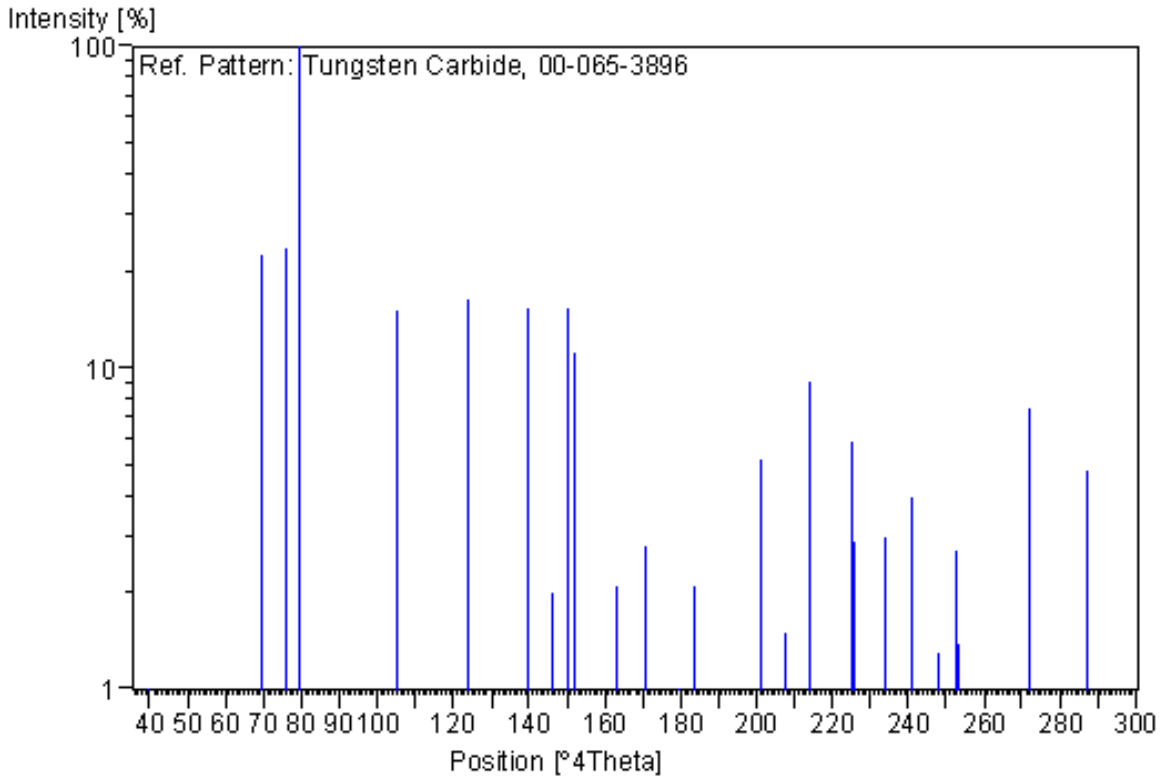


Figure B1. XRD reference peaks for W_2C, 00-065-3896.

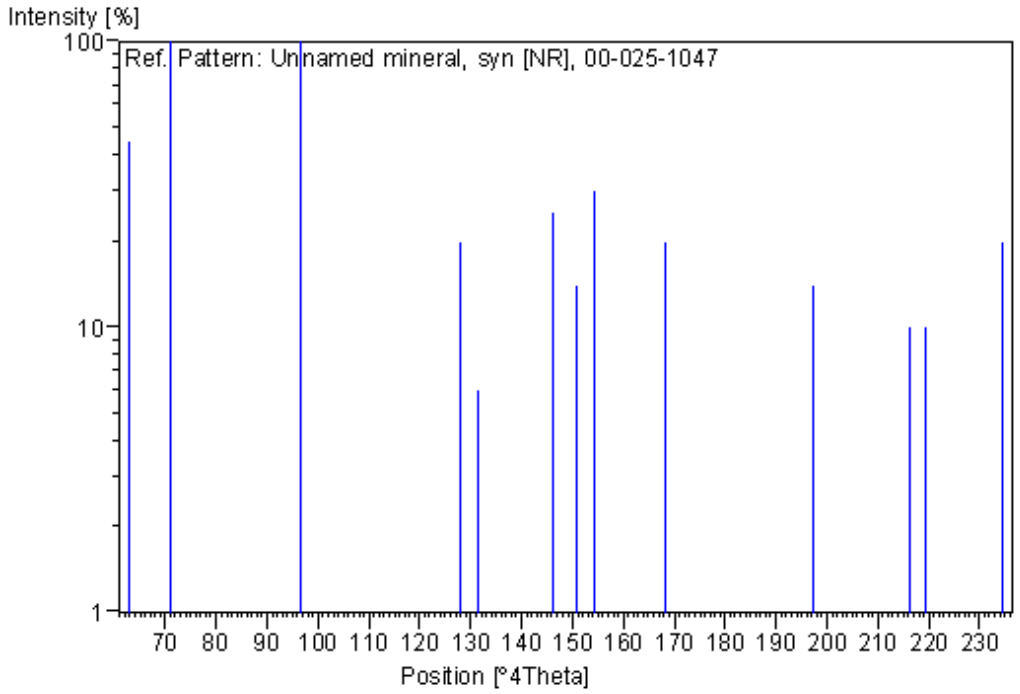


Figure B2. XRD reference peaks for WC, 00-025-1047.

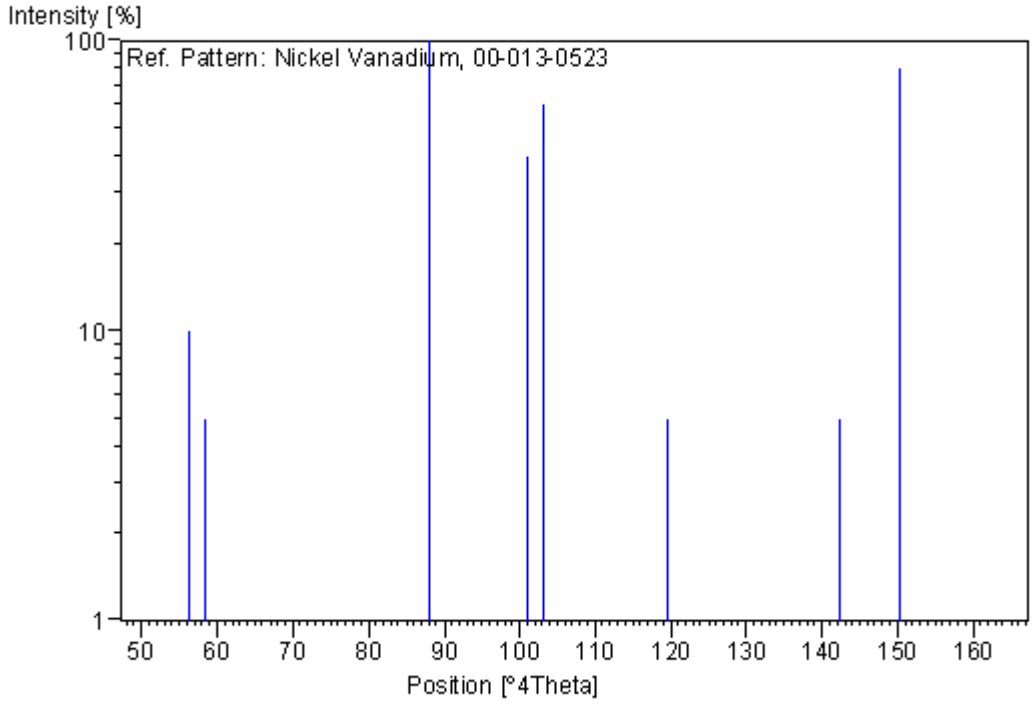


Figure B3. XRD reference peaks for Ni_3V, 00-013-0523.

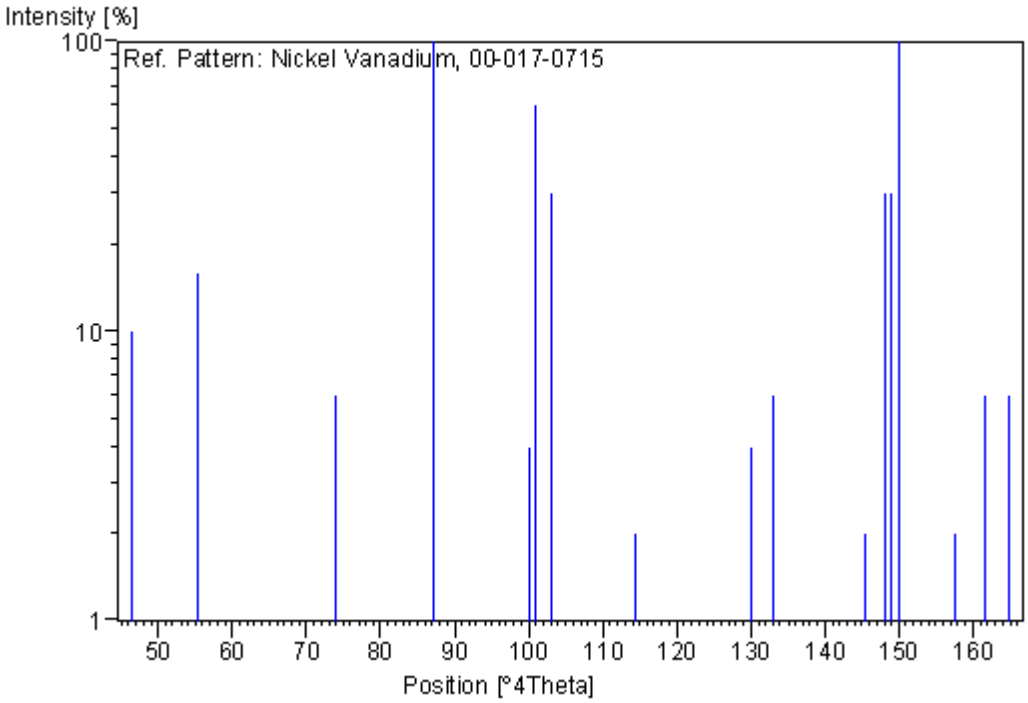


Figure B4. XRD reference peaks for Ni_2V, 00-017-0715.

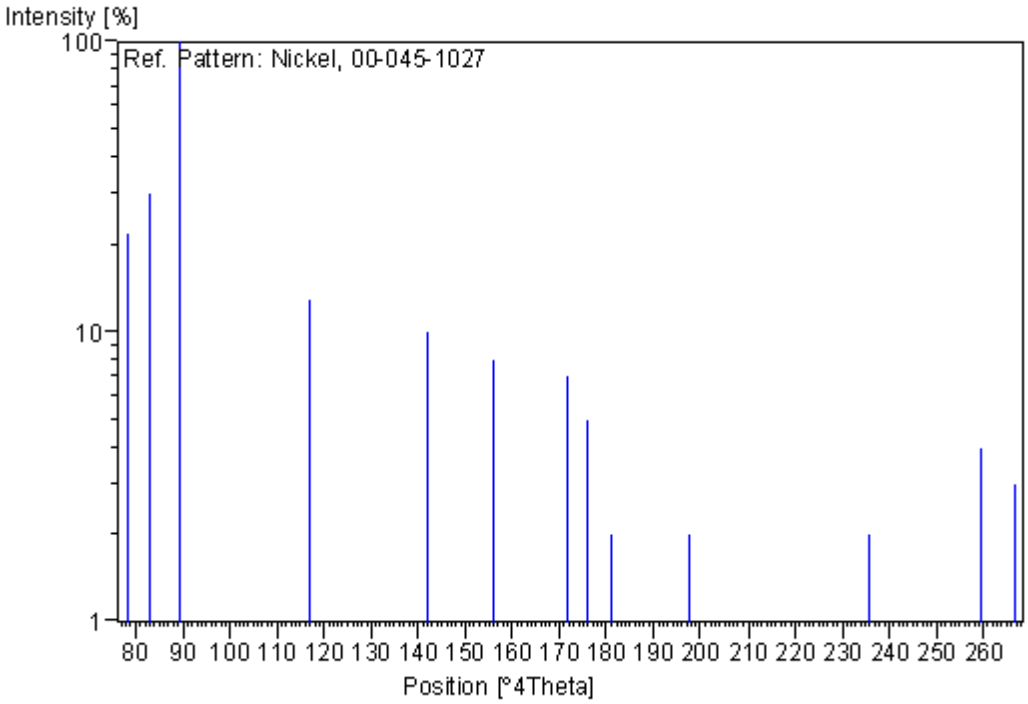


Figure B5. XRD reference peaks for Ni, 00-045-1027.

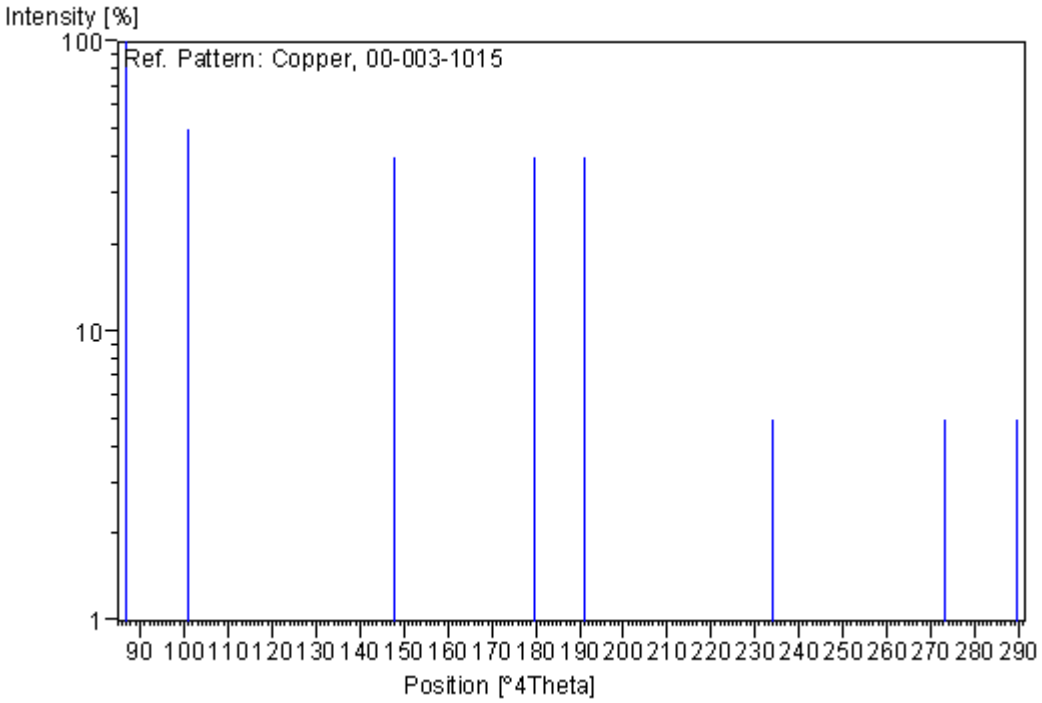


Figure B6. XRD reference peaks for Cu, 00-003-1015.

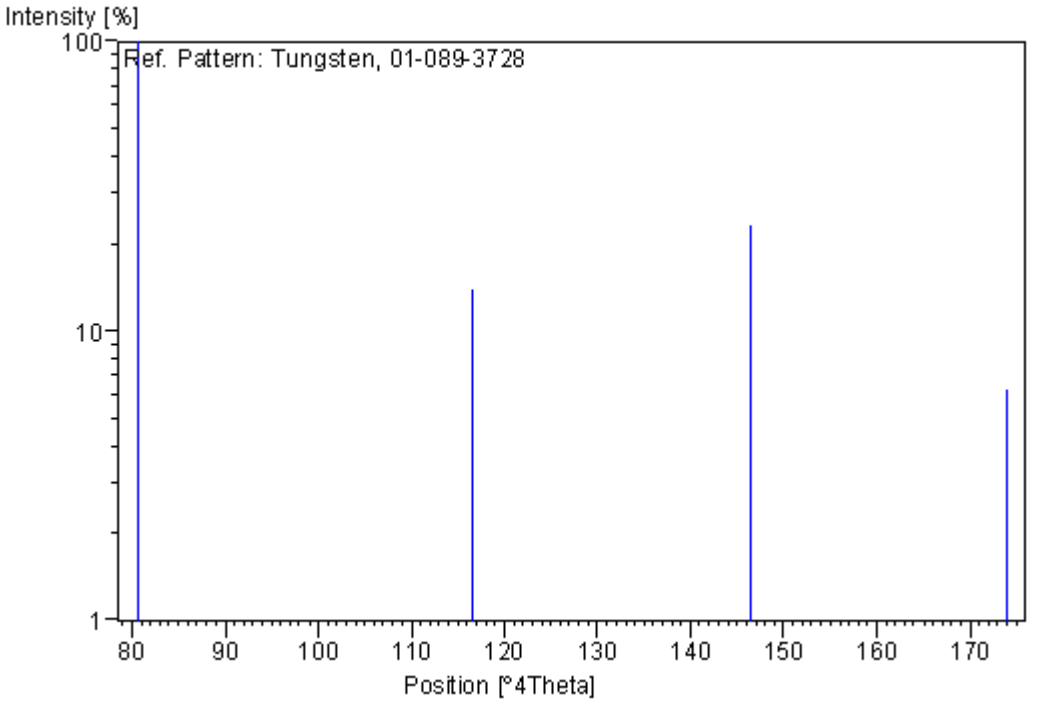


Figure B7. XRD reference peaks for W, 01-089-3728.

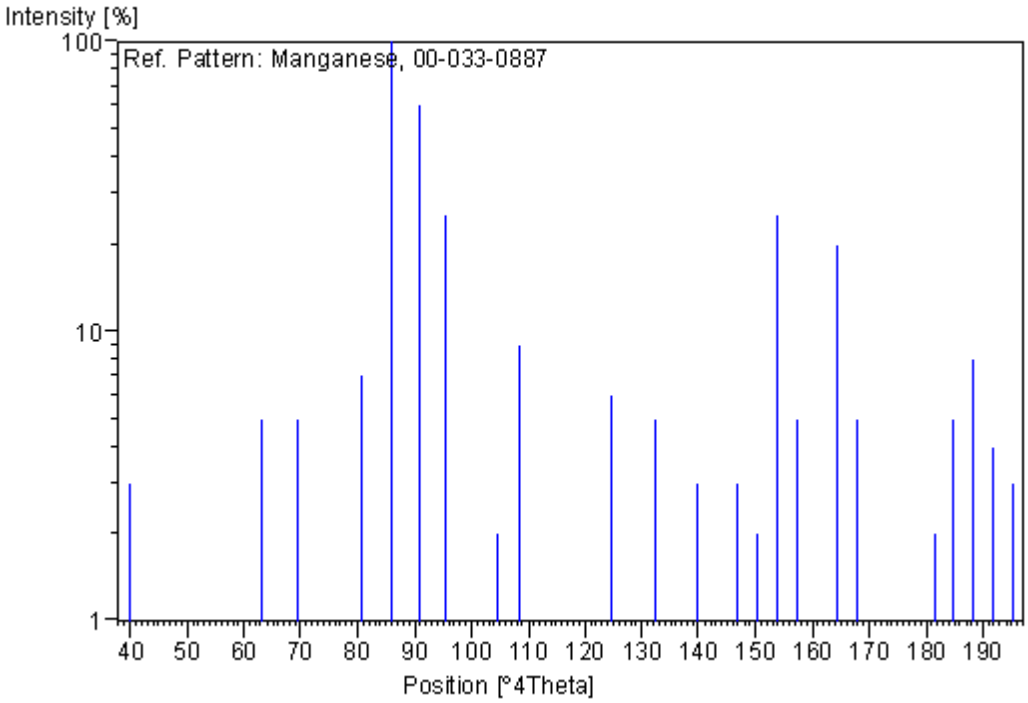


Figure B8. XRD reference peaks for Mn, 00-033-0887.

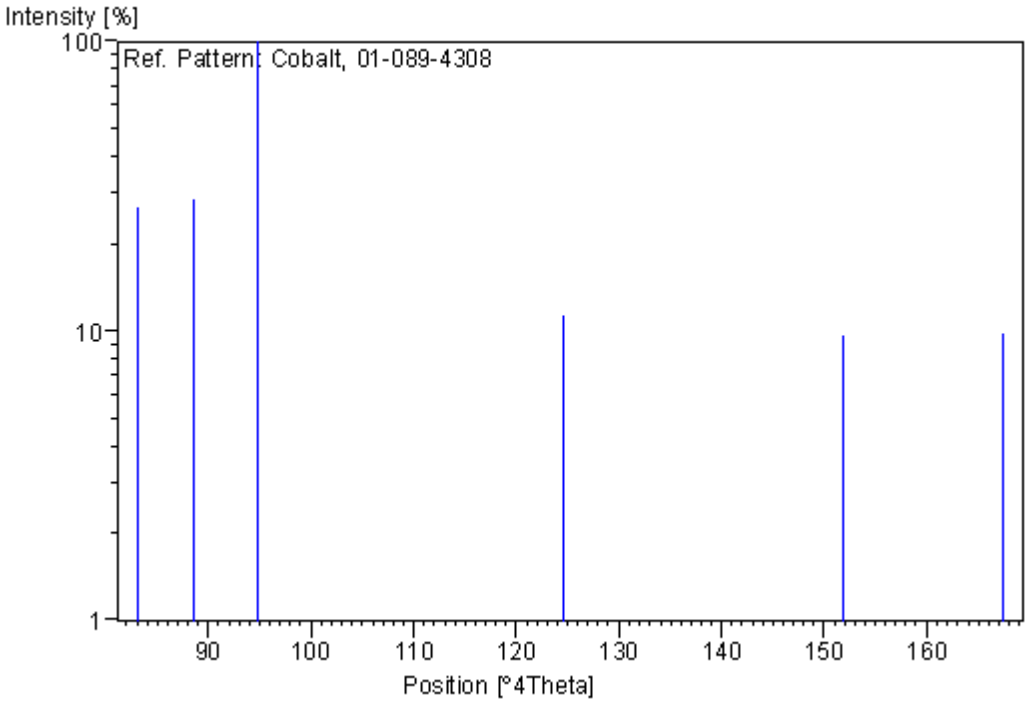


Figure B9. XRD reference peaks for Co, 01-089-4308.

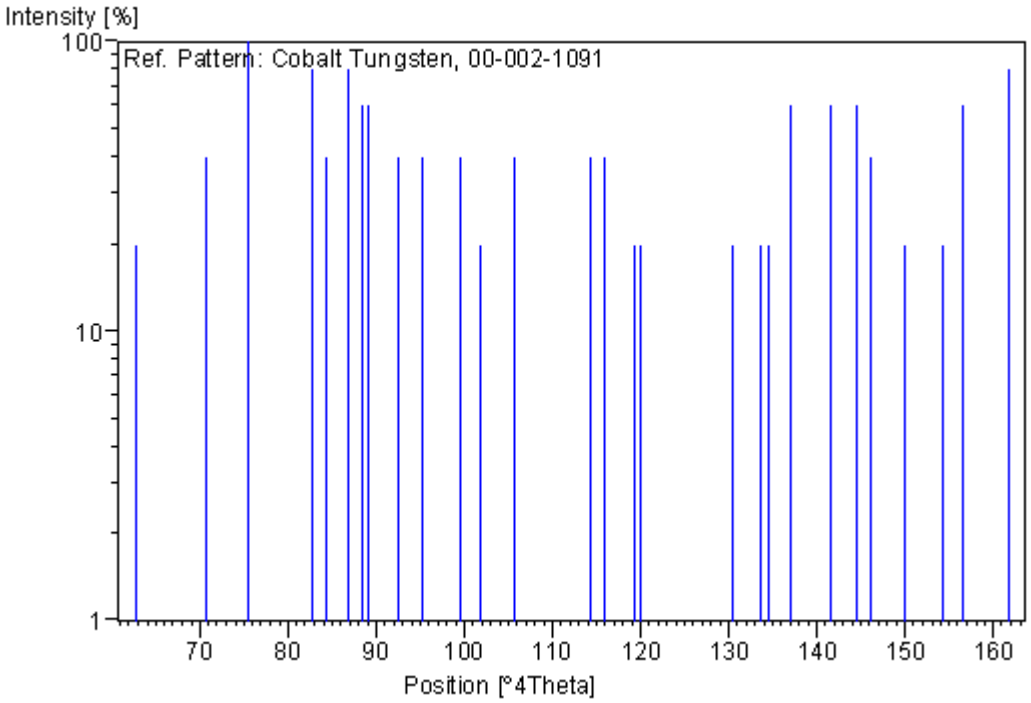


Figure B10. XRD reference peaks for Co_7W_6, 00-002-1091.

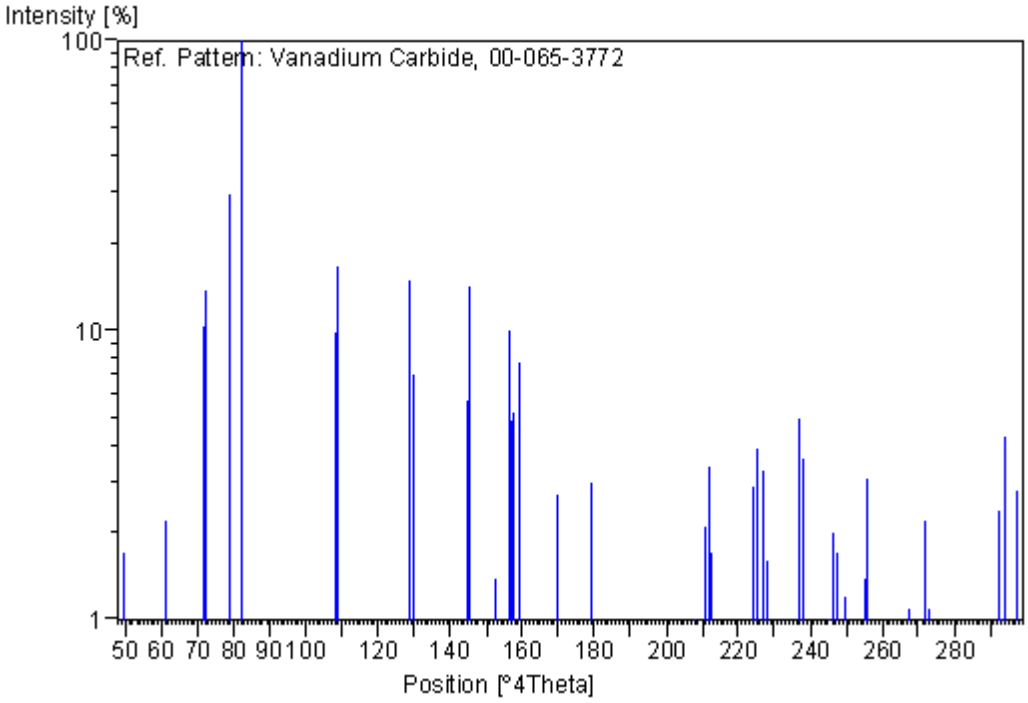


Figure B11. XRD reference peaks for V_2C, 00-065-3772.

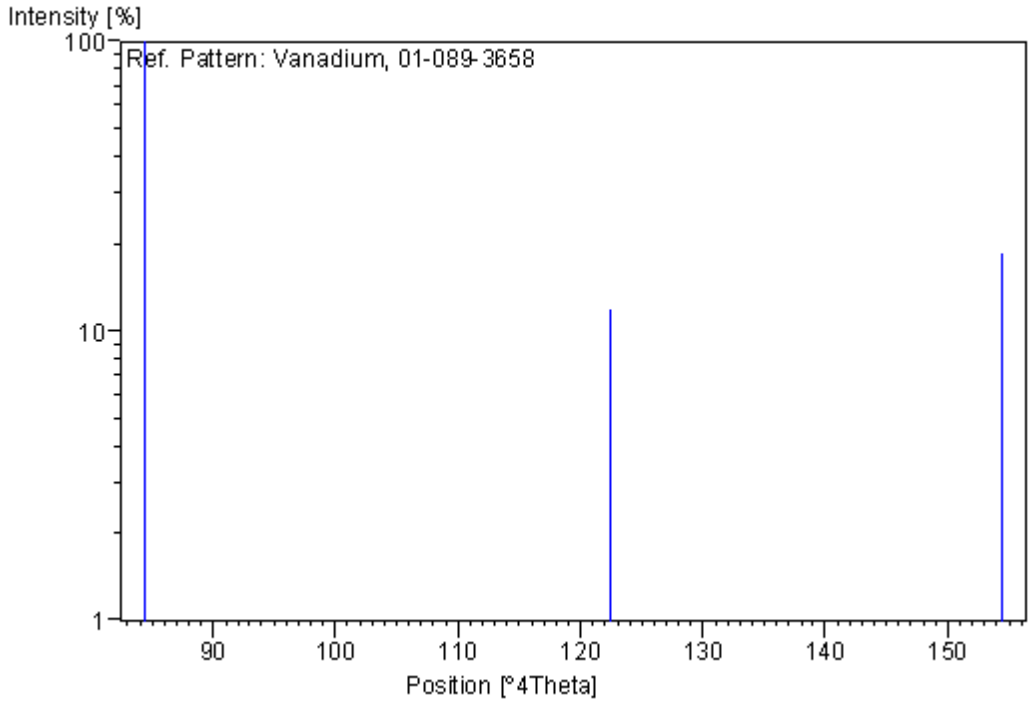


Figure B12. XRD reference peaks for V, 01-089-3658.

APPENDIX C: E-MAIL DESCRIBING THE DIFFERENT STANDARDS USED IN ANALYZING THE AS-CAST SAMPLES (UB)

Dear Lesley:

The story is just getting more bizarre with more standards Analyses of the standards as received:

We have purchased a standard with VC, WC and W2C in it from MAC UK.
I am giving you the analyses of V2O5 and VC to show that the standard less analyses is not totally miles out and give a reasonable indication if the standards might be reliable.

The WC from MAC analysed with Zero standards non normalised (contains Oxygen)
W at.% 8.2 sdev 0.1 C at% 79.8 sdev 0.5

The W2C gives:
W at.% 3.5 sdev 0.1
C at% 87.0 sdev 0.1

Clearly they are just ways off and not even suitable. What if we ignore the O and cut C from the VC and the W from pure W: this should compensate for the C in the coating since both standards are mounted in the same block and both have the same amount of additional C from the C coating

Then WC goes to
W 10.8 at%
C 89.2 at%

and W2C goes to:
W 4.8 at%
C 95.2 at%

WC supplied from WITS container 1
W 24.9 at%
C 75.1 at%

WC supplied from Wits container 2
W 21.5 at%
C 78.5.2 at%

I can play more but basically when it comes to W and C, I am lost and cannot use standards since I cannot find 1 reliable standard.

My suggestion is still to keep to standardless for David.

The standards supplied by Davis is a bit better, but again two totally different answers from the standards supplied during the two visits:

First visit (I think)
Details of the analyses below

If we analyse the V2O5 using Zero standards ZAF correction method we get:

Analyses of V2O5
C:\Users\Stephan\EDX experiment\V2O5\V2O5 area 01 larger area.spc Label :EMU University of Botswana

Acquisition Time : 13:03:21   Date : 8-Feb-2011

Elem	Wt %	At %	K-Ratio	Z	A	F
C K	21.32	37.60	0.0807	1.0893	0.3472	1.0006
O K	32.67	43.26	0.0434	1.0710	0.1241	1.0000
V K	46.02	19.14	0.4173	0.8922	1.0164	1.0000
Total	100.00	100.00				

Element	Net Inte.	Backgrd Inte.	Error	P/B
C K	58.36	1.15	1.22	50.75
O K	82.91	2.42	1.03	34.31
V K	469.83	5.84	0.43	80.43

kV: 20.00 Tilt: 0.30 Take-off: 35.21 Tc: 50.0
Det Type:SUTW, Sapphire   Res: 133.71 Lsec: 120

Lets assume the C is from the C-coating and can be ignored then:

C:\Users\Stephan\EDX experiment\V2O5\V2O5 area 01 larger area.spc Label :EMU University of Botswana

Acquisition Time : 13:03:21   Date : 8-Feb-2011

Elem	Wt %	At %	K-Ratio	Z	A	F
O K	41.89	69.65	0.0560	1.0989	0.1217	1.0000
V K	58.11	30.35	0.5384	0.9168	1.0104	1.0000
Total	100.00	100.00				

Element	Net Inte.	Backgrd Inte.	Error	P/B
O K	82.91	2.42	1.03	34.31
V K	469.83	5.84	0.43	80.43

kV: 20.00 Tilt: 0.30 Take-off: 35.21 Tc: 50.0
Det Type:SUTW, Sapphire   Res: 133.71 Lsec: 120

VC

C:\Users\Stephan\EDX experiment\VC\VC particle 01.spc Label :EMU University of Botswana

Acquisition Time : 13:11:58   Date : 8-Feb-2011

Elem	Wt %	At %	K-Ratio	Z	A	F
C K	24.11	57.41	0.0848	1.1494	0.3058	1.0006
V K	75.89	42.59	0.7233	0.9440	1.0098	1.0000
Total	100.00	100.00				

The ratio of C to V atoms should be 50:50 and since the additional C comes from the coating, the VC standard seems reasonable.

Taking the above into account, I analysed the WC and W2C using Zero standards\ I have done 3 areas and the statistical values are:

W
C

WC standard powder purchased form MAC

Large overall area 01

C:\Users\Stephan\EDX experiment\WC\WC large area 01.spc Label :EMU University of Botswana

Acquisition Time : 14:33:47   Date : 8-Feb-2011

Elem	Wt %	At %	K-Ratio	Z	A	F
C K	35.68	79.19	0.1033	1.1588	0.2497	1.0000
O K	7.55	12.59	0.0150	1.1388	0.1748	1.0000
W L	56.76	8.23	0.4537	0.7779	1.0274	1.0000
Total	100.00	100.00				

Element	Net Inte.	Backgrd Inte.	Error	P/B
C K	126.26	3.35	0.83	37.69
O K	48.52	6.95	1.49	6.98
W L	125.62	12.50	0.89	10.05

kV: 20.00 Tilt: 0.30 Take-off: 35.23 Tc: 50.0
Det Type:SUTW, Sapphire   Res: 133.71 Lsec: 120

Large Overall Area 02

Elem	Wt %	At %	K-Ratio	Z	A	F
C K	36.18	80.12	0.1049	1.1588	0.2501	1.0000
O K	7.01	11.66	0.0139	1.1388	0.1739	1.0000
W L	56.80	8.22	0.4540	0.7780	1.0274	1.0000
Total	100.00	100.00				

Element	Net Inte.	Backgrd Inte.	Error	P/B
C K	128.96	3.74	0.83	34.47
O K	45.07	7.77	1.58	5.80
W L	126.42	12.22	0.89	10.34

kV: 20.00 Tilt: 0.30 Take-off: 35.23 Tc: 50.0
Det Type:SUTW, Sapphire   Res: 133.71 Lsec: 120

Large overall area 03
C:\Users\Stephan\EDX experiment\WC\WC large area 03.spc Label :EMU University of Botswana

Acquisition Time : 14:43:34   Date : 8-Feb-2011

```
 Elem     Wt %  At % K-Ratio    Z       A       F
------------------------------------------------------------
  C K   35.70  80.19  0.1028  1.1618  0.2480  1.0000
  O K    6.73  11.36  0.0134  1.1417  0.1737  1.0000
  W L   57.57   8.45  0.4616  0.7807  1.0270  1.0000
Total  100.00 100.00

Element  Net Inte.  Backgrd  Inte. Error  P/B
-------------------------------------------------
 C K     126.59       3.93      0.84     32.18
 O K      43.37       8.17      1.63      5.31
 W L     128.65      12.20      0.88     10.55

kV: 20.00  Tilt: 0.30  Take-off: 35.23  Tc: 50.0
Det Type:SUTW, Sapphire   Res: 133.71  Lsec: 120

Then I did collect spectrum from the W2C standard purchased from

W2C Large area 01

C:\Users\Stephan\EDX experiment\W2C\W2C Large area 01.spc Label :EMU
University of Botswana

Acquisition Time  : 15:41:19   Date :  8-Feb-2011

 Elem     Wt %  At % K-Ratio    Z       A       F
------------------------------------------------------------
  C K   56.30  86.91  0.2067  1.0861  0.3380  1.0001
  O K    8.21   9.51  0.0145  1.0677  0.1654  1.0000
  W L   35.49   3.58  0.2624  0.7115  1.0390  1.0000
Total  100.00 100.00

Element  Net Inte.  Backgrd  Inte. Error  P/B
-------------------------------------------------
 C K     253.00       2.67      0.58     94.58
 O K      46.83       5.55      1.48      8.44
 W L      72.83       8.40      1.19      8.67

kV: 20.00  Tilt: 0.30  Take-off: 35.17  Tc: 50.0
Det Type:SUTW, Sapphire   Res: 133.71  Lsec: 120

 W2C Large are 02
C:\Users\Stephan\EDX experiment\W2C\W2C Large area 02.spc Label :EMU
University of Botswana

Acquisition Time  : 15:45:51   Date :  8-Feb-2011

 Elem     Wt %  At % K-Ratio    Z       A       F
------------------------------------------------------------
  C K   56.37  86.88  0.2072  1.0857  0.3386  1.0001
  O K    8.26   9.56  0.0146  1.0673  0.1654  1.0000
  W L   35.37   3.56  0.2613  0.7111  1.0391  1.0000
Total  100.00 100.00

Element  Net Inte.  Backgrd  Inte. Error  P/B
```

```
-------------------------------------------------
 C K     258.39       2.71      0.57     95.41
 O K      48.02       5.52      1.46      8.69
 W L      73.89       8.43      1.18      8.76

kV: 20.00  Tilt: 0.30  Take-off: 35.17  Tc: 50.0
Det Type:SUTW, Sapphire   Res: 133.71  Lsec: 120

W2C Large area 03
C:\Users\Stephan\EDX experiment\W2C\W2C Large area 03.spc Label :EMU
University of Botswana

Acquisition Time  : 15:49:14   Date :  8-Feb-2011

 Elem     Wt %  At % K-Ratio    Z       A       F
------------------------------------------------------------
  C K   57.33  87.14  0.2137  1.0829  0.3442  1.0001
  O K    8.28   9.45  0.0145  1.0645  0.1649  1.0000
  W L   34.39   3.41  0.2533  0.7085  1.0396  1.0000
Total  100.00 100.00

Element  Net Inte.  Backgrd  Inte. Error  P/B
-------------------------------------------------
 C K     264.92       2.40      0.57    110.38
 O K      47.57       4.97      1.46      9.56
 W L      71.20       8.95      1.21      7.96

kV: 20.00  Tilt: 0.30  Take-off: 35.17  Tc: 50.0
Det Type:SUTW, Sapphire   Res: 133.71  Lsec: 120

Then I got two standards from David
Note remember that he used this material to create his samples!
Looking at the numbers the starting material is already bad.

1st visit standard analysed using Zero standards:

C:\Users\Stephan\WITS\David\standards\WC  330 pA Standard.spc Label :EMU
University of Botswana

Acquisition Time  : 12:56:09   Date :  6-Sep-2010

 Elem     Wt %  At % K-Ratio    Z       A       F
------------------------------------------------------------
  C K   17.26  66.27  0.0428  1.2578  0.1971  1.0000
  O K    4.93  14.21  0.0108  1.2355  0.1769  1.0000
  W L   77.81  19.52  0.6845  0.8665  1.0152  1.0000
Total  100.00 100.00

Element  Net Inte.  Backgrd  Inte. Error  P/B
-------------------------------------------------
 C K      47.71       4.18      1.43     11.40
 O K      31.57       9.64      2.06      3.27
 W L     171.04      17.13      0.76      9.98

kV: 20.00  Tilt: 0.70  Take-off: 35.76  Tc: 10.0
Det Type:SUTW, Sapphire   Res: 142.28  Lsec: 120
```

standard supplied on second visit from a different bottle?

C:\Users\Stephan\WITS\David\Sampl-a2\Satandard WC 333 Pico amp.spc Label :EMU University of Botswana

Acquisition Time : 17:12:10   Date : 22-Feb-2010

Elem	Wt %	At %	K-Ratio	Z	A	F
C K	14.98	65.12	0.0362	1.2783	0.1892	1.0000
O K	3.60	11.76	0.0078	1.2555	0.1734	1.0000
W L	81.42	23.12	0.7297	0.8845	1.0132	1.0000
Total	100.00	100.00				

Element	Net Inte.	Backgrd	Inte. Error	P/B
C K	39.73	1.42	1.50	27.88
O K	22.72	2.51	2.12	9.06
W L	181.83	17.50	0.74	10.39

kV: 20.00 Tilt: 0.00 Take-off: 35.06 Tc: 10.0
Det Type:SUTW, Sapphire   Res: 145.25 Lsec: 120

You see my problem?
You must tell me from where to cut the standard and I will do it but this is all basically total rubbish!

Assume the zero standards are useless, then I can cut a W standard from Pure W and C from VC.
Here is the analyses of the VC standard analysed using a standardless analyses

:\Users\Stephan\EDX experiment\VC\VC particle 01.spc Label :EMU University of Botswana

Acquisition Time : 13:11:58   Date : 8-Feb-2011

Elem	Wt %	At %	K-Ratio	Z	A	F
C K	24.11	57.41	0.0848	1.1494	0.3058	1.0006
V K	75.89	42.59	0.7233	0.9440	1.0098	1.0000
Total	100.00	100.00				

Element	Net Inte.	Backgrd	Inte. Error	P/B
C K	67.54	1.21	1.13	55.90
V K	896.60	8.96	0.31	100.09

kV: 20.00 Tilt: 0.30 Take-off: 35.21 Tc: 50.0
Det Type:SUTW, Sapphire   Res: 133.71 Lsec: 120

From this you can see it is closer to the stoichiometic of 50/50 at %. Thus the value given of 18.3 was altered to 18.7 with V being the balance, to get a analysis closer to the 50/50 stoichiomety.

Then I used standards of Pure W and the C from the VC to analyse the supplied WC and W2C

WC analysed:
C:\Users\Stephan\EDX experiment\WC\WC large area 01.spc Label :EMU University of Botswana

Acquisition Time : 14:33:47   Date : 8-Feb-2011

Elem	Wt %	At %	K-Ratio	Z	A	F
C K	35.05	89.20	0.1174	1.1910	0.2324	1.0000
W L	64.95	10.80	0.6426	0.8073	1.0231	1.0000
Total	100.00	100.00				

Supplied W2C

C:\Users\Stephan\EDX experiment\W2C\W2C Large area 01.spc Label :EMU University of Botswana

Acquisition Time : 15:41:19   Date : 8-Feb-2011

Elem	Wt %	At %	K-Ratio	Z	A	F
C K	56.44	95.20	0.2352	1.1090	0.3094	1.0000
W L	43.56	4.80	0.3726	0.7329	1.0349	1.0000
Total	100.00	100.00				

Element	Net Inte.	Backgrd Inte. Error	P/B
C K	253.00	2.67	0.58	94.58
W L	72.83	8.40	1.19	8.67

kV: 20.00 Tilt: 0.30 Take-off: 35.17 Tc: 50.0
Det Type:SUTW, Sapphire   Res: 133.71 Lsec: 120

WC supplied from Wits bought from container 1

C:\Users\Stephan\WITS\David\standards\WC 330 pA Standard.spc Label :EMU University of Botswana

Acquisition Time : 12:56:09   Date : 6-Sep-2010

Elem	Wt %	At %	K-Ratio	Z	A	F
C K	16.43	75.05	0.0444	1.2899	0.1874	1.0000
W L	83.57	24.95	0.8749	0.8949	1.0118	1.0000
Total	100.00	100.00				

Element	Net Inte.	Backgrd Inte. Error	P/B
C K	47.71	4.18	1.43	11.40
W L	171.04	17.13	0.76	9.98

kV: 20.00 Tilt: 0.70 Take-off: 35.76 Tc: 10.0
Det Type:SUTW, Sapphire   Res: 142.28 Lsec: 120

WC supplied by Wits
holder 1

C:\Users\Stephan\WITS\David\sampl-a6\Standard WC 333 Pico Amp.spc Label :EMU
University of Botswana

Acquisition Time : 16:34:44   Date : 23-Feb-2010

Elem	Wt %	At %	K-Ratio	Z	A	F
C K	19.28	78.52	0.0554	1.2725	0.1926	1.0000
W L	80.72	21.48	0.8802	0.8797	1.0140	1.0000
Total	100.00	100.00				

Element	Net Inte.	Backgrd Inte. Error	P/B
C K	59.63	3.69	1.25	16.15
W L	172.07	16.50	0.76	10.43

kV: 20.00 Tilt: 0.00 Take-off: 34.67 Tc: 50.0
Det Type:SUTW, Sapphire   Res: 131.05 Lsec: 120

APPENDIX D: PRESENTATIONS DURING THE COURSE OF THIS STUDY

- **Kumi, D. O**., Cornish, L. A., The Study of WC-X Systems for Potential Binder for WC, Annual Hard Metals Workshop. Hofmeyr House, Wits University, Johannesburg, 20 April 2009 (oral presentation).
- **Kumi, D. O**., Cornish, L. A., A Phase Diagram of WC-X systems for Potential Binder for WC, Annual SA Powder Metallurgy Association Conference. Debtech Auditorium Crown Mines, Johannesburg, 27 October 2010 (abstract: oral presentation).
- **Kumi, D. O**., and Cornish, L. A., The Study of WC-X Systems for Potential Binder for WC, Microscopy Society of Southern Africa (2010), Forever Resorts Warmbaths, Bela-Bela. 26 October to 29 October 2010 (extended abstract: oral presentation).

APPENDIX E: CODES FOR THE SAMPLES

Nominal Sample	Code
$W_{25}:C_{25}:Ni_{45}:V_5$	A2
$W_{25}:C_{25}:Ni_{43}:V_7$	A5
$W_{25}:C_{25}:Ni_{42.5}:Zn_{7.5}$	A3
$W_{25}:C_{25}:Ni_{45}:Zn_5$	A6
$W_{25}:C_{25}:Co_{30}:Mn_{20}$	A9
$W_{25}:C_{25}:Co_{12.5}:Mn_{37.5}$	A8
$W_{25}:C_{25}:Cu_{42.5}:Ni_{7.5}$	A4
$W_{25}:C_{25}:Cu_{40}:Ni_{10}$	A1
$W_{45}:C_{45}:Ni_{40}:Zn_{10}$	A7
$W_{25}:C_{25}:Cu:_{45}:Zn_5$	A12
$W_{25}:C_{25}:Mn_{25}:V_{25}$	A11
$W_{25}:C_{25}:Mn_{2.5}:Cu_{47.5}$	A10

Table E1. Codes for the samples.